

University of St Andrews



Full metadata for this thesis is available in
St Andrews Research Repository
at:

<http://research-repository.st-andrews.ac.uk/>

This thesis is protected by original copyright

Studies on oxygen excess perovskite-based titanates for SOFC fuel electrodes

A thesis presented for examination for the title of Ph.D

by

Jesús Canales Vázquez



University of St. Andrews

October 2003

Supervised by Prof. John T. S. Irvine and Dr. Wuzong Zhou



Study on nitrogen oxides particulate-
based catalysts for SOF fuel electrodes

The present study is concerned with the effect of

nitrogen oxides



TL
E532

Library of Congress

Control 506

Copyrighted by the Library of Congress, Washington, D.C.

Table of Contents

Declaration	i
Acknowledgements	ii
Abstract	iv
Chapter 1. Introduction. Fuel Cells	1
1.1. Classification	3
1.1.1. Alkaline Fuel Cells (AFCs)	3
1.1.2. Polymer Electrolyte Fuel Cells (PEFCs)	4
1.1.3. Phosphoric Acid Fuel Cells (PAFCs)	4
1.1.4. Molten Carbonate Fuel Cells	5
1.1.5. Solid Oxide Fuel Cells (SOFCs)	6
1.2. SOFC Components	7
1.2.1. Electrolyte	7
1.2.2. Interconnects	11
1.2.3. Electrodes	12
1.2.3.1. Cathode	12
1.2.3.2. Anode	14
1.3. References	18
Chapter 2. Experimental	22
2.1. Synthesis	22
2.2. X-Ray Diffraction (XRD)	23
2.2.1. Background	23
2.2.2. Experiment	25

2.3. AC Impedance Spectroscopy	25
2.3.1. Background	25
2.3.2. Temperature dependence of the conductivity	28
2.3.3. Impedance experiments	29
2.4. Four Terminal Measurements	29
2.5. Fuel Cell Tests	31
2.6. Thermogravimetric Analysis (TGA)	33
2.7. Electron Microscopy	33
2.7.1. Transmission Electron Microscopy (TEM)	34
2.7.2. Imaging	37
2.7.3. Selected Area Electron Diffraction (SAED)	44
2.7.4. Energy Dispersive Spectroscopy (EDS)	45
2.7.5. Simulation of images	48
2.7.6. Preparation of specimens	49
2.8. References	49
Chapter 3. Structural studies on the layered $\text{La}_4\text{Sr}_{n-4}\text{Ti}_n\text{O}_{3n+2}$ series	51
3.1. Introduction. Layered perovskites and cubic phases.	51
3.2. Layered structures in $\text{La}_4\text{Sr}_{n-4}\text{Ti}_n\text{O}_{3n+2}$	59
3.2.1. Synthesis conditions	60
3.2.2. XRD results	61
3.2.3. TEM studies on SrTiO_3 ($n=\infty$)	67
3.2.4. TEM studies on $\text{La}_2\text{Ti}_2\text{O}_7$ ($n=4$)	68
3.2.5. Structural elucidation of $\text{La}_4\text{SrTi}_5\text{O}_{17}$ and $\text{La}_4\text{Sr}_2\text{Ti}_6\text{O}_{20}$	74
3.2.5.1. Synthesis conditions	75
3.2.5.2. Structural elucidation of the $n=5$ member	75

3.2.4.2.1. TEM	75
3.2.4.2.2. XRD	80
3.2.5.3. Structural elucidation of the n=6 member	84
3.2.4.3.1. TEM	84
3.2.4.3.2. XRD	87
3.2.6. Intermediate members	92
3.2.5.1. TEM	92
3.2.5.2. XRD	94
3.2.7. Conclusions (layered phases)	96
3.3. Cubic phases	99
3.3.1 $\text{La}_4\text{Sr}_8\text{Ti}_{12}\text{O}_{38-\delta}$ (n=12)	99
3.3.1.1. XRD results	99
3.3.1.2. Magnetic measurements and TGA	102
3.3.1.3. Density measurements	105
3.3.1.4. TEM	109
3.3.2. $\text{La}_4\text{Sr}_{10}\text{Ti}_{14}\text{O}_{44}$ (n=14)	115
3.3.3. Discussion	119
3.4. Summary	121
3.5. References	123
Chapter 4. Electrical properties of the $\text{La}_4\text{Sr}_{n-4}\text{Ti}_n\text{O}_{3n+2}$ series	127
4.1. Introduction	127
4.2 Impedance studies of $\text{La}_4\text{Sr}_{n-4}\text{Ti}_n\text{O}_{3n+2}$	128
4.2.1. Layered Phases	128
4.2.1.1. $\text{La}_2\text{Ti}_2\text{O}_7$ (n=4)	129
4.2.1.2. $\text{La}_4\text{SrTi}_5\text{O}_{17}$ (n=5)	135
4.2.1.3. $\text{La}_4\text{Sr}_2\text{Ti}_6\text{O}_{20}$ (n=6)	139
4.2.1.4. $\text{La}_4\text{Sr}_4\text{Ti}_8\text{O}_{26}$ (n=8)	143

4.2.2. Cubic Phases	145
4.2.2.1. $\text{La}_4\text{Sr}_8\text{Ti}_{12}\text{O}_{38}$ (n=12)	145
4.2.2.2. ACIS under different atmospheres in n=12	149
4.2.2.3. $\text{La}_4\text{Sr}_{10}\text{Ti}_{14}\text{O}_{44}$ (n=14)	151
4.2.2.4. SrTiO_3 (n= ∞)	153
4.2.3. Conclusions	155
4.3. Four terminal techniques	160
4.3.1. Temperature dependence	161
4.3.2. Conductivity as a function of $\text{P}(\text{O}_2)$	163
4.3.3. Thermopower measurements	164
4.4. Fuel Cell Tests	167
4.5. Conclusions	169
4.6. References	170
Chapter 5. Sc-substituted $\text{La}_4\text{Sr}_{n-4}\text{Ti}_n\text{O}_{3n+2}$	172
5.1. Introduction	172
5.2. Synthesis	173
5.3. Structural characterisation	173
5.3.1. XRD	173
5.3.2. TGA	179
5.3.3. TEM on Sc-substituted $\text{La}_4\text{Sr}_8\text{Ti}_{12}\text{O}_{38-\delta}$	181
5.3.3.1. $\text{La}_2\text{Sr}_4\text{Ti}_{5.7}\text{Sc}_{0.3}\text{Ti}_{18.85}$ (x=0.3)	181
5.3.3.2. $\text{La}_2\text{Sr}_4\text{Ti}_{5.5}\text{Sc}_{0.5}\text{Ti}_{18.75}$ (x=0.5)	184
5.4. Electrical properties on Sc-substituted phases	189
5.4.1. $\text{La}_2\text{Sr}_4\text{Ti}_{5.7}\text{Sc}_{0.3}\text{Ti}_{18.85}$ (x=0.3)	190

5.4.2. $\text{La}_2\text{Sr}_4\text{Ti}_{5.5}\text{Sc}_{0.5}\text{Ti}_{18.75}$ ($x=0.5$)	191
5.4.2.1. Ac impedance spectroscopy	191
5.4.2.2. Four terminal techniques	193
5.4.3. $\text{La}_2\text{Sr}_4\text{Ti}_{5.0}\text{Sc}_{1.0}\text{Ti}_{18.50}$ ($x=1.0$)	194
5.4.4. $\text{La}_2\text{Sr}_4\text{Ti}_{5.0}\text{Sc}_{1.5}\text{Ti}_{18.25}$ ($x=1.5$)	197
5.5. Summary	199
5.6. References	201
Chapter 6. Nb-substituted $\text{La}_4\text{Sr}_{n-4}\text{Ti}_n\text{O}_{3n+2}$	202
6.1. Introduction	202
6.2. Structural characterisation	203
6.3. Electrical properties on Nb-substituted phases	216
6.3.1. $\text{La}_2\text{Sr}_4\text{Ti}_{5.7}\text{Nb}_{0.3}\text{Ti}_{19.15}$ ($x=0.3$)	216
6.3.2. $\text{La}_2\text{Sr}_4\text{Ti}_{5.5}\text{Nb}_{0.5}\text{Ti}_{19.25}$ ($x=0.5$)	219
6.4. Conclusions	224
Chapter 7. Conclusions	227
Appendix	231
A.1. Introduction	231
A.2. Transmission Electron Microscopy	234
A.3. Conclusions	244
A.4. References	245

DECLARATION

I, Jesús Canales Vázquez, hereby certify that this thesis, which is approximately 42000 words in length, has been written by me, that it is the record of work carried out by me and that it has not been submitted in any previous application for a higher degree.

Date 29/10/2003

Signature of ~~Candidate~~

I was admitted as a research student in November 2000 and as a candidate for the degree of Doctor of Philosophy in November 2001, the higher study for which this is a record was carried out in the University of St Andrews between 2000 ~~and 2003~~.

Date 29/10/2003

Signature of ~~Candidate~~

I hereby certify that the candidate has fulfilled the conditions of the Resolution and Regulations appropriate for the Degree of Philosophy in the University of St Andrews and that the candidate is qualified to submit this thesis in application for that degree.

Date 29/10/2003

Signature of Supervisor

In submitting this thesis to the University of St Andrews I understand that I am giving permission for it to be made available for use in accordance with the regulations of the University Library for the time being in force, subject to any copyright vested in the work not being affected thereby. I also understand that the title and abstract will be published, and that a copy of the work may be made and supplied by any bona fide library or research worker.

Date 29/10/2003

Signature of Candidate

Acknowledgements.

After three years of work, it is time to first express my gratitude to all those who helped me to carry out this work

A big sincere thank you goes to my supervisor Prof. John Irvine for giving me the opportunity of doing a PhD and for all his permanent support, advice, and encouragement. It has been a pleasure to work in his group for the last past three years.

I am also indebted to my second supervisor Dr Wuzong Zhou for so many helpful discussions about TEM and structural chemistry, always dressed with his unique sense of humour and stories of big fishes and small potatoes.

I ended up in St Andrews thanks to Dr Susana García Martín at Universidad Complutense de Madrid, who considered that it was worth sending me here. Susana, siempre te estaré agradecido. Muchas gracias.

I also would like to acknowledge Dr. Filipe Figueiredo, Dr. Rodolfo Fuentes (now back to Argentina) and Prof. Jorge Frade, for making my stay at the University of Aveiro enjoyable. Filipe has been also so kind of providing $\text{CaTi}_{1-x}\text{Fe}_x\text{O}_{3-\delta}$ samples and never ending discussions about almost everything. Muito obrigado.

Thanks to Prof. Miguel Alario-Franco and his group, especially Dr. Myriam Aguirre and Dr. Rocío Ruiz-Bustos, for their friendship and advice on TEM.

In the JTSI group: Juan Carlos Ruiz Morales (Puntal) for the impedance stuff and some proof reading; Martin Smith for all his help, advice and company in the writing up process and before; John Bradley for the impedance spectroscopy, proof reading and some tequila tastings; Shanwen Tao among other things for the fuel cell tests and advice; Fran Jones and Cristian Savaniu providing humour and Paul Connor for the permanent computer support.

To the technical staff for their readiness to help, especially Sylvia Williamson (TGA), Ross Blackley (TEM, SEM and XRD) and Bobby Carthcart (fixing the impedance jigs once and again).

To my friends here in St Andrews (I hope I can include all the above in this category as well): Mike Johnston, Cristina Jiménez (siempre ahí), Jorge González (Yorgui), Robbie Hodgkins (yeah baby!), Pierrot Attidekou (papaya man), Anna Lashtabeg, Fabio Caiani, Rakel Fernández (no cambies, please), Naiara Elejalde (paseos por el monte), David Mepiku, Santi Pérez, Ali Gómez, Costas Petridis (basket), Anna Hovris, Rubén Rodríguez, Luis Villaescusa; and back home: Luyx, JB, Epi, Rafa, Iván, Bruno, Punish, Oscar, Isra, Andrés and others I forget for so many good times.

The last but not the least, a mis padres a quienes debo todo lo que soy y he hecho y que siempre me han apoyado. A mi hermana Laura que me ha mantenido informado de las novedades en Parla y que ha conseguido ser maestra en tiempo récord. A Pili por hacer que todo me parezca mejor.

*...ya sabemos cómo es sin las respuestas, mas ¿cómo será el mundo sin preguntas? **Mario Benedetti** (Viento del Exilio).*

(...we already know how it is without the answers, but how will the world be without questions?)

Abstract.

A new family of layered perovskites with formula $\text{La}_4\text{Sr}_{n-4}\text{Ti}_n\text{O}_{3n+2}$ has been investigated in the search of alternative anode materials for fuel cell technology. Such layered perovskites are known to be able to accommodate extra oxygen beyond the parental ABO_3 perovskite in crystallographic shears (CS planes). The structure evolves with increasing n . Firstly, the perovskite blocks become more extensive and the oxygen intergrowth layers move further apart; then the spacing between intergrowth layers increases further and their repetition becomes more sporadic. Finally, the layered structure is lost for the $n=12$ member ($\text{La}_2\text{Sr}_4\text{Ti}_6\text{O}_{19.8}$). In this structure, excess oxygen is accommodated within the perovskite framework in randomly distributed short-range linear defects. These defects become more dilute as the cubic perovskite, i.e. $n=\infty$, composition is approached.

Layered phases showed rather poor overall conductivity due to the insulating nature of the oxygen shears. When the shears become dilute, the conductivity increases dramatically, specially under reducing conditions. High total conductivity was found for the $n=12$ member in 5% H_2/Ar (60Scm^{-1} at room temperature), which made of this material a candidate for fuel electrode. Indeed its performance is comparable to the state of the art anode materials ($76\text{mW}/\text{cm}^2$ both measured in wet H_2 at 900°C).

Substitution of Ti(IV) with Sc(III) was performed in the $n=12$ member of the series, which resulted in a decrease in the excess oxygen content. That facilitated the process of re-oxidation for samples prepared in reducing conditions. Conductivity

drops with increasing Sc content due to gradual decrease of the charge carriers concentration.

Substitution with a higher valence cation, Nb(V), was also attempted, giving rise to a mixture of layered and cubic phases as a consequence of the higher oxygen content. A great improvement of the grain boundary response is achieved in the Nb-substituted phases.

From the combined studies performed on the $\text{La}_4\text{Sr}_{n-4}\text{Ti}_n\text{O}_{3n+2}$ series and Sc and Nb-substituted phases, one may assume that the transition from layered domains to random linear defects (pseudocubic) occurs at $\delta \approx 0.167$.

Chapter 1. Introduction. Fuel Cells	1
1.1. Classification	3
1.1.1. Alkaline Fuel Cells (AFCs)	3
1.1.2. Polymer Electrolyte Fuel Cells (PEFCs)	4
1.1.3. Phosphoric Acid Fuel Cells (PAFCs)	4
1.1.4. Molten Carbonate Fuel Cells	5
1.1.5. Solid Oxide Fuel Cells (SOFCs)	6
1.2. SOFC Components	7
1.2.1. Electrolyte	7
1.2.2. Interconnects	11
1.2.3. Electrodes	12
1.2.3.1. Cathode	12
1.2.3.2. Anode	14
1.3. References	18

1. Introduction. Fuel cells.

Climate changes observed during the last decades have originated a concern in the search for environmentally friendly resources for the generation of energy. Among others, fuel cells have been contemplated as highly efficient generators of electrical power alternatively to the combustion of fuels. These electrochemical devices obtain energy from fuel avoiding combustion as an intermediate stage and the limitations dictated by Carnot's cycle are thus avoided, which consequently implies higher theoretical efficiencies.

Fuel cells consist of two electrodes, an anode and a cathode, separated by an electrolyte, which is ideally an ionic conductor but an electronic insulator. At the anode, the fuel containing H_2 is oxidised yielding H^+ and liberating electrons, whilst O^{2-} ions are produced at the cathode side (figure 1.1).

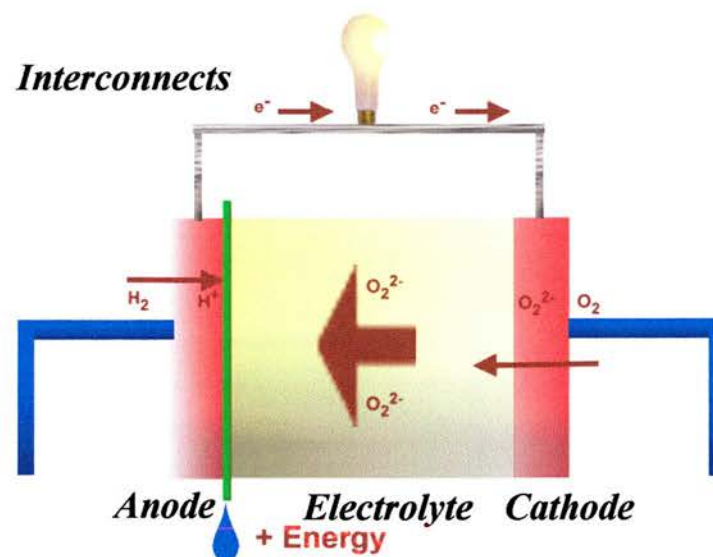


Figure 1.1. Schematic fuel cell.

Depending on whether the electrolyte is oxide ion conductor or proton conductor, ions will move from the anode to the cathode or *vice versa* and the reaction responsible for the generation of energy, i.e. formation of water, will take place at the interface between the electrode and the electrolyte. The electrons required at the cathode site for the reduction are provided by the anode via interconnects (figure 1.2).

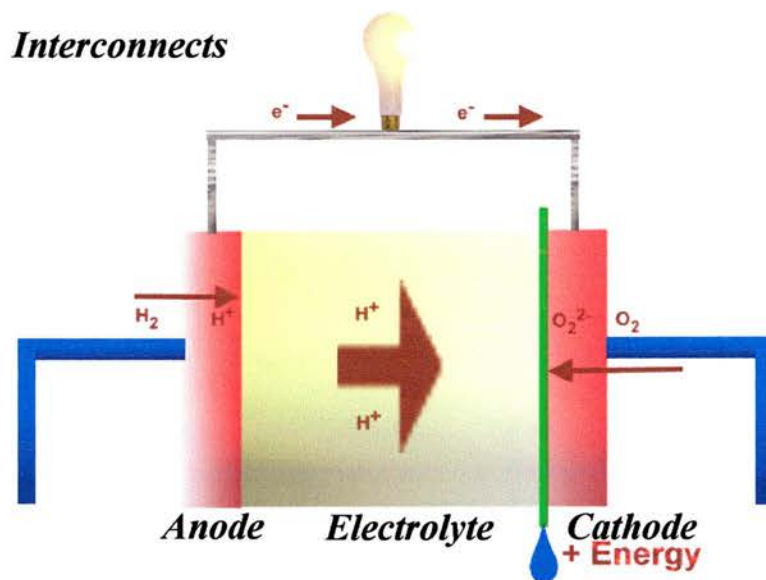


Figure 1.2. Fuel cell operating with a proton conductor electrolyte.

Obviously, the operating principles are similar to those of batteries. However, while batteries require recharging, fuel cells use gases as reactants and they run as long as fuel and oxidant are supplied to the electrodes.

1.1. Classification¹⁻⁵.

Fuel cells can be classified according to the electrolyte in: alkaline fuel cells, polymer electrolyte fuel cells, phosphoric acid fuel cells, molten carbonate fuel cells and solid oxide fuel cells. Table 1 shows a summary of these fuel cell types. Details of each are also presented below.

	AFC	PEFC	PAFC	MCFC	SOFC
Electrolyte	KOH	Polymer	H ₃ PO ₄	Carbonate	Solid Oxide
Fuel	H ₂	H ₂ /CO/CH ₃ OH	H ₂ /CO	H ₂ /CO	H ₂ /CO
Temperature(°C)	80-200	60-130	200	650	800-1000
Efficiency (%)	70	40-50	40-80	60-80	65-85
Applications	Space	Transport	Portable	Stationary	Stationary
	Transport	Portable	Transport	power	power
Drawbacks	Expensive	Fuel purity	Corrosive	Two gas	Long time
	Reactivity	Hydration	electrolyte	flows	operation

Table 1. Types of fuel cells and main characteristics.

1.1.1. Alkaline Fuel Cells (AFCs).

AFCs use concentrated KOH as electrolyte within an asbestos matrix. It operates between 150 and 200°C using compressed oxygen and hydrogen achieving efficiencies up to 70%. There is a wide choice of materials employed as catalysts, such as Ni, Pt or metal oxides. The main drawback of this type of fuel cell is the cost of fabrication together with the sensitivity of KOH to react with CO and CO₂, which implies the use of

high purity H_2 as fuel. AFCs have been developed for transport applications using Co as catalyst to reduce costs (ZEVCO cells¹). They have also been used in space programs, such as the Apollo missions.

1.1.2. Polymer Electrolyte Fuel Cells (PEFCs).

In PEFCs the electrolyte is a proton conductor, usually a fluorinated sulphonic acid polymer (Nafion®) or related, which acts as a solid ion exchange membrane. The electrodes consist of Pt supported on carbon within a polymer matrix. PEFCs operate at 80-120°C with efficiencies of 40-50%. The low working temperature makes PEFCs interesting from the point of view of domestic use and portable applications (laptops, mobiles). Transport applications have also been considered and the most important companies in transportation such as BMW, Toyota, Daimler-Chrysler, Fiat, Ford, General Motors, Renault or Ballard systems¹⁻⁴, have developed fuel cell buses and fuel cell duty vehicles working with PEFCs since 1995.

1.1.3. Phosphoric acid fuel cells (PAFCs).

PAFCs were the first commercial fuel cells in electric power industry. The electrolyte is H_3PO_4 and the electrodes are made of carbon paper coated with finely dispersed Pt catalyst. PAFCs operate at 150-200°C with efficiencies ranging from 40 to 80% in the case of steam co-generation. In fact, the use of phosphoric acid vs. other acidic electrolytes is justified by the ability of operating above the boiling temperature of

water. Another advantage of the use of PAFCs is that they tolerate a CO content up to 1.5%, which widens the choice of fuels. As main drawbacks, the use of Pt catalyst affecting the costs of fabrication and the corrosive nature of phosphoric acid that affects the choice of materials.

Being the first commercial fuel cells they have been used for transport means (despite the long warming up period required), stationary power generation and military interests.

The above mentioned fuel cells operate at relatively low temperatures. There are however fuel cells that operate at higher temperatures, which facilitates the co-generation of power and thus increasing the total efficiency.

1.1.4. Molten carbonate fuel cells (MCFCs).

These operate at 600-700°C using $(\text{Li,K})_2\text{CO}_3$ as electrolyte and achieving efficiencies in the range of 60-80 %. One of the major advantages of this type of fuel cells is the limitation of CO poisoning due to the high operating temperatures². An additional advantage is the possibility of using Ni as catalyst in the electrodes, which decreases the cost of fabrication. Within the drawbacks it is worth mentioning the necessity of two flows (O_2 and CO_2) at the cathode and the formation of water at the anode site, which may dilute the fuel.

1.1.5. Solid Oxide Fuel Cells (SOFCs).

SOFCs use the ability of certain oxides to let oxygen ions pass through them at moderately high temperatures (800-1000°C). Efficiencies up to 85% can be achieved with SOFCs considering co-generation of power provided by the production of steam as by-product. Due to their high operating temperature, fuels with high purity are not necessary and internal reforming natural gas and co-generation are facilitated. On the other hand, the use of high temperatures has negative effects as well such as limitations in long lifetime operations. Also the production of water at the anode site may dilute the fuel affecting negatively the performance.

The state of the art SOFC electrolyte is yttria-stabilised zirconia (YSZ) which is a relatively good oxide ion conductor at temperatures ranging from 800°C. Ni-YSZ cermet is the presently used anode and Sr-doped LaMnO₃ is used as cathode.

There also exists the possibility of SOFCs operating with a proton conductor electrolyte. In this case the protons generated at the anode side are transported through the electrolyte to the cathode, where they react with oxide ions forming water, providing energy. Electrons move from the anode to the cathode via the external circuit.

SOFCs have their main use in large stationary power applications. There are some other world-wide known companies such as Rolls Royce or BMW, which are investing in

the search for commercial SOFCs. For instance, Siemens-Westinghouse has developed SOFC-GC hybrid power systems capable of generating up to 300 kW⁵. Furthermore, BMW presented in 2001 the BMW 745h, the first car in the world using electrical power provided by the so-called SOFC-APU (auxiliary power unit)⁶. Therefore it can be stated that SOFCs seem to be one of the stronger candidates to replace combustion of fuels providing clean energy.

1.2. SOFC Components⁷.

1.2.1. Electrolyte.

SOFCs are based on oxygen ions moving from the air electrode (cathode) to the fuel electrode (anode), where they react with protons provided by the fuel. The electrolyte is responsible for the transport of oxide ions, so high ionic conductivity is required at the operating conditions. Another important role played by the electrolyte is to separate the fuel electrode from the air electrode. Thus, the electrolyte must present negligible electronic conductivity in order to prevent a loss in efficiency. In addition to conductivity, there are also several other very important requirements:

- **Stability:** The electrolyte must show stability in a range of oxygen partial pressure, from the reducing conditions of the anode to the oxidising conditions at the cathode.

- **Compatibility:** The electrolyte must be chemically inert with the other components of the fuel cell not only at the operating temperatures but also at the higher temperature needed during the fabrication process.
- **Thermal Expansion:** Each component must show a similar thermal expansion in order to avoid mismatch and therefore a loss in efficiency.
- **Porosity:** The electrolyte must present a high density to prevent gas leakage.

There are also other desirable requirements when considering mass scale production such as high strength, facilities for processing and, of course, low cost.

Yttria Stabilised Zirconia (YSZ) is the most widely used material as electrolyte because this material meets a great part of the requirements summarised above. As YSZ “only” shows an oxide ionic conductivity above 0.1 Scm^{-1} at $1000^\circ\text{C}^{8,9}$, it is desirable to develop alternate solid electrolytes to improve the efficiency of the fuel cell by reducing the operating temperature maintaining the conductivity or even increasing the conductivity operating at lower temperatures. Operating at lower temperatures could allow the use of stainless steel in the fabrication, which would certainly reduce the processing costs.

An alternative to YSZ is the use of scandia-stabilised zirconia (ScSZ), or ytterbia-stabilised zirconia (YbSZ) typically 8-12%. It has been reported that both systems do improve the oxide ion conductivity exhibited by YSZ. At 800°C it has been

found that 11-12 ScSZ present acceptable oxide ion conductivity just above the targeted 0.1 Scm^{-1} . Nevertheless, ageing effects on these phases must be considered because they could affect the performance of the fuel cell provoking efficiency losses with time. These problems seem to be overcome with 12 ScSZ since its conductivity did not drop with time¹⁰⁻¹¹.

Rare earth doped-ceria (typically 10 to 20% Gd or Sm) has been considered as a good material to replace YSZ due to its relatively high oxide ion conductivity at lower temperatures, typically 5 mScm^{-1} at 500°C ^{12,13}. Its use at higher temperatures has been rejected due to the importance of the electronic contribution arising from the partial reduction of Ce^{4+} to Ce^{3+} ¹⁴. There are numerous examples in the literature of the use of this oxide ion conductor as potential electrolyte for intermediate temperature SOFCs (IT-SOFC)¹²⁻¹⁶.

Doped-lanthanum gallates (LSGM) discovered by Ishihara *et al*¹⁷⁻²⁰, exhibit a high purely oxide ion conductivity at temperatures close to 1000°C . Despite these promising values in ionic conductivity they evince the same drawback of YSZ: the necessity of operation at high temperature. At lower temperatures the performance drops substantially. Table 2 lists the conductivity of the most relevant ion conductors considered as electrolytes (oxide ion conductors) for fuel cells.

Material	Conductivity	Conductivity	Ref
	(Scm^{-1}) @ 800°C	(Scm^{-1}) @ 1000°C	
YSZ	0.03	0.13	9
8 YbSZ	0.063	0.20	10
8 ScSZ	0.13	0.30	10
12 ScSZ	0.12	0.26	10
LSGM	0.18	0.39	19
LnLSGM	0.15	0.5	19
CGO	-	0.1	13

Table 2. Conductivity for some of the most relevant oxide ion conductors used in fuel cells technology.

As already mentioned, an interesting alternative to YSZ (oxide ion conductor) would be the use of proton conductors as the electrolyte, such as the perovskite ACeO_3 -based compounds ($A = \text{Sr}, \text{Ba}$)²¹⁻²⁵. Proton conductors show a lower ionic conductivity than YSZ at high temperatures, but with the advantage that they have a better performance at lower temperatures (600°C) and that could lead to the development of high efficiency fuel cells operating at intermediate temperature. Another advantage derived from the use of such oxides would be the already mentioned formation of water at the cathode site and thus preventing fuel dilution. However, oxides with high proton conductivity usually also show problems of poor stability (formation of carbonates or hydroxides) at operating temperatures²⁶, degrading and causing a drop in performance. Doping ACeO_3 with rare earth elements²¹⁻²⁸ (usually 5-10%) has been found to overcome somehow stability problems but its performance should be improved. Some attempts have been directed towards the use of AZrO_3 -based compounds, but despite their stability at operating conditions they are not suitable for fuel cell technology due to their rather

low conductivity²⁹⁻³⁰. In the last few years attempts to prepare solid solutions in the system BaO-ZrO₂-CeO₂ have been considered trying to combine the stability of the zirconates with the electrical properties of the cerate³¹⁻³².

There are numerous examples of systems, such as Ba₃Ca_{1+x}Nb_{2-x}O_{9-3x/2}, Sr₃Ca_{1+x}Nb_{2-x}O_{9-3x/2} or doped-LaScO₃, presenting proton conductivity³³⁻³⁵, but due to their relatively low conductivity, none of them could improve significantly the performance of cerates and zirconates in SOFCs.

1.2.2. Interconnects.

The main function of the SOFCs interconnect is to connect the anode and the cathode supporting a flow of electrons necessary to carry out the reaction in a fuel cell and the material must be stable under both oxidising and reducing conditions. Interconnects also must meet the general requirements of SOFC components, i.e. stability, compatibility and a thermal expansion coefficient close to that showed by the other components of the device. Finally, interconnects should be dense to avoid gas leaks or, at least, low permeability to oxygen and hydrogen.

Doped-LaCrO₃ has been the most common interconnect material due to its suitable properties: high electronic conductivity in oxidising and reducing atmosphere, thermal and chemical stability under operation conditions and a thermal expansion coefficient close to that of the other components. However, problems due to cost and Cr-

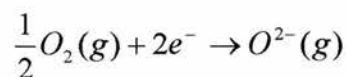
volatilisation³⁶ have lead to considerable interest in ferritic materials^{37,38}. A decrease on the operating temperatures would permit the use of steel-based materials as interconnects and thus decreasing dramatically the production costs.

1.2.3. Electrodes.

The cathode and the anode are responsible for the reduction and oxidation reactions respectively. At the cathode, oxygen is reduced and at the anode the fuel is oxidised. A common requirement of both the electrodes is that they must be mixed conductors, i.e. they must show electronic and ionic conductivity. Ionic conductivity is required to give or accept the ions that move through the electrolyte. Electronic conductivity is needed to support the movement of electrons from the cathode to the anode through the interconnects.

1.2.3.1. Cathode (Air Electrode).

The cathode of a SOFC works in an oxidising environment and it must catalyse the reduction of O₂:



As explained before, the cathode must show both electronic and ionic conductivity. Electronic conductivity is necessary to facilitate the transport of the

electrons produced in the cathode to the anode where the reaction of water formation takes place. Ionic conductivity is also required to allow the flow of the oxide ions to the anode via the electrolyte³⁹.

In addition, there are several other requirements:

1. Chemical stability in an oxidising environment not only at operating temperatures but also at the higher temperatures needed during fabrication.
2. Thermal expansion coefficients close to that of the other components to avoid mismatch.
3. Porosity to facilitate transport of oxygen to the reaction sites. However, too much porosity is not desirable due to the negative effects on the mechanical strength.
4. The cathode must have sufficient catalytic activity to accelerate the reduction of oxygen.

In addition, properties such as strength, facilities for processing and low cost are also desirable, as potential materials for mass scale production should be targeted.

Because of the high operating temperatures in the current SOFCs, only noble metals and mixed oxides with electronic conductivity can be used as cathodes in these devices. Due to their extremely high cost, noble metals (Pd, Pt) are not desirable and just some few mixed oxides roughly satisfy the above mentioned requirements. LaMnO_3

doped with alkaline elements (Sr, Ba) has been used as cathode material^{40,41}. However, doped-LaMnO₃ reacts with YSZ at high temperatures, forming by-products such as La₂Zr₂O₇ that are insulators and this results in a reduction of the performance of the fuel cell⁴². In addition, rather low oxygen ion conductivity limits the application of LSM as air electrode for fuel cells. In this respect, other mixed oxides have been studied to improve the properties shown by doped LaMnO₃ such as (La,Sr)CoO₃, (Sr,La)FeO₃ or (Ln,Sr)(Co,Fe)O₃ with higher ionic contribution to the total conductivity⁴³⁻⁴⁸.

1.2.3.2. Anode (Fuel Electrode).

The principal role of the anode in a SOFC is to provide reaction sites for the electrochemical oxidation of the fuel. Thus, the anode material must be stable in the fuel environment and have sufficient electronic conductivity to support the electron flow necessary to carry out the electrochemical reaction and to minimise ohmic losses. It must also present catalytic activity to promote the oxidation of the fuel at the operating conditions. Since the SOFC operates at high temperatures (600 to 1000°C), the anode must be chemically and thermally compatible with the other cell components from room temperature to those operating temperatures and must be tolerant of various contaminants that may be present in the fuel.

The Ni-YSZ cermet is the state of the art anode material because it complies with most of the requirements. The reducing conditions present in the anode of a fuel cell

allow the use of metals such as nickel, cobalt or ruthenium^{49,50}. However, metals show large thermal expansion and also may sinter. A YSZ support is used to minimise the coarsening of the nickel particles and to modify the thermal expansion coefficient of the anode so that it is sufficiently close to that of the other components and thus the overpotential is reduced.

There are however some drawbacks derived from the use of Ni/YSZ cermets that should be considered, such as poor adhesion between the anode and the electrolyte, thermal expansion mismatch and chemical interactions between components. Moreover when operating with natural gas, Ni-YSZ can suffer from carbon build-up and poisoning due to sulphur affecting the anode performance and there also might appear problems related to long term degradation due to the agglomeration of Ni-particles⁴⁴. In order to avoid problems related to carbon build-up, reforming of the fuel must be carried-out. However, reforming of the fuel reduces the efficiency, facilitates degradation and it also increases the expense^{51,52}. Therefore, an improvement in the tailoring of a high performance anode for fuel cells is required.

Currently, the search for an improvement in the anode performance is focused in two main areas: improvement by optimising the Ni-YSZ cermet anode properties or improvement through the use of new materials. To decrease the costs in anode supported fuel cells, anode substrates based on Ni-Al₂O₃ or Ni-TiO₂ cermets have been developed⁵³. When using these substrates the anode is basically separated into two layers, a structural support layer consisting of Ni-Al₂O₃ or Ni-TiO₂ and a thin functional anode layer

consisting of Ni-YSZ on which the oxidation reaction of the fuel takes place. Ni-TiO₂ cermets seem to reduce problems related to coarsening of the Ni particles and show good electrical properties. Other factors are also improved such as thermal expansion coefficient or electronic conductivity due to the possibility of reduction of Ti⁴⁺ to Ti³⁺. However, by introducing TiO₂ as dopant, ionic conductivity decreases. Ni-Al₂O₃ cermets present low electrical conductivity due to the lack of formation of continuous electrically conducting nickel pathways in the electrode matrix.

Mixed oxide materials promise an improvement over YSZ cermets, especially due to the “ability” of transition metals to present multiple oxidation states. Presence of multiple oxidation states leads to a potential enhancement of the electronic conductivity and it also facilitates catalytic activity. Finally, mixed oxides are less likely to suffer from carbon build-up than YSZ-cermets⁵⁴. Several groups have already performed some work in this field. For example, there are reported studies in systems such as Y- and Ti- doped YSZ^{55,56}, CeO₂ based materials^{57,58}, tungsten bronzes⁵⁹ or Sr gallium-niobates⁶⁰

Perovskite materials have been considered good candidate anodes because materials with this structural type are known to exhibit suitable characteristics for efficient anode operation such as high electronic conductivity, high oxide ion conductivity and good catalytic activity⁶¹. In fact, a perovskite-based anode material developed in our research group, La_{0.75}Sr_{0.25}Cr_{0.5}Mn_{0.5}O_{3-δ}, shows comparable electrochemical performance to Ni/YSZ and, furthermore, improving the catalytic activity⁶².

Some other perovskite-based materials, especially titanates such as chromite/titanates⁶³⁻⁶⁴ or lanthanum-doped⁶⁵⁻⁶⁷ and yttrium-doped⁶⁸⁻⁶⁹ SrTiO₃, have been recently reported as candidates for anodes in fuel cells with very promising results, which motivated the project presented herein.

1.3. References.

1. www.fuelcells.org
2. www.fuelcells.si.edu
3. www.ballard.com
4. www.fuelcellworld.org
5. www.siemenswestinghouse.com
6. www.bmwworld.com
7. N. Q. Minh and T. Takahasi: "Science and Technology of Ceramic Fuel Cells", Ed. Elsevier, Amsterdam, 1994.
8. D. W. Strickler, N. G. Carlson, *J. Am. Ceram. Soc.*, **47**(1964), 122.
9. S. P. S. Badwal, *Solid State Ionics*, **52** (1992), 23-32.
10. O. Yamamoto, Y. Arati, Y. Takeda, N. Imanishi, Y. Mizutani, M. Kawai and Y. Nakamura, *Solid State Ionics*, **79** (1995), 137-142.
11. S. P. S. Badwal, F. T. Ciacchi and D. Milosevic, *Solid State Ionics*, **136-137** (2000), 91-99.
12. H. Inaba and H. Tagawa, *Solid State Ionics*, **83** (1996), 1-16
13. V. Dusastre and J. A. Kilner, *Solid State Ionics*, **126** (1999), 163-174.

14. M. Panhans and R. N. Blumenthal, *Solid State Ionics*, **60** (1993), 279.
15. K. Zheng, B. C. H. Steele, M. Sahibzada, I. S. Metcalfe, *Solid State Ionics*, **86-88** (1996), 1241-1244.
16. G. M. Christie, F. P. F. van Berkel, *Solid State Ionics*, **83** (1996), 17-27.
17. T. Ishihara, H. Matsuda and Y. Takita, *J. Am. Chem. Soc.*, **116** (1994), 3810.
18. T. Ishihara, H. Matsuda and Y. Takita, *Solid State Ionics*, **79** (1995), 147-151.
19. T. Ishihara, Y. Hiei and Y. Takita, *Solid State Ionics*, **79** (1995), 371-375.
20. T. Ishihara, H. Matsuda, M. Azmin bin Bustam and Y. Takita, *Solid State Ionics*, **86-88** (1996), 197-201.
21. T. Yahima and H. Iwahara, *Solid State Ionics*, **53-56** (1992), 983-988.
22. H. Iwahara, T. Yahima, T. Hibino and H. Ushida, *J. Electrochem. Soc.*, **140** (1993), 1687-1691.
23. H. Iwahara, *Solid State Ionics*, **52** (1992), 99-104.
24. H. Iwahara, *Solid State Ionics*, **34** (1989), 103.
25. T. Matzke and M. Cappadonia, *Solid State Ionics*, **86-88** (1996), 659-663.
26. K. D. Kreuer, *Solid State Ionics*, **97** (1997), 1.
27. N. Bonanos, K. S. Knight and B. Ellis, *Solid State Ionics*, **79** (1995), 161-170.
28. K. J. de Vries, *Solid State Ionics*, **100** (1997), 193-200.
29. K. D. Kreuer, *Solid State Ionics*, **125** (1999), 285-302.
30. K. D. Kreuer, S. Adams, W. Munch, A. Fuchs, U. Klock and J. Maier, *Solid State Ionics*, **145** (2001), 295-306.
31. K. Katahira, Y. Kohchi, T. Shimura and H. Iwahara, *Solid State Ionics*, **138** (2000), 91-98.

32. K. H. Ryu, S. M. Haile, *Solid State Ionics*, **125** (1999), 355-367.
33. T. Schober, F. Krug and W. Schilling, *Solid State Ionics*, **97** (1997), 369.
34. D. J. D. Corcoran and J. T. S. Irvine, *Solid State Ionics*, **145** (2001), 307-313.
35. D. Lybye and N. Bonanos, *Solid State Ionics*, **125** (1999), 339-344.
36. N. Q. Minh, *J. Am. Ceram. Soc.*, **76** (1993), 563.
37. D. S. Patil *et al.*, *Solid State Ionics*, **52** (1992), 189-196.
38. K. Q. Huang, P. Y. Hou and J. B. Goodenough, *Solid State Ionics*, **129** (2000), 237-250.
39. R. J. Gorte *et al.*, *Adv. Materials*, **12** (2000), 1465-1469.
40. B. C. H. Steele, *Solid State Ionics*, **86-88** (1996), 1223-1234.
41. T. Hibino, S. Wang, S. Kakimoto and M. Sano, *Solid State Ionics*, **127** (2000), 89-98.
42. H. Yokokawa, N. Sakai, T. Kawada and M. Dokiya, *J. Electrochem. Soc.*, **138** (1991), 2710-2727.
43. Y. Takeda, R. Kanno, M. Noda, Y. Tomida and O. Yamamota, *J. Electrochem. Soc.*, **134** (1987), 2656.
44. B. C. H. Steele, *Solid State Ionics*, **86-88** (1996), 1223-1234.
45. S. P. Jiang, *Solid State Ionics*, **146** (2002), 1-22.
46. L. Qiu, T. Ichikawa, A. Hirano, N. Imanishi and Y. Takeda, *Solid State Ionics*, **158** (2003), 55-65.
47. S. Carter, A. Selcuk, R. J. Charter, J. Kajda, J. A. Kilner. B.C. H. Steele, *Solid State Ionics*, **53-56** (1992), 597.

48. T. Inagaki, K. Miura, H. Yoshida, R. Maric, S. Ohara, X. Zhang, K. Mukai and T. Fukui, *J. Power Sources*, **86** (2000), 347-351.
49. Suzuki, Sasaki, Ootoshi, Kajimura and Ippommatsu, *Solid State Ionics*, **62** (1993), 125-131.
50. Tang, Ivey and Etsell, *MRS Symposium Proceedings*, **527** (1998), 539-544.
51. A. Abudula, M. Ihara, H. Komiyama and K. Yamada, *Solid State Ionics*, **86-88** (1996), 1203-1209.
52. S. H. Clarke, A. L. Dicks, K. Pointon, T. A. Smith and A. Swann, *Catalysis Today*, **38** (1997), 411-423.
53. D. Skarmoutsos, A. Tsoga, A. Naoumidis and P. Nikolopoulos, *Solid State Ionics*, **135** (2000), 439-444.
54. T. Norby, *Solid State Ionics*, **125** (1999), 1-11.
55. E. Ruiz-Trejo and J. A. Kilner, *Solid State Ionics*, **97** (1997), 529-534.
56. S. C. Singhal, *Solid State Ionics*, **135** (2000), 305-313.
57. N. Bonanos and F. W. Poulsen, *J. Mater. Chem.*, **9** (1999), 431-434.
58. B. C. H. Steele, J. F. Kelly, P. H. Middleton and R. A. Rudkin, *Solid State Ionics*, **40/41** (1990), 810.
59. A. Kaiser, J. L. Bradley, P. R. Slater and J. T. S. Irvine, *Solid State Ionics*, **135** (2000), 519-524.
60. T. D. McColm and J. T. S. Irvine, *Solid State Ionics*, **152-153** (2002), 615-623.
61. N. Bonanos, *Solid State Ionics*, **53-56** (1992), 967-974.

62. S. Tao and J. T. S. Irvine, *Nature Materials*, advanced online publication, www.nature.com/naturematerials, March 2003.
63. G. Pudmich, B. A. Boukamp, M. González-Cuenca, W. Jungen and W. Zipprich and F. Tietz, *Solid State Ionics*, **135** (2000), 433-438.
64. M. González-Cuenca, W. Zipprich, B. A. Boukamp, G. Pudmich and F. Tietz, *Fuel Cells*, **1** (2001), 256-264.
65. P. R. Slater, D. P. Fagg and J. T. S. Irvine, *J. Mater. Chem.*, **7**(12) (1997), 2495-2498.
66. O. A. Marina, N. L. Canfield and J. W. Stevenson, *Solid State Ionics*, **149** (2002), 21-28.
67. O.A. Marina and L.R. Pederson, *Proceedings of the 5th European Solid Oxide Fuel Cell Forum*, Edited by Joep Huijsmans, 1-5 July 2002, Lucerne/Switzerland, 481-489.
68. S. Hui and A. Petric, *J. European Ceram. Soc.*, **22** (2002), 1673-1681.
69. S. Hui and A. Petric, *J. Electrochem. Soc.*, **149** (1) (2002), J1-J10.

Chapter 2. Experimental	22
2.1. Synthesis	22
2.2. X-Ray Diffraction (XRD)	23
2.2.1. Background	23
2.2.2. Experiment	25
2.3. AC Impedance Spectroscopy	25
2.3.1. Background	25
2.3.2. Temperature dependence of the conductivity	28
2.3.3. Impedance experiments	29
2.4. Four Terminal Measurements	29
2.5. Fuel Cell Tests	31
2.6. Thermogravimetric Analysis (TGA)	33
2.7. Electron Microscopy	33
2.7.1. Transmission Electron Microscopy (TEM)	34
2.7.2. Imaging	37
2.7.3. Selected Area Electron Diffraction (SAED)	44
2.7.4. Energy Dispersive Spectroscopy (EDS)	45
2.7.5. Simulation of images	48
2.7.6. Preparation of specimens	49
2.8. References	49

2. Experimental.

In this chapter, an outline of the techniques most frequently used during the course of this work is presented. First, some comments are given on the preparation of samples and then a summary of XRD, TGA and ac impedance spectroscopy. A more detailed description of TEM is also given.

Some additional techniques such as fuel cell tests, 4-terminal measurements in controlled oxygen partial pressure ($P(O_2)$) were also used, although not on a regular basis. In relation to these, some short comments are added to facilitate the comprehension in the corresponding sections.

2.1. Synthesis.

The preparation of samples in the present work was always carried out by traditional solid state reaction, which consists in mixing and grinding the stoichiometric amounts of the appropriate oxides (excepting Sr that was used as carbonate) in acetone. After drying, the mixture was calcined typically at 1200°C for 6-12 hours to decompose the carbonates. Then it was ground and pressed uniaxially at 1.5-2.0 tons for 1 minute. The resulting pellets were fired at 1400-1600°C for 48 hours and then ground, pressed and fired at the same temperature for further 48 hours yielding generally pale yellow pellets. Reduced phases were obtained by further firing at 1000°C for 48 hours in flowing dry 5% H_2 /Ar yielding dark blue pellets.

Dense samples were obtained by ball milling in Zr containers for 30-45 minutes between every step of the mentioned above.

2.2. X-ray diffraction (XRD).

2.2.1. Background [1].

XRD is a routine technique in solid state chemistry in the elucidation of structures and also to verify phase purity. XRD usually leads to the determination of the 'average' unit cell of a given polycrystalline compound. Information of local structure can be obtained with other techniques that may be more sensitive such as powder neutron diffraction (PND) or selected area electron diffraction (SAED).

W. H. and W. L. Bragg first discovered diffraction of X-rays in 1913, when they found that radiation was diffracted giving rise to a constructive interference only when the difference between the path lengths of two rays was an integral multiple of the wavelength (figure 2.1)

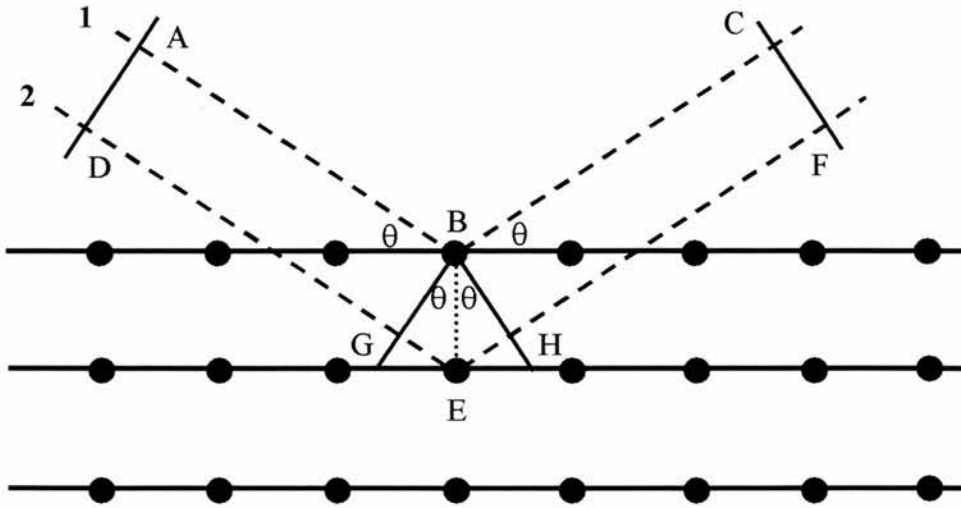


Figure 2.1. Schematic diagram illustrating Bragg's law for diffraction phenomena.

The difference in the path length between rays 1 and 2 is:

$$\Delta d = AB + BC - (DE + EF) = AB + BC - (DG + GE + EH + HF) \text{ [equation 2-1]}$$

considering that

$$AB = DG \text{ [equation 2-2]}$$

$$BC = HF \text{ [equation 2-3]}$$

then

$$\Delta d = GE + EH = 2BE \sin \theta \text{ [equation 2-4]}$$

BE corresponds to the distance between atomic planes d_{hkl} . Thus, Bragg's law can be expressed as:

$$n\lambda = 2d_{hkl} \sin \theta \text{ [equation 2-5]}$$

The experiment consists on X-rays radiation interacting with a powdered sample in a range of incident angles (θ). When Bragg's conditions are fulfilled, the phenomenon of diffraction occurs. Diffracted beams are recognised by a detector, which translates them into intensities. Thus, plotting intensities vs. the angle 2θ , the typical XRD pattern is obtained. The dimensions of the unit cell can be calculated from the positions of the peaks, as well as the crystallographic system. Refinement of the structure consists of calculating precise atomic positions from the structural factors by methods such as that of Rietveld [2], which also allows calculating estimations of occupancy factors.

2.2.2. Experiment.

In the present work, XRD data were collected with a Stoe StadiP Transmission X-ray diffractometer, using $\text{CuK}\alpha_1$ radiation. The measurement range was typically from 10 to 70°, although for specific cases measurements at lower 2θ values were also performed.

2.3. Ac impedance spectroscopy.

2.3.1. Background [3-5].

Ac Impedance spectroscopy is a suitable technique to investigate and characterise the electrical properties of ceramic materials because it differentiates between different electrochemical responses due to bulk, grain boundary, electrode phenomena, etc [4-5].

In the experiments, a voltage is applied across the sample:

$$V(t) = V_o \sin(\omega t) \text{ [equation 2-6]}$$

with $\omega=2\pi f$, which results in a current that may show a phase shift ϕ , that is measured over a range of frequency, typically from 0.1 Hz to 1MHz.

$$I(t) = I_o \sin(\omega t + \phi) \text{ [equation 2-7]}$$

When $\phi=0$, the system behaves as a pure resistor, whilst for $\phi=90$ the system resembles a pure capacitor. A real system usually shows both components, which can be determined by investigating the impedance deduced from Ohm's law and is defined as the opposition of the system to flow of charge:

$$Z^* = \frac{V(t)}{I(t)} \text{ [equation 2-8]}$$

The total impedance Z^* , can be described as the sum of two contributions: real and complex impedance.

$$Z^* = Z' - iZ'' \text{ [equation 2-9]}$$

The real contribution (Z') relates to resistive components, whilst the complex (Z'') refers to the capacitive contribution. When an electrochemical process is described as a RC element, i.e. a resistance and a capacitor in parallel, the impedance can be expressed as:

$$\frac{1}{Z^*} = \sum \frac{1}{Z_i^*} = \frac{1}{R} + i\omega C \text{ [equation 2-10]}$$

Equation 2-10 can also be expressed as:

$$Z^* = \left(\frac{1}{R} + i\omega C \right)^{-1} = \frac{R}{1+i\omega RC} \times \frac{1-i\omega RC}{1-i\omega RC} = \frac{R}{1+(\omega RC)^2} - \frac{i\omega R^2 C}{1+(\omega RC)^2} \text{ [equation 2-11]}$$

Routine studies involve the use of the so-called Nyquist plots, which result from plotting Z'' vs. Z' . In such plots there appear as many semicircles in the complex plane as electrochemical (RC) processes occur, being each RC process associated to a time constant (τ):

$$\tau = RC = \frac{1}{2\pi f} \text{ [equation 2-12]}$$

The magnitude of capacitance associated to a RC process allows discerning between processes occurring in the electrodes, grain boundaries, grain bulk or other processes as listed in table 2-1.

Capacitance (F)	Phenomenon
10^{-12}	Bulk
10^{-8} - 10^{-11}	Grain boundary
10^{-9} - 10^{-11}	Bulk ferroelectric
10^{-5} - 10^{-7}	Sample-electrode interface
10^{-4}	Electrochemical processes

Table 2-1. Capacitance values and their possible interpretation (adapted from [4]).

Often, the semicircles are not symmetric and show depressions due to deviations from the ideal situation represented by the so-called “brick-layer” model. In these cases, a constant phase element (CPE) is introduced substituting the

capacitance. CPE elements can be considered as an illustration of the frequency dispersion of the electrochemical processes taking place in the sample.

There are some other formalisms related to the impedance, used to study the electrical behaviour of materials such as the admittance or the complex electric modulus (M^*). M^* is a very good complement to the impedance, because whilst the latter picks out the most resistive component, the first highlights the component with smallest capacitance.

$$M^* = i\omega C_o Z^* \text{ [equation 2-13]}$$

M^* plots are especially helpful when the grain boundary responses are dominant and, sometimes, mask the responses of other electrochemical processes occurring at higher frequencies (bulk) in the impedance plots.

2.3.2. Temperature dependence of the conductivity.

Values of conductivity corresponding to various electrochemical processes can be deduced from the interception of the arcs with the real axis in the Nyquist plots. In addition to the assignment of the RC (or R-CPE) processes to the different phenomena taking place in the sample, routinely examinations involve studies of the temperature dependence of the conductivity. Conductivity in semiconductors is sometimes explained in terms of the so-called hopping model for transport of species. In the case of semiconductors, it considers that the electrons are localised on individual atoms. They become mobile by 'hopping' to adjacent atoms if they

received sufficient energy, E_a (activation energy). This is a thermally activated process, which can be expressed as:

$$\sigma T = \sigma_0 e^{-\frac{E_a}{RT}} \text{ [equation 2-14]}$$

where E_a is the activation energy and σ_0 is a pre-exponential factor related with the entropy (ΔS). Plotting $\text{Log } \sigma T$ vs. T^{-1} straight lines are obtained, being the slope the activation energy for the process. The so-called Arrhenius plots allow contemplating changes in the mechanisms of conduction or phase transitions in the temperature range studied.

The dependence of the capacitance with the temperature may also be studied, especially when investigating ferroelectric materials.

2.3.3. Impedance experiments.

Ac impedance data in the present work were acquired using a 1260 Solartron impedance analyser typically over the frequency range 0.1 Hz-1.0 MHz. Measurements were performed on pellets (75-99% dense) coated with organo-platinum paste on each face and fired afterwards at 900°C for 30 minutes. The samples were mounted in a compression jig with Pt wire electrodes. The measurements were performed in a range of water and oxygen partial pressures (static air, wet Ar and dry Ar).

2.4. Four terminal dc measurements.

When the resistance due to the jig design is higher than the resistance of the studied material, ac impedance spectroscopy becomes obsolete. In this situation, four terminal dc measurements can be used to estimate conductivity [6], although it is not able to differentiate between processes occurring at the bulk, grain boundaries, etc.

Four equally spaced Pt strips of about 1mm are adhered to one bar of the sintered sample. Current is applied to the outer electrodes and a potential difference generated across the inner electrodes. By Ohm's law, the relation between the current applied and the voltage generated is the resistance of the material.

Controlled atmospheres can be achieved by performing the measurements in electrochemical cells with ion pumps attached. The pump-gauge system allows an accurate control of the $P(O_2)$ inside the cell [7]. The $P(O_2)$ monitored by measuring the voltage of a zirconia sensor (figure 3.2). The use of mixtures of gases is preferred because it improves the kinetics of the equilibrium processes and also renders accuracy in the measurements.

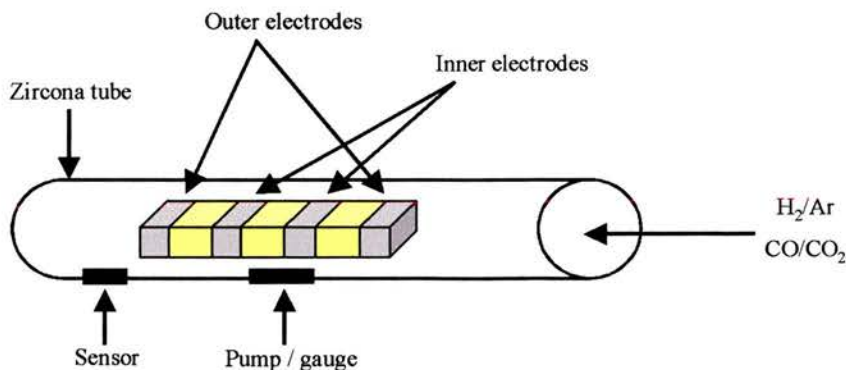


Figure 3.2. Schematic representation of the cell used for the controlled atmosphere measurements.

2.5. Fuel cell tests.

Fuel cell tests were performed using $\text{La}_2\text{Sr}_4\text{Ti}_6\text{O}_{19.8}$ as anode material. Powders synthesised at 1500°C that had been subsequently reduced at 1000°C for 48 hours were used to form ethanol-based slurry. The slurry was then coated onto YSZ pellets and fired at 1300°C for 4 hour to form a thin layer of anode for the fuel cell test.

A three-probe cell was prepared for ac impedance measurements to investigate the anode polarisation. The arrangement of working, counter and reference electrode is schematised in figure 2.3. The electrolyte is 20mm in diameter and 2mm in thickness. A gold current collector was applied onto the working electrode (active area 1cm^2) using Au mesh with a thin partially covering layer of Au paste between the oxide and the mesh.

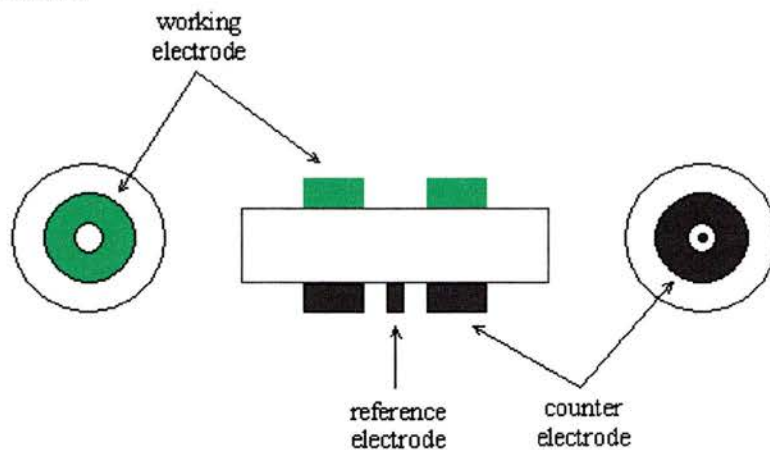


Figure 2-3. Schematic drawing of the three-electrode arrangement of the electrochemical cell.

On the other hand, the fuel cell performance was measured in a normal two-electrode configuration cell (figure 2.4). The electrolyte for cell performance measurements is YSZ added with 17% alumina with 0.2mm thickness Ceramatec due to its superior mechanical properties. The cathode material used was commercial

$\text{La}_{0.8}\text{Sr}_{0.2}\text{MnO}_3$ (Praxair, USA) with platinum paste acting as cathode current collector. For both types of cells, the thickness of anode was about $50\mu\text{m}$, a thickness that has been found to be fairly optimum in previous studies of oxides in our laboratory.

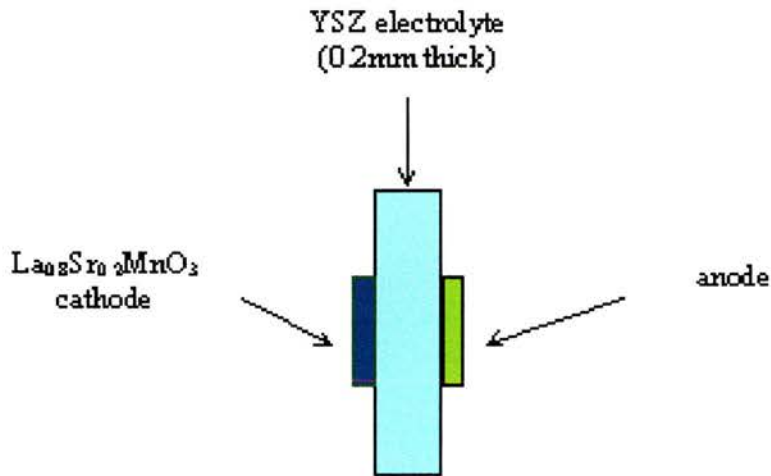


Figure 2.4. Schematic plot of the two-cell configuration to study the fuel cell performance.

The impedance of the electrochemical cell was recorded at 900°C at open circuit voltage (OCV) and at different atmospheres with 20mV as ac signal amplitude in the $1 \times 10^5 \sim 0.01\text{Hz}$ frequency domain.

Humidified $5\%\text{H}_2$ in Ar, $100\%\text{H}_2$ and $100\%\text{CH}_4$ were used as the fuel at the working electrode, O_2 being supplied at the counter electrode. The fuel cell performance was recorded by cyclic-voltammetry at a scan rate of 1mVs^{-1} . All electrochemical tests were performed after reducing the $\text{La}_2\text{Sr}_4\text{Ti}_6\text{O}_{19.8}$ anode in $5\%\text{H}_2$ at 850°C for two days to achieve the highest conductivity due to the slow kinetic process of reduction.

2.6. Thermogravimetric analysis (TGA).

TGA is a quite simple technique that can give very helpful results. It consists in registering the difference in mass when thermally treating a sample in various atmospheric conditions. Mass changes can be used to monitor processes such as oxidation-reduction, loss-uptake of water or loss-uptake of CO₂.

The instrumentation consists on an ultra-sensitive balance with a sample pan inside a furnace whose temperature can be accurately controlled. Inside the furnace the sample can be studied under different atmospheric conditions, i.e. flowing wet or dry air, Ar or 5% H₂/Ar. Wet conditions are achieved by making the gases flow through a pipe containing soaked cotton wool. The experiment typically consists of heating a sample up to 800-900°C at a fixed rate of 5-10K/min. Then the temperature is held for 6 hours to finally cool down at room temperature.

The balance used in this work was a ReoTherm TG 1000M Thermogravimetric analyser (vertically hanging Pt sample pan) with Rheometric Scientific Plus V v.5.44 Software. The furnace is capable of temperatures up to 1000°C.

2.7. Electron Microscopy [8-10].

Electron microscopes are based on electron-solid interactions. Depending on the nature of those we can classify electron microscopy in different techniques, reflected in figure 2.5: Auger electron spectroscopy (AES), cathodoluminescence

(CL), scanning electron microscopy (SEM), energy dispersive spectroscopy (EDS), electron diffraction (ED), transmission electron microscopy (TEM), energy loss electron spectroscopy (EELS) and scanning-transmission electron microscopy (STEM).

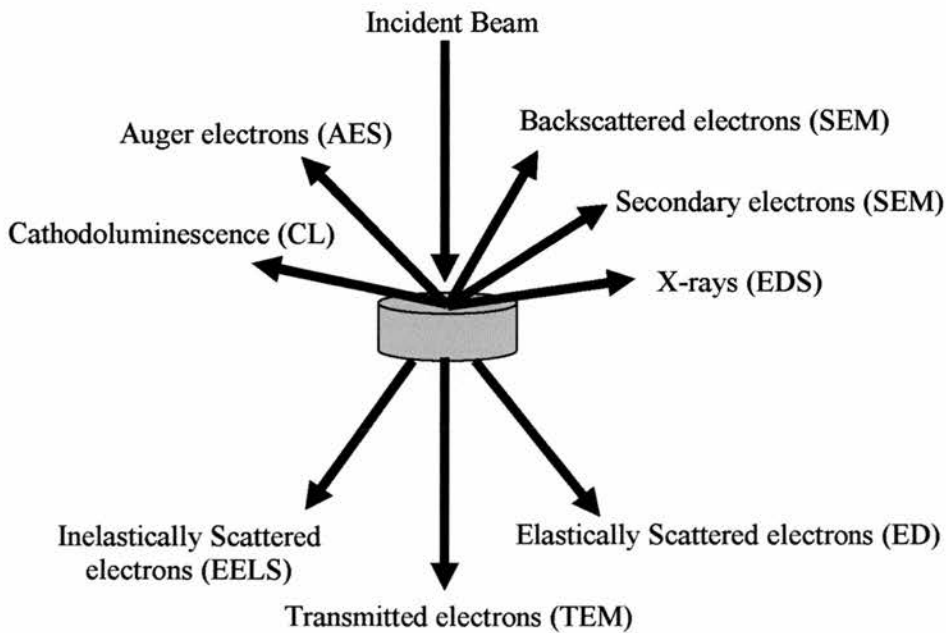


Figure 2.5. Interaction of the electron beam with the specimen leading to the different electron microscopy techniques.

2.7.1. Transmission Electron Microscopy (TEM).

TEM generates images from the transmitted and the elastically scattered electrons as displayed in figure 2.2. It consists of the same functional components as light microscopes and accordingly they can be classified in five groups:

1. Illumination system. It covers the source (electron gun) and the condenser lenses. There are two sets of condenser lenses. The first (C1)

controls the spot size, whereas the second (C2) controls the convergence of the beam.

2. Sample Holder.

3. Objective Lens. It is the most important part of the microscope and it produces a first image of the sample (usually with a magnification of x50-x100).

4. Projection system formed by several types of lenses (intermediate lenses and projector lens).

5. Screen or similar device (CCD camera) in which the final image can be observed.

The principle of a TEM experiment can be described as follows: the electron gun (typically made of LaB_6) generates an electron beam that is focused by the condenser lenses (C1 and C2). After that, the beam interacts with the specimen and passes through it. The transmitted and diffracted electrons are then recombined and focused by the objective lens to form a diffraction pattern and an intermediate image at the backfocal plane. The beams then diverge and are focused by the projector lens to form the final image. Whether an electron diffraction pattern and an image is achieved is determined by choosing images from the backfocal plane or the image plane (figure 2.6). Resolution down to less than 2\AA can be achieved by a JEOL JEM

2011 electron microscope, which is the one used in the course of this work at St Andrews.

Source: LaB₆

Condenser Lenses: C1 (spot size), C2 (convergence)

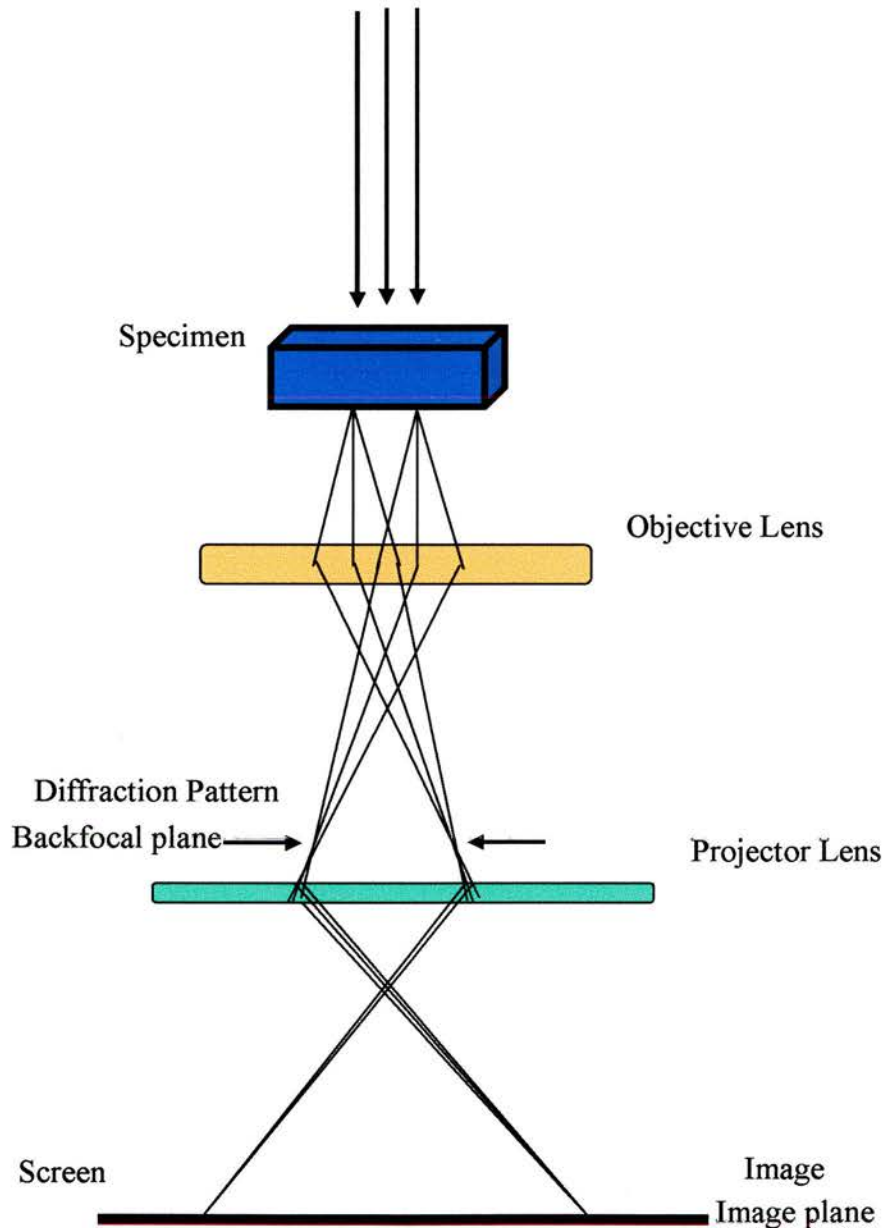


Figure 2.6. Schematic diagram of the operation of a transmission electron microscope.

The JEOL-JEM 2011 electron microscope operates at 200 kV and is equipped with a side entry $\pm 20^\circ$ double tilt specimen holder. It is regulated by

FasTEM™ computer control system, which keeps the detectors automatically calibrated for alignment and lens values and thus facilitating the operation and making the instrument more stable [11]. Table 2-2 lists the specifications.

Source	LaB ₆ (thermoionic)
Lattice resolution	1.4 Å
Point resolution	1.94 Å
Spherical aberration coefficient	0.5 mm
Chromatic aberration coefficient	1.1 mm
Minimum focal step	1.0 nm
Goniometer	± 20°

Table 2-2. Specification of the JEOL-JEM 2011 microscope at St Andrews.

Routine studies on a transmission electron microscope involve three main techniques: imaging, electron diffraction (ED) and energy dispersive spectroscopy (EDS). The combination of these techniques makes TEM one of most efficient and versatile tools for the characterisation of solid state materials. In addition, there exist the possibility of simulating the high resolution images with specific software (in the present case MacTempas), which allows a comparison between the experimental image and a calculated one from the atomic positions that describe the structure of the material object of study. The correlation (or non-correlation) between calculated images and the experimental ones indicates how close (or far) a given structural model is from the real structure of the material studied on to the electron microscope.

2.7.2. Imaging.

High-resolution transmission electron microscopy provides two dimensional (2D) structural images of the specimens down to Å scale. The main advantage of this technique is that the arrangement of the atoms can be determined from the scattering

experimented by the electrons after interacting with the potential caused by the arrangement of the atoms itself.

Electron microscopes were developed because of the limited image resolution in conventional light microscopes. The reason for such limitation is the relatively long wavelength of visible light as exposed by Ernst Abbe on the first theory on image formation for microscopes:

$$d = \frac{0.61\lambda}{\mu \sin(\beta)} \text{ [equation 2-15]}$$

Where μ is the refractive index and β the semiangle of collection of the magnifying lenses. Considering this equation, the highest resolution that can be reached by using an optical microscope is about 300 nm. This could seem a small dimension, but it corresponds to about 1000 atom diameters and therefore most of the features that control properties of materials are on a scale well below the resolution of light microscopes.

Louis de Broglie “solved” this problem with the idea of wavelength associated to a particle with a linear momentum p in one of the major breakthroughs of the last century:

$$\lambda = \frac{h}{p} \text{ [equation 2-16]}$$

Therefore, by applying a high voltage, electrons are accelerated and their wavelength is diminished.

$$\lambda = \frac{h}{\sqrt{2meE\left(1 + \frac{eE}{2mc^2}\right)}} \quad \text{[equation 2-17]}$$

Since accelerated electrons have a much shorter wavelength than natural light, it would be possible to build a microscope that would be able to differentiate details below the atomic level. Thus, applying a voltage of 100 keV we could reach a resolution power of 0.004 Å, which is much smaller than the diameter of a single atom. Unfortunately, there exist technical limitations and it is impossible to fabricate perfect electron lenses (magnetic lenses), which are governed by the spherical aberration coefficient C_s . C_s limits the resolution of an electron microscope:

$$d = 0.66C_s^{1/4} \lambda^{-3/4} \quad \text{[equation 2-18]}$$

The most important concept when talking about HRTEM is the concept of contrast, which is the difference in intensity between two adjacent areas. This difference in intensity is what gives the possibility of perceiving the features of an image. Contrast arises from the non-uniform intensity of the scattered electron beams after interaction with the specimen. There are three formation mechanisms of image contrast: mass-thickness contrast, diffraction contrast and phase contrast.

Mass-thickness contrast arises from the morphology of the specimen and it is due to the incoherent elastic scattering of electrons. This type of contrast is dominant at low magnification and at low scattering angle. Thicker regions will back-scatter (or absorb) more electrons than thin regions and therefore fewer electrons will reach the

image plane), giving rise to dark areas and vice versa, thinner regions will back-scatter fewer electrons and consequently more electrons will go through the sample and reach the screen, causing lighter regions. Mass-thickness contrast can be enhanced by selecting small objective apertures or by decreasing the accelerating voltage.

Diffraction contrast arises because the intensity of diffracted beams is different in different regions of the specimen (grain boundaries, dislocations...) and is due to the coherent elastic scattering of electrons. Therefore, TEM is the instrument of choice when the specimen shows defects, i.e. when the feature of interest is what makes the material imperfect or, paradoxically, useful. Diffraction contrast is important at intermediate magnifications.

Finally, contrast in TEM images can be caused by differences in the phase of the electron waves scattered through a thin specimen, due to local changes in thickness, orientation, scattering factor or variations in the focus. Phase shifts between the wavefunctions before and after interaction with the specimen are responsible for the contrast on TEM images. Working in “in-focus” conditions would give rise to no contrast. Therefore, in order to provide the necessary contrast in high-resolution images it is required to work in out of focus conditions that will enhance contrast by generating phase shift. The better performances are achieved using the so-called Scherzer conditions, i.e. slightly underfocus conditions.

Underfocus conditions are preferred vs. overfocus conditions as a consequence of defects in the electromagnetic lenses, i.e. the already mentioned spherical aberration C_s . Spherical aberration results in a negative phase shift ($\Delta\phi$):

$$\Delta\phi = -\frac{2\pi}{\lambda} \left(\frac{1}{4} C_s \alpha^4 \right) \text{ [equation 2-19]}$$

being α the aperture of the objective lens. Figure 2.7 depicts the effect of the spherical aberration in the formation of the image, causing a confusion disk (Δr) because some rays converge before the Gaussian image plane:

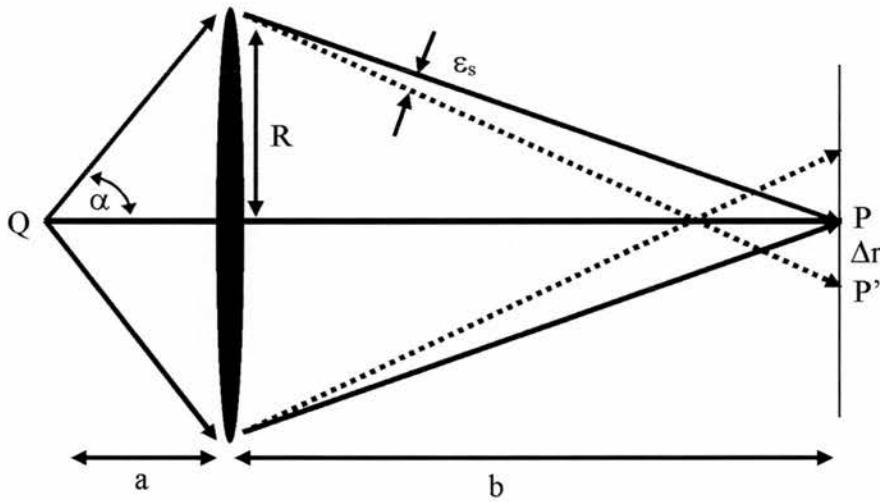


Fig 2.7. Schematic diagram showing the effect of spherical aberration in the formation of an image.

Operating in slightly underfocus conditions can compensate such an effect by introducing a positive phase shift as depicted in figure 2.8 (a) and expressed by:

$$\Delta\phi = \frac{2\pi}{\lambda} \left(\frac{1}{2} \Delta f \alpha^2 \right) \text{ [equation 2-20]}$$

Overfocus conditions would enhance the negative effect of spherical aberration (figure 2.8 (b)), because the phase shift would be <0 as well:

$$\Delta\phi = -\frac{2\pi}{\lambda} \left(\frac{1}{2} \Delta f \alpha^2 \right) \text{ [equation 2-21]}$$

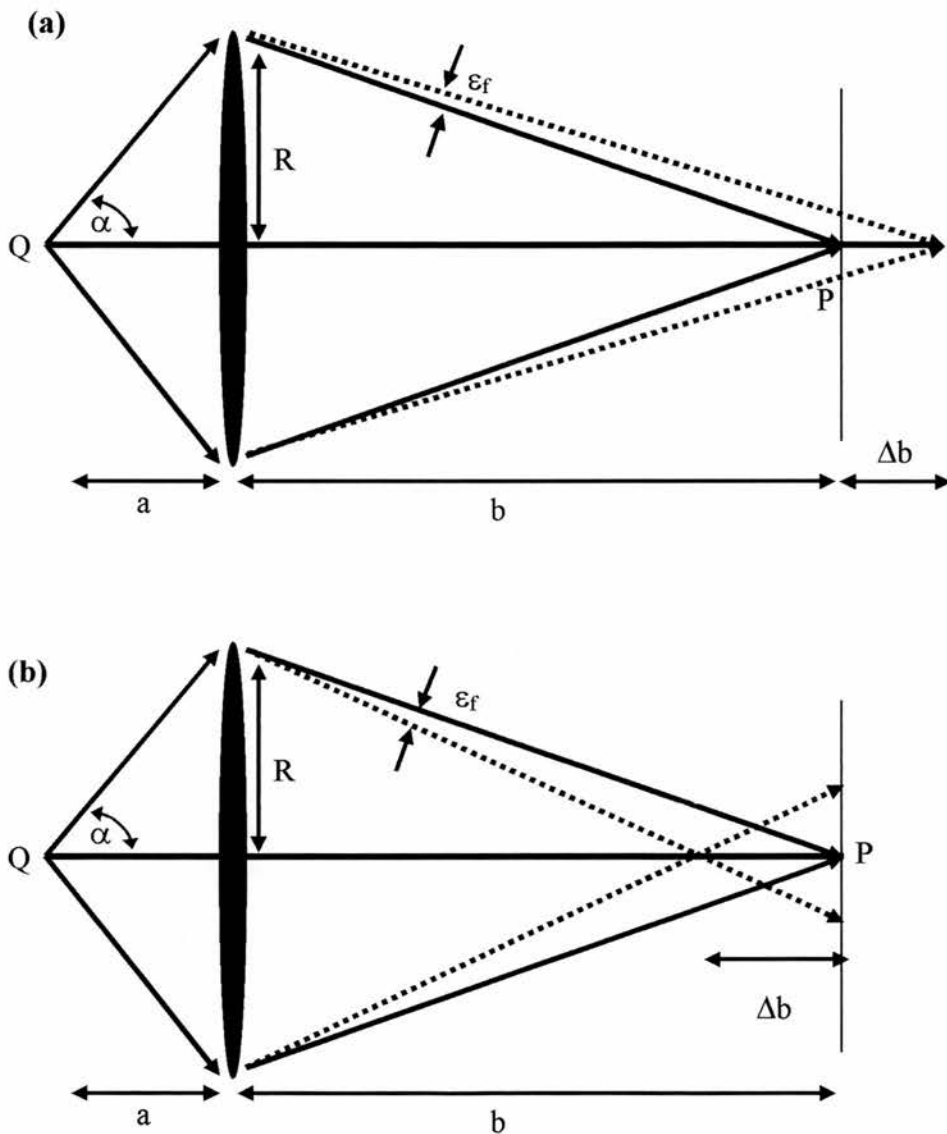


Figure 2.8. Schematic diagrams showing the differences between operating in underfocus (a) and overfocus (b) conditions.

Therefore, the total phase shift ($\chi(\alpha)$) when operating in underfocus conditions may be expressed as:

$$\chi(\alpha) = \frac{2\pi}{\lambda} \left(\frac{1}{2} \Delta f \alpha^2 - \frac{1}{4} C_s \alpha^4 \right) \text{ [equation 2-22]}$$

Considering that:

$$|S| = 2 \sin \frac{\theta}{\lambda} \approx \frac{\alpha}{\lambda} \text{ [equation 2-23]}$$

The total phase shift is

$$\chi(S) = \frac{2\pi}{\lambda} \left(\frac{1}{2} \Delta f \lambda^2 |S|^2 - \frac{1}{4} C_s \lambda^4 |S|^4 \right) \text{ [equation 2-24]}$$

which is the so-called phase contrast transfer function. Plotting $\sin \chi(S)$ vs. reciprocal distance, there exists a flat region where defocus and spherical aberration cancel each other. The limits of such flat region determine the limit of resolution on the electron microscope.

In addition to the spherical aberration there are also other factors that reduce the resolution of an electron microscope, which usually appear as chromatic aberration. Thus, the coefficient of chromatic aberration (C_c) includes the effects of fluctuation in the accelerating voltage and in the current of the objective lens coils and also variations in the electron energies due to thermal effects.

2.7.3. Selected area electron diffraction (SAED).

The periodic structure in crystals gives rise to electron diffraction if the Bragg conditions are satisfied, i.e. the crystallographic planes of a family diffract in a coherent way with the incident beam as it occurs in X-rays ($n\lambda = 2d\sin\theta$).

SAED patterns are representations of the reciprocal structure of the specimens. Therefore, distances have to be transformed in real d-spacings by:

$$d^* = \frac{\lambda l}{d_{hkl}} \text{ [equation 2-25]}$$

d^* being the distance measured on the SAED pattern, l the camera length (chosen by operator) and λ the wavelength of the electron beam (0.0251 Å when operating at 200kV). Generally, calibration using standards is performed to obtain accurate camera constant values, i.e. the product λl , and thus accurate d_{hkl} .

Electron diffraction shares the same principles as XRD and therefore it can be also used to determine unit cell dimensions and the corresponding atomic coordinates.

Probably the most important advantage of SAED vs. XRD is the better accuracy to detect the presence of superstructures and also is more sensitive to light elements. In addition, SAED gives information about the local structure compared to the average structure obtained by XRD. Therefore SAED is more sensitive to features such as microtwinning, microdomains texture, disorder, etc.

SAED is also a suitable technique for the determination of space groups because it permits differentiating between families of reflections, e.g. the (100) reflection appears separated from the (010) reflection in materials with cubic symmetry. However care is required when using SAED for space group determination due to the importance of phenomena such as multiple scattering. Multiple scattering affects the intensity of the reflections and therefore, it would affect the calculation of the structure factors. Multiple scattering can be minimised by choosing thin areas of the specimen, but it can never be neglected.

The combination of XRD, HRTEM and SAED results in a powerful tool in the structural elucidation of solid materials as it will be found in this work.

2.7.4. Energy dispersive spectroscopy (EDS).

EDS is based on the generation of the characteristic X-ray of the elements of the specimen. The electron beam interacts with the specimen and due to the high energy of the beam, the specimen generates X-ray radiation. This radiation is characteristic and different for each element in the periodic table and is collected by a semiconductor detector. The mechanism of the detector is quite simple: when the X-rays from the sample interact with the semiconductor, electrons are promoted from the valence band to the conduction band, forming electron-hole couples, i.e. charge in the detector. The number of electron-hole couples formed is a function of both the radiation of the element and the gap of energy of the semiconductor. For instance, Si shows a gap of energy of 3.8 eV at liquid nitrogen temperature (the operating temperature of the detector). Ca K_{α} (3.7 KeV) radiation will produce around 1000

electron-hole couples per photon emitted. The charge collected in the detector is translated into voltage steps, which are collected for a specific period of time giving the user the spectrum of the sample as shown in figure 2.9.

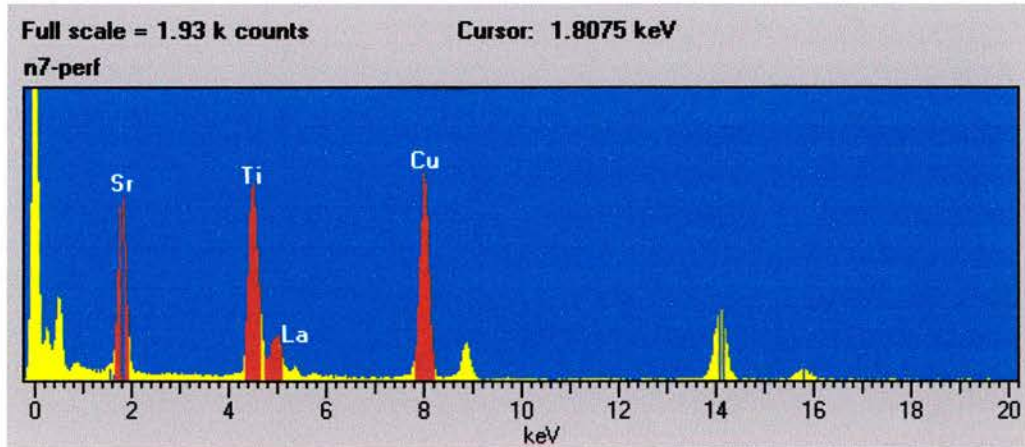


Figure 2.9. Typical EDS spectrum corresponding to $\text{La}_2\text{Sr}_5\text{Ti}_7\text{O}_{22}$.

It should be noted that the detector does not always accept pulses. The dead time is defined as the total time the system is not available to accept pulses and ideally should be lower than 60%, although in lower systems it may be 30%. If the dead time correction is working properly, there should be a linear relation between the input rate and the output rate until it reaches a maximum to then drop off as a consequence of the detector being more time closed than open. It is very inefficient to use the system beyond that maximum as shown in figure 2.10.

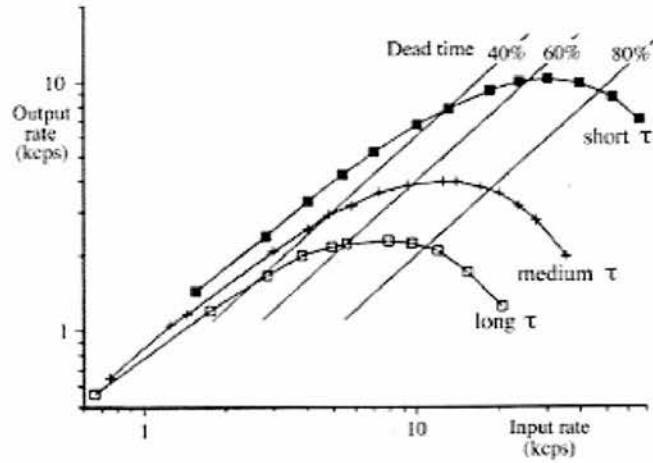


Figure 2.10. Output rate as a function of the input rate at different times (τ). It is very inefficient to operate beyond the output rate maximum.

EDS is a powerful technique that gives the user the possibility of knowing the elemental composition of a region of the sample and, therefore, the possibility of identifying the nature of the specimen studied by HRTEM and electron diffraction. Without knowing the elemental composition of the specimen it is quite difficult to properly interpret the data obtained by the other TEM techniques. Quantitative analysis are usually performed using the Cliff-Lorimer ratio technique, which relates the weight fraction of each element (C_x) with its intensity (I_x) by:

$$\frac{C_A}{C_B} = k_{AB} \frac{I_A}{I_B} \text{ [equation 2-26]}$$

where k_{AB} is the correlation factor. The weight fractions can be calculated simply considering:

$$C_A + C_B = 100 \text{ [equation 2-27]}$$

This is the case of a binary system, which can be extended to ternary or quaternary systems analogously.

The major problems in EDS are related to absorption phenomena, which may affect the reading of the peak intensities, especially at low energy values. To overcome such limitation and to obtain good results, some requirements must be complied:

1. Thin specimen area to reduce absorption phenomena.
2. Small beam size, i.e. low brightness to reduce the rate count.
3. Proper grid, whose lines do not overlap those from specimen.

In addition, recording many spectra helps to reduce the experimental error and allows the user to perform statistical treatment on the data and therefore check the elemental composition of the specimen.

Finally, it is vital choosing the right peaks for quantification. Choosing peaks that overlap with peaks due to other elements in the specimen or peaks affected by absorption phenomena could mean large errors in the quantification.

2.7.5. Simulation of images.

As mentioned above the simulation of high-resolution images using appropriate software is a powerful technique to test the reliability of structural models. These analyses are based in the reconstruction of the interactions of the electron beam with the specimen. Using an approximate model that describes the structure of the specimen, the projected potential of the wavefunctions of the electron fronts after the interaction is calculated considering crystal factors: structure, orientation and

thickness. Usually, the crystal is divided in several slices perpendicular to the direction of the electron beam, which is called the multi-slice approximation. From the projected potential resulting after the interaction with the crystal slices, the theoretical image can be calculated for different optical conditions: defocus, astigmatism, beam tilt and focus spread, which should be optimised by the experimenter. The resulting images should reasonably match the experimental images in the case that the structural model and the optical conditions are right or about right.

2.7.6. Preparation of samples.

The samples for TEM observation are typically prepared by suspending a small amount of the powdered sample in acetone. Few drops of such suspension are deposited onto a perforated carbon-coated copper grid. After evaporation of the acetone, the grid is placed in the microscope sample-holder and then put into the system.

2.8. References.

1. A. R. West: "Solid State Chemistry and its Applications", Wiley & Sons (1992).
2. H. M. Rietveld, *J. Appl. Cryst.*, **2** (1969), 65.
3. A. K. Jonscher: "Dielectric Relaxation in Solids", Chelsea Dielectrics Press, London (1983).
4. J. T. S. Irvine, D. C. Sinclair and A. R. West, *Adv. Mater.*, **2** (1990), 132.

5. D. C. Sinclair, F. D. Morrison and A. R. West, *International Ceramics*, **2** (2000), 33.
6. L. J. van der Pauw, *Philips Res. Rep.*, **13** (1958), 1.
7. Filipe Figueiredo, Ph. D Thesis, University of Aveiro (Portugal), 1999.
8. D. B. Williams and C. B. Carter: "Transmission Electron Microscopy", Plenum Press, New York (1996).
9. J. C. H. Spence: "Experimental High-Resolution Electron Microscopy", Clarendon Press, Oxford (1981).
10. R. Gonzalez, R. Pareja and C. Ballesteros: "Microscopía Electrónica", Ed. Eudema, Madrid (1992).
11. www.jeol.com

Chapter 3. Structural studies on the layered $\text{La}_4\text{Sr}_{n-4}\text{Ti}_n\text{O}_{3n+2}$ series	51
3.1. Introduction. Layered perovskites and cubic phases.	51
3.2. Layered structures in $\text{La}_4\text{Sr}_{n-4}\text{Ti}_n\text{O}_{3n+2}$	59
3.2.1. Synthesis conditions	60
3.2.2. XRD results	61
3.2.3. TEM studies on SrTiO_3 ($n=\infty$)	67
3.2.4. TEM studies on $\text{La}_2\text{Ti}_2\text{O}_7$ ($n=4$)	68
3.2.5. Structural elucidation of $\text{La}_4\text{SrTi}_5\text{O}_{17}$ and $\text{La}_4\text{Sr}_2\text{Ti}_6\text{O}_{20}$	74
3.2.5.1. Synthesis conditions	75
3.2.5.2. Structural elucidation of the $n=5$ member	75
3.2.4.2.1. TEM	75
3.2.4.2.2. XRD	80
3.2.5.3. Structural elucidation of the $n=6$ member	84
3.2.4.3.1. TEM	84
3.2.4.3.2. XRD	87
3.2.6. Intermediate members	92
3.2.5.1. TEM	92
3.2.5.2. XRD	94
3.2.7. Conclusions (layered phases)	96
3.3. Cubic phases	99
3.3.1 $\text{La}_4\text{Sr}_8\text{Ti}_{12}\text{O}_{38-\delta}$ ($n=12$)	99
3.3.1.1. XRD results	99
3.3.1.2. Magnetic measurements and TGA	102
3.3.1.3. Density measurements	105
3.3.1.4. TEM	109
3.3.2. $\text{La}_4\text{Sr}_{10}\text{Ti}_{14}\text{O}_{44}$ ($n=14$)	115
3.3.3. Discussion	119
3.4. Summary	121
3.5. References	123

3. Structural studies on the layered $\text{La}_4\text{Sr}_{n-4}\text{Ti}_n\text{O}_{3n+2}$ series.

3.1. Introduction. Layered perovskites and cubic phases.

SrTiO_3 is the archetype of the perovskite structure, which can be described as a 3D-framework of TiO_6 octahedra sharing corners and the larger Sr^{2+} occupying the 12-coordinated sites surrounded by eight of such network of octahedra (figure 3.1). There are some other valid descriptions for this structure; one of the most useful is a cubic close packed (ccp) array of Sr and O together with the layers parallel to the $\{111\}$ planes and Ti in $\frac{1}{4}$ of the octahedral sites left that do not border with Sr cations.

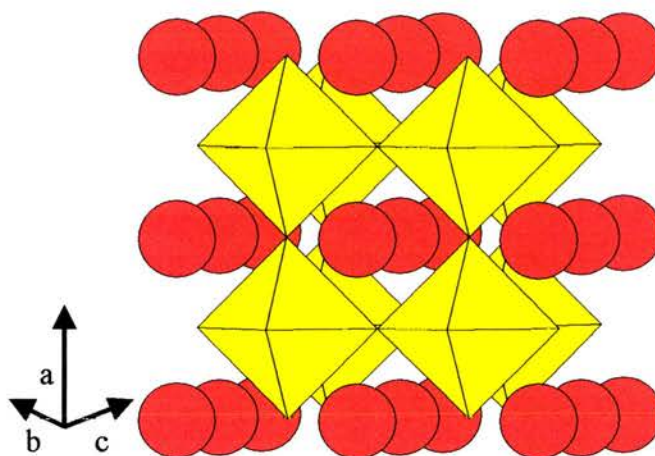


Figure 3.1. Structure of the cubic perovskite SrTiO_3 .

There are several hundreds of oxides and halides described as perovskites, including a large number of compounds showing distortions from the perfect ABO_3 , which is a consequence of the variety in size of the cations involved. In fact, the perovskite mineral giving the name to this structure is CaTiO_3 , a distorted orthorhombic perovskite resulting from the tilting of the octahedra due to the small size of Ca^{2+} . Hence, there exist tetragonal, orthorhombic, rhombohedral, monoclinic

and even triclinic perovskites, which also present a wide range of technological applications: semiconductors, dielectrics, piezoelectrics, electronic conductors, ionic conductors, superconductors, ferroelectrics, etc.

Non-stoichiometry in perovskites is also an extensively investigated topic. Changes in the stoichiometry may affect both cations and oxygen and figure 3.2 shows several non-stoichiometric families of compounds. Perovskites may accept up to 100% vacancies in the A-site, which would result in the structure of ReO_3 , that consists of a 3D network of BO_6 octahedra sharing corners. Between BO_3 and ABO_3 , there exist a wide range of compositions known as bronzes A_xBO_3 . As for oxygen non-stoichiometry, most of the examples in the literature deal with deficiency. In some cases oxygen vacancies are ordered giving rise to new structures as occurs for the brownmillerite ($A_2B_2O_5$) and related Grenier phases that will be described in detail in chapter 7.

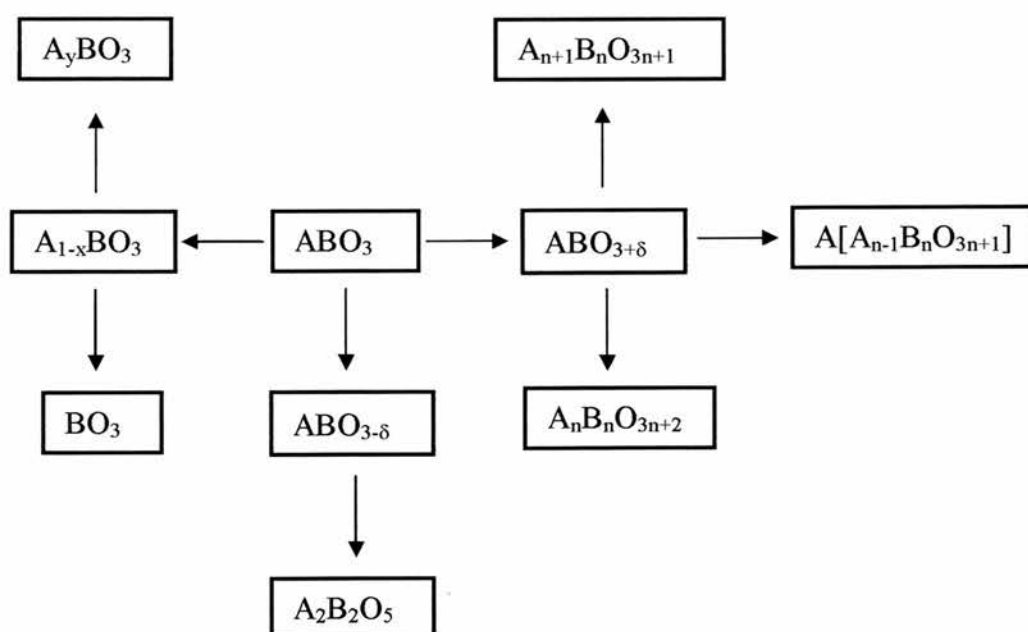


Figure 3.2. Schematic diagram of several non-stoichiometric perovskites.

Oxygen over-stoichiometry is not an intuitive concept in perovskites, because in a ccp arrangement there is no space for interstitial elements, it is often addressed as cation deficiency rather than excess oxygen. There have been however many studies on the so-called layered perovskites, especially Ruddlesden-Popper phases [1-4], Aurivillius and related phases [5-9], Dion-Jacobson [10-12] and the $A_nB_nO_{3n+2}$ homologous series [13], which accommodate excess oxygen in comparison to the parental ABO_3 stoichiometry. Ruddlesden-Popper phases are based on the ability of perovskites to intergrow with rock salt layers. Thus, $A_{n+1}B_nO_{3n+1}$ phases are made of rock salt intergrowths n layers thick with perovskite blocks and they have been subjects of numerous studies, especially in the search of superconducting phases [3-4]. Aurivillius and the related Sillén phases consist typically of $[Bi_2O_2]^{2+}$ and $[M_2O_2]X_2$ fluorite layers respectively, intercalated with perovskite blocks. These are also well known for their ferroelectric properties [5] as occurs with the related Dion-Jacobson phases. As for the $A_nB_nO_{3n+2}$ homologous series, an exhaustive review has been recently published by Lichtenberg and co-workers [13], where studies from several research groups during the last three decades were presented. Some of the most relevant works are listed in Refs [14-26].

There is a general agreement in describing the structure of $A_nB_nO_{3n+2}$ phases as $\{110\}$ perovskite slabs containing n -layers joined by crystallographic shearing along the $[100]_p$. $La_2Ti_2O_7$ constitutes one example of these phases and its structure is derived from perovskite blocks containing 4 layers, with adjacent slabs offset from one another by $\frac{1}{2}[100]_p$. The connectivity between octahedra sharing corners is broken at the crystallographic shears, where the oxygens beyond the ABO_3 stoichiometry are situated (figure 3.3). The octahedra are strongly distorted and tilted

as reported elsewhere [7-9], and La is shifted from the A site of the hypothetical perovskite towards the crystallographic shears at the end of the blocks, which is the cause of the broken connectivity at these specific locations. Obviously, as one moves towards higher members of the $\text{A}_n\text{B}_n\text{O}_{3n+2}$ series the perovskite blocks become larger with increasing n , which is reflected in the gradual increase of the c -axis. Therefore the $\text{A}_n\text{B}_n\text{O}_{3n+2}$ series differs from the rest of the layered families because it is derived entirely from the primitive ABO_3 rather than intergrowths with other structures.

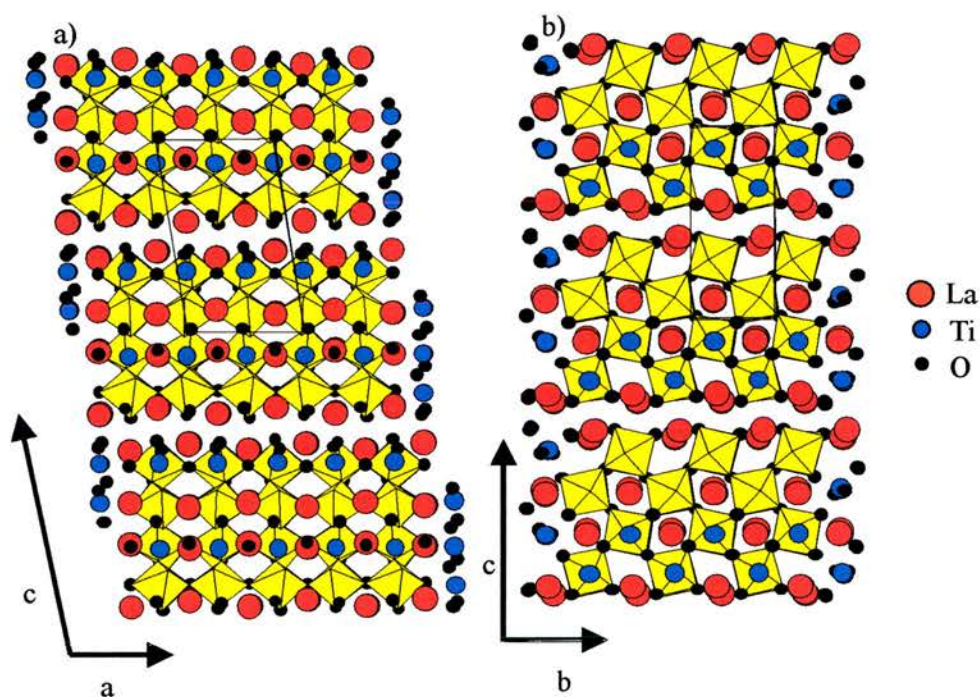


Figure 3.3. Structural models for $\text{La}_2\text{Ti}_2\text{O}_7$ viewed down the $[010]$ projection (a) and the $[100]$ projection (b). In the former the shift by $\frac{1}{2}(100)_p$ that causes the breakage in the connectivity the octahedra belonging to two consecutive blocks is quite evident. In the latter the shift of La from the A-site on a perovskite towards the crystallographic shear is especially clear.

In figure 3.4 the oxygen framework is presented alone to highlight the oxygen rich planes that join consecutive blocks.

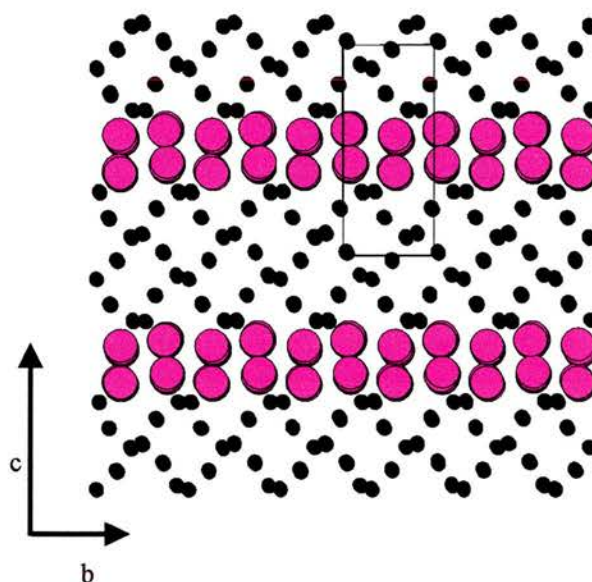


Figure 3.4. Oxygen framework in $\text{La}_2\text{Ti}_2\text{O}_7$. The oxygen ions in the crystallographic shears that join two consecutive blocks are in purple.

The unit cell of $\text{La}_2\text{Ti}_2\text{O}_7$ is monoclinic with $a=7.81 \text{ \AA}$, $b=5.56 \text{ \AA}$, $c=13.01 \text{ \AA}$ and $\beta=98.66$ (space group $P2_1$) and it was first reported simultaneously by Gasperin and Ishizawa *et al.* [14-15]. The relation with perovskite is still clear and thus $a=2a_p$, $b=2\sqrt{2}a_p$ and $c=2\sqrt{2}a_p+\alpha$. The parameter α is the distance between consecutive blocks and it would reflect the length of the crystallographic shears, which in the present case is around 2 \AA . Equivalent structures have been found for other ‘227’ phases such as $\text{Ca}_2\text{Nb}_2\text{O}_7$ [25], $\text{Nd}_2\text{Ti}_2\text{O}_7$ [19] or $\text{Sr}_2\text{Nb}_2\text{O}_7$ [15,21], differing in some cases with the a -axis not being doubled and occasionally the unit cells are orthorhombic rather than monoclinic.

The $n=5$ member has also been subject of a number of various systems investigations especially in niobates and titanates, such as $\text{Ca}_5\text{Nb}_5\text{O}_{17}$ [13], $\text{Sr}_5\text{Nb}_5\text{O}_{17}$

[35], $La_5Ti_5O_{17}$ [25], $Ca_5Nb_4TiO_{17}$ [36] or $La_4SrTi_5O_{17}$ [17]. The structure has been described as derived from perovskite blocks containing 5-layers each and joined by shearing as well. In most of the cases, the c-axis appeared to be doubled in comparison to that of the n=4 member due to slight canting between consecutive blocks. Surprisingly, there is no reported discussion on the effect of such doubling on the monoclinic angle (β), which will be properly addressed in the present chapter. It is also very interesting to note that for some of these phases, the a-unit cell parameter was halved in comparison to the n=4 member arguing that the $[(2h+1)kl]$ were not observed by SAED. Compounds with n=5 structural-type are especially interesting because of their high conductivity which arises when there is mixed valence of the B-cations, i.e. $Ti^{III/IV}$ and $Nb^{IV/V}$. Indeed, quasi-1D metallic behaviour has been reported in several of these niobates and titanates at room temperature [13].

For the n=6 member, there are only a few well-described examples in the literature. Investigations mainly based on XRD on $Nd_4Ca_2Ti_6O_{20}$ and $La_4Ca_2Ti_6O_{20}$ reported by Nanot *et al.* [23-24] are the only crystallographic studies in the bibliography. Their structure can be described as derived from 6-layers perovskite blocks joined by shearing, although the samples studied seemed to be a mixture of phases. Additionally, an incommensurate modulation was also suggested from the satellite reflections linked by diffuse streaking in the XRD patterns. Pasero *et al* [20] investigated the $SrTiO_3$ - $Sr_2Nb_2O_7$ system and they described the formation of the n=6 ($Sr_6Nb_4Ti_2O_{20}$) and the n=7 member ($Sr_7Nb_4Ti_3O_{23}$) intergrowing with $SrTiO_3$. Similar examples were also found in the $Nd_2Ti_2O_7$ - $NdTiO_3$ system [19].

All the mentioned investigations share a common feature: compounds with $n > 5$ could not be obtained as a single or, even a major phase, although one of the models predict larger perovskite blocks with advancing towards until the $n=\infty$ member, which is a cubic perovskite. Figure 3.5 presents a schematic structural model for the $A_nB_nO_{3n+2}$ series.

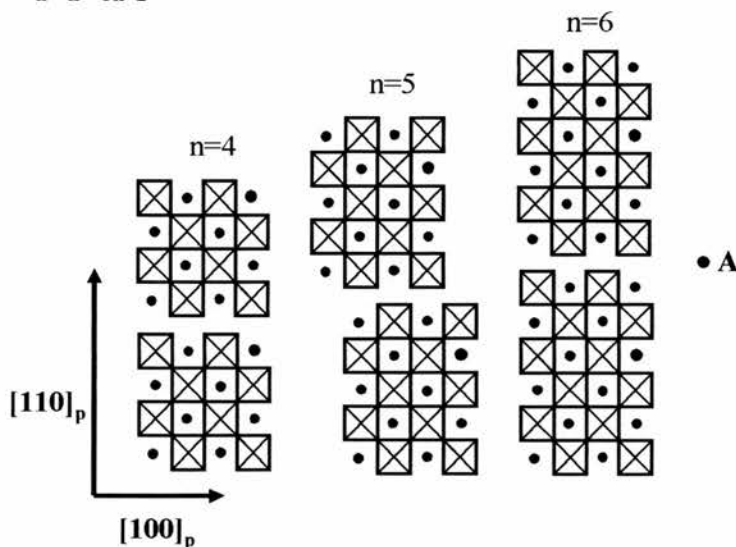


Figure 3.5. Schematic model for the $A_nB_nO_{3n+2}$ series as reported elsewhere [13].

Cubic Phases.

The substitution of Sr^{2+} by La^{3+} in the A-site of $SrTiO_3$ under oxidising conditions represents an intriguing case because charge neutrality dictates the presence of additional oxygen beyond the ABO_3 stoichiometry. That is a difficult situation to imagine considering that in a ccp arrangement there is no space for interstitial elements; unless cation vacancies are introduced into the pseudocubic perovskite structure.

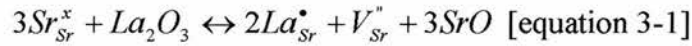
During the last two decades numerous works have been published on La substituting Sr in $SrTiO_3$. Some of those investigations focused on A-site deficient

perovskites to compensate the different charge of the cations involved. Thus, 2 La^{3+} would substitute 3 Sr^{2+} in the lattice creating one cation vacancy and giving rise to the $La_xSr_{1-3x/2}TiO_3$ system. La contents up to $x=0.4$ yield simple cubic perovskite unit cells. For higher La contents, vacancies seem to become ordered yielding lower symmetry unit cells as reported in the detailed TEM investigations carried out by Battle *et al* [27].

Some investigations on the $La_{1-x}Sr_xTiO_3$ system have been also published, i.e. without cation deficiency. The surplus of positive charge caused by La^{3+} substituting Sr^{2+} is counterbalanced by Ti as Ti(III) under reducing conditions and thus maintain the electroneutrality of the crystal. These phases are usually achieved by using precursors containing Ti^{3+} and operating always in reducing conditions. For $x>0.80$ the unit cell remained as cubic, although at higher La contents the compounds crystallise in the orthorhombic space groups *Ibmm* and *Pbnm* ($x<0.30$), which is consistent with the unit cell of the end members of the system. $SrTiO_3$ has a cubic unit cell $a=3.9059\text{Å}$, space group *Pm-3m*, whilst $LaTiO_3$ has an orthorhombic unit cell with parameters $a=5.629\text{Å}$, 5.612Å , $c=7.915\text{Å}$, with space group *Pbnm* [28].

When the conditions are oxidising, there exists some controversy although most of the studies conclude that the excess of positive charge is compensated by the formation of vacancies on the A-site, preferentially as Sr vacancies [29-31]. This would lead to the formation of compounds with structure analogous to the Ruddlesden-Popper $Sr_{n+1}Ti_nO_{3n+1}$ series [32]. In other words, Sr vacancies are accommodated by the creation of SrO layers that regularly intergrow with perovskite layers.

This can be expressed using Kroger-Vink notation as:



Furthermore, Bowden *et al.* [17] attributed the presence of excess oxygen to the creation of planar defects similar to the crystallographic shears observed in $La_2Ti_2O_7$. These were observed distributed randomly within a perovskite matrix. There are still some unanswered questions such as how the crystallographic shears are formed, what is their size, what is their effect on the properties, etc.

In the structural studies presented herein, we introduce the family of layered perovskites $La_4Sr_{n-4}Ti_nO_{3n+2}$ ($La_2Ti_2O_7$ - $SrTiO_3$ system) and it is demonstrated how excess oxygen can be incorporated into a titanate perovskite-based lattice. Of special interest is the region where the oxygen rich planes become so dilute that are not able to form regular shear intergrowths, because that could be the link between layered perovskites and the formation of linear defects in La-doped $SrTiO_3$. On the other hand, it is very attractive to find out whether it is possible to synthesise layered perovskites with n greater than 5 as a single phase or, at least, as a major phase. To our best knowledge, there have not been published any complete structural studies considering this system as layered perovskite. It is the purpose of this chapter to give an insight to these structures.

3.2. Layered structures in $La_4Sr_{n-4}Ti_nO_{3n+2}$.

The target was to synthesise new layered perovskites by modulating the size of the slabs and test their potential as anodes for fuel cell technology. To facilitate the

comprehension of the earliest idea of the project, it must be mentioned that the $\text{La}_4\text{Sr}_{n-4}\text{Ti}_n\text{O}_{3n+2}$ family can be regarded as an intergrowth between the two end members: SrTiO_3 ($n=\infty$) and $\text{La}_2\text{Ti}_2\text{O}_7$ ($n=4$, $\text{La}_4\text{Ti}_4\text{O}_{14}$). Advancing towards higher values of n , the number of layers per block gradually increases, i.e. n layers per slab as described in the introduction, until $n=\infty$ which is a perfect cubic perovskite.

Some oxide ion conductivity might be achieved due to the presence of oxygen-rich planes. Moreover the reduction of some Ti^{4+} to Ti^{3+} could also enhance the electronic conductivity as occurs for $\text{La}_5\text{Ti}_5\text{O}_{17}$, which has been reported to have quasi-1D metallic conductivity within the layers as mentioned above. The possibility of mixed conductivity of both ionic species and electrons makes these phases candidates as fuel electrode materials in fuel cell technology, especially if the excess oxygen can be made to disorder. The electrical studies performed in this series of compounds are presented in chapter 4.

3.2.1. Synthesis conditions.

Preparation of the samples was carried out using the traditional ceramic route described in section 2.1, according to the following equation:



It is worth mentioning that from now on, the different members will be named after their respective n . For instance, the $n=8$ member corresponds to the formula $\text{La}_2\text{Sr}_2\text{Ti}_4\text{O}_{13}$ (i.e. $\text{La}_4\text{Sr}_4\text{Ti}_8\text{O}_{26}$).

3.2.2. XRD results.

The XRD patterns of the end members are in agreement with literature data. $SrTiO_3$, the archetype of the perovskite structure, shows a cubic unit cell, space group $Pm-3m$ and $a=3.9039(5)$ Å, whilst $La_2Ti_2O_7$ shows a monoclinic symmetry (space group $P2_1$, $a=7.812(2)$ Å, $b=5.542(1)$ Å, $c=13.010(2)$ Å, $\beta=98.66(1)^\circ$. (figures 3.6-3.7, tables 3-1-3.2).

2θ	hkl	$2\theta_{cal}$	Int	d_{obs}	d_{cal}
22.764	100	22.760	6	3.9032	3.9039
32.408	110	32.407	100	2.7603	2.7605
39.964	111	39.968	21	2.2542	2.2539
46.481	200	46.486	36	1.9521	1.9519
52.357	210	52.362	3	1.7460	1.7459
57.813	211	57.805	30	1.5936	1.5938
67.848	220	67.848	16	1.3802	1.3802

Table 3.1. Refined XRD data for $SrTiO_3$

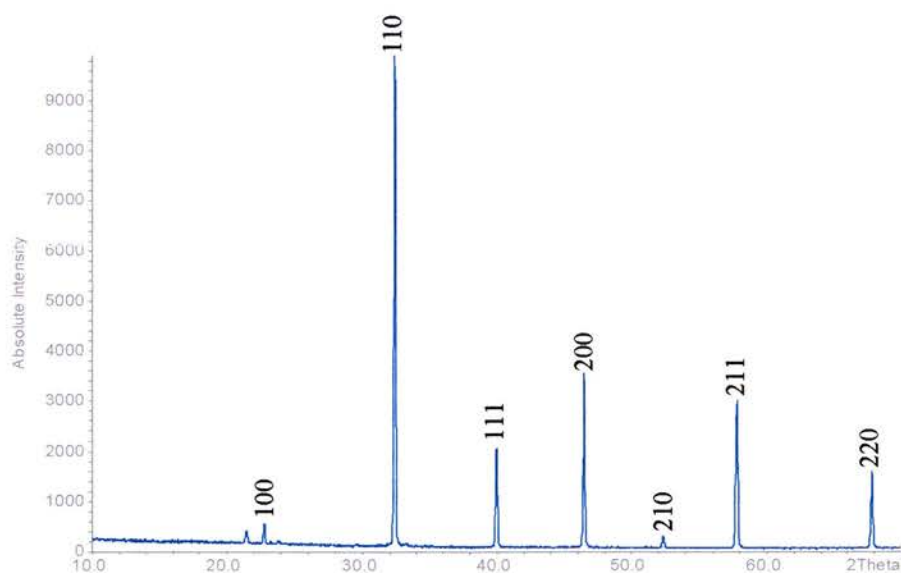
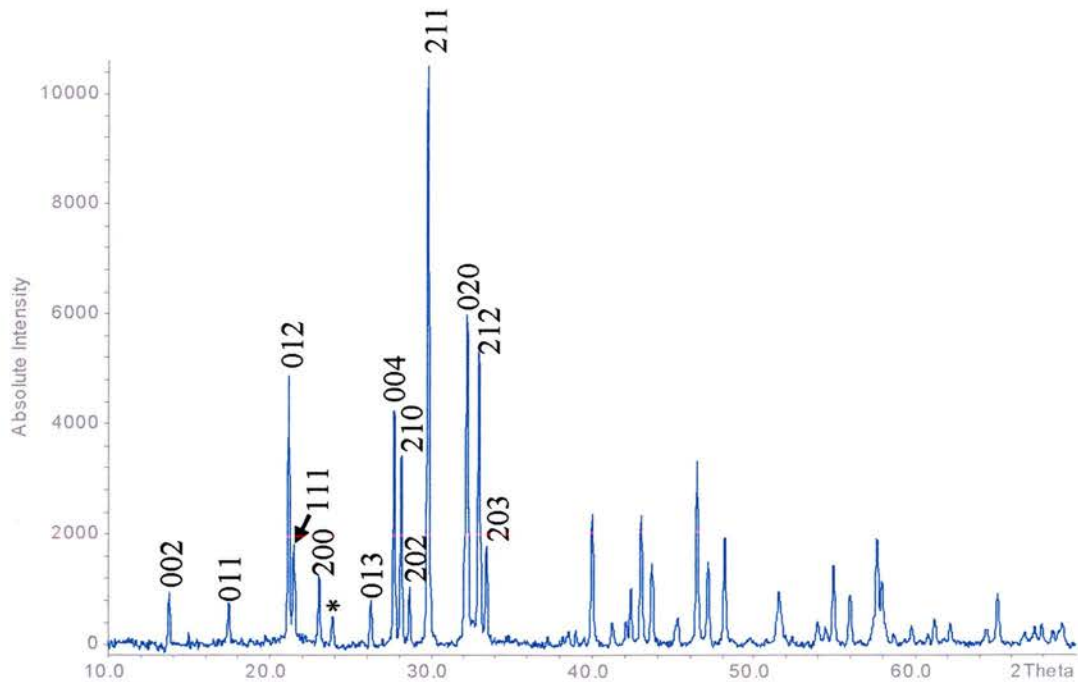


Figure 3.6 XRD pattern of the $n=\infty$ member ($SrTiO_3$).

2θ	hkl	$2\theta_{\text{cal}}$	Int	dobs	dcal
13.751	002	13.762	24	6.4345	6.4294
17.399	011	17.392	21	5.0929	5.0948
21.138	012	21.132	55	4.1997	4.2008
21.452	111	21.458	28	4.1388	4.1378
23.020	200	23.028	26	3.8603	3.8591
26.259	013	26.251	22	3.3912	3.3921
27.717	004	27.728	52	3.2160	3.2147
28.144	-211	28.146	39	3.1681	3.1679
28.682	202	28.682	24	3.1099	3.1099
29.841	211	29.838	100	2.9917	2.9920
32.227	020	32.239	49	2.7754	2.7745
32.994	212	32.992	60	2.7126	2.7129
33.463	203	33.462	28	2.6757	2.6758
40.006	-221	39.993	29	2.2519	2.2526
42.415	-215	42.428	20	2.1294	2.1288
43.030	024	43.030	30	2.1004	2.1004
43.698	-223	43.693	22	2.0698	2.0699
45.344	016	45.325	14	1.9984	1.9992
46.508	-401	46.497	33	1.9511	1.9515
47.165	-224	47.161	24	1.9254	1.9256
48.204	320	48.200	27	1.8863	1.8865
51.609	-413	51.607	18	1.7696	1.7696
54.028	026	54.023	13	1.6959	1.6961
55.010	230	55.010	21	1.6680	1.6679
56.888	126	56.902	17	1.6173	1.6169
57.694	-421	57.709	22	1.5966	1.5962
61.336	-218	61.335	12	1.5102	1.5102
65.192	423	65.193	18	1.4299	1.4299

Table 3-2. Refined XRD data for $\text{La}_2\text{Ti}_2\text{O}_7$.Figure 3.7. Indexed XRD pattern for $\text{La}_2\text{Ti}_2\text{O}_7$. Vaseline peak is marked with *.

The evolution from the monoclinic $\text{La}_2\text{Ti}_2\text{O}_7$ through to the simple cubic unit cell of SrTiO_3 via intermediate members is quite evident in the XRD pattern of the intermediate members (figure 3.8). In fact, the situation of a simple cubic unit cell is apparently achieved for the $n=12$ member, i.e. $\text{La}_4\text{Sr}_8\text{Ti}_{12}\text{O}_{38}$. Moving from this compound to lower values of n , both splitting of the perovskite peaks and the presence of new reflections are observed, leading to the much lower symmetry found for $\text{La}_2\text{Ti}_2\text{O}_7$.

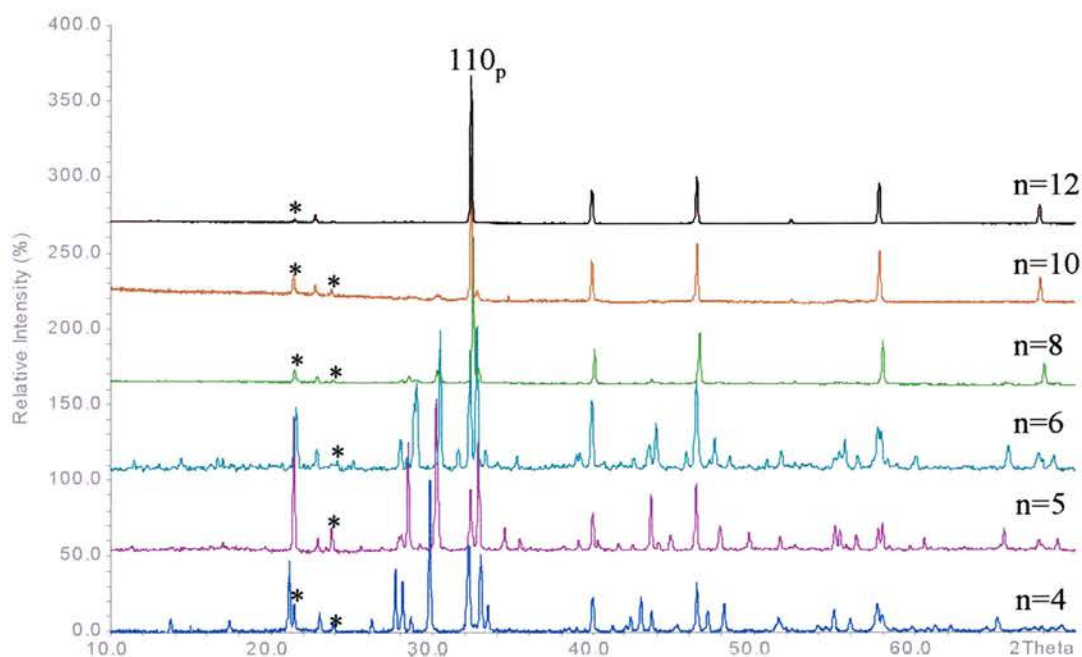


Figure 3.8. XRD patterns of the $\text{La}_4\text{Sr}_{n-4}\text{Ti}_n\text{O}_{3n+2}$ series. The 110 reflection for a cubic perovskite is indexed. * indicates vaseline peaks.

The evolution of the (110) reflection in the perovskite unit cell, i.e. $n=12$ or SrTiO_3 , through to the $n=4$ member shows how the series evolves (figure 3.9). For the $n=10$ member a weak extra reflection appears at slightly higher 2θ values, which becomes larger for the $n=8$ member and larger still for the $n=6$ member together with a subtle shift towards higher 2θ values. Simultaneously, the primitive $(110)_p$ shifts to lower 2θ values as the symmetry of the system decreases. This happens not only in

the case of the $(110)_p$ reflection but also for rest of the primitive perovskite reflections, which is a clear evidence of the loss of symmetry when moving towards lower n members.

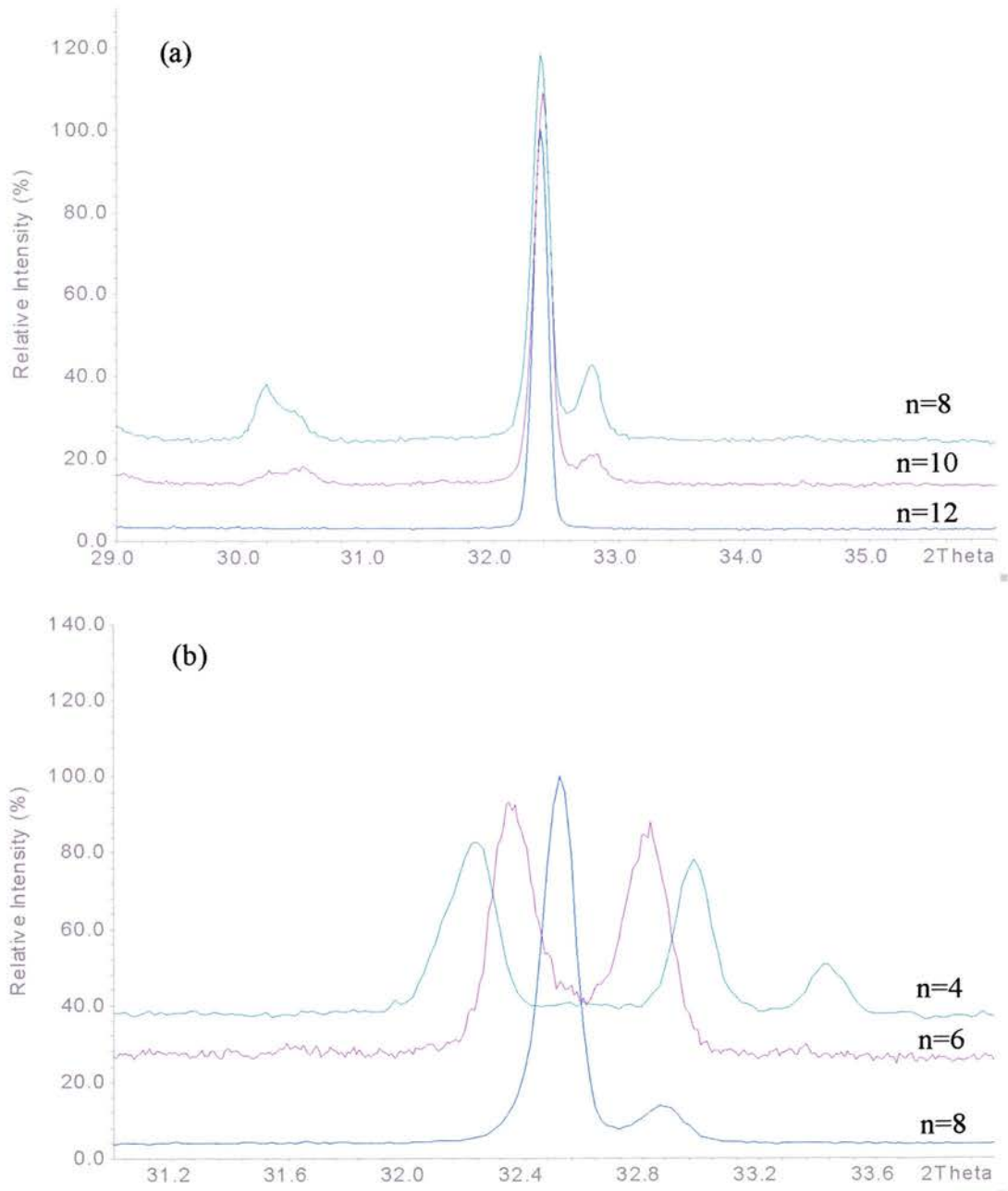


Figure 3.9. Evolution of the 110 perovskite reflection through to the $\text{La}_4\text{Sr}_{n-4}\text{Ti}_n\text{O}_{3n+2}$ series.

In summary, it seems that there is a gradual evolution in the structure between the two end members. The possibility of a mixture of phases could be contemplated, although the perovskite peaks seem to evolve gradually, shifting simultaneously and therefore that approach seems wrong. On the other hand, an interesting question that may arise at this point is whether the first member with cubic perovskite unit cell is definitely the $n=12$ member. XRD performed on the $n=11$ member ($\text{La}_4\text{Sr}_7\text{Ti}_{11}\text{O}_{35}$) revealed that the extra reflections characteristic of the lower members in comparison to the $n=12$ member start to be detected (figure 3.10).

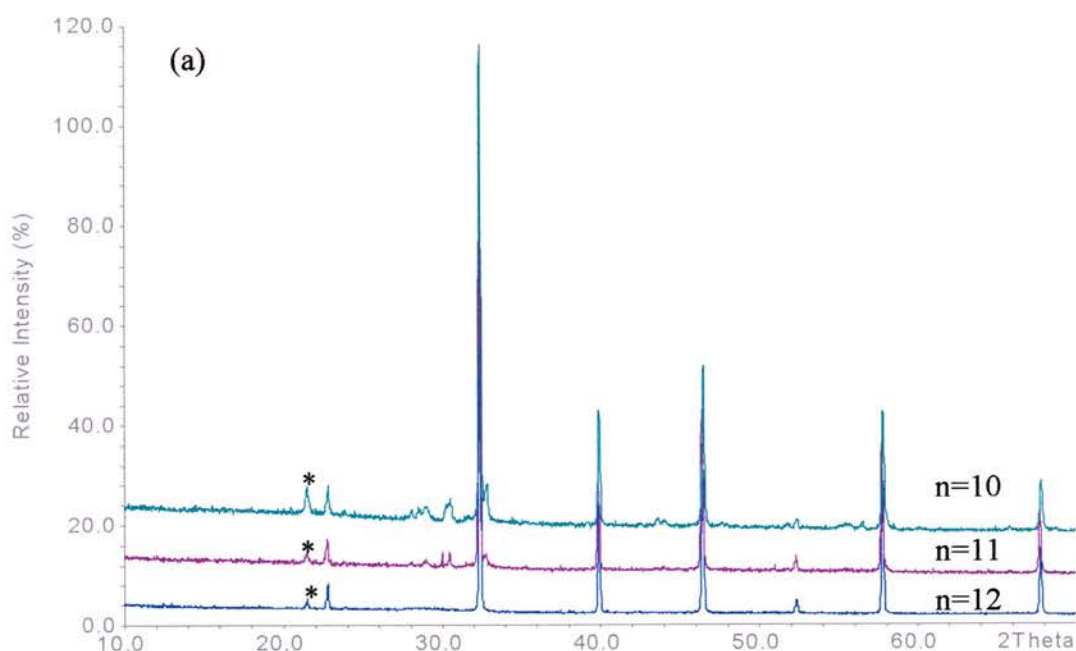


Figure 3.10a. XRD patterns showing the transition through to the cubic perovskite $n=12$ member.

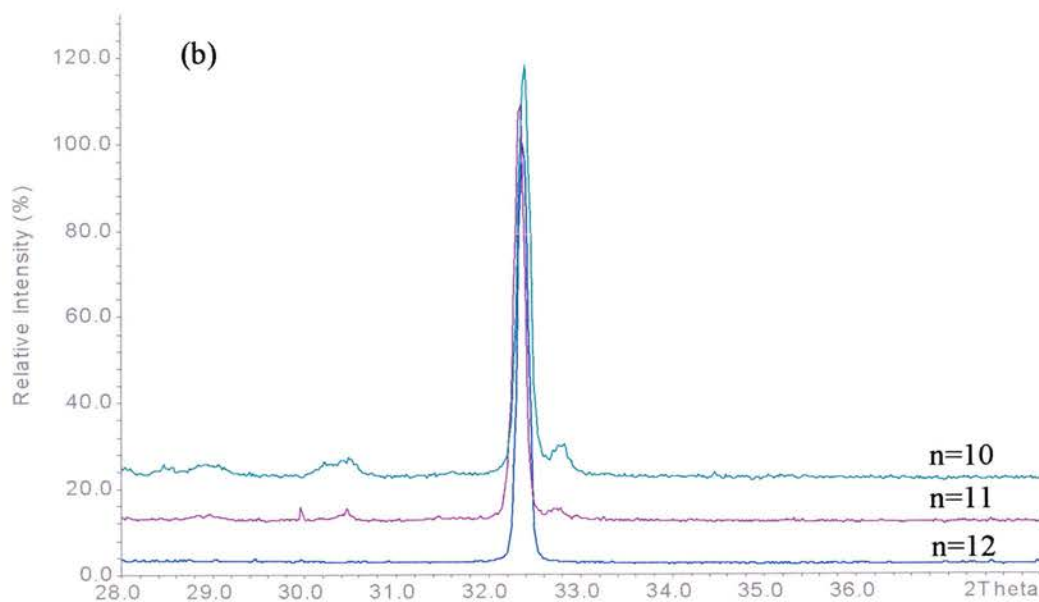


Figure 3.10b. Detail of the evolution on the $(110)_p$ reflection for the $n=10,11$ and 12

members.

Therefore the $n=12$ member should be considered as the first compound in this series having a cubic perovskite unit cell. Obviously for higher values of n , the corresponding XRD patterns were indexed as cubic perovskites until reaching the other end member, SrTiO_3 ($n=\infty$) (figure 3.11)(table3-3).

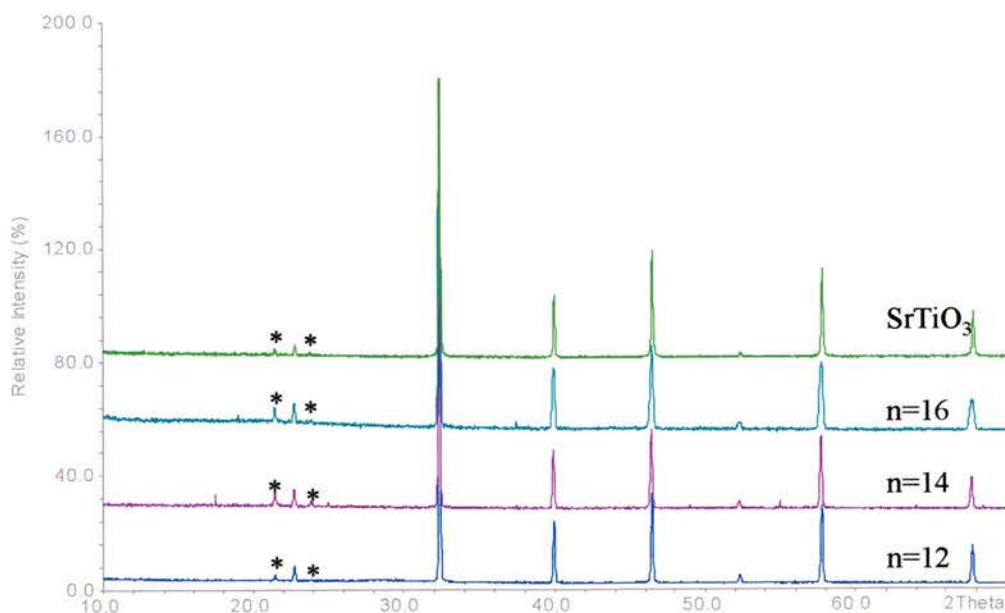


Figure 3.11. XRD pattern of the cubic phases on the $\text{La}_4\text{Sr}_{n-4}\text{Ti}_n\text{O}_{3n+2}$ series. * denotes vaseline peaks.

n	a(Å)	V(Å ³)
12	3.9094(4)	59.75(1)
14	3.9128(2)	59.91(1)
16	3.910(1)	59.79(3)
∞	3.9039(5)	59.50(1)

Table 3.3. Refined cell parameters for the cubic phases of the $\text{La}_4\text{Sr}_{n-4}\text{Ti}_n\text{O}_{3n+2}$ series.

3.2.3. TEM studies on SrTiO_3 ($n=\infty$).

Preliminary studies carried out by TEM give complementary information about the structure of these mixed oxides that could lead to the complete indexing of the XRD patterns. Obviously the first choice is a study of the end members of the family because of their well-known structure. Figure 3.12 shows the main zone axes of SrTiO_3 , where the cubic unit cell is confirmed. No superstructure reflections are evident as expected from the XRD data.

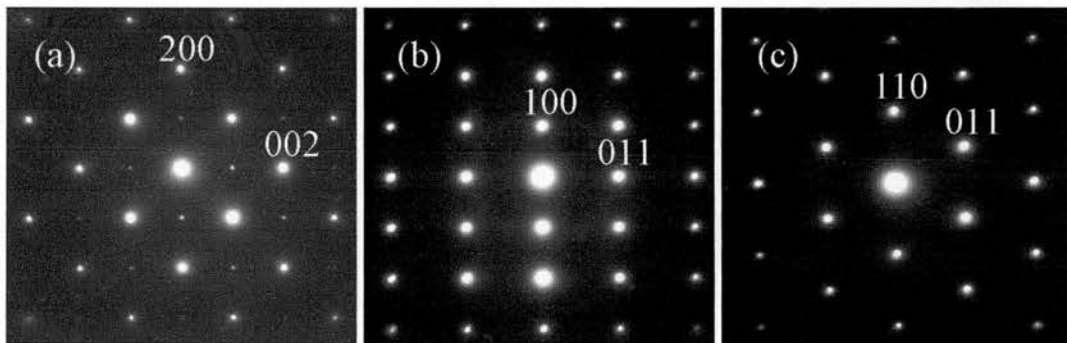


Figure 3.12. SAED patterns viewing down the $[100]_p$ (a), $[110]_p$ (b) and $[111]_p$ (c) projections for SrTiO_3 . No superstructure reflection are observed as expected from literature data.

3.2.4. TEM studies on $\text{La}_2\text{Ti}_2\text{O}_7$ ($n=4$).

For $La_2Ti_2O_7$, the information given by XRD and data in the literature were confirmed, and figure 3.13 shows some SAED of the main zone axes.

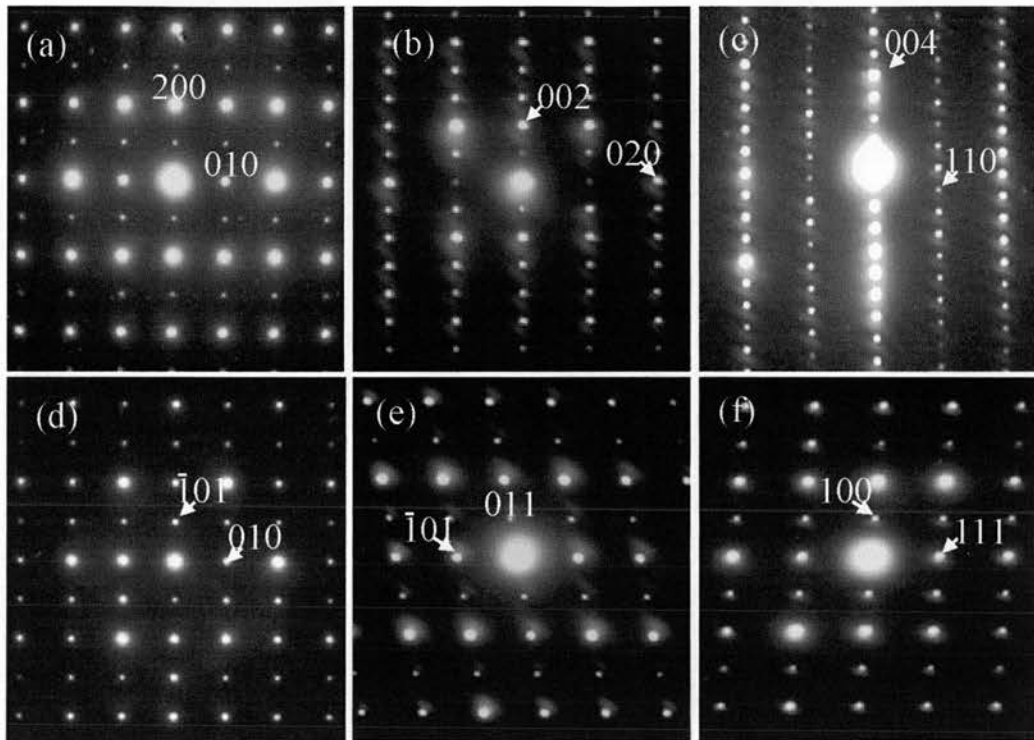


Figure 3.13. SAED pattern viewing down the main projections in $La_2Ti_2O_7$: (a) $[001]$, (b) $[100]$, (c) $[1-10]$, (d) $[-101]$, (e) $[1-11]$ and (f) $[01-1]$.

Figures 3.14-3.19 show some relevant HRTEM images of $\text{La}_2\text{Ti}_2\text{O}_7$. In some of them the layered nature of this compound is highlighted with 4 layers per block.

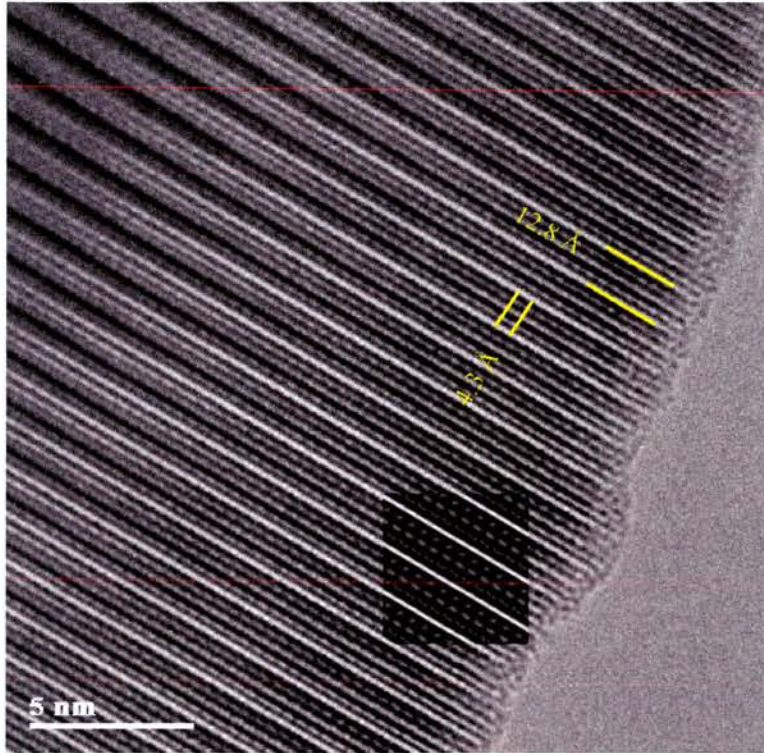


Figure 3.14. HRTEM image viewing down the [1-10] projection of $\text{La}_2\text{Ti}_2\text{O}_7$. It is very clear that each block contains four layers. The inset shows the calculated image recorded at defocus -300Å and thickness 140Å .

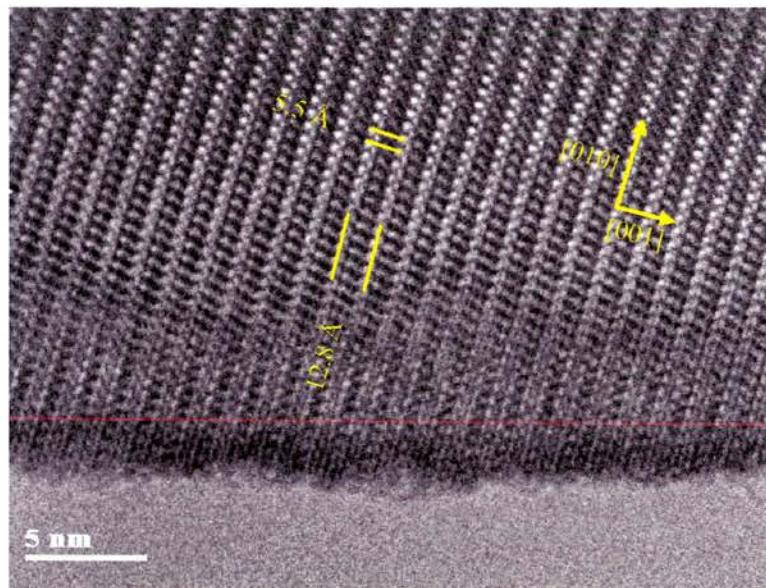


Figure 3.15. HRTEM picture corresponding to the [100] projection of $\text{La}_2\text{Ti}_2\text{O}_7$.

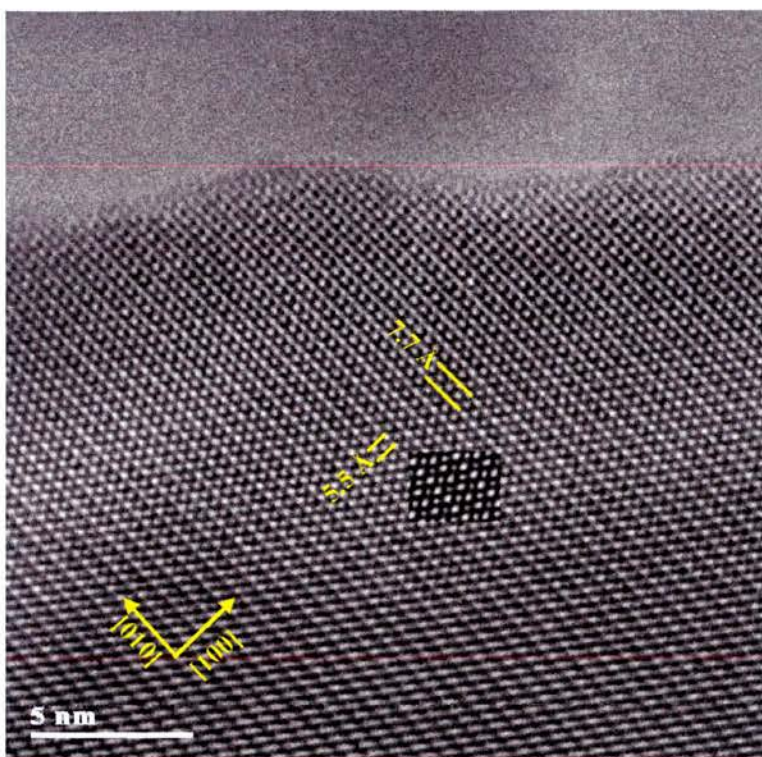


Figure 3.16. HRTEM image showing the projection down the [001] direction of $\text{La}_2\text{Ti}_2\text{O}_7$. The inset shows the simulated image at defocus -300\AA and thickness of the crystal 150\AA .

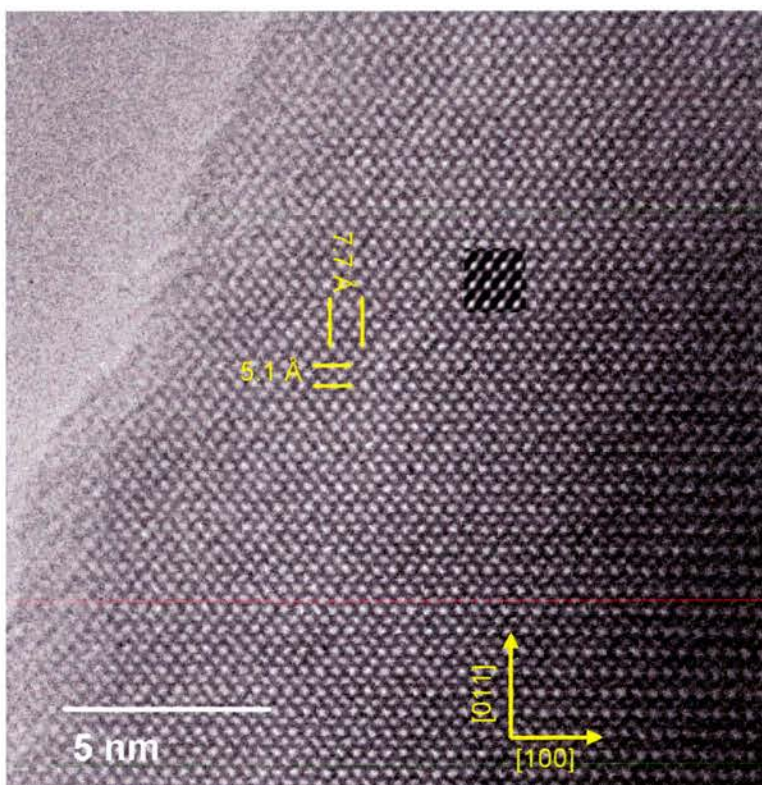


Figure 3.17. HRTEM image showing a view down the [01-1] direction of $\text{La}_2\text{Ti}_2\text{O}_7$. The corresponding calculated image (inset) was recorded at defocus -250\AA and thickness 80\AA .

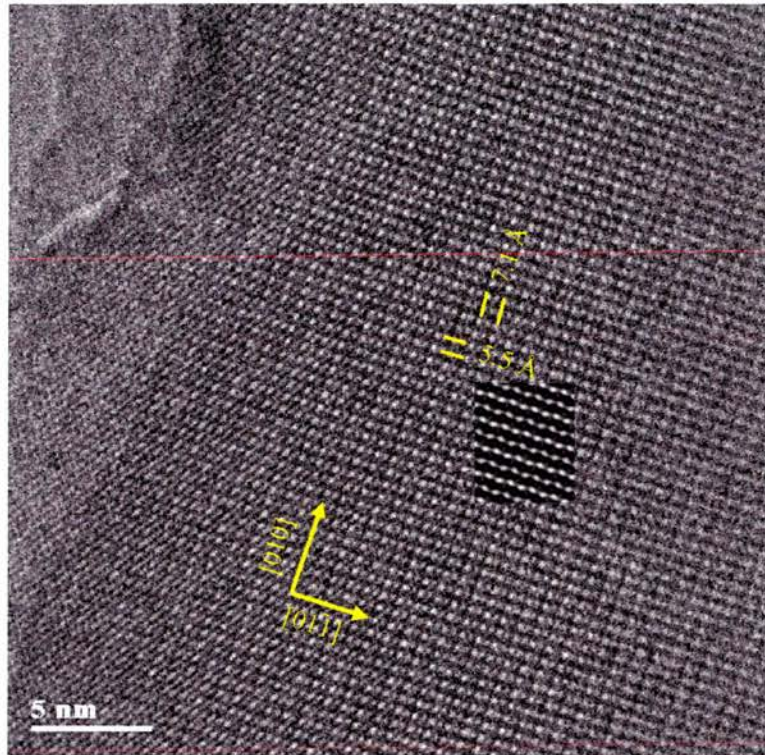


Figure 3.18. HRTEM viewing down the $[-101]$ projection of $\text{La}_2\text{Ti}_2\text{O}_7$. The corresponding calculated image (inset) was recorded at defocus -300 \AA and thickness 420 \AA .

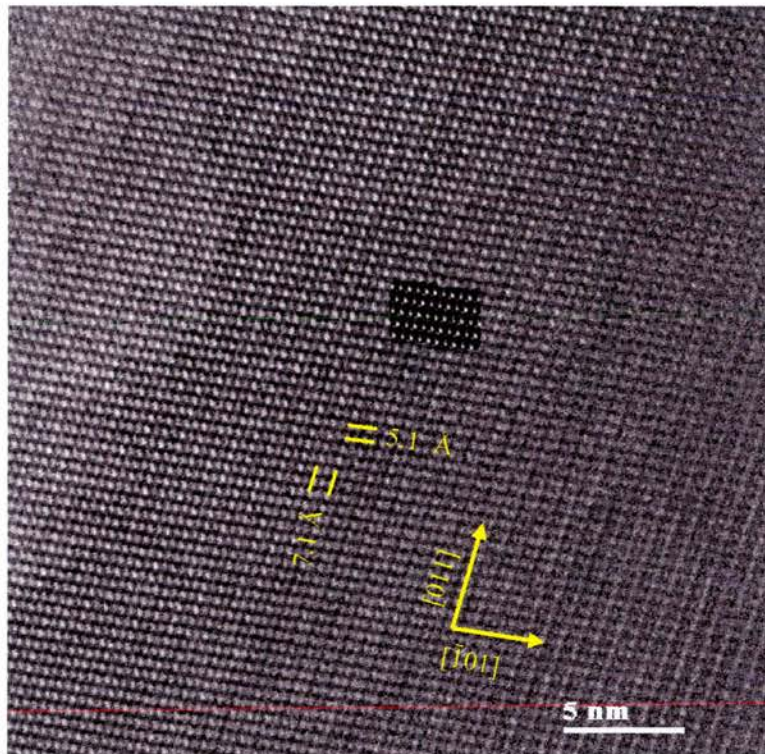


Figure 3.19. HRTEM showing the $[1-11]$ zone axis of $\text{La}_2\text{Ti}_2\text{O}_7$. The inset shows the calculated image recorded at defocus -300 \AA and thickness 205 \AA .

The insets presented on the previous figures represent the calculated images for the structural model proposed in the literature by Schmalte et al. [16] by using the multi-slice method. The coincidence of the so-calculated images with the experimental images is in every case very good, indicating the suitability of the model, which will be used as reference in the structural elucidation of the subsequent members of the $\text{La}_4\text{Sr}_{n-4}\text{Ti}_n\text{O}_{3n+2}$ series.

Before that, it is worth discussing about the presence of defects in $\text{La}_2\text{Ti}_2\text{O}_7$, to help to understand the complexity of these compounds. Occasionally, there appears doubling of the c axis (i.e. $c=26\text{\AA}$) as illustrated in figure 3.20, which can be attributed to microtwinning as has been well established before.

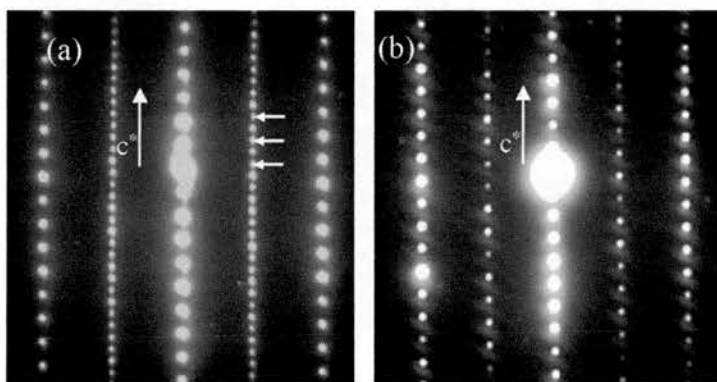


Figure 3.20. SAED patterns corresponding to the $[1-10]_m$ projection showing a doubled (a) and single (b) c -axis. The apparent doubling of the c -axis is due to microtwinning.

Defects are a common feature of these phases and they appear in various zone axes. As an example, figure 3.21 shows a SAED pattern that could mislead in the estimation of the unit cell parameters, because there appear reflections at approximately 7.7\AA in perpendicular directions. One might think that $b \approx a = 7.7\text{\AA}$. In fact, such diffuse reflections do not correspond to identical d -spacings, being larger in one direction than in the other (7.8\AA vs. 7.6\AA). The most reasonable explanation for

such a doubling is, one more time, microtwinning. Therefore, the presence of microdomains rotated 90° from each other would lead (in this case mislead) to an apparent doubling of the a -axis in two perpendicular directions as schematically represented in figure 3.21b. However, there are no hkl families of planes with d-spacing $\approx \frac{1}{2} [100]$ and perpendicular to it. Performing some quick calculations it can be found that $\sqrt{2}[010] = 7.8\text{\AA}$ and $\sqrt{2}[-102] = 7.6\text{\AA}$, being $[010] \perp [-102]$. Consequently, there exists microtwinning of perpendicularly set $[201]$ domains. Indeed, in the corresponding HRTEM image (figure 3.21c), it is possible to observe the presence of the nanodomain texture, derived from $[201]$ the domains rotated 90° from each other, which give rise to a strong contrast at d-spacings of 7.6-7.8 \AA .

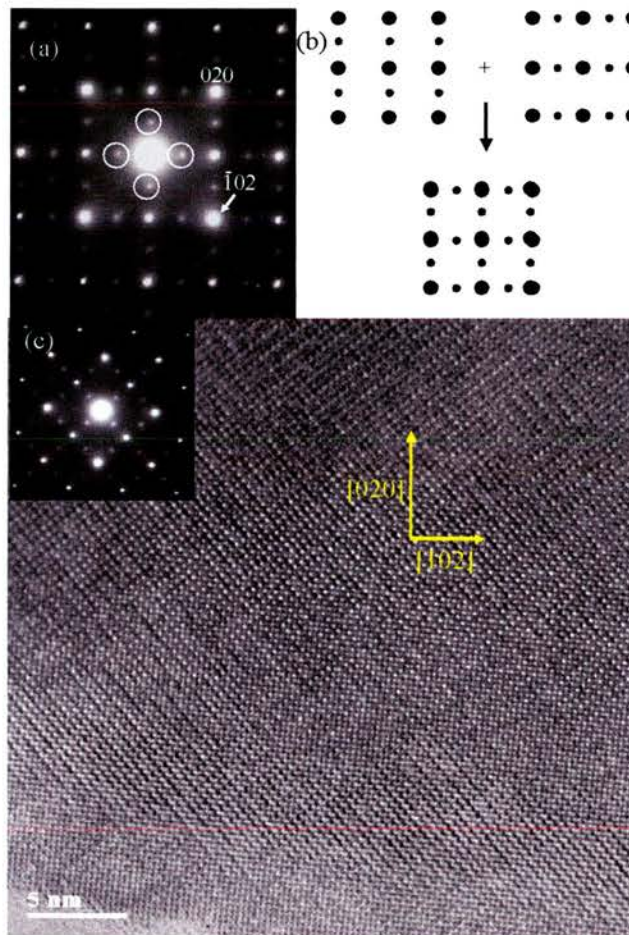


Figure 3.21. SAED pattern showing microtwinning on the $[201]$ zone axis (a) and the corresponding HRTEM image. (b) represents the superposition of the SAED patterns of two identical domains rotated 90° from each other.

3.2.5. Structural elucidation of $\text{La}_4\text{SrTi}_5\text{O}_{17}$ (n=5) and $\text{La}_4\text{Sr}_2\text{Ti}_6\text{O}_{20}$ (n=6).

3.2.5.1. Synthesis conditions.

Specimens of the n=5 and n=6 member have been prepared under different conditions of reaction time and temperature as listed in table 3-4 and thus the phase formation can be monitored by XRD and TEM. The n=5 member could be synthesised using relatively short reaction times as happens for $\text{La}_2\text{Ti}_2\text{O}_7$, whilst the n=6 member required extremely long annealing times to yield a major phase. This indicates the increased difficulty in achieving homogeneous samples when ordering in gradually larger perovskite blocks. The following discussion will only apply to samples A and D, which were essentially single phase.

Sample	Member	T (°C)	t(days)	n=4	n=5	n=6	n=∞	Other n
A	5	1500	3	-	D	-	T	-
B	6	1500	2	-	D	-	S	T
C		1500	2+2	-	S	T	S	T
D		1600	3+3+3	-	-	D	T	-

Table 3-4. Reaction conditions and phase formation for the n=5, 6 members of the $\text{La}_4\text{Sr}_{n-4}\text{Ti}_n\text{O}_{3n+2}$ series. D: dominant. S: significant. T: traces. The reaction times are referred as the addition of consecutive steps separated by an intermediate process of grinding and mixing.

3.2.5.2. Structural elucidation of the $n=5$ member.

3.2.5.2.1. TEM.

On the SAED patterns obtained for the $n=5$ it is found that most of the main zone axes resemble with those of $\text{La}_2\text{Ti}_2\text{O}_7$. This suggests that the unit cells should be related having basically the same a and b cell parameters and different c -axes, which can be explained in terms of adding successive $\{110\}$ perovskite layers to $\text{La}_2\text{Ti}_2\text{O}_7$. In fact, the dimensions of the c -axis have d -spacings of 15.6 \AA are found in the $n=5$ member. Those values agree with adding one $\{110\}_p$ layer to the c -axis of $\text{La}_2\text{Ti}_2\text{O}_7$ (figure 3.22).

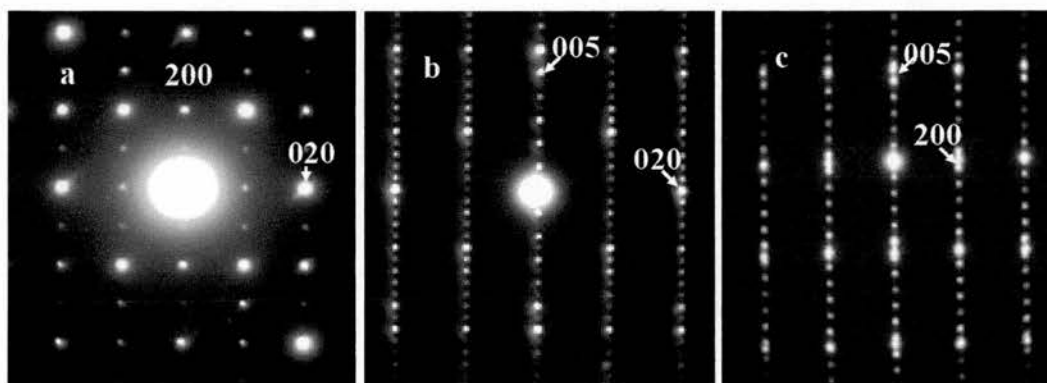


Figure 3.22. Representative SAED patterns showing the main zone axes for the $n=5$ member: [001] (a), [100] (b) and [010] (c), considering $c=15.65 \text{ \AA}$.

The situation in the case of the odd members of the family is special as will be discussed next. A close look to the SAED patterns obtained for the $n=5$ member reveals the presence of two sets of reflections weak and strong, the former (31.3 \AA) doubling the latter (15.6 \AA). One might think that microtwinning is taking place as occurred for $\text{La}_2\text{Ti}_2\text{O}_7$. However SAED patterns from several other zone axes revealed an identical situation (figure 3.23). Thus, the true dimension of the c -axis is

31.3Å. In other words, the blocks are not crystallographically the same, but are distributed into two types (X and Y) mainly due to the different tilting orientations of octahedra (canting) and have an arrangement of XYXY along the c axis. Hence, the structure of the $n=5$ member is derived from 2 sub-units containing 5 layers each. This rule applies when the number of layers per block is odd.

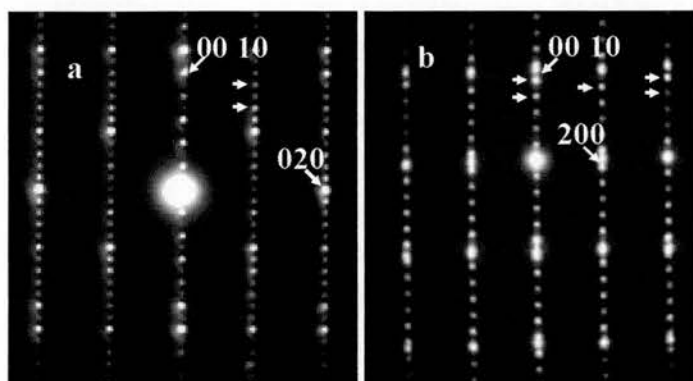


Figure 3.23. SAED patterns corresponding to views down the $[100]_m$ (a) and $[200]_m$ (b) zone axes respectively for the $n=5$ member. Small arrows indicate the doubling of the c -axis.

The corresponding HRTEM images reveal that indeed, the $n=5$ member is derived from regular perovskite blocks with 5 layers per block (3+2), joined by crystallographic shears along the c direction (figure 3.24).

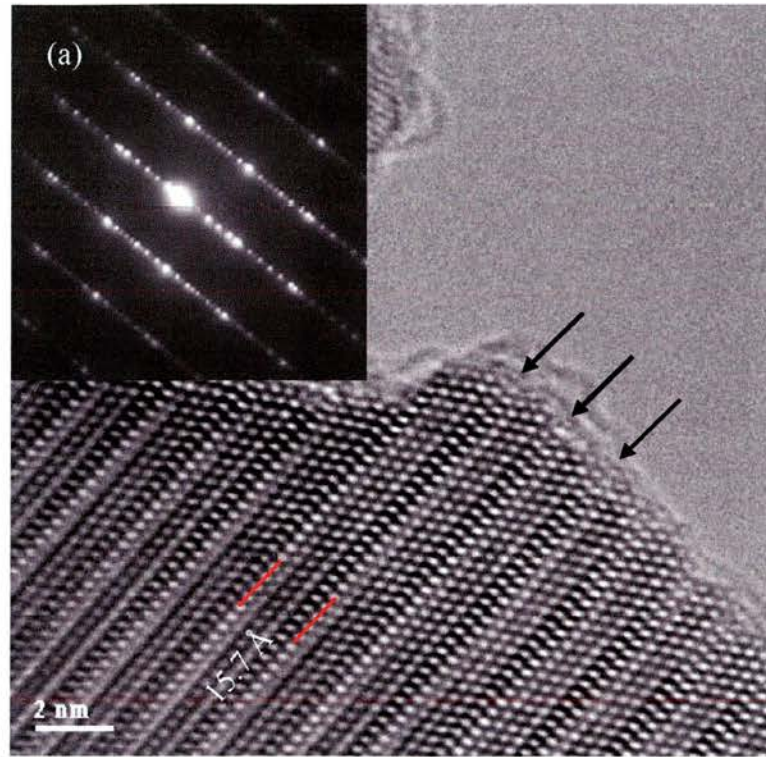


Figure 3.24.a. HRTEM viewing down the [1-20] zone axis for the n=5 member. The arrows indicate the crystallographic shears. The inset shows the corresponding SAED pattern.

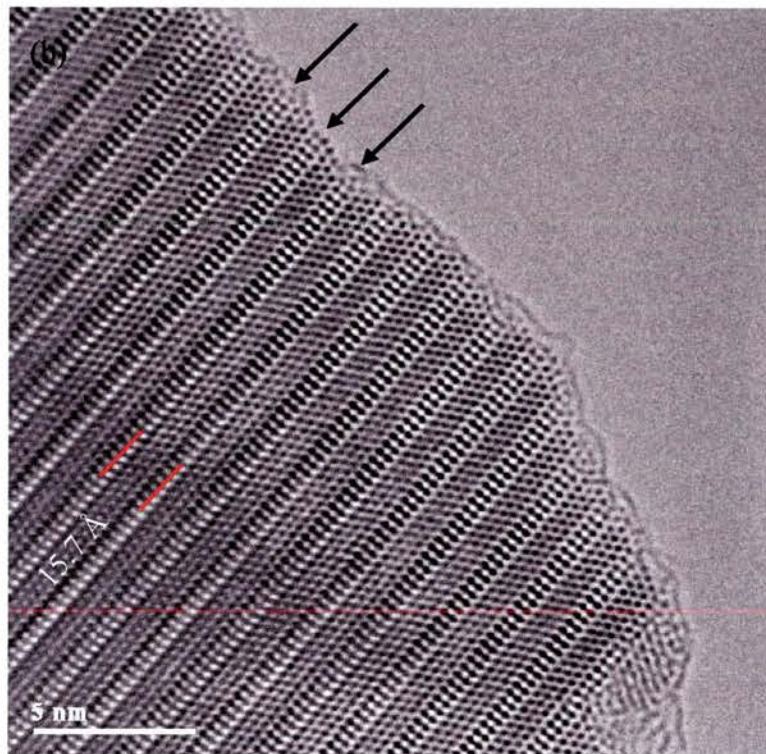


Figure 3.24. b. HRTEM viewing down the [1-20] projection for n=5. The arrows indicate the crystallographic shears.

HRTEM images taken down the $[1-20]_m$ direction are preferred because they clearly show the relation between the primitive perovskite and the layered phases. The $[1-20]_m$ zone axis corresponds to the $[111]_p$ zone axis on a simple cubic perovskite, which explains the honeycomb-like pattern in the bulk of the perovskite blocks. At the crystallographic shears the zigzag pattern is broken giving rise to a square pattern, which is symptomatic of the different nature of the oxygen-rich planes.

The structure projection of $La_2Ti_2O_7$ down the $[1-20]_m$ zone axis, shows a good agreement with the images, since the perovskite blocks show the hexagonal pattern characteristic of the $[111]_p$ zone axis in cubic unit cells and also the square-like pattern at the crystallographic shears, i.e. the oxygen rich planes (figure 3.25). In the model is also possible to detect the shifting of $\frac{1}{2} [100]_p$ between consecutive blocks. This indicates the adequacy of the model.

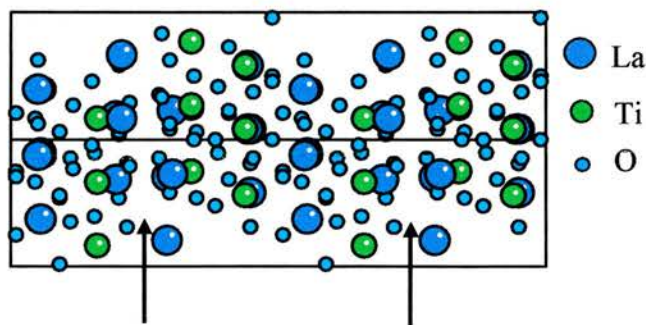


Figure 3.25. Structure projection of $La_2Ti_2O_7$ showing the $[1-20]$ zone axis, where the hexagonal pattern in the bulk of perovskite blocks. The arrows indicate the crystallographic shears, where the pattern changes from hexagonal to square.

Other zone axes also offered valuable information, although the relation with the cubic perovskite is not so simple (figure 3.26).

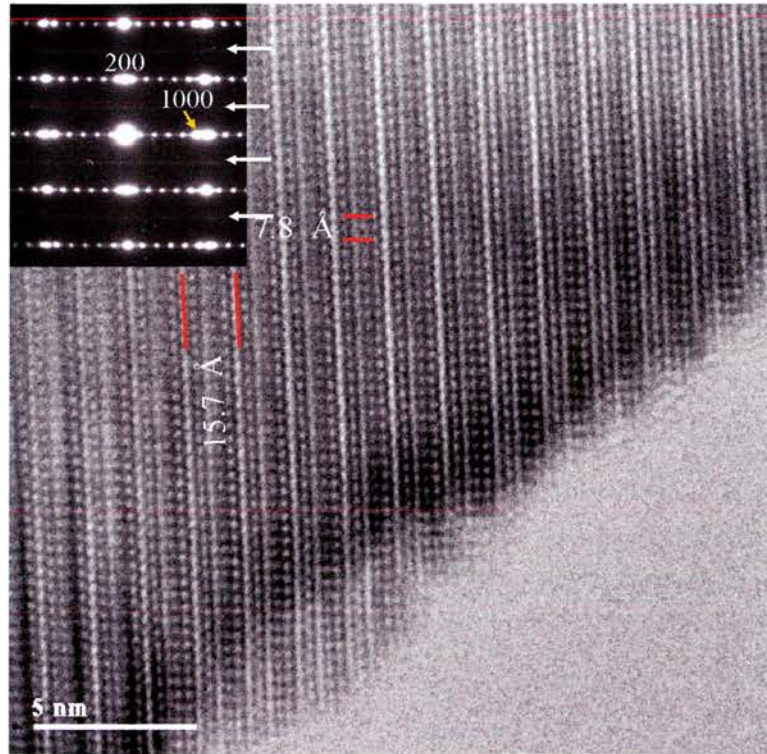


Figure 3.26. HRTEM showing the [010] projection for the $n=5$ member. The presence of 5 layers per block is very clear. The inset shows the corresponding SAED pattern, where diffuse scattering corresponding to the $(h0l)$ when $h=2n+1$ is present as marked with arrows.

On the HRTEM images it is also possible to detect the modulation between consecutive perovskite blocks, which results in the doubling of the expected c parameter (figure 3.27) for the $n=5$ member.

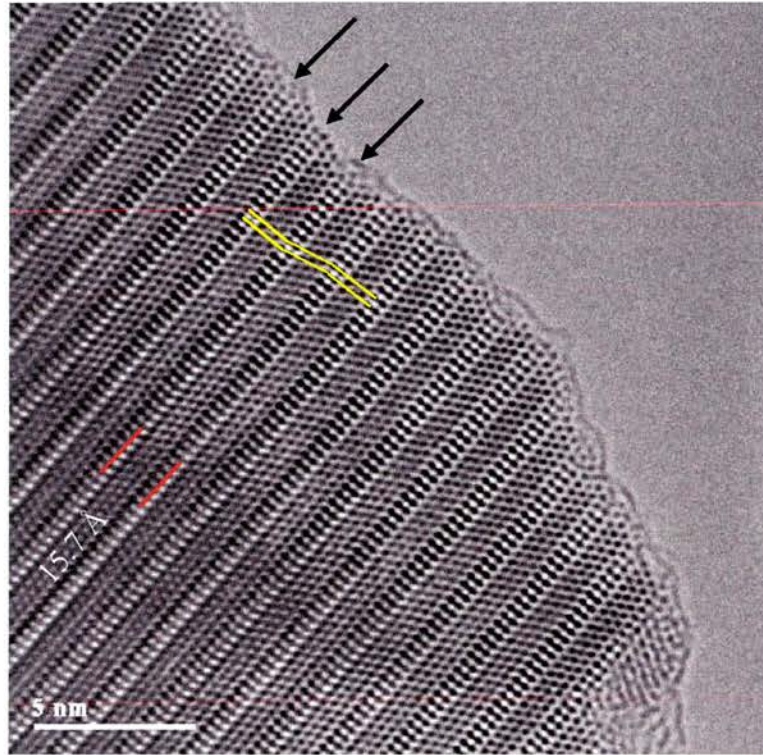


Figure 3.27 HRTEM corresponding to the [1-20] projection in the n=5 member. The inset shows canting between consecutive blocks, which leads to the doubling of the c-axis.

3.2.5.2.2. XRD.

The unit cell dimensions can be extracted from the TEM results, which give reliable starting parameters for XRD refinement, except for the angle β . In this respect, some discussion may arise from the choice of β . There are obviously two possibilities: a) to keep it constant and identical to that of $\text{La}_2\text{Ti}_2\text{O}_7$, i.e. 98.67° or b) to modify it. Keeping β constant might seem reasonable considering that the only cell parameter affected is the c-axis. However, by quite simple trigonometry it is found that β would decrease with increasing the size of the blocks as shown in figure 3.28.

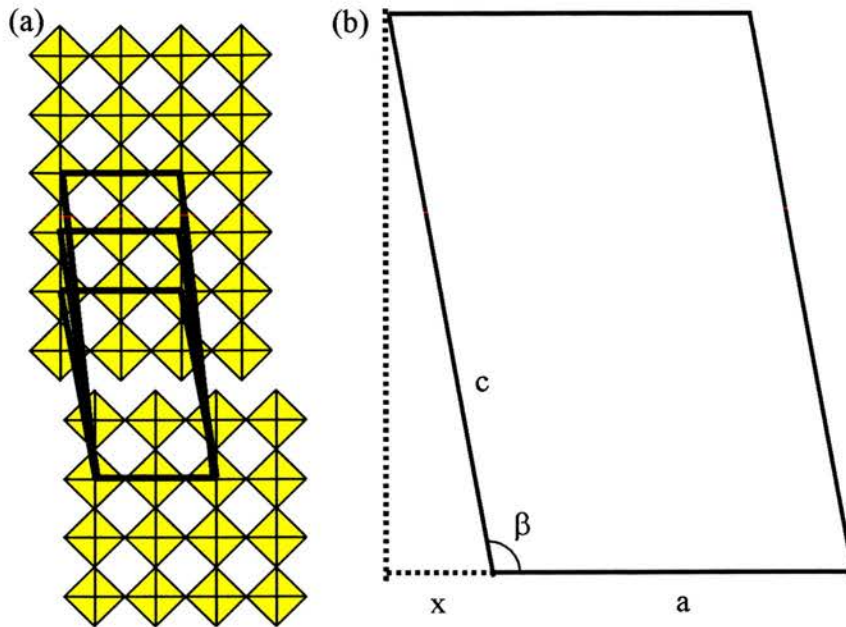


Figure 3.28. Schematic representation of the variation of the angle β with increasing the number of layers per block (a). (b) shows the relation between the cell parameters, knowing that x and a are considered to remain constant.

Changes in the value of β can certainly affect the position of the peaks and hence the indexing of the XRD pattern. β would become gradually smaller until reaching 90° for the $n=\infty$ member, i.e. cubic perovskite. The value of β can be estimated from the cell parameters. From figure 3.28.b it can be easily deduced that:

$$\beta = 180^\circ - \arccos\left(\frac{x}{c}\right)$$

x is a constant because it will not change from one layered compound to another. Thus x can be calculated for $La_2Ti_2O_7$ ($\beta=1.96117$, $c=13.01\text{\AA}$).

$$x = c \cos(180 - \beta) = 1.9612 \text{\AA}$$

This leads to an expression that is a function of c uniquely:

$$\beta = 180 - \arccos\left(\frac{1.9612}{c}\right)$$

Thus β would be 97.1° in the present case.

It should be noted however that in the case of the $n=5$ member, the real unit cell is derived from two perovskite blocks instead of one, due to the reversed tilting of the octahedra (canting). Hence, there are two possibilities: a) the real unit cell is monoclinic or, b) the unit cell is orthorhombic as depicted in figure 3.29. In the former case, the second “sub-unit cell” keeps the shift between blocks and thus the angle remains 97.1° . On the other hand, the second unit cell could “shift back”, which would relieve the monoclinic distortion in the $n=5$ member unit cell rendering it orthorhombic.

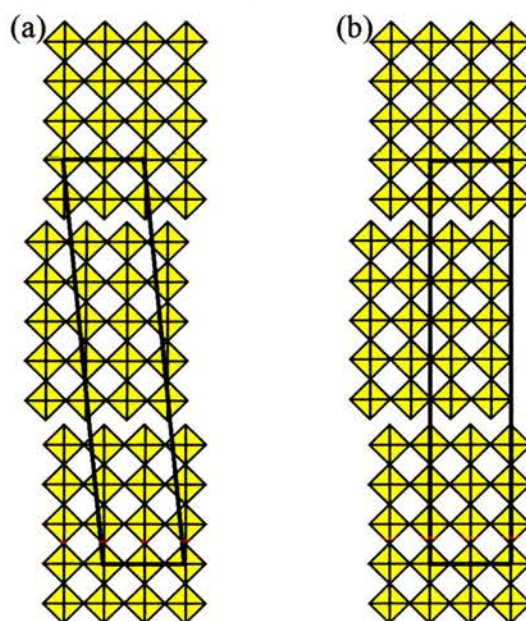


Figure 3.29. Schematic models representing two possible unit cells for the $n=5$ member of the $\text{La}_4\text{Sr}_{n-4}\text{Ti}_n\text{O}_{3n+2}$ series: monoclinic (a) and orthorhombic (b).

XRD patterns can be indexed using the two models, although the best results correspond to the orthorhombic unit cell as listed in table 3-5. Figure 3.30 shows the XRD pattern indexed for $\text{La}_4\text{SrTi}_5\text{O}_{17}$. Williams *et al.* found a similar situation for $\text{La}_5\text{Ti}_5\text{O}_{17}$, which they solved by choosing the monoclinic unit cell, maybe to keep the relation within consecutive members of the system [22]. Also, they halved the a -axis arguing that they could not find evidence that it was kept constant. In the present case, the a -axis is similar to that of the $n=4$ member, because the (100) reflections were observed by SAED and the orthorhombic unit cell is preferred because of its higher symmetry and offers the best results. Bowden *et al.* [17] also characterised this phase mostly by means of TEM, although they chose a monoclinic unit cell. The major difference found was their considerably longer c -axis (31.5 Å), but the lack of detailed XRD work does not allow further argument.

$2\theta_{\text{obs}}$	hkl	$2\theta_{\text{cal}}$	Int	d_{obs}	d_{cal}
5.644	002	5.643	4	15.65	15.65
11.31	004	11.30	3	7.819	7.825
16.26	011	16.24	4	5.449	5.455
16.97	012	16.96	5	5.219	5.222
18.12	013	18.12	2	4.893	4.885
21.43	113	21.41	75	4.413	4.416
22.90	107	22.90	9	3.880	3.880
23.42	016	23.40	5	3.795	3.797
25.60	017	25.58	4	3.476	3.479
27.93	210	27.93	10	3.192	3.196
28.05	117	28.05	12	3.178	3.178
28.49	0010	28.49	75	3.130	3.130
29.21	213	29.24	6	3.055	3.052
30.20	214	30.22	100	2.957	2.955
32.32	020	32.29	42	2.767	2.770
32.85	0110	32.84	79	2.724	2.725
34.47	121	34.44	15	2.600	2.602
35.43	0111	35.436	7	2.531	2.531
39.11	1013	39.12	7	2.302	2.301
39.98	221	39.98	25	2.254	2.253

Table 3-5 XRD data for the $n=5$ member, considering an orthorhombic unit cell with parameters $a=7.818(5)\text{Å}$, $b=5.534(3)\text{Å}$ and $c=31.29(2)\text{Å}$.

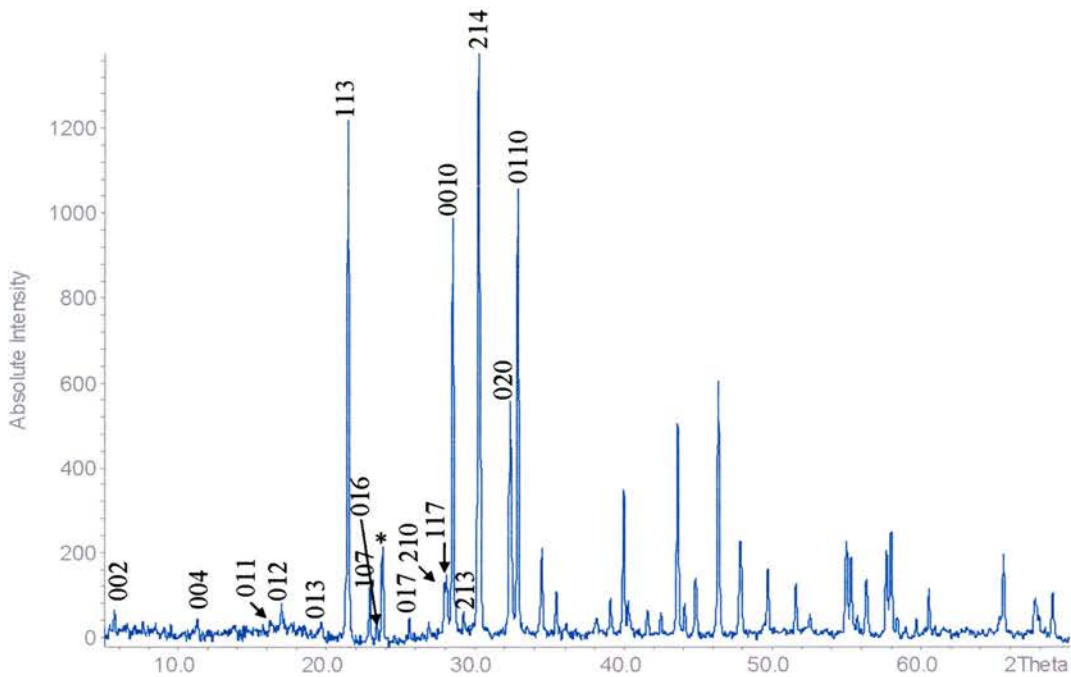


Figure 3.30. XRD pattern corresponding to the $n=5$ member of the $\text{La}_4\text{Sr}_{n-4}\text{Ti}_n\text{O}_{3n+2}$ series.*

* denotes vaseline peak.

3.2.5.3. Structural elucidation of the $n=6$ member.

3.2.5.3.1. TEM.

SAED performed on the $n=6$ member indicates the presence of d -spacings of 18.4 \AA as depicted in figure 3.31, which corresponds to the c -axis and matches with the addition of two $\{110\}$ perovskite layers per block in $\text{La}_2\text{Ti}_2\text{O}_7$ ($13.01 + 5.5 \text{ \AA}$). Obviously the c -axis is not doubled because there is no reverse tilting between consecutive blocks.

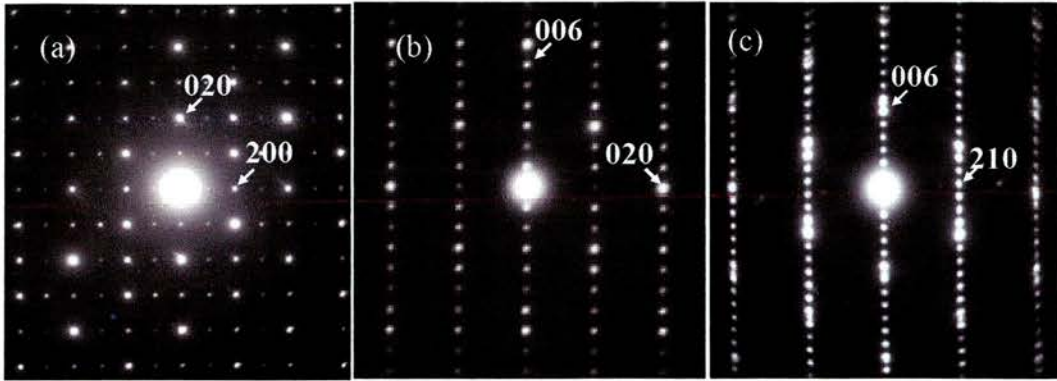


Figure 3.31. SAED patterns corresponding to views down the $[001]_m$ (a), $[100]_m$ (b) and $[1-20]_m$ (c) projections respectively for the $n=6$ member.

The corresponding HRTEM images confirm that the structure is derived from perovskite blocks containing 6 layers joined by oxygen rich planes, i.e. CS planes (figure 3.32).

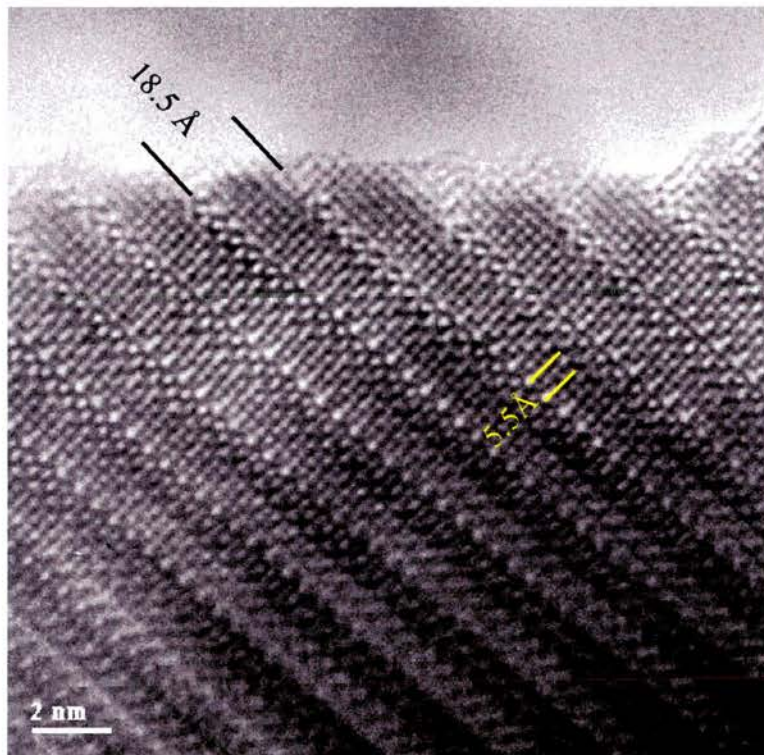


Figure 3.32. HRTEM image viewing down the $[100]_m$ projection corresponding to the $n=6$ member.

As for the $n=5$ member, HRTEM images viewing down the $[120]_m$ projection show that the perovskite blocks present the hexagonal pattern typical of the $[111]_p$ projection on a perovskite whereas at the shears it becomes square-like (figure 3.33). Obviously, there is no doubling of the c -axis because there is an even number of layers per block, and therefore the orientation between the first layers of octahedra in every block is the same.

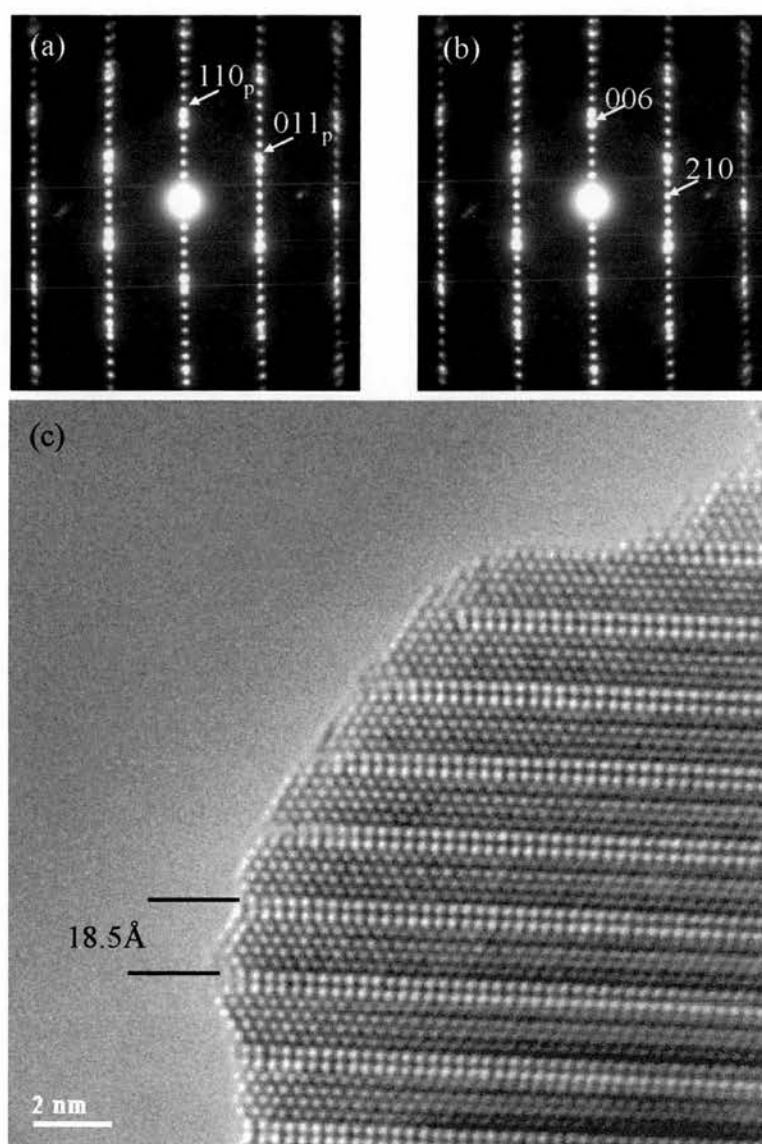


Figure 3.33. SAED patterns indexed as the $[111]_p$ on a cubic perovskite(a) and $[1-20]$ on a monoclinic unit cell (b), zone axes respectively and the corresponding HRTEM image (c).

3.2.5.3.2. XRD.

In the case of the $n=6$ member, the estimation of β using the model above should not be open to any controversy because the even number of layers per block implies the annihilation of canting between consecutive slabs and therefore the possibility of doubling of the c -axis must be rejected. Considering that the projection of the c -axis over the a -axis, i.e. x (figure 3.28), should be constant throughout the series

$$x = 1.9612$$

then

$$\beta = 180 - \arccos\left(\frac{1.9612}{c}\right) = 96.1^\circ$$

On his review, Lichtenberg *et al.* reported an estimated orthorhombic unit cell with $c=18.4\text{\AA}$, without providing any XRD or any other technique data [13]. The TEM results presented above indicate that the c -axis is close to 18.5\AA and also the best results to fit the XRD data were obtained considering $\beta=96.1^\circ$ rather than the orthorhombic unit cell. This could be due to the different sintering temperatures used in the present work, which is reasonable considering that monoclinic-orthorhombic phase transitions are quite frequent in layered perovskites, as is the case for $\text{La}_2\text{Ti}_2\text{O}_7$. The XRD indexing results are listed in table 3-6 (figure 3.34).

$2\theta_{\text{obs}}$	hkl	$2\theta_{\text{cal}}$	Int	d_{obs}	d_{cal}
14.41	003	14.43	8	6.140	6.138
16.70	011	16.70	8	5.305	5.305
21.57	013	21.59	43	4.117	4.113
22.84	-201	22.88	15	3.890	3.883
25.11	014	25.13	6	3.544	3.541
28.04	-211	28.02	21	3.182	3.180
28.44	-204	28.43	9	3.136	3.137
28.88	-212	28.88	48	3.090	3.090
29.06	006	29.07	60	3.071	3.069
30.47	-213	30.49	94	2.932	2.929
31.59	-205	31.63	14	2.83	2.826
32.31	020	32.29	84	2.769	2.770
32.75	-214	32.78	100	2.732	2.730
33.30	016	33.35	14	2.689	2.685

Table 3-6. Refined XRD data for the n=6 member, considering a monoclinic unit cell with parameters $a=7.834(5)$ Å, $b=5.544(3)$ Å, $c=18.57(1)$ Å and $\beta=96.0(1)^\circ$.

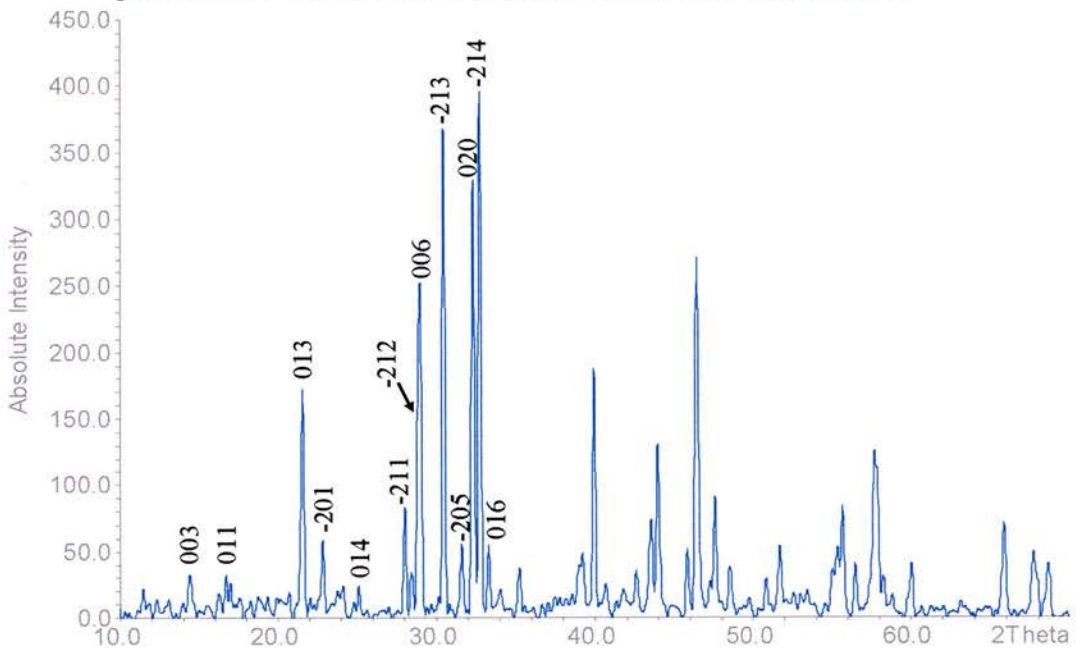


Figure 3.34. XRD pattern for $\text{La}_4\text{Sr}_2\text{Ti}_6\text{O}_{20}$ indexed onto a monoclinic unit cell.

3.2.5.4. Irregular intergrowth.

A layered system such as this offers considerable chances for structural disorder. Phenomena such as faults in the stacking sequence can be expected. In fact, HRTEM images viewing down the $[1-20]_0$ projection in the n=5 and 6 members show

clearly the presence of stacking faults, i.e. larger perovskite blocks intergrowing irregularly with the 5 or 6 layers blocks when sintering “only” for 48 hours at 1500°C (figure 3.35). The cause of such intergrowth must be found in the increased difficulty of ordering to obtain homogeneous samples with increasing the perovskite blocks size. In other words, diverse-sized perovskite blocks cohabit in these mixed oxides due to the slow processes of ordering as was suggested before in the SrTiO_3 - $\text{Sr}_2\text{Nb}_2\text{O}_7$ system [21]. It has been observed that annealing at high temperature for longer periods of time result in the homogenisation of the sample.

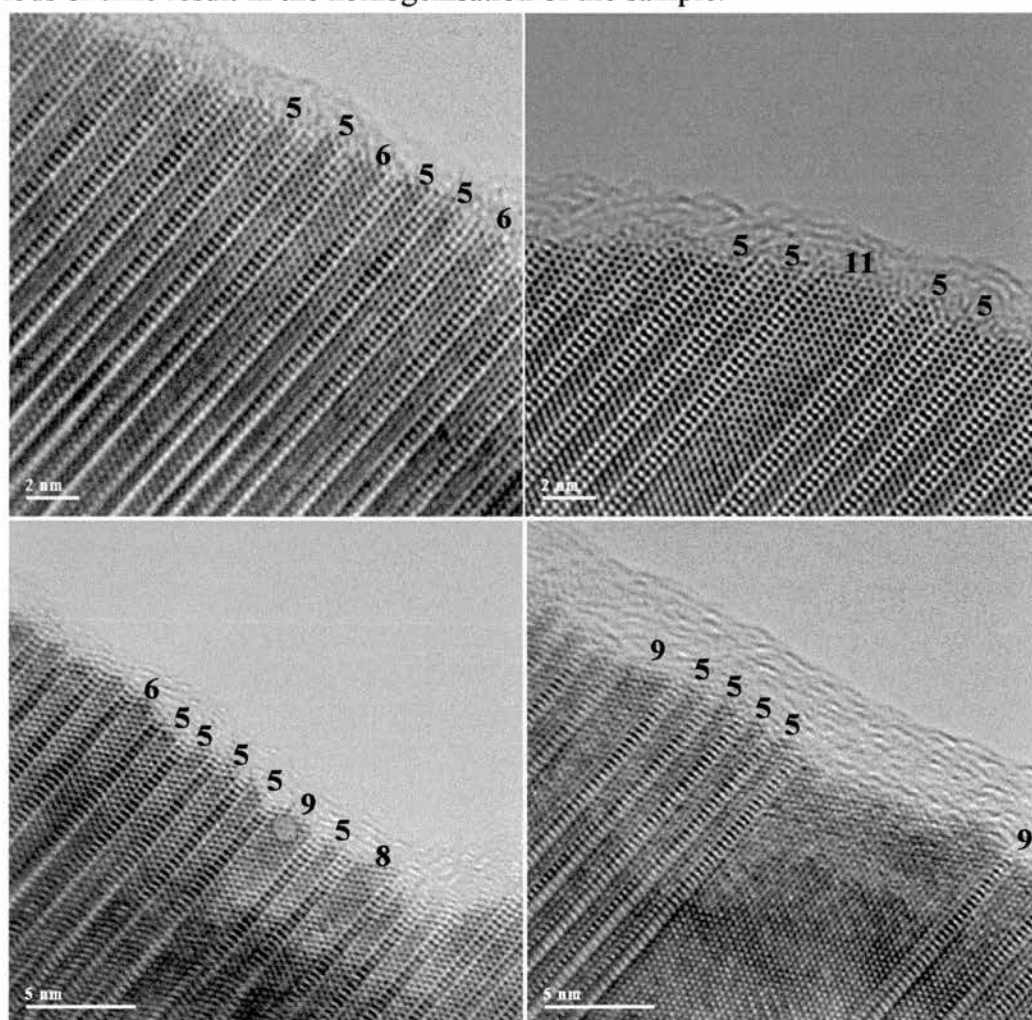


Figure 3.35. Selected HRTEM images down the $[1-20]_m$ projection for $\text{La}_4\text{SrTi}_5\text{O}_{17}$ insufficiently annealed, showing irregular intergrowth of diverse-sized perovskite slabs. The stacking faults are a consequence of the increased difficulty in obtaining homogeneous samples with increasing n .

In some regions it is also possible to see the termination of a crystallographic shear within a perovskite matrix (figure 3.36). These regions are of special interest because they might indicate that excess oxygen could be reversibly removed from the structure, which would imply certain mobility of oxygen ion through the structure. They could be induced by the very high energy required to form the crystallographic shears in the surface of the crystal.

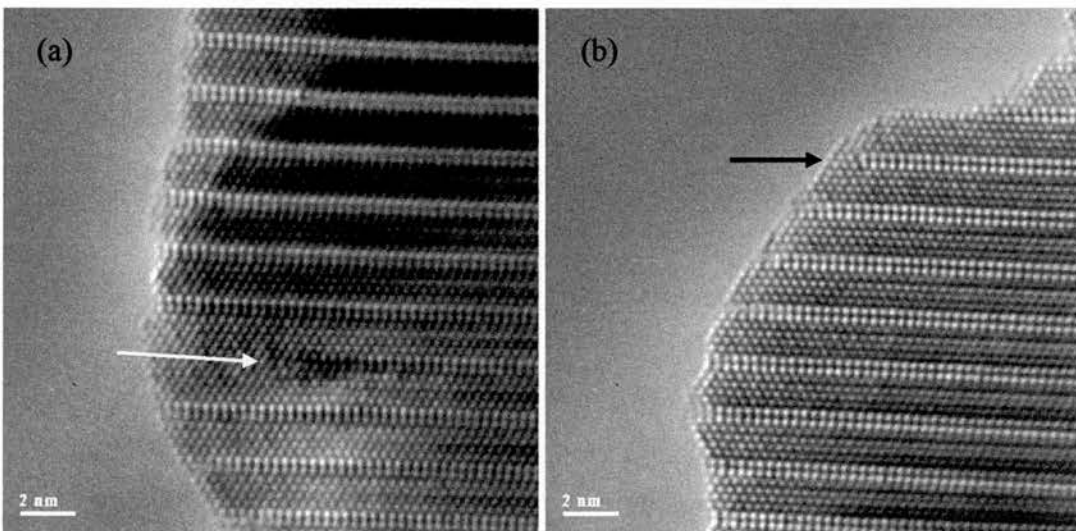


Figure 3.36. HRTEM images corresponding to a view down the $[1-20]_m$ zone axis for the $n=6$ member fired for 6 days at 1500°C , showing the termination of crystallographic shears within the bulk of a perovskite matrix (a) and near the surface of the crystal (b).

In other occasions, layered domains cohabit with perovskite domains, which occasionally were present together with crystallographic shear terminations (figure 3.37). In both cases, the “border” regions would present a certain degree of distortion. Moreover, occasionally there also appear very disordered regions where the crystallographic shears are tilted and with some discontinuity as shown in figure 3.38. Thus, the $\text{La}_4\text{Sr}_{n-4}\text{Ti}_n\text{O}_{3n+2}$ series offers quite a wide range of disorder as a consequence of the difficulty of ordering in regular slabs, which may certainly affect the properties.

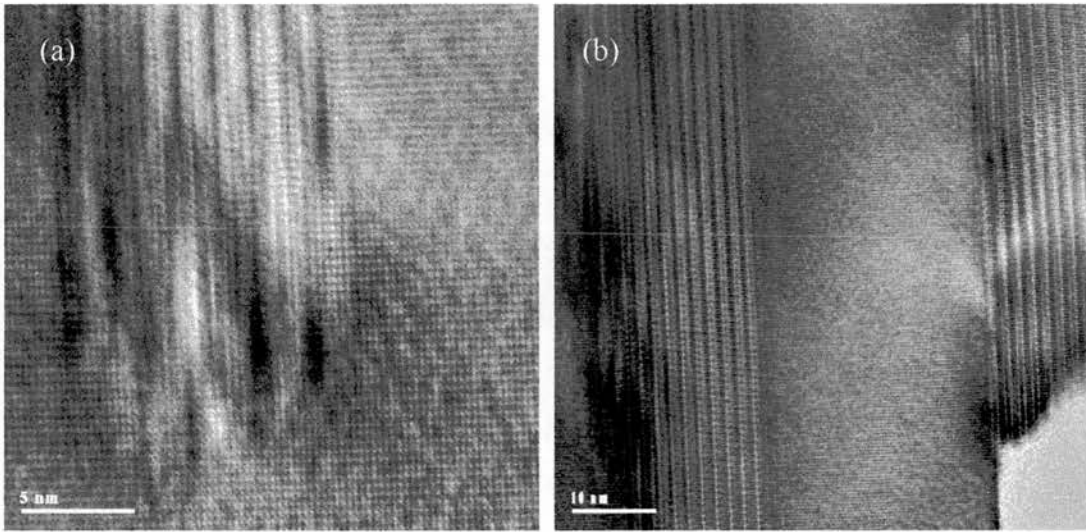


Figure 3.37. HRTEM images showing the presence of layered domains cohabiting with perovskite domains in the $n=6$ member, annealed for 48 hours at high temperature. In some cases the layered domains terminated within the bulk of the crystal (a), whilst in some other the layered domains reached the surface (b).

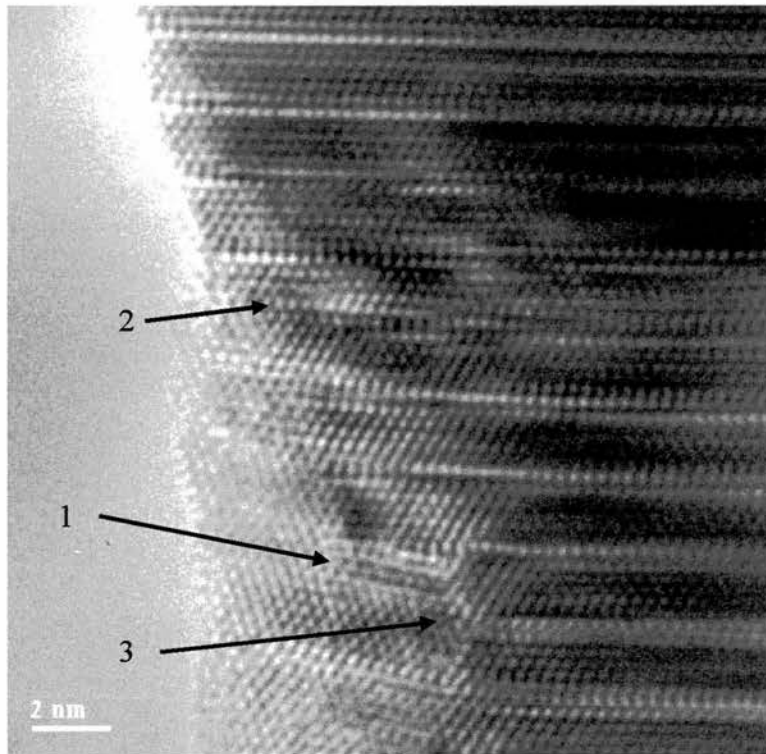


Figure 3.38. HRTEM picture of the $n=6$ member ($[1-20]_m$) showing a highly distorted domain. Stacking faults (1), tilting (2) or termination (3) of the crystallographic shears are evident.

3.2.6. Intermediate compositions.

3.2.6.1. TEM.

TEM studies performed on the $n=10$ attempted composition agree with the results presented for the lower members of the series and, as can be expected, there exist a mixture of perovskite domains with layered domains. Although some SAED patterns obtained can be indexed as a simple cubic perovskite, $a = 3.90 \text{ \AA}$ (figures 3.39.a and b), there are some others revealing the presence of layered domains (figures 3.39.c and d). The layered domains would have identical a and b cell parameters compared to the rest of the series (figure 3.39.d).

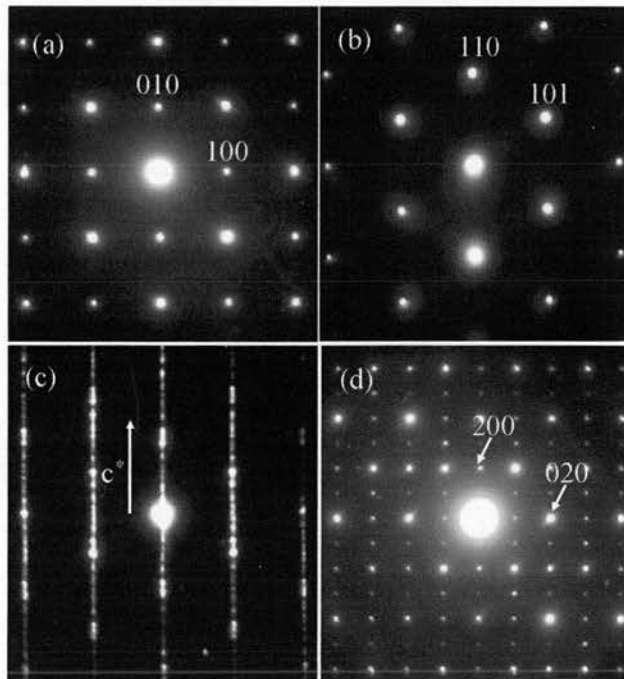


Figure 3.39. SAED patterns corresponding to the $n=10$ composition, showing a view down $[001]_p$ (a) and $[111]_p$ (b) on perovskite domains. (c) and (d) correspond to the $[1-20]_m$ and $[100]_m$ on layered domains respectively.

Incommensurate reflections were present along the c^* axis (figure 3.39.c), which could certainly indicate the presence of perovskite blocks with different number of layers irregularly distributed in the same crystal. In fact, figures 3.39b and 3.39c correspond to a view down the same projection, i.e. the $[111]_p$ zone axis on a cubic perovskite. The former is representative of cubic domains, whereas the latter shows the superstructure reflections characteristic of layered phases, equivalent to the $[1-20]_m$ zone axis of the lower members.

This is similar to the observations for lower members when annealed inadequately, i.e. too short reaction time, as mentioned before. Thus, the same conclusion could be stated in the present case in order to achieve homogeneous samples it is required to anneal at high temperatures for extremely long periods. Indeed, the corresponding HRTEM images agree with electron diffraction and reveal diverse-size perovskite blocks co-existing in the structure, with the difference that for the $n=10$ composition, the perovskite blocks are larger in average as depicted in figure 3.40. The poor quality of the image is due to the vibration of the crystallites under the electron beam. It was observed that for members of the $\text{La}_4\text{Sr}_{n-4}\text{Ti}_n\text{O}_{3n+2}$ showing layered structure cohabiting with perovskite domains, the crystallites were not very stable and they strongly vibrate under the beam, impeding the adjustment of the best conditions of operation and therefore affecting to the quality of the recorded images. In certain cases, reduced samples were used for microscopy studies because that may diminish the vibration, since such instability seems to be related with the oxygen content of the sample. Nevertheless, the presence of layered domains cohabiting with perovskite domains is distinguishable at rather low magnification (figure 3.40.b).

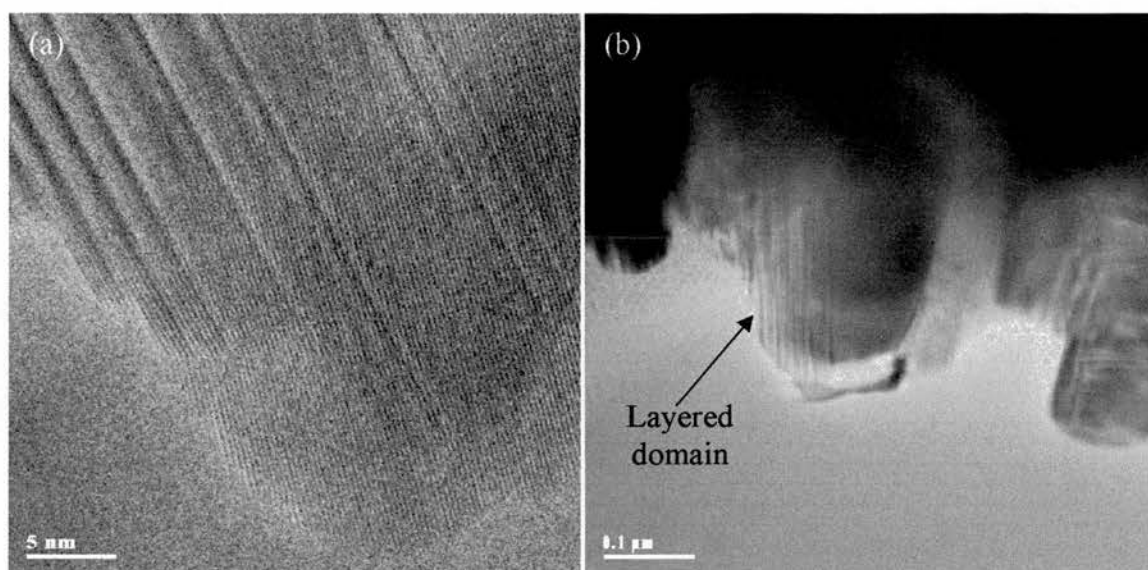


Figure 3.40. HRTEM images showing the presence of layered domains for the $n=10$ composition.

3.2.6.2. XRD.

From the TEM data presented above, it can be seen that the formation of layered phases is limited by the very slow kinetics in the formation of homogeneous samples of regularly distributed perovskite blocks. The HRTEM images obtained for the $n=10$ composition demonstrate that there exists irregular intergrowth between cubic perovskite and layered domains as shown in figure 3.40. Indeed, a careful study of the XRD patterns of the $n=8$ and $n=10$ compositions suggests that a mixture of phases occurs, i.e. cubic perovskite and several monoclinic layered phases. It is clear that the group of peaks that appear at 2θ values from 25 to 30 is related with the presence of layered domains.

There is some similarity between the two structural motifs and hence it could be relatively easy for them to intergrow in a manner, which if sufficiently large domains are present, would result in XRD presenting a mixture of several layered

phases together with perovskite domains. As discussed before, in the border regions between domains some distortion might be expected. Table 3-7 lists the XRD data for the $n=8$ and $n=10$ compositions of the $\text{La}_4\text{Sr}_{n-4}\text{Ti}_n\text{O}_{3n+2}$ series and their possible indexing. Several unit cells were used for this, i.e. cubic perovskite, the $n=4$ member (taken from literature data [16]), and the estimated unit cells for the $n=5$ and $n=6$ members.

n	d_{obs}	Int	n=5		n=6		Cubic	
			d_{calc}	hkl	d_{calc}	hkl	d_{calc}	hkl
6	6.1529	8	6.2575	103	6.1568	003		
	4.1223	43	4.1445	015	4.1198	013		
	3.8962	15	3.8817	107	3.8984	200		
	3.1868	21	3.1777	109	3.1872	210		
	3.0782	60	3.0528	213	3.0784	006		
	2.9349	98	2.9434	207	2.9351	-213		
	2.8332	15	2.8441	215	2.8329	-205		
	2.7717	83	2.7657	208	2.7719	020		
	2.7348	100	2.7236	01 10	2.7351	-214		
	2.6914	14	2.6739	10 11	2.6913	016		
8	4.1487	17	4.1445	015	4.1198	013		
	3.9050	11	3.9100	200	3.8984	200	3.9034	100
	3.1859	9	3.1777	109	3.1872	210		
	3.1326	13	3.1282	212	3.1350	114		
	3.1130*	10						
	3.0929*	11			3.0977	211		
	3.0780	10	3.0529	213	3.0784	006		
	2.9573	20	2.9559	214	2.9475	-115		
	2.9373	14	2.9434	207	2.9351	-213		
	2.7624	100	2.7657	208	2.7719	020	2.7605	110
	2.7303	25	2.7236	01 10	2.7348	-214		
10	4.1416	38	4.1445	015	4.1198	013		
	3.9080	15	3.9100	200	3.8984	200	3.9034	100
	3.1821	7	3.1777	109	3.1872	210		
	3.1339	8	3.1282	212	3.1350	114		
	2.9605	9	2.9559	214	2.9475	-115		
	2.9347	14	2.9434	207	2.9351	-213		
	2.8268*	6	2.8440	215	2.8333	-205		
	2.7619	100	2.7657	208	2.7719	020	2.7617	110
	2.7302	11	2.7236	01 10	2.7348	-214		

Table 3.7a. XRD data for the $n=8$ and $n=10$ compositions of the $\text{La}_4\text{Sr}_{n-4}\text{Ti}_n\text{O}_{3n+2}$ series. The best fitting is indicated in bold case. Note that the unit cell of the $n=5$ member could also be used in the indexing. This table tries to show the presence of mixture of phases for these compositions.

n	A	b (Å)	c (Å)	β
4	7.81	5.54	13.01	98.66
5	7.81	5.54	31.3*	90
6	7.81	5.54	18.52	96.1

Table 3-7b. Estimated unit cells for the n=4, n=5 and n=6 members.

3.2.7. Conclusions.

New layered perovskites belonging to the $\text{La}_4\text{Sr}_{n-4}\text{Ti}_n\text{O}_{3n+2}$ series have been synthesised and structurally characterised, showing the possibility of modulating the size of the perovskite blocks. To our best knowledge, it is the first time that the n=5 and n=6 members of the $\text{La}_4\text{Sr}_{n-4}\text{Ti}_n\text{O}_{3n+2}$ have been reported as a single phase or, at least, major phase. The structure can be described as perovskite blocks containing n TiO_6 layers and joined by crystallographic shearing. Consecutive blocks are shifted by $\frac{1}{2}[100]_p$ along the a-axis. The c-axis is doubled due to reverse tilting between consecutive blocks when the number of layers is odd. This phenomenon renders orthorhombic unit cells. Figure 3.41 shows a relevant model.

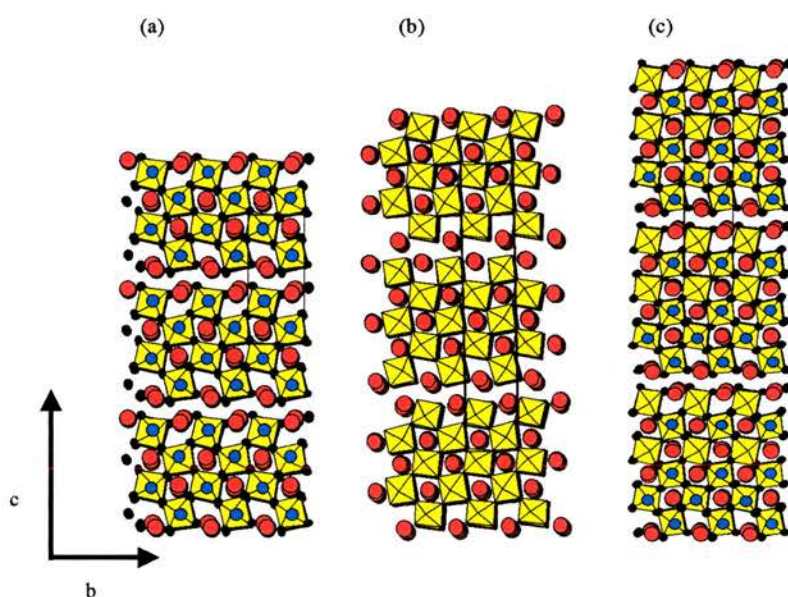


Figure 3.42. Structural models for the $\text{La}_4\text{Sr}_{n-4}\text{Ti}_n\text{O}_{3n+2}$ series. (a) $\text{La}_2\text{Ti}_2\text{O}_7$ (n=4), (b) $\text{La}_4\text{SrTi}_5\text{O}_{17}$ (n=5) and (c) $\text{La}_4\text{Sr}_2\text{Ti}_6\text{O}_{20}$ (n=6).

It should be noted however that an increased difficulty in obtaining homogeneous samples must be expected for larger slabs. Indeed, our efforts in the synthesis and characterisation of the $n=8$ and $n=10$ members resulted in a mixture of diverse-sized perovskite blocks irregularly distributed within the crystal when inadequately annealed, 48-72 hours at 1500°C . Therefore, extremely long annealing periods of time at high temperature (1500°C) are required to synthesise homogeneous samples of higher members of this series of layered perovskites. Interesting properties such as ferroelectricity with very high T_c can be expected from this series, considering that the $n=4$ member, $\text{La}_2\text{Ti}_2\text{O}_7$, is the ferroelectric material with the highest T_c reported (1770 K) [10].

Finally, to remark the complexity of the system studied, it is worth noting another interesting feature detected by HRTEM: the characteristic excess oxygen accommodated on the CS planes is somehow more accessible with increasing the size of the perovskite blocks. SAED performed on the $n=8$ member showed that superstructure reflections disappear under the electron beam interaction after exposure of 5 minutes (figure 3.41).

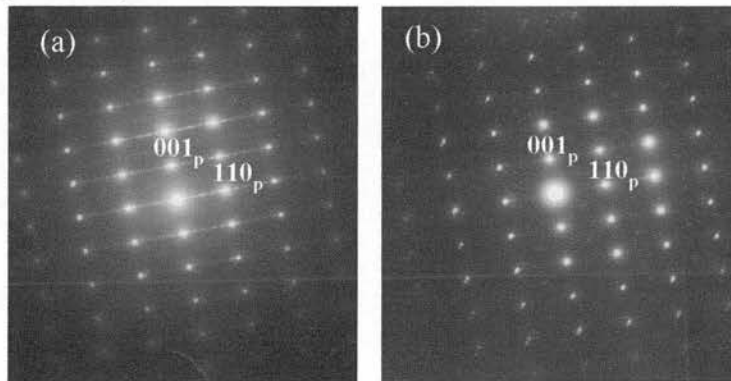


Figure 3.41. SAED patterns corresponding to the $n=8$ composition, showing the changes undergone by the sample under the beam irradiation. At first instance, superstructure reflections were observed along the $[110]_p$ (a). After 10 minutes they disappeared (b).

There exist a number of possible explanations for this phenomenon. For instance, it could be an *in situ* reduction due to the conditions inside the column, consisting in the removal of part of the excess oxygen, leaving the perovskite blocks. It could be also due to a re-arrangement of the perovskite blocks under the beam interaction, leading to a randomisation of the structure. The layered structure would collapse leading to an average perovskite-like structure. The crystallographic shears might remain but not in a regular distribution somehow similar to that observed in the $n=12$ member as it will be described next. Such structural change under the beam radiation was not commonly observed. HRTEM images of such structural re-arrangement could not be obtained because of the vibration suffered by the crystals under the beam interaction.

3.3. Cubic phases.

In the XRD data it was found that the layered features were lost for compounds with $n > 11$, which could be indexed as simple cubic perovskites. It is the aim of this section to study the transition from layered to cubic phases and also to study the mechanism of accommodating the excess oxygen in the latter.

3.3.1. $\text{La}_4\text{Sr}_8\text{Ti}_{12}\text{O}_{38}$ ($n=12$).

$\text{La}_4\text{Sr}_8\text{Ti}_{12}\text{O}_{38}$, i.e. the $n=12$ member, is a key compound for the understanding of these phases because it can bring light on how the transition between layered and cubic phases takes place.

3.3.1.1. XRD results.

The XRD patterns can be indexed as simple cubic perovskite unit cells $a=3.9094(4)$ Å, with space group Pm-3m (table 3-8) (figure 3.43). Despite the evident change of colour from pale yellow in oxidising conditions to dark blue in reducing conditions, no significant changes in the structure were observed. In the case of reduced phases, the pattern can also be indexed with a simple cubic perovskite unit cell with parameter $a=3.9065(3)$ Å. Such noticeable change in colour is due to the presence of Ti^{3+} in the reduced phases. No extra peaks involving layered phases or corresponding to secondary phases appear, indicating that the specimens are X-ray single phase.

n=12 (oxidised)				n=12 (reduced)			
d_{obs}	d_{calc}	Int	hkl	d_{obs}	d_{calc}	Int	hkl
3.9101	3.9094	8	100	3.9070	3.9065	10	100
2.7642	2.7643	100	110	2.7622	2.7623	100	110
2.2571	2.2571	24	111	2.2553	2.2554	28	111
1.9545	1.9547	34	200	1.9531	1.9532	39	200
1.7483	1.7483	5	210	1.7471	1.7470	6	210
1.5929	1.5960	29	211	1.5948	1.5948	35	211
1.3823	1.3822	15	220	1.3812	1.3812	18	220

Table 3-8. XRD data for the n=12 member synthesised in both oxidised (left) and reducing conditions (right). Both phases were indexed as simple cubic perovskites (space group Pm-3m). Cell parameters are $a=3.9094(4)$ Å and $3.9065(4)$ Å respectively.

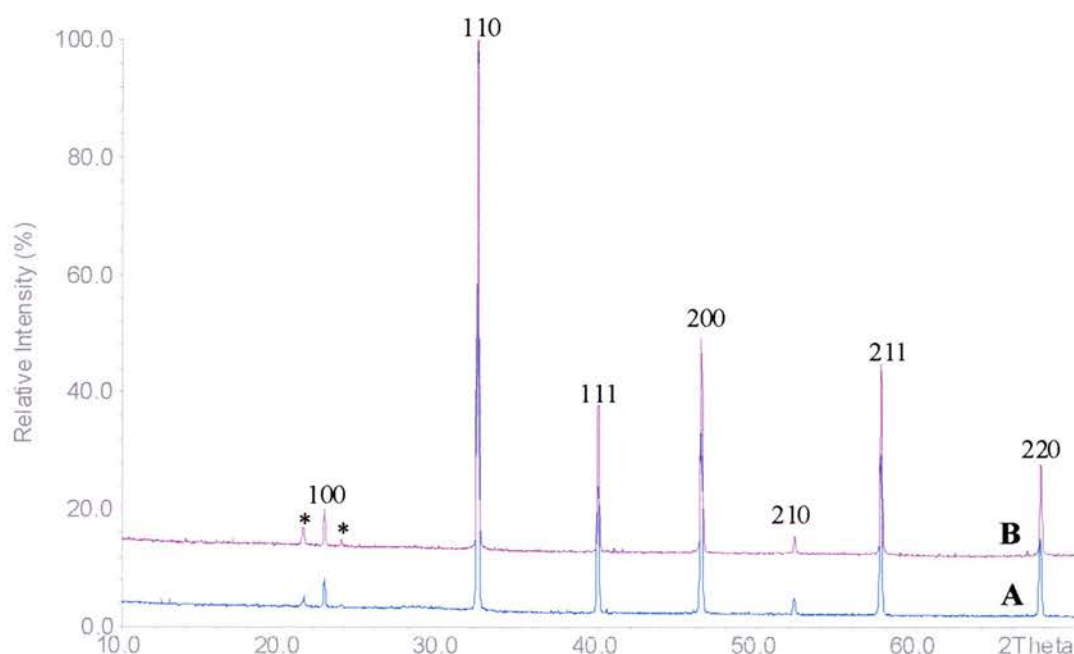


Figure 3.43. XRD patterns of the n=12 member prepared in oxidising (A) and reducing conditions (B). Both phases were indexed as cubic perovskites.

The fit is very good as can be extracted from table 3-7. However, the estimated stoichiometry indicates excess oxygen beyond the ABO_3 perovskite, which is a difficult situation to imagine considering that on a cubic close packed (ccp) arrangement there is no space for interstitial elements.

It is not surprising that the disordered phase is cubic, if the estimated tolerance factors are considered ignoring the excess oxygen in first instance. The tolerance factor (t) of a perovskite structure ABO_3 is calculated from:

$$t = \frac{R_A + R_O}{\sqrt{2}(R_B + R_O)}$$

R_A , R_B and R_O being the ionic radii of A, B and oxide ion respectively (table 3-9). In the case of having more than one cation on A or B positions of the perovskite, the corresponding ionic radius is calculated from the weight average. Thus, t is 0.978 for the oxidised phase ($La_{1/3}Sr_{2/3}Ti^{IV}O_3$) whereas is 0.976 for the reduced one ($La_{1/3}Sr_{2/3}Ti^{IV}_{0.9}Ti^{III}_{0.1}O_3$), both of them very close to the value of the archetype of the perovskite structure $SrTiO_3$ ($t=0.987$) and within the range of non-distortion for cubic perovskites. It should be noticed that the difference between oxidised and reduced phase is miniscule, which is reasonable considering that Ti^{3+} substitutes “only” 10% of the Ti^{4+} as indicated from the thermogravimetric analysis (TGA) results presented next.

Ion	Ionic radius (Å)
Sr^{2+}	1.40
La^{3+}	1.32
Ti^{4+}	0.605
Ti^{3+}	0.67
O^{2-}	1.4

Table 3-9. Ionic radii for the species present in the n=12 member [33].

3.3.1.2. Magnetic measurements [34] and TGA.

The expected stoichiometry indicates the presence of excess oxygen that cannot be accommodated within in a simple cubic perovskite. Hence, there should exist a mechanism to explain how interstitial oxygen can be placed within the perovskite framework. A classical approach to the problem of substituting Sr^{2+} by La^{3+} would be that the extra positive charge caused would be balanced by reduction of Ti^{4+} to Ti^{3+} , which would lead to a stoichiometry $\text{La}_{1/3}\text{Sr}_{2/3}\text{Ti}_{1/3}^{\text{III}}\text{Ti}_{2/3}^{\text{IV}}\text{O}_3$ matching the so-called self-compensation mechanism in reducing conditions [28-29]. However, it is very well known that very small amounts of Ti^{3+} causes the sample to be black, whereas the samples prepared in air showed white-yellow colour.

Magnetic susceptibility measurements can provide further information about the presence of Ti^{3+} in oxidised phases. Theoretically, in the oxidised phases Ti should be present essentially as Ti^{4+} , i.e. there should not be d-electrons and hence it should be very close to diamagnetism. On the other hand, the presence of Ti^{3+} in reduced phases should be detected leading to a clear paramagnetic response caused by unpaired electrons. Magnetic susceptibility measurements were performed using a Quantum Design Magnetic Property Measurement System (MPMS) equipped with a Superconducting SQUID amplifier system in the temperature range from 1K up to 300K. The experiments showed that indeed, for samples prepared in air there exists only a tiny fraction of unpaired electrons (very weak paramagnetism), less than 0.1% of Ti being Ti^{3+} . On the other hand, the reduced sample shows dark-blue colour (Ti^{3+}) and is found to be paramagnetic, corresponding to approximately 10 % of Ti being Ti^{3+} (figure 3.43).

From Curie's law, it is found that the magnetic susceptibility (χ_m) is a function of the reciprocal temperature, written as

$$\chi_m = \frac{M}{H} = \frac{c}{T + \theta} + \chi_0$$

C is the Curie constant that is one of the parameters calculated in the regression to fit the experimental. When there is no spin-orbital coupling, the constant c can be related with the number of unpaired electrons by:

$$p^2 = \frac{3k_B C}{N\mu_B^2} = n(n+2)$$

where p is the effective momentum, k_B is Boltzmann constant, N is Avogadro's constant, μ_B is Bohr magneton and n is the number of unpaired electrons. Thus, by estimating c it is possible to give the number of unpaired electrons, which are related to the presence of Ti^{3+} .

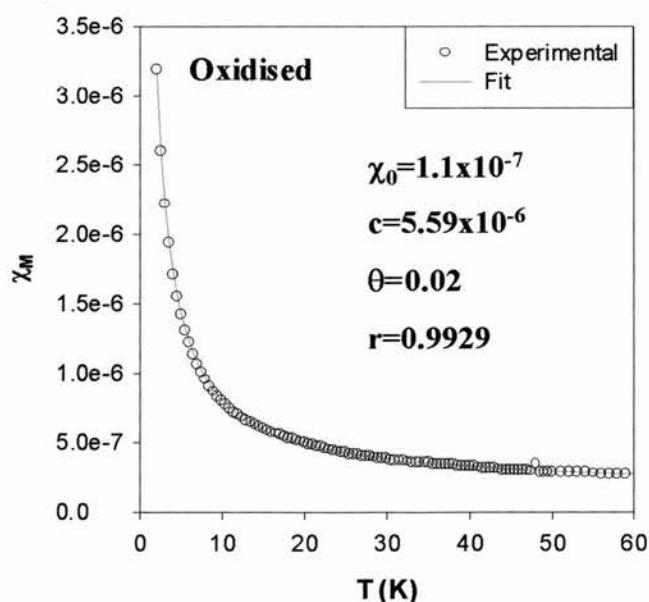


Figure 3.43a. Molar susceptibility vs. temperature plot for the n=12 member prepared in oxidising conditions. Results from the fit are also given in the inset.

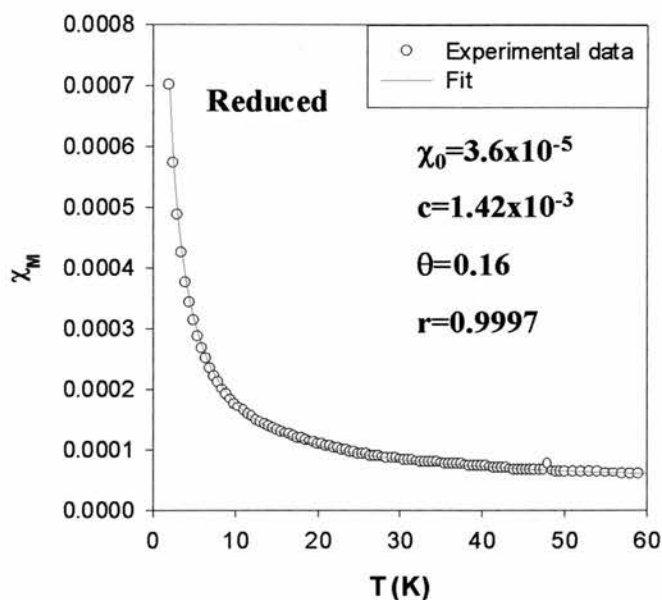


Figure 3.43b. Molar susceptibility vs. temperature plot for the $n=12$ member prepared in reducing conditions. The response is much stronger in the case of the reduced phase due to the presence of 10% of Ti as Ti^{3+} . Fit parameters are given in the inset.

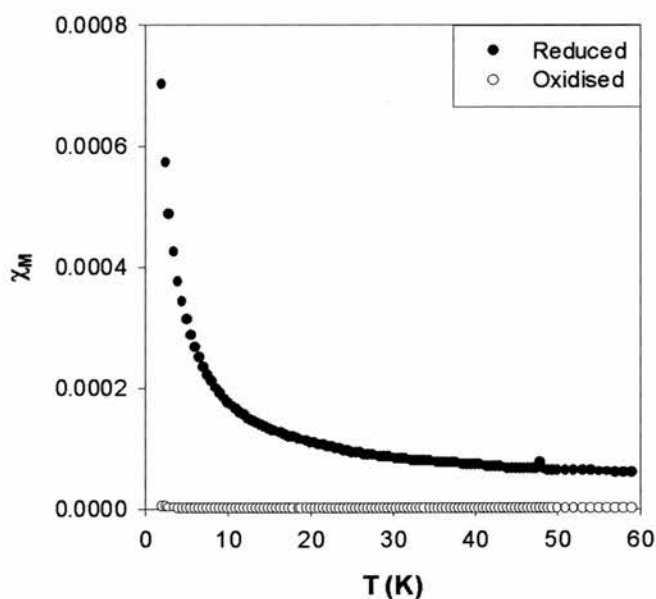


Figure 3.43c. Molar susceptibility vs. temperature plots for the $n=12$ member prepared in oxidising and reducing conditions. It is evident that the response is much stronger for the latter.

The very low values of χ_0 and the correlation coefficients close to 1 indicate that the model is correct. Hence it can be concluded that the amount of Ti^{3+} in the oxidising conditions can be considered negligible.

TGA experiments were carried out to confirm the data collected from magnetic measurements. They were performed during the oxidation at 800°C in air of a pre-reduced sample as described in the experimental chapter (section 2.6). Figure 3.4. shows that there is a change of about 0.04 oxygen atoms per formula unit, i.e. approximately 10% of Ti as Ti^{3+} . This leads to a stoichiometry of $\text{La}_{1/3}\text{Sr}_{2/3}\text{TiO}_{3.167}$ for the oxidised sample and $\text{La}_{1/3}\text{Sr}_{2/3}\text{TiO}_{3.125}$ for the reduced. These results indicate that the oxidised phase is essentially Ti^{IV} and hence, the idea of a perovskite $\text{La}_{1/3}\text{Sr}_{2/3}\text{Ti}^{\text{III}}\text{Ti}^{\text{IV}}\text{O}_3$ must be rejected. Also these results would indicate the presence of significant excess oxygen in reducing conditions.

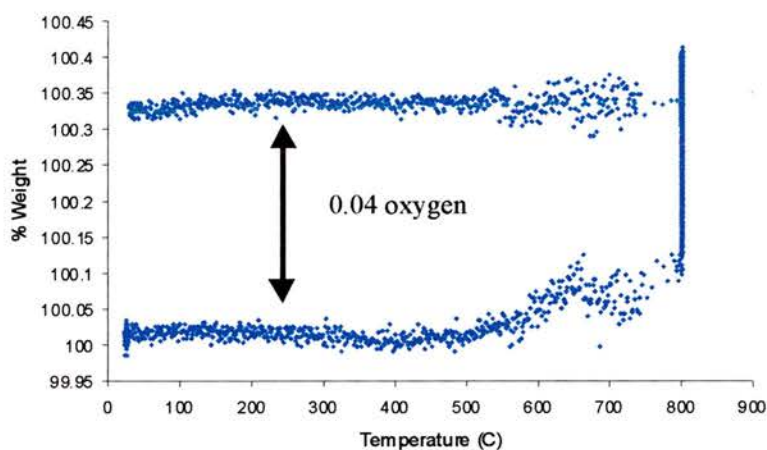


Figure 3.44. TGA experiment recorded during the oxidation of a pre-reduced sample. The change in weight from reduced to oxidised samples corresponds to 0.04 oxygen per formula unit.

3.3.1.3. Density Measurements.

Another mechanism of accommodating extra oxygen would be by the creation of cation vacancies as reported extensively in the literature [see for example 31]. Density measurements are a suitable technique to discern between different structural models because each structural model would give different density and

hence the solution of this particular enigma might be found by comparing the real density with the predicted ones.

The density measurements are performed following Archimedes principle, estimating the volume of a known amount of powder on a Quantumchrome Multipycnometer. The displaced fluid is a gas able to penetrate the finest pores to assure maximum accuracy. Helium is a suitable choice due to its small atomic dimension and behaviour as an ideal gas.

Three models are considered in the present case:

- a) Extra charge introduced by substitution of Sr^{2+} by La^{3+} is balanced by reduction of Ti^{4+} to Ti^{3+} yielding to a perovskite with formula $La_{1/3}Sr_{2/3}Ti^{III}Ti^{IV}O_3$, although previous section shows this to be wrong.
- b) Oxygen stoichiometry beyond the ABO_3 parental perovskite is explained by cation vacancies, i.e. $La_{12/38}Sr_{24/38}Ti_{36/38}O_3$. This model suggests that all the oxygen sites are fully occupied and the excess of positive charge is compensated by the creation of cation vacancies in the A- and B-sites. The creation of vacancies in both the A- and B-sites is unlikely, but the values obtained could give an idea of whether this approach could be possible.

- c) $La_4Sr_8Ti_{12}O_{38}$ explained as an intergrowth of the two end members, $SrTiO_3$ and $La_2Ti_2O_7$. Considering this mixed oxide as the weighed average between the two end members of the $La_4Sr_{n-4}Ti_nO_{3n+2}$ series.

The X-ray theoretical density is calculated from:

$$\rho = \frac{M \cdot Z}{V \cdot N}$$

where M is the molecular weight, Z the number of formula units per unit cell, N is Avogadro's constant and V the volume of the unit cell. Hence it is possible to calculate the theoretical density from the unit cell parameters ($a=3.9094\text{\AA}$). In the present case V is obviously constant for the different models and $Z=1$. Molecular weight is the sole parameter that varies as a function of the chosen model. In the case of the two perovskitic models (a) and (b), theoretical density is extracted from the formula above, whilst for the intergrowth model, the weighed average between the end members is used, i.e. 5.79 and 5.11gcm^{-3} for $La_2Ti_2O_7$ and $SrTiO_3$ respectively (table 3-10).

Model	Formula	Molecular Weight (g/mol)	Density (g/cm^3)
A	$La_{1/3}Sr_{2/3}Ti^{III}Ti^{IV}O_3$	200.59	5.58
B	$La_{6/19}Sr_{12/19}Ti_{18/19}O_3$	192.56	5.35
C	$La_2Ti_2O_7 + 4 SrTiO_3$	-	5.25
-	$La_2Ti_2O_7$	485.65	5.79
-	$SrTiO_3$	183.50	5.11

Table 3-10. Density corresponding to the different models considered.

The measured density of $La_4Sr_8Ti_{12}O_{38-\delta}$ is 5.18gcm^{-3} . Hence model c is the one that best approaches the density values. $SrTiO_3$ and $La_2Ti_2O_7$ are used to test the reliability of the method due to their well-known structures. In addition, the density of

some other members of the $\text{La}_4\text{Sr}_{n-4}\text{Ti}_n\text{O}_{3n+2}$ series was recorded, confirming that these phases can be regarded as intergrowths of the end members (Table 3-11). It is observed that there exists a systematic shift of the density values that is always slightly lower than the expected (figure 3.45). Despite this, it seems that the intergrowth model is correct for the $\text{La}_4\text{Sr}_{n-4}\text{Ti}_n\text{O}_{3n+2}$ family of compounds. For the $n=12$ member, the models considering a perovskite with cation vacancies or partial reduction of Ti must be neglected, because the experimental data are much lower than the predicted ones. After calibration by removing this shift using $\text{La}_2\text{Ti}_2\text{O}_7$ and SrTiO_3 as the standards, the experimental and theoretical densities match each other very well and the intergrowth model (c) is the best approximation for the $n=12$ member, although no evidence of intergrowth was obtained by XRD.

n	Formula	Estimated density (gcm^{-3})	Observed density (gcm^{-3})
4	$\text{La}_4\text{Ti}_4\text{O}_{14}$	5.79	5.71
∞	SrTiO_3	5.11	5.04
8	$\text{La}_4\text{Sr}_4\text{Ti}_8\text{O}_{26}$	5.34	5.25
10	$\text{La}_4\text{Sr}_6\text{Ti}_{10}\text{O}_{32}$	5.28	5.20
12	$\text{La}_4\text{Sr}_8\text{Ti}_{12}\text{O}_{38}$	5.25	5.18

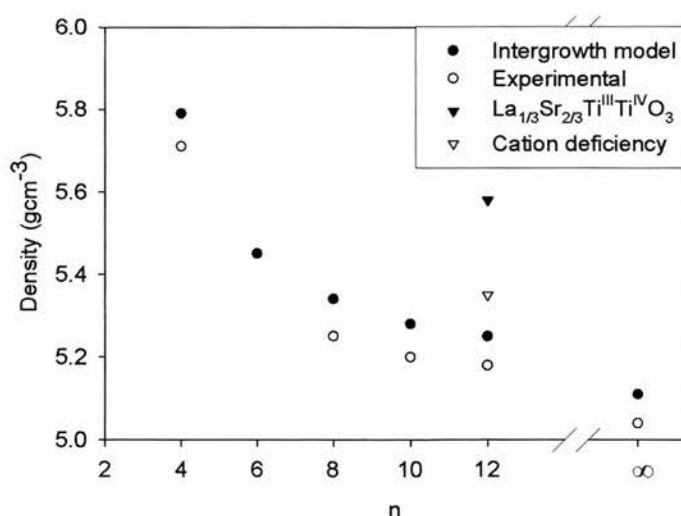
Table 3-11. Density of different members of the $\text{La}_4\text{Sr}_{n-4}\text{Ti}_n\text{O}_{3n+2}$ family.

Figure 3.45. Comparison between theoretical and experimental density values for several members of the $\text{La}_4\text{Sr}_{n-4}\text{Ti}_n\text{O}_{3n+2}$ series.

A larger amount of cation vacancies could give density values as low as the experimental observed. However it should be mentioned that the model considered contains 5.5% of vacancies in the A-site and 5.5% in the B-site. More cation vacancies should be detected by techniques such as neutron diffraction or TEM in the form of impurities of the corresponding binary oxides, which could not be found in the present case. Previous works claimed that substitution of Sr by La in SrTiO_3 was accommodated mainly via the formation of Sr vacancies, which would be accommodated as Sr-O layers [30-31]. That would lead to 17% SrO, which is too large not to be detected by XRD. Formation of La_2O_3 layers on the other hand, is quite unlikely because this oxide is very hygroscopic and tend to forms $\text{La}(\text{OH})_3$ and therefore pellets would break after exposure with wet atmospheres, which is not the present case. Cation vacancies should not be completely rejected as they still could be present, but it seems that is not the main mechanism involved to explain the excess oxygen.

3.3.1.4. TEM.

TEM can help to solve this particular dilemma and the studies carried out on this phase reveal, first of all, a far more complex situation than a simple cubic perovskite as previously found by XRD and PND. The first striking features were found by means of electron diffraction. SAED patterns viewing down the $[-110]_p$ and $[11-2]_p$ zone axes (figure 3.46) reveal the existence of superstructure reflections along the $[111]_p$ direction, which is rather surprising because that was not detected by the other diffraction techniques used in the present work. The superstructure reflections appear at $\frac{1}{2}\{111\}$, which is approximately 4.5 Å and therefore the simple cubic

perovskite unit cell with parameter $a \approx 3.91 \text{ \AA}$ is not enough to describe the structure of the $n=12$ member. SAED performed in other zone axes do not show superstructure reflections along any direction other than $[111]_p$ (figure 3.46.c) and relates to the higher sensitivity of electron diffraction to superlattices of light elements. In fact, even the HRTEM image corresponding to a view down the $[11-2]_p$ does not show clearly such doubling of the $(111)_p$, and in some regions it is barely distinguishable (figure 3.47).

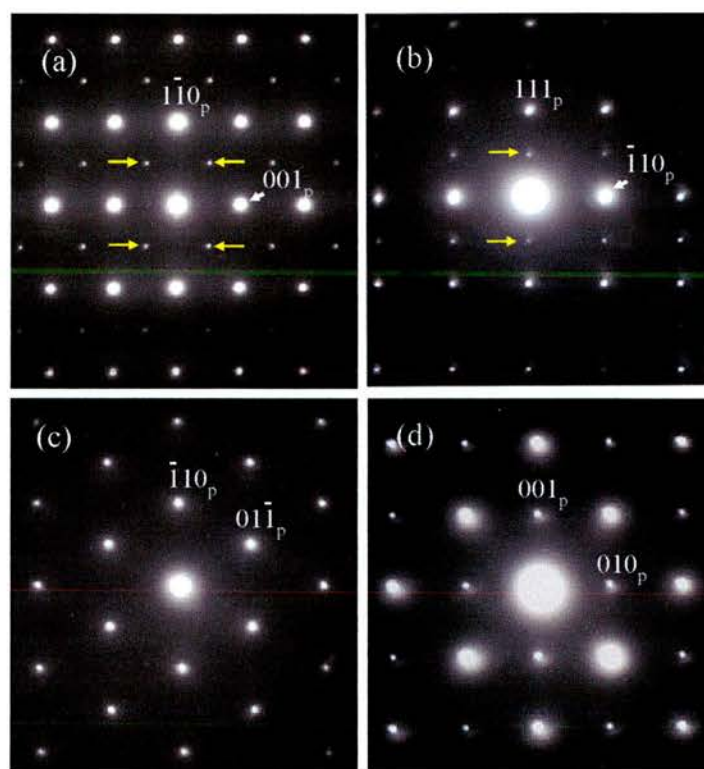


Figure 3.46. SAED pattern corresponding to views down the main zone axes for the $n=12$ member, i.e. $[-110]_p$ (a), $[11-2]_p$ (b), $[111]_p$ (c) and $[100]_p$ (d). Superstructure reflections are present at $(\frac{1}{2} \frac{1}{2} \frac{1}{2})$ as marked with arrows.

Subtle tilting of the BO_6 octahedra in the perovskite network is considered the most likely explanation for such a superstructure. Tilting of octahedra is one of the most common distortions from the ideal perovskite unit cells and usually it renders tetragonal or even orthorhombic unit cells as occurs in CaTiO_3 or $\text{Li}_x\text{La}_{1-x}\text{TiO}_3$, the so-called diagonal perovskites. The cell parameters of diagonal perovskites derive

from the primitive perovskite unit cell parameter (a_p) as $a=\sqrt{2}a_p$, $b=\sqrt{2}a_p$ and $c=2a_p$, although the axes may be interchanged depending on symmetry considerations. In the present case however the unit cell remains cubic because no extra reflections or splitting of peaks corresponding to losses in symmetry were found in both the XRD and PND patterns. Hence the unit cell would be a face centred cubic superstructure with $a=2a_p$.

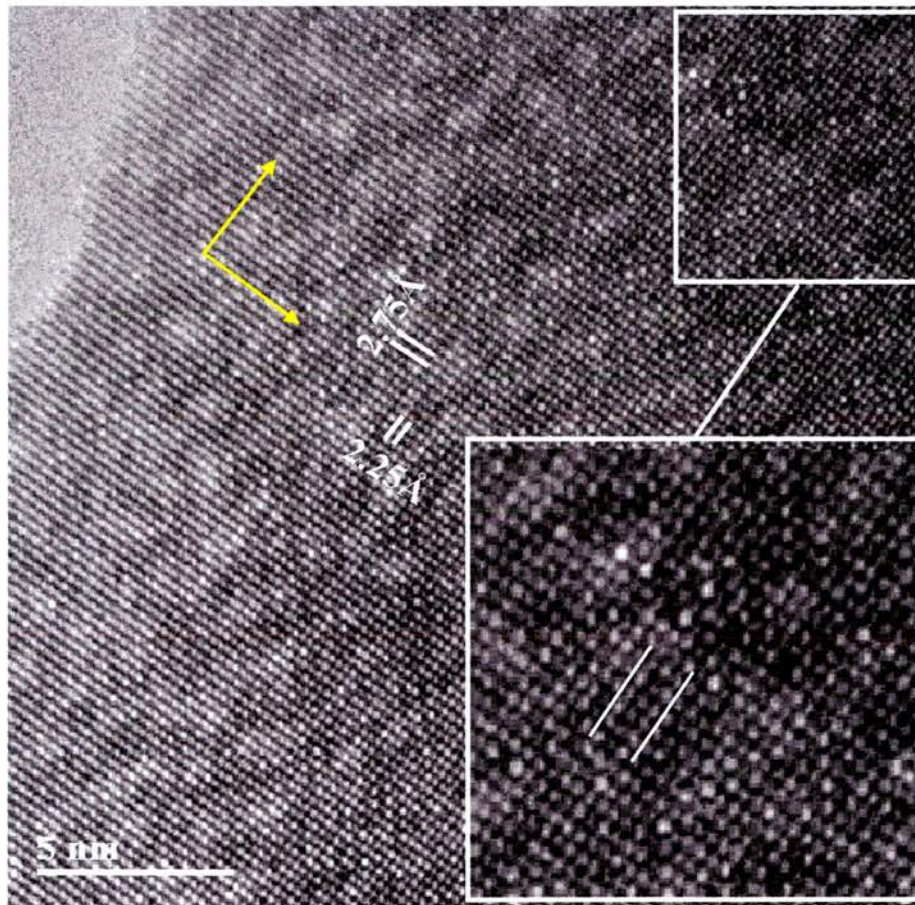


Figure 3.47. HRTEM image viewing down the $[11-2]_p$ zone axis for the $n=12$ member. The inset shows zooms an area where the doubling of the $[111]_p$ is barely distinguishable as marked with two parallel bars.

High-resolution images taken down the $[100]_p$ uncovered even more complexities: a large amount of nanodomains (tiny dark areas marked in figure 3.48) randomly distributed, indicating the presence of local defects. A close look to such

nanodomains brings to light that what happens is that one or a few columns are slightly displaced from their expected position if the structure was an ideal cubic perovskite (inset in figure 3.48).

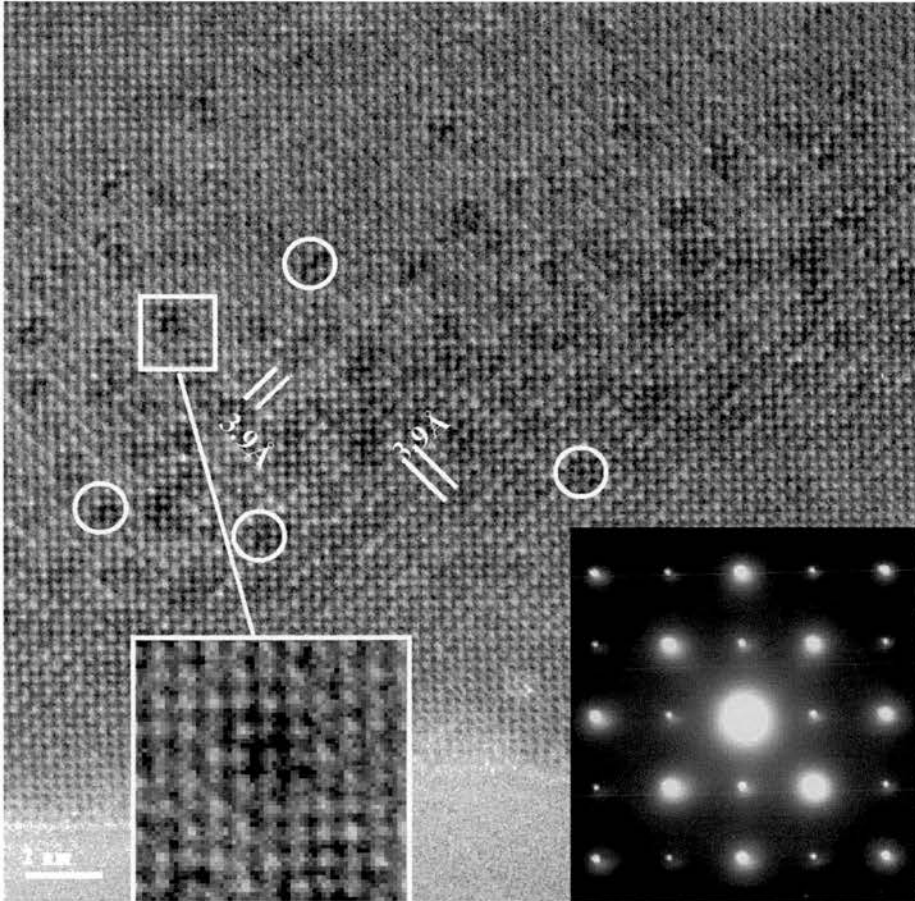


Figure 3.48. HRTEM image corresponding to the $[100]_p$ zone axis in the $n=12$ member.

Randomly distributed local defects are visible and marked with circles. The inset shows in detail one of such domains.

Such a contrast is not so obvious in the images on any other projections as can be observed in figure 3.49 corresponding to a view down the $[111]_p$ direction, indicating that the shape of these defect areas is linear along the $[100]$ direction.

HRTEM images corresponding to the $[110]_p$ zone axis give further information about the nature of such linear defects. In some regions it was possible to observe some sort of modulated structure (figure 3.50) that could be regarded as a

short-range crystallographic shear similar to those characteristic of $\text{La}_2\text{Ti}_2\text{O}_7$ covering just few nanometers. It is quite intuitive to think that these larger defects are related with the small linear defects, having both the same structural principles with crystallographic shears where the excess oxygen is accommodated. As mentioned in the introduction, TiO_6 octahedra in $\text{La}_2\text{Ti}_2\text{O}_7$ are strongly tilted and distorted, especially those close to the crystallographic shears. That could certainly occur in the domains in question and it could explain the doubling of the $(111)_p$ observed by SAED. The strong distortions in the surroundings of the crystallographic shears are accommodated within the perovskite framework by inducing an averaged subtle tilting of the octahedra.

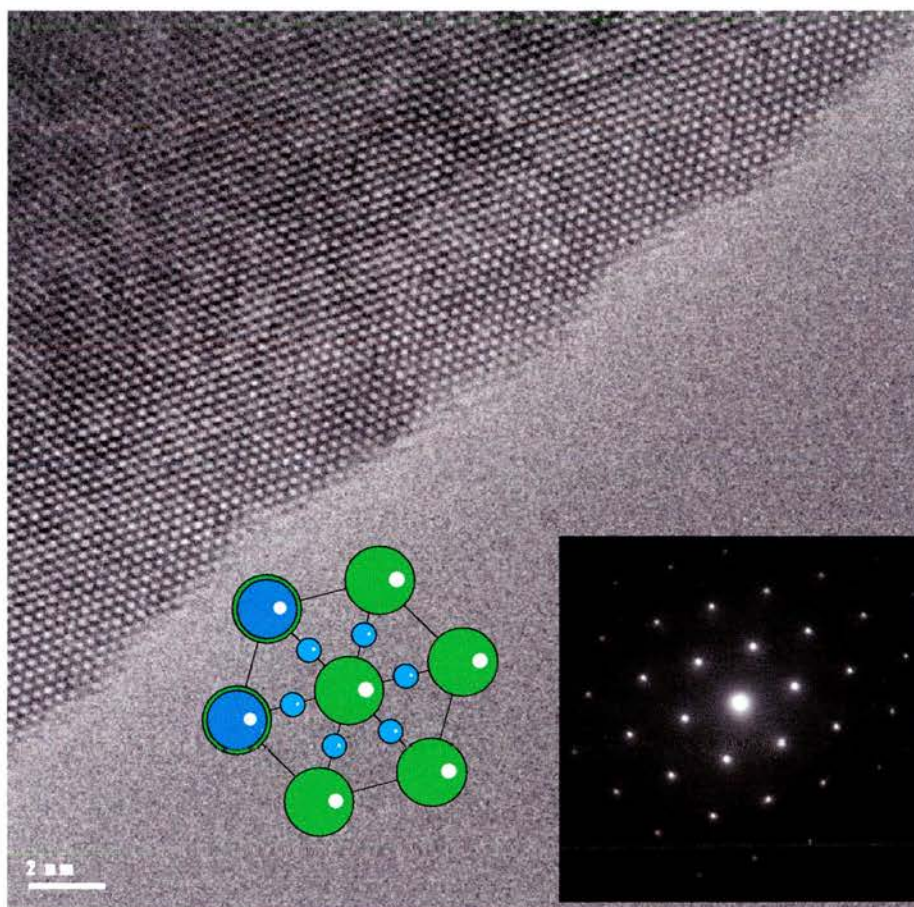


Figure 3.49. HRTEM image viewing down the $[111]_p$ projection in $\text{La}_4\text{Sr}_8\text{Ti}_{12}\text{O}_{38}$. The hexagonal pattern is typical of this particular zone axis in cubic symmetry as shows the inset containing the structural model. The other inset shows the corresponding SAED pattern.

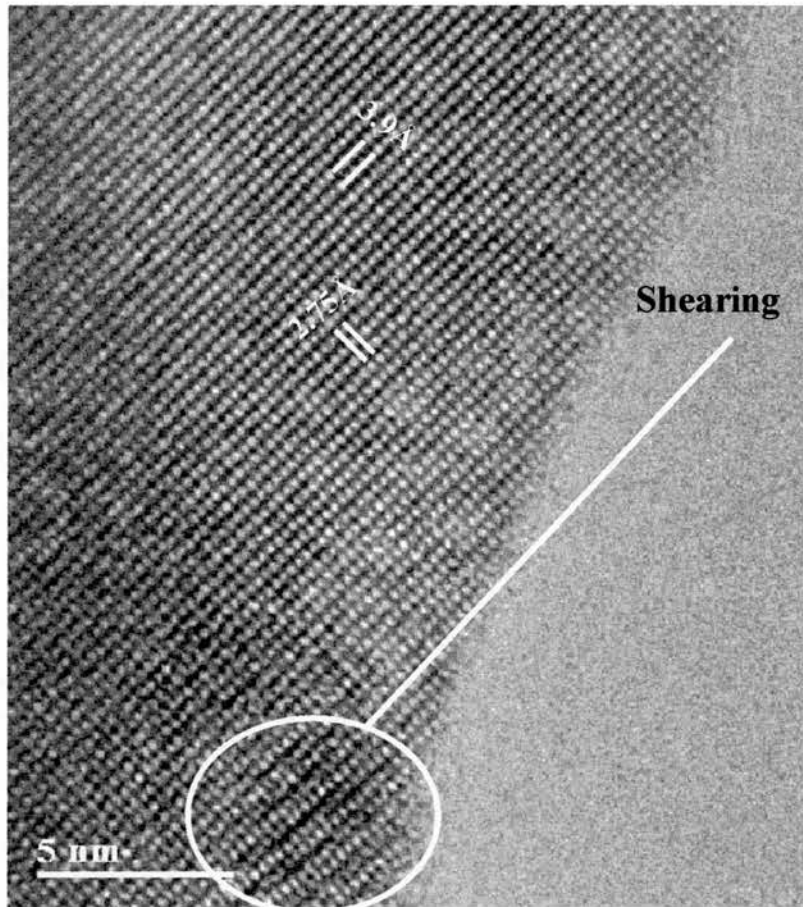


Figure 3.50. HRTEM image viewing down the $[-110]_p$ projection the formation of domains with crystallographic shears.

A relevant model of the defects is shown in figure 3.51. The atomic dislocation and La-rich composition are the two main sources of the dark contrast in the images. The crystallographic shear occurs along the $[-110]_p$, as can be appreciated in figure 3.50, which would agree with the model of such shear planes being related to those present in the lower members of the $\text{La}_4\text{Sr}_{n-4}\text{Ti}_n\text{O}_{3n+2}$. It is worth noting that such short-range crystallographic shears are randomly distributed within the perovskite matrix, which would explain why XRD or PND could not detect them. It should also be noticed that after all, cation vacancies and excess oxygen are two different approaches for the same conclusion. In fact, the crystallographic shears could be considered as either cation-deficient or excess-oxygen domains, but in the

case of short-range shears, the excess oxygen domain is a better elucidation of the real structure. At a very low level of substitution, local defects are created. At higher La contents, defects interact giving rise to linear defects as those observed for the $n=12$ member. At sufficient La concentration, the linear defects become extended (planar) originating crystallographic shears “regularly” distributed in the structure as observed in the lower members of the $\text{La}_4\text{Sr}_{n-4}\text{Ti}_n\text{O}_{3n+2}$ family. Therefore, the short-range crystallographic shears observed for the $n=12$ member would be the first stage in the formation of layered perovskites. These results would then prove Tilley’s hypothesis for SrTiO_3 [32] accommodating changes in stoichiometry by forming planar defects or intergrowths, although the planar defects are not Ruddlesden-Popper structures as suggested on those pioneering works but linear defects instead.

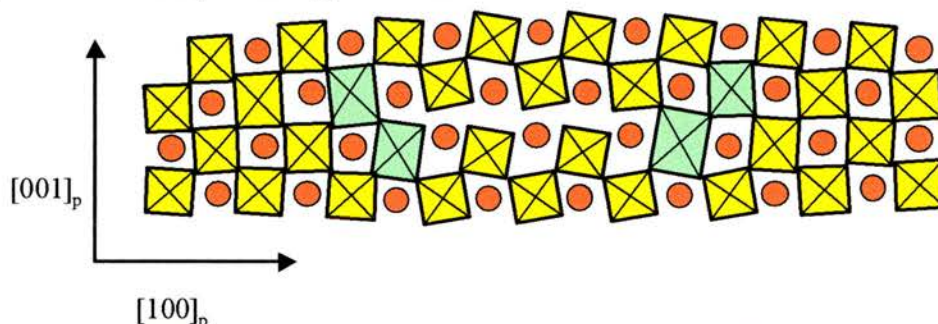


Figure 3.51. Structural model proposed for the short range shearing (linear defect) in the $n=12$ member.

3.3.2. $\text{La}_4\text{Sr}_{10}\text{Ti}_{14}\text{O}_{44}$ ($n=14$).

XRD and HRTEM studies on the $n=14$ ($\text{La}_4\text{Sr}_{10}\text{Ti}_{14}\text{O}_{44}$) member seem to further confirm the evidences pointed so far. First of all, XRD indicated that the unit cell was a simple cubic perovskite, as expected for n values larger than 11 (figure 3.52, table 3-12). Obviously, the unit cell will tend to be gradually closer to that of SrTiO_3 with increasing n .

$2\theta_{\text{obs}}$	hkl	$2\theta_{\text{cal}}$	Int	d_{obs}	d_{cal}
22.735	100	22.740	11	3.9081	3.9072
32.381	110	32.378	100	2.7626	2.7628
39.935	111	39.933	26	2.2557	2.2558
46.449	200	46.444	35	1.9534	1.9536
52.307	210	52.314	5	1.7476	1.7474
57.756	211	57.751	28	1.5950	1.5951
67.778	220	67.782	13	1.3815	1.3814

Table 3-12. XRD data for the $n=14$ member of the $\text{La}_4\text{Sr}_{n-4}\text{Ti}_n\text{O}_{3n+2}$ series, which was indexed as a simple cubic perovskite ($a=3.9072(5)$ Å).

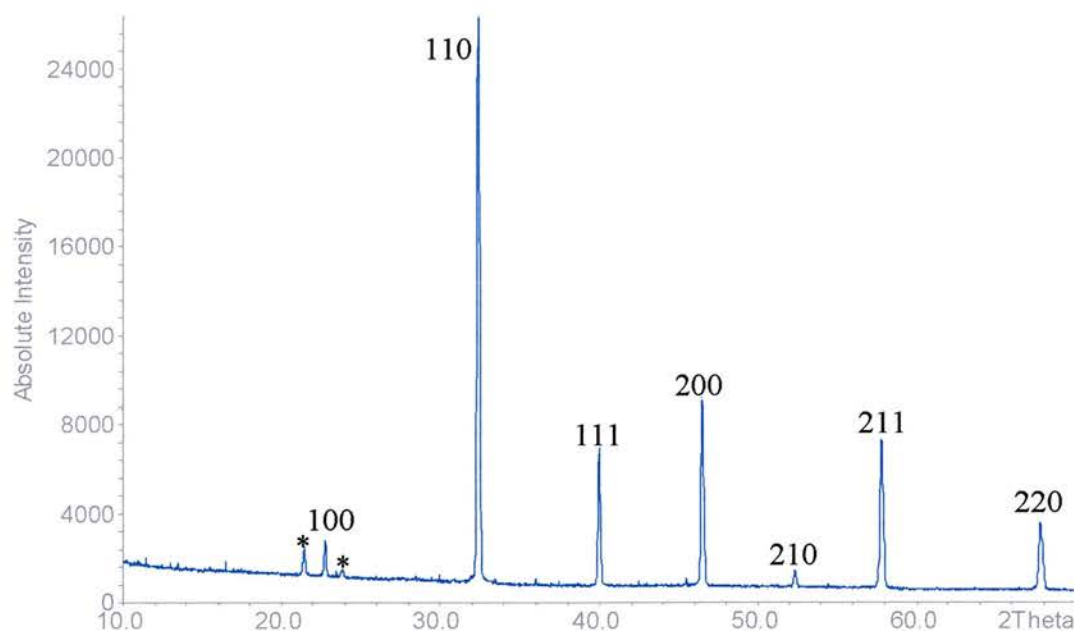


Figure 3.52. XRD pattern for $\text{La}_4\text{Sr}_{10}\text{Ti}_{14}\text{O}_{44}$, which was indexed as a cubic perovskite as was the case of the $n=12$ member.

TEM observations were in agreement with the results found for the $n=12$ member. Again, superstructure reflections doubling the $(111)_p$ were observed on the SAED patterns (figure 3.53). However the average tilting in the octahedra network would be smaller because of the lower concentration of La in comparison to the $n=12$

member, which implies less excess oxygen and therefore less amount of linear defects along the $[110]_p$ direction.

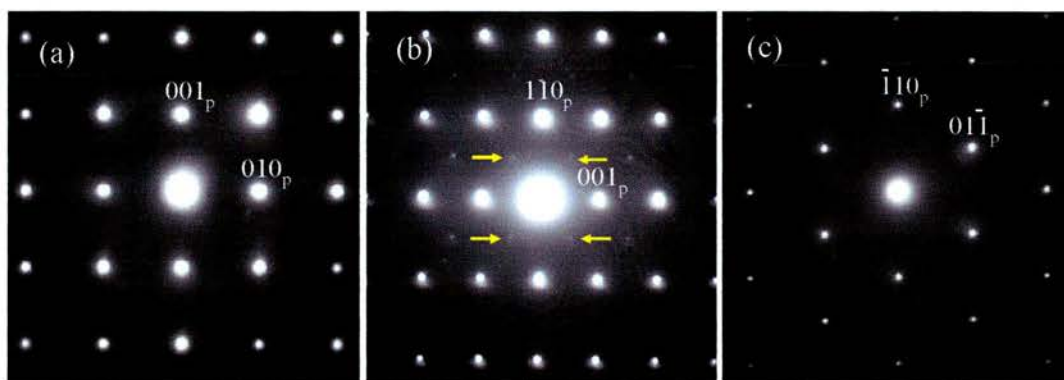


Figure 3.53. SAED patterns corresponding to views down the main zone axes, i.e. $[100]_p$ (a), $[-110]_p$ (b) and $[111]_p$ (c), for the $n=14$ member. As occurred for the $n=12$ member, superstructure reflections doubling the $[111]_p$ were present (marked with arrows).

The corresponding HRTEM images revealed that in fact, the lower concentration of excess oxygen seems to imply lower concentration of the nanodomain defects described for the $n=12$ member, although still visible (figure 3.54).

For the $n=14$ member the formation of short-range crystallographic shears was not as clear as was the case of the $n=12$ member, notwithstanding that local defects were still noticeable as some sort of subtle distortion as shown in figure 3.55. Such distortion would be related with the short range crystallographic shears observed before, the latter being a partially extended version of the former. In other words, the modulation could be interpreted as shorter range shearing affecting even fewer unit cells. From these results, one can extract valuable information about the nature of these phases. On one hand, these observations completely agree with the model proposed for the $n=12$ member, where the extra oxygen is accommodated via short

range shears. Furthermore, they would indicate that there exists a correlation between excess oxygen concentration and defect concentration. Hence advancing through the series until SrTiO_3 would result in a gradual dilution of defects. On the other hand, the defects are more difficult to detect possibly due to their “localisation”. From defect chemistry it is known that at a certain concentration defects usually tend to cluster due to energy consideration. However, if the concentration is sufficient low, they will remain isolated as presumably is the case for n values close to ∞ .

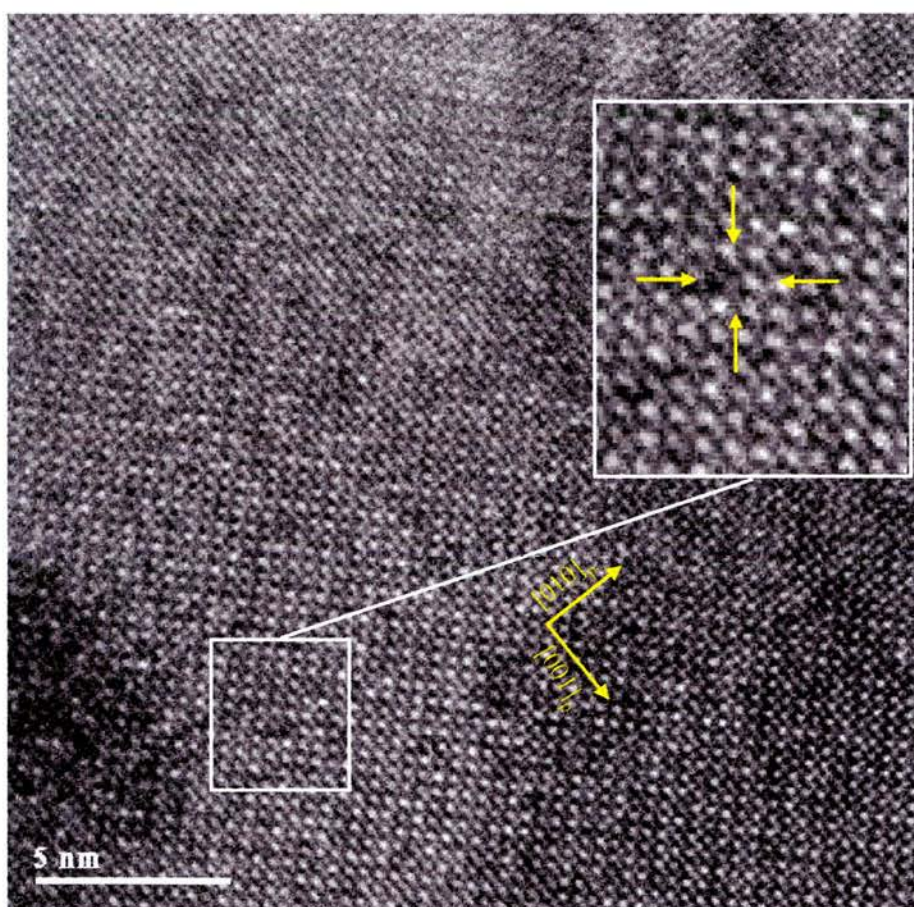


Figure 3.54. HRTEM image viewing along the $[100]_p$ projection. The presence of nanodomain-defects is still clear as shown in the inset. Arrows indicate a clear example of atomic columns deviated from their theoretical position, which in the end result in the dark contrast observed in the high-resolution images.

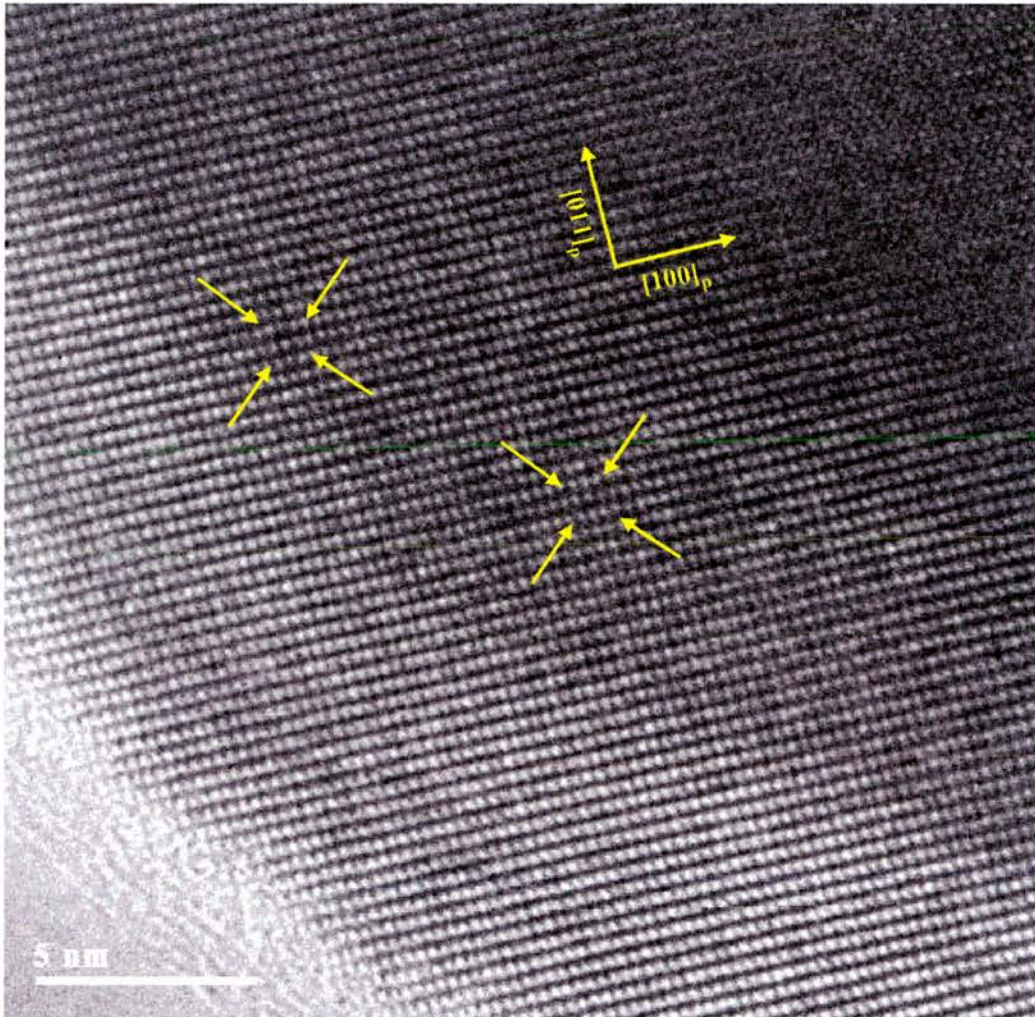


Figure 3.55. HRTEM image corresponding to the $[-110]_p$ zone axis. The presence of local distortions is indicated with arrows.

3.3.3. Discussion.

Advancing to higher values of n in the $\text{La}_4\text{Sr}_{n-4}\text{Ti}_n\text{O}_{3n+2}$ series, the relative amount of excess oxygen decreases as listed in table 3-13. Therefore, for members with $n > 11$, i.e. $\delta < 0.18$, the formation of extended crystallographic shears is not

favoured and the extra oxygen is preferentially distributed in linear defects. If these defects are dilute (as is the case) they will remain isolated rather than clustering to give the energetically favoured extended defects. In other words, when the excess oxygen is in sufficiently low concentration, the crystallographic oxygen shears have a range of just few unit cells and they would be randomly distributed within the crystals. The results obtained for the $n=14$ member seem to show further evidence to prove this hypothesis, because the defects seem to be even more “localised” and they become barely distinguishable even by HRTEM.

n	Formula	δ
4	$\text{La}_4\text{Ti}_4\text{O}_{14}$	0.500
6	$\text{La}_4\text{Sr}_2\text{Ti}_6\text{O}_{20}$	0.333
8	$\text{La}_4\text{Sr}_4\text{Ti}_8\text{O}_{26}$	0.250
10	$\text{La}_4\text{Sr}_6\text{Ti}_{10}\text{O}_{32}$	0.200
12	$\text{La}_4\text{Sr}_8\text{Ti}_{12}\text{O}_{38}$ (ox)	0.167
14	$\text{La}_4\text{Sr}_{10}\text{Ti}_{14}\text{O}_{44}$	0.142

Table 3-13. Variation of the excess oxygen (δ) through the $\text{La}_4\text{Sr}_{n-4}\text{Ti}_n\text{O}_{3n+2}$ series of compounds.

Hence, it has been shown that excess oxygen can be accommodated in nanodomain defects, rather than the formation of Ruddlesden-Popper phases suggested by previous works. It should be remarked that the mechanism of accommodating excess oxygen in nanodomain defects is quite intuitive and the relation between lower and higher members of the system studied seems reasonable and is entirely a consequence of the excess oxygen concentration. Also the model proposed would explain the formation of crystallographic shears in solids from an early stage of local defects to the formation of extended defects, which appear as a regular feature in the crystal structure.

The presence of linear defects on a perovskite matrix for the higher members ($n=12$ and $n=14$) vs. extended defects in the form of crystallographic shears for the lower members should affect the properties of these materials and a noticeable change should be expected. Chapter 4 will deal with the electrochemical properties of the $\text{La}_4\text{Sr}_{n-4}\text{Ti}_n\text{O}_{3n+2}$ series.

The presence of local defects should not be addressed uniquely to this series of compounds and thus it could be highly relevant, if not demanded, to carry out HRTEM studies in some of the state of the art materials used in fuel cell technology. Their structural characterisation is not always rigorous and some relevant local structural information missed by diffraction techniques could be found and that might help to understand why some materials present better performance than others do. Also the formulation of mechanisms should consider the local structure because it is the local environment that is responsible for transport properties and not average structures, which is the information obtained by XRD or PND after all.

3.4 Summary.

A new family of layered perovskites $\text{La}_4\text{Sr}_{n-4}\text{Ti}_n\text{O}_{3n+2}$ has been investigated and a structural model proposed. The structures can be described as comprising n -layers thick $\{110\}$ perovskite blocks, joined by crystallographic oxygen shears along the $[001]_p$ direction where excess oxygen is accommodated. There is a significant difference between even and odd number of layers per block. For an odd number of layers per block the phases the c -axis needs to be doubled because of the reverse tilting of the octahedral between consecutive blocks (canting), whereas for even

numbers the c -axis corresponds to a single block repeat distance. The doubling of the c -axis relieves the unit cell from its monoclinic distortion rendering orthorhombic unit cells. When n is greater than 6, diverse-sized perovskite blocks cohabit as both XRD and TEM suggest. Annealing for much longer times until the equilibrium is achieved would presumably yield perovskite blocks of identical size as happened for the $n=6$ member. For n values higher than 11, the layered structure apparently disappears and a pseudocubic symmetry is achieved. However, HRTEM studies prove that the substitution of Sr^{2+} by La^{3+} leads to the presence of short-range crystallographic shears imbedded in the perovskite matrix, where the excess oxygen is accommodated. Therefore, when the amount extra oxygen is low enough, the crystallographic shears do not appear as a regular feature of the crystal structure, but they are randomly distributed as linear defects. It also can be stated that the extra oxygen beyond the ABO_3 stoichiometry in these phases is accommodated in oxygen-rich planes rather than cation vacancies as it was widely believed.

As for the properties and applications of the layered properties, they may present ferroelectricity with rather high T_c , considering that $\text{La}_2\text{Ti}_2\text{O}_7$ is the material with highest T_c reported. Therefore, the $\text{La}_4\text{Sr}_{n-4}\text{Ti}_n\text{O}_{3n+2}$ series offers a very interesting research field for the future.

In the cubic phases, the presence of local defects randomly distributed will affect the properties of the material. Indeed, the total conductivity of $\text{La}_4\text{Sr}_8\text{Ti}_{12}\text{O}_{38-\delta}$ ($n=12$) [37] under reducing conditions was higher than that reported by Slater *et al.* [38] for the A-cation deficient $\text{La}_x\text{Sr}_{1-3x/2}\text{TiO}_3$, possibly due to the presence of excess

oxygen facilitating the reduction of these phases. Hence, under the same conditions, more Ti^{4+} would be reduced to Ti^{3+} and, consequently, more charge carriers created.

The electrochemical characterisation of the $\text{La}_4\text{Sr}_{n-4}\text{Ti}_n\text{O}_{3n+2}$ series of compounds, both layered and cubic phases will be presented in the next chapter, where the potential of some of the members as anode materials for fuel cell technology will also be discussed.

3.5. References.

1. S. N. Ruddlesden and P. Popper, *Acta Crystallographica*, **10** (1957), 538.
2. S. N. Ruddlesden and P. Popper, *Acta Crystallographica*, **11** (1958), 54.
3. J. G. Bednorz and K Müller, *Z Phys B.*, **64** (1986), 189.
4. H. K. Wu, J. R. Ashburn, C. J. Torng, P. H. Hor, R. L. Meng, L. Gao, Z. J. Huang, Y. Q. Wang and C. W. Chu, *Phys. Rev Lett.*, **58** (9) (1987), 908.
5. B. Aurivillius, *Ark. Kemi.*, **1** (1949), 499.
6. C. A. P. de Araujo, J. D. Cuchiaro, D. McMillan, M. Scott and J. F. Scott, *Nature*, **374** (1995), 627.
7. C. H. Hervoches, J. T. S. Irvine and P. Lightfoot, *Phys. Rev. B*, **64** (2001), 100102.
8. A. Snedden, C. H. Hervoches and P. Lightfoot, *Phys. Rev. B*, **67** (2003), 092102.

9. A. M. Kusainova, S. Yu Stefanovich, J. T. S. Irvine and P. Lightfoot, *J. Mater. Chem.*, **12** (2002), 3413.
10. M. Dion, M. Ganne, M. Tournoux, *Mater. Res. Bull.*, **16** (1981), 1429.
11. A. J. Jacobson, J. W. Johnson and J. T. Lewandowski, *Inorg. Chem.*, **24** (1985), 3727.
12. M. M. J. Treacy, S. B. Rice, A. J. Jacobson and J. T. Lewandowski, *Chem. Mater.*, **2** (1990), 279.
13. F. Lichtenberg, A. Herrnberger, K. Wiedenmann and J. Mannhart, *Progress in Solid State Chemistry*, **29** (2001), 1-70.
14. M. Gasperin, *Acta Crystallographica*, **B31** (1975), 2129.
15. N. Ishizawa, F. Narumo, T. Kawamura and M. Kimura, *Acta Crystallographica*, **B31** (1975), 1912.
16. H. W. Schmalle, T. Williams, A. Reller, A. Linden, J. G. Bednorz, *Acta Crystallographica*, **B49** (1993), 235.
17. M. E. Bowden, D. A. Jefferson and I. W. M. Brown, *J. Solid State Chem.*, **117** (1995), 88.
18. M. E. Bowden, D. A. Jefferson and I. W. M. Brown, *J. Solid State Chem.*, **119** (1995), 412.
19. J. Sloan, *Ph. D thesis*, Cardiff (1995).
20. D. Pasero, R. J. D. Tilley, *J. Solid State Chem.*, **135** (1998), 260.
21. I. Levin, L. A. Bendersky, T. A. Vanderah, R. S. Roth and O. M. Stafsudd, *Materials Research Bulletin*, **33[3]** (1998), 501-517.
22. T. Williams, F. Lichtenberg, D. Widmer, J. G. Bednorz and A. Reller, *J. Solid State Chem.*, **103** (1993), 375.

23. M. Nanot, F. Queyroux, J. C. Gilles and R. Portier, *J. Solid State Chem.*, **38** (1981), 74.
24. M. Nanot, F. Queyroux, J. C. Gilles and J. J. Capponi, *J. Solid State Chem.*, **61** (1986), 315.
25. T. Williams, H. W. Schmalle, A. Reller, F. Lichtenberg, D. Widmer and J. G. Bednorz, *J. Solid State Chem.*, **93** (1991), 534.
26. S. Nanamatsu, M. Kimura, K. Doi, S. Matsushita, N. Yamada, *Ferroelectrics*, **8** (1974), 511.
27. P. D. Battle, J. E. Bennet, J. Sloan, R. J. D. Tilley and J. F. Vente, *J. Solid State Chem.*, **149** (2000), 360.
28. Joseph E. Sustron, Susan M. Kauzlarich and P. Klavins, *Chemistry of Materials*, **4** (1992), 346.
29. N. G. Eror and U. Balachandran, *J. Solid State Chemistry* **40** (1981), 85-91.
30. U. Balachadran and N. G. Eror, *J. Electrochem. Soc.*, **129** (1982), 1021.
31. R. Moos, T. Bischoff, W. Menesklou and K. H. Härdtl, *J. Mater. Sci.*, **32** (1997), 4247.
32. R. J. D. Tilley, *J. Solid State Chem.*, **21** (1977), 293.
33. R. D. Shannon, C. T. Prewitt, *Acta Crystallographica*, **B25** (1969), 925.
34. John B. Goodenough: "Magnetism and the Chemical Bond", John Wiley and Sons (1963), New York-London.
35. H. W. Schmalle, T. Williams, A. Reller, F. Lichtenberg, D. Widmer and J. G. Bednorz, *Acta Cryst. C*, **51** (1995), 1243.
36. M. Nanot, F. Queyroux, J. C. Gilles, *J. Solid State Chem.*, **28** (1979), 137.

37. J. Canales-Vázquez, S. Tao and J. T. S. Irvine, *Solid State Ionics*, **159** (2003), 159.
38. P. R. Slater, D. P. Fagg and J. T. S. Irvine, *J. Mater. Chem.*, **7-12** (1997), 2495.

Chapter 4. Electrical properties of the $\text{La}_4\text{Sr}_{n-4}\text{Ti}_n\text{O}_{3n+2}$ series	127
4.1. Introduction	127
4.2 Impedance studies of $\text{La}_4\text{Sr}_{n-4}\text{Ti}_n\text{O}_{3n+2}$	128
4.2.1. Layered Phases	128
4.2.1.1. $\text{La}_2\text{Ti}_2\text{O}_7$ (n=4)	129
4.2.1.2. $\text{La}_4\text{SrTi}_5\text{O}_{17}$ (n=5)	135
4.2.1.3. $\text{La}_4\text{Sr}_2\text{Ti}_6\text{O}_{20}$ (n=6)	139
4.2.1.4. $\text{La}_4\text{Sr}_4\text{Ti}_8\text{O}_{26}$ (n=8)	143
4.2.2. Cubic Phases	145
4.2.2.1. $\text{La}_4\text{Sr}_8\text{Ti}_{12}\text{O}_{38}$ (n=12)	145
4.2.2.2. ACIS under different atmospheres in n=12	149
4.2.2.3. $\text{La}_4\text{Sr}_{10}\text{Ti}_{14}\text{O}_{44}$ (n=14)	151
4.2.2.4. SrTiO_3 (n= ∞)	153
4.2.3. Conclusions	155
4.3. Four terminal techniques	160
4.3.1. Temperature dependence	161
4.3.2. Conductivity as a function of $P(\text{O}_2)$	163
4.3.3. Thermopower measurements	164
4.4. Fuel Cell Tests	167
4.5. Conclusions	169
4.6. References	170

4. Electrical properties of the $\text{La}_4\text{Sr}_{n-4}\text{Ti}_n\text{O}_{3n+2}$ series.

4.1. Introduction.

Members of the $\text{La}_4\text{Sr}_{n-4}\text{Ti}_n\text{O}_{3n+2}$ series could be considered as potential oxygen ion conductors due to the significant amount of interstitial oxygen in preferential locations found in both reducing and oxidising conditions, especially if the defects can be made to disorder as extensively discussed in the previous section. Partial removal of the excess oxygen by reduction of Ti^{4+} might lead to an enhancement of the ionic conductivity together with electronic conductivity due to the presence of Ti^{3+} . In fact, $\text{La}_2\text{Sr}_4\text{Ti}_6\text{O}_{19.8}$ (the $n=12$ member) has been reported to be a good candidate as an anode material for fuel cells due to its high total conductivity (e.g. 60 Scm^{-1} at 900°C) in reducing conditions [1-2] as discussed in this section. Moreover, ceria composites of a La-substituted SrTiO_3 with very close stoichiometry to the $n=12$ member presents very promising performance in fuel cell tests [3], which indicates the relevance of such titanates from the point of view of technological applications. Therefore studies on the electrical properties of these compounds are highly demanded.

The electrical properties of electroceramics can be investigated using a range of techniques such as ac impedance spectroscopy, four terminal dc measurements and electrochemical tests. As mentioned in section 2.3, impedance spectroscopy yields separated responses for bulk, grain boundaries and electrode processes. Such responses are often dependent on the microstructure of the material. Four terminal dc measurements are chosen to evaluate the total conductivity when the resistance of the

material is lower than the resistance due to the jig design. Finally, the electrochemical tests are used to probe the performance of materials under different operating conditions and hence they give an idea of the potential of the studied materials as anodes in fuel cells.

4.2 Impedance studies of $\text{La}_4\text{Sr}_{n-4}\text{Ti}_n\text{O}_{3n+2}$.

Impedance studies were carried out on some members of the $\text{La}_4\text{Sr}_{n-4}\text{Ti}_n\text{O}_{3n+2}$ series, in static air and over a range of temperatures. On some occasions the experiments were performed in flowing wet and dry Ar and these instances will be precisely specified. The results are described in two sections according to the structure: layered phases and (pseudo) cubic phases. The compounds considered as layered phases are those showing XRD extra reflections compared to the simple cubic perovskite (see chapter 3), i.e. $n < 12$. Larger values of n are considered as cubic phases.

4.2.1. Layered phases.

Impedance plots typically gave complex responses that could change dramatically with the temperature. A detailed description of the responses of each member will be described below.

4.2.1.1. $La_2Ti_2O_7$ ($n=4$).

The complex impedance plots showed the presence of two arcs at high temperature, that can be attributed to the ferroelectric bulk (typically $C=1 \times 10^{-11} \text{Fcm}^{-1}$) and to the grain boundary ($C=3 \times 10^{-8} \text{Fcm}^{-1}$) respectively as shown in figure 4.1.

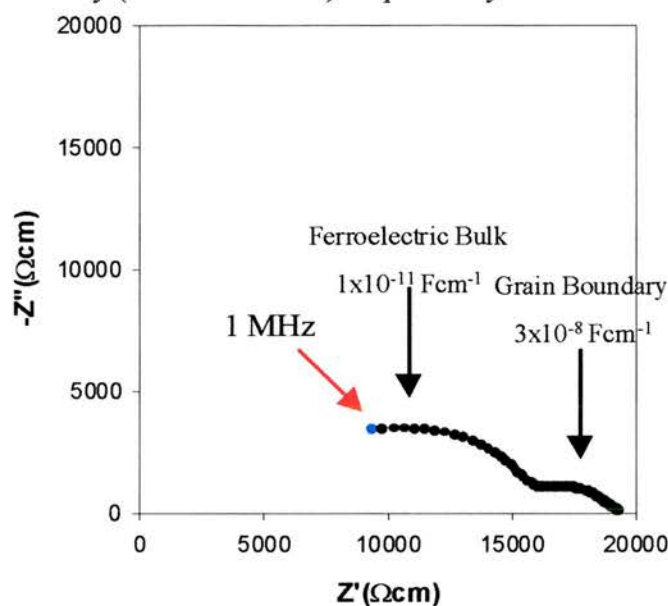


Figure 4.1. Geometry corrected Nyquist plot of $La_2Ti_2O_7$ obtained at 857°C in static air. There are two arcs that correspond to the responses of the ferroelectric bulk and the grain boundary respectively as marked with arrows.

At lower temperatures the bulk response gradually has a lower relaxation frequency, which results in the observation of a complete semicircle at 537°C in the high frequency range (figure 4.2). One might consider whether the arc at high frequency range has one or two components because is a fairly broad semicircle. The Z'' and M'' peaks for the bulk in the corresponding spectroscopic plots seem quite separate, which is symptomatic of two different processes. However, experiments performed under open circuit revealed that above 100 kHz the system (cell and/or impedance analyser) “generates” a background (it is not simply a capacitance in parallel) that may result in the distortion of the bulk response. Therefore, it seems that

there is only one bulk response, which is artificially distorted. Figure 4.2c shows the Z'' and M'' spectroscopic plots collected at lower temperature (400°C), where the M'' peak corresponding to the bulk is more evident and appears in the same order of frequency as the Z'' peak.

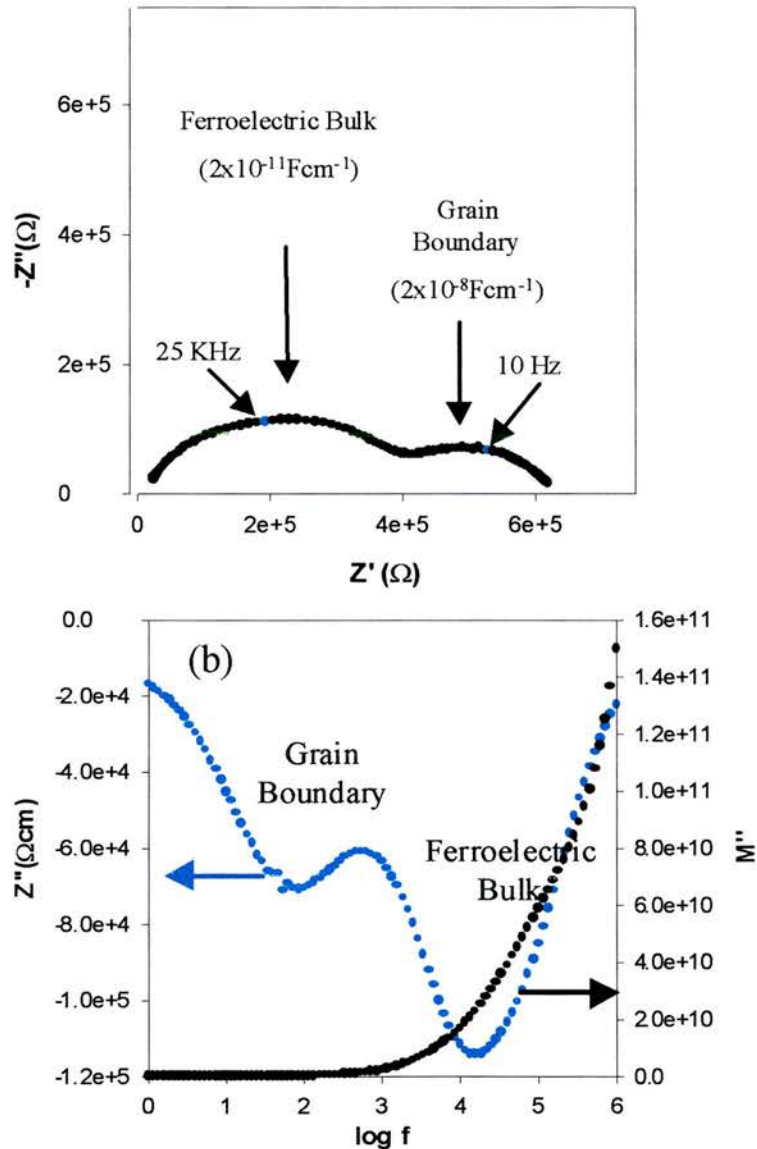


Figure 4.2. Geometry corrected Nyquist plot (a) and the corresponding spectroscopic plots of M'' and Z'' (b) for the $n=4$ member at 810 K. In the M'' plot, the bulk response is masked by an artifact caused by the experimental setup.

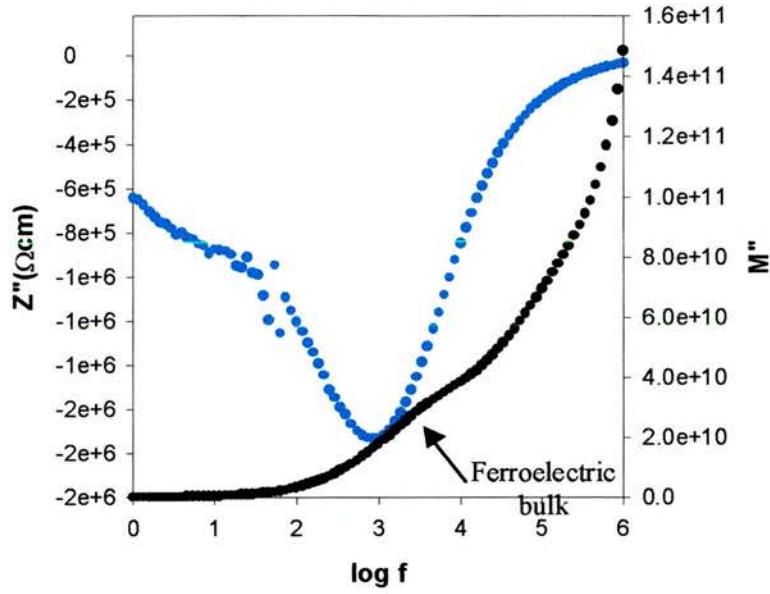


Figure 4.2c. Spectroscopic plots of Z'' and M'' . The response of the ferroelectric bulk can be discerned easily from the background caused by the instrument.

The analyses of the impedance spectra was carried out by using equivalent circuits (non-linear fitting) with two R-CPE elements in series, due to the dispersion in the relaxation frequency values (figure 4.3).

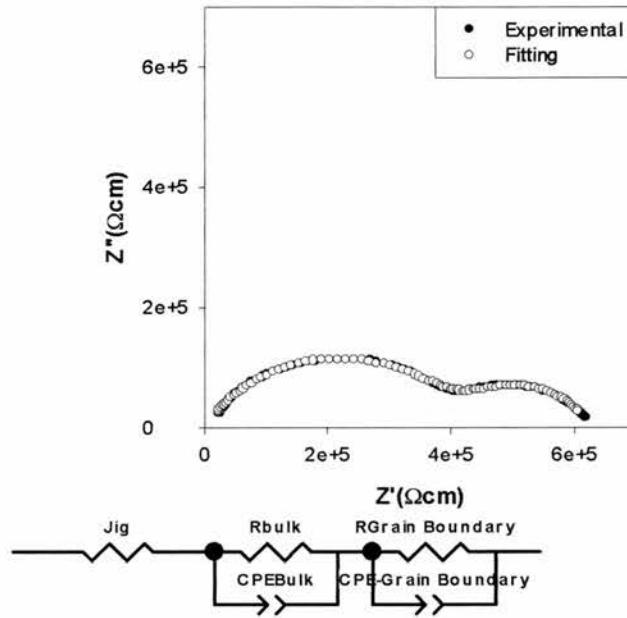
The parameter CPE-T obtained using a non-linear fitting method is not the capacitance associated to the process. In this case, the capacitance can be estimated from the definition of the relaxation frequency:

$$RC = \frac{1}{2\pi f} = (RCPE - T)^{1/n} \quad [\text{equation 4-1}]$$

where n is CPE-P in the data fit table (bottom figure 4.3). From equation 4-1, the capacitance can be calculated as

$$C = R^{-\frac{n+1}{n}} CPE - T^{1/n} \quad [\text{equation 4-2}]$$

Thus, the capacitance associated with the bulk at 537°C is $2 \times 10^{-11} \text{ Fcm}^{-1}$ whilst is $2 \times 10^{-8} \text{ Fcm}^{-1}$ in the case of the grain boundary. The rather low values of n (CPE-P) may explain the broad response for the bulk in addition to the distortion caused by the experimental setup.



Element	Freedom	Value	Error	Error %
Jig	Fixed(X)	1	N/A	N/A
Rbulk	Free(+)	4.212E5	0.9669	0.00022956
CPEBulk-T	Free(+)	1.6687E-9	2.06E-14	0.0012345
CPEBulk-P	Free(+)	0.61959	8.8043E-7	0.0001421
RGrain Boundary	Free(+)	2.0436E5	1.0547	0.0005161
CPE-Grain Bound	Free(+)	9.8013E-8	1.2333E-12	0.0012583
CPE-Grain Bound	Free(+)	0.68335	3.1399E-6	0.00045949
Chi-Squared:		1.1869E-10		
Weighted Sum of Squares:		1.899E-8		

Figure 4.3. Nyquist plot for $La_2Ti_2O_7$ at 537°C adjusted using equivalent circuits. The fit is quite good as can be extracted from both the plot and the fitting parameters. The low CPE-P values (n) indicate a large deviation from the ideal bricklayer model (n=1).

The capacitance (C) associated to a given response should be fairly constant with the temperature, unless phase transitions are involved or in the case of ferroelectric materials. $La_2Ti_2O_7$ is the ferroelectric material with the highest T_c

(>1500 K) reported [16] and therefore a Curie-Weiss temperature dependence of the capacitance can be expected (figure 4.4).

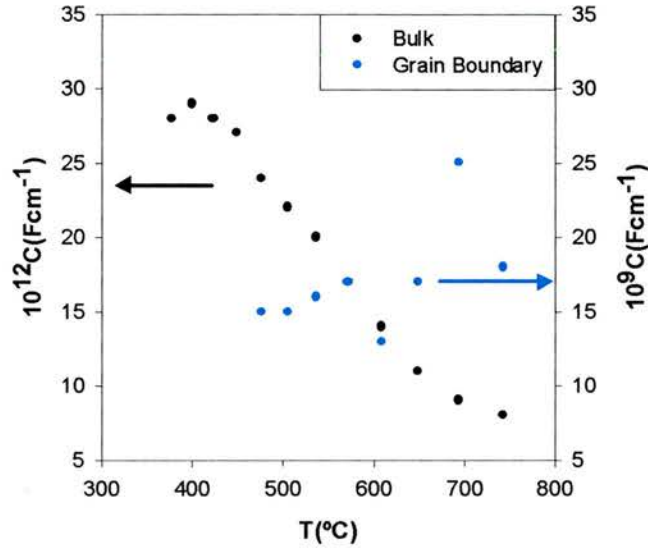


Figure 4.4. Capacitance vs. temperature plots for both bulk and grain boundary. The capacitance associated with the bulk decreases gradually with the temperature, whereas in the case of the grain boundary it was a random distribution of values.

At temperatures of around 400°C it seems that a ferroelectric transition takes place. $La_2Ti_2O_7$ is ferroelectric because of the strong distortions existing in the perovskite blocks in which one of the axes of the TiO_6 octahedra is much shorter than the other two as reported by Schmalke *et al* [6]. This is surprising since the reported T_c in the literature is well above 1000°C. It should be considered however that several incommensurate phase transitions occur at lower temperatures as reported by Ohi *et al* [3]. It is not the purpose of the present work to go into more rigorous study of the ferroelectric nature of this phase, but to clarify that the rather high bulk capacitance is due to ferroelectricity rather than necking or other phenomena related to poor sintering. Also it should be noted that in previous studies performed by Sinclair *et al* on the dielectric properties of $LiTaO_3$ [4], they concluded that dispersive elements

should be added in the equivalent circuit to obtain an accurate representation of the ac response in the case of ferroelectric materials, rather than single R and C values. This is in clear agreement with the results presented in this study.

The Arrhenius plots of this phase corresponding to overall, bulk and grain boundary conductivities are shown in figure 4.5. $\text{La}_2\text{Ti}_2\text{O}_7$ is a semiconductor with activation energy (E_a) of 1.09eV. The overall resistivity is dominated by the bulk response ($E_a=1.03$ eV) especially at high temperature. The grain boundary response becomes more important at low temperatures ($E_a=1.31$ eV). Thus, the relatively low overall conductivity of this material cannot be attributed to porosity (the relative density is 87%) and the explanation should be found in the layered nature of the phases of this study. Some layered perovskites as $\text{La}_5\text{Ti}_5\text{O}_{17}$ have been reported to present quasi-1D metallic behaviour along preferential directions, i.e. within the perovskite blocks, due to the presence of Ti^{3+} [5]. In this compound however Ti is essentially all in the 4+ state, i.e. therefore there are no d-electrons, and furthermore, the oxygen-rich planes act as insulating barriers. Such oxygen-rich planes will impede the transport of charged species between adjacent blocks. Moreover, in the present work, samples were prepared by solid state reaction leading to anisotropy that results in insulating barriers along every possible direction depending on the orientation of the grains, which would explain the poor conductivity with no effect from the direction in which the measurements are performed.

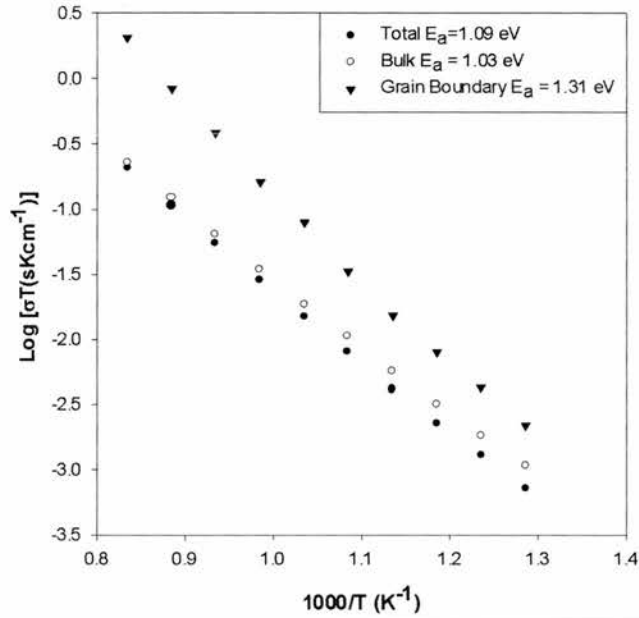


Figure 4.5. Arrhenius plots of the bulk, grain boundary and overall (total) conductivity in $La_2Ti_2O_7$. The total conductivity is limited by the bulk contribution.

4.2.1.2. $La_4SrTi_5O_{17}$ (n=5).

Grain boundary contribution dominates the responses of the n=5 member, with an assigned capacitance of typically $2 \times 10^{-8} \text{Fcm}^{-1}$. At high temperatures (e.g. 1170K) only one semicircle assigned to the grain boundary is discernible (figure 4.6a), whilst at lower temperatures, the bulk response becomes distinguishable as a small lump at high frequencies (figure 4.6b). The use of the spectroscopic plot of the complex modulus formalism (M'') highlights that such high frequency lump is indeed another electrochemical process with associated capacitance of around $2 \times 10^{-12} \text{Fcm}^{-1}$, i.e. the bulk response (figure 4.6.c). It should be noted that impedance plots emphasise the most resistive component, whereas the modulus plots enhance the contribution with the lowest capacitance.

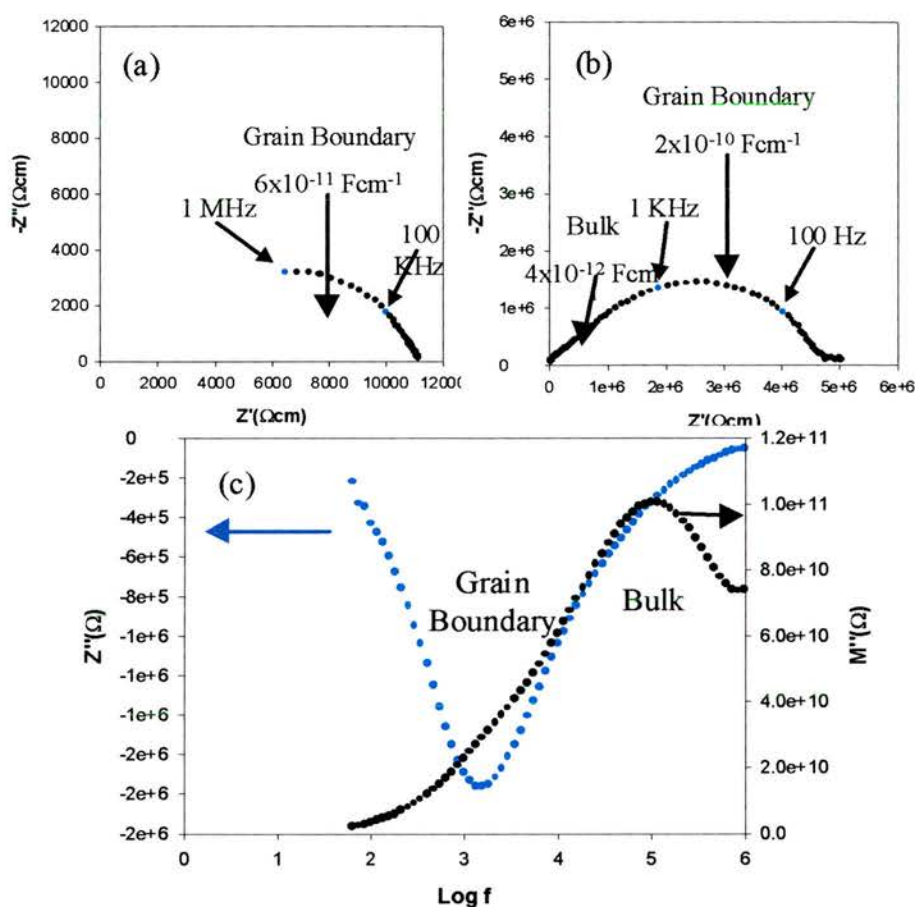


Figure 4.6 Nyquist plots of the $n=5$ member at 1130 K (a) and 844 K (b). The spectroscopic plots of the imaginary part of the impedance and modulus highlight the presence of two electrochemical processes at 844 K, i.e. grain boundary and bulk (c).

The capacitance associated to the bulk is one order of magnitude lower compared to the $n=4$ member in the whole range of temperatures. The $n=5$ member does not show features of a ferroelectric, which could be related with the doubling of the c -axis, although the distortion in the TiO_6 octahedra still remains. Thus there would exist a permanent polarisation may exist on each individual perovskite block. However the reverse tilting (canting) of octahedra between consecutive blocks renders the annihilation of the permanent polarisation. In other words, a centrosymmetric

space group does not allow ferroelectricity (figure 4.7). Other members of the $\text{La}_4\text{Sr}_{n-4}\text{Ti}_n\text{O}_{3n+2}$ series with odd number of layers per block should give analogous effects.

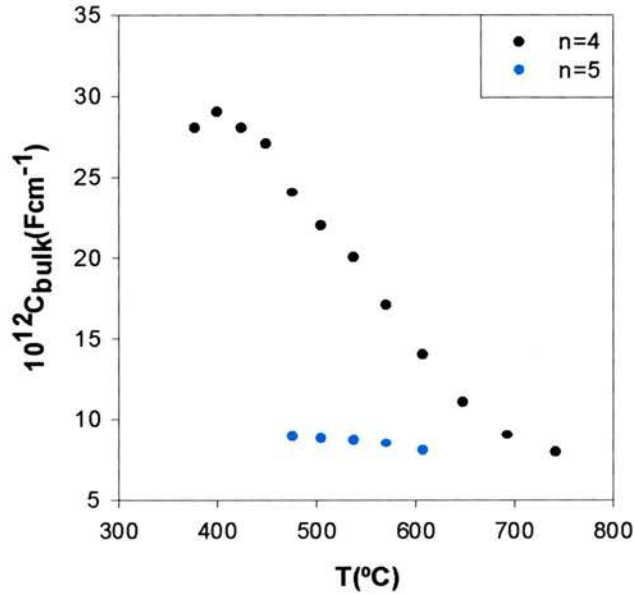


Figure 4.7. Temperature dependence of the capacitance for the n=4 and n=5 member. Whereas the former presents a clear change of the capacitance with the temperature related to ferroelectricity, in the latter it does not show it. The capacitance associated to the bulk in n=5 is high and might be due to the presence of traces of ferroelectric secondary phases (e.g. n=4 or 6).

Figure 4.8 shows the corresponding Arrhenius plot revealing that the n=5 member is a semiconductor with rather low overall conductivity (even lower than for the n=4 member), which may be related with the low relative density (74%). It should be noted that only the bulk conductivity is intrinsically related to the material, whereas the grain boundary response is more a function of the microstructure. In most of the cases the overall conductivity is dominated by the grain boundary response and therefore, the comparison between different members of the $\text{La}_4\text{Sr}_{n-4}\text{Ti}_n\text{O}_{3n+2}$ series should be done in terms of the bulk contribution.

In porous samples, the connectivity between grain is rather poor, with the presence of “necks”, rather than extended junctions that impede the transport of charged samples across the sample. Such lower relative density could also be related with the increased difficulty in sintering larger perovskite blocks regularly distributed and this is enough to cause a drop in the total conductivity. There are numerous investigations in the effect of porosity to the already low conductivity, which conclude that pores act as insulating regions because conduction cannot occur in “empty” areas [6].

The bulk conductivity of the $n=5$ member is similar to the bulk conductivity in the previous member $La_2Ti_2O_7$ at relatively low temperatures, i.e. 400-500°C, perhaps somewhat higher. The addition of one TiO_6 layer per block seems to facilitate the (electronic) conduction, which is also related with the gradual increase in the spacing between the insulating oxygen-rich planes.

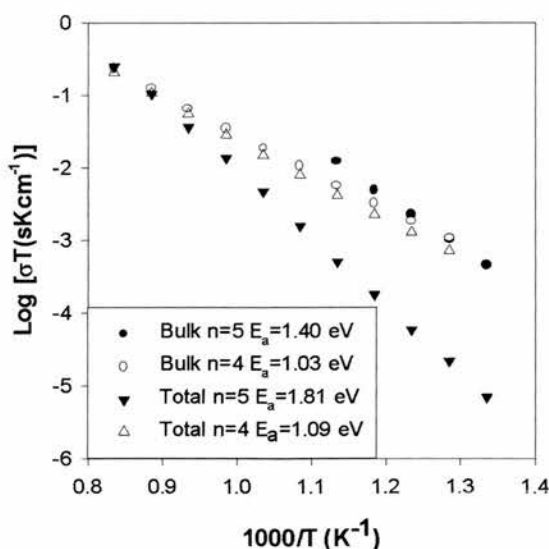


Figure 4.8. Arrhenius plots corresponding to the $n=5$ member. The bulk behaviour changes with adding one perovskite layer per block from ferroelectric to normal semiconductor (paraelectric).

4.2.1.3. $\text{La}_2\text{SrTi}_3\text{O}_{10}$ (n=6).

The responses of the n=6 member are dominated again by the grain boundary contribution, as a consequence of the low relative density (68%). Thus, at high temperatures only the grain boundary response is discernible (figure 4.9) whilst at low temperatures the bulk response becomes more important.

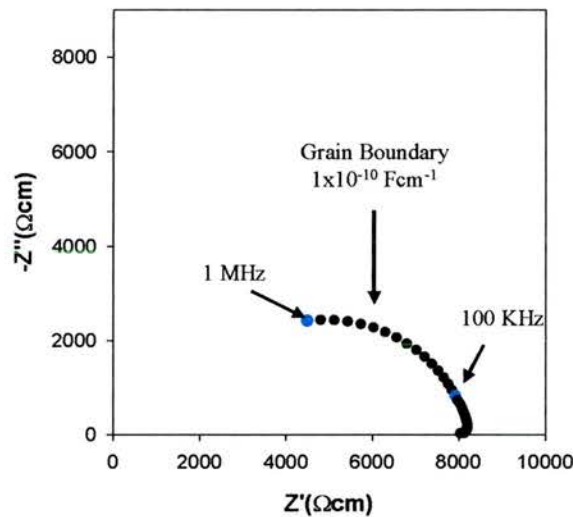


Figure 4.9. Geometry corrected Nyquist plot for the n=6 member at 1130 K. Only a single arc corresponding to the grain boundary response (1×10^{-10} F) is discernible.

A close look at the evolution of the bulk response with the temperature renders some relevant information. At temperatures below 500°C , the bulk response is clear with an associated response of approximately $1 \times 10^{-11} \text{ Fcm}^{-1}$, i.e. ferroelectric bulk. At higher temperatures, the response becomes gradually weaker to finally disappear at 649°C (figure 4.10), leaving a high frequency tail that could be interpreted as a bulk response. The presence of two different bulk responses must be attributed to the artificial background caused by the experimental setup as discussed in section 4.2.1.1 causing the latter. The background of the M'' plots was corrected

using the response collected at a temperature that did not show any indication of ferroelectric bulk, leaving a single peak per temperature (figure 4.11).

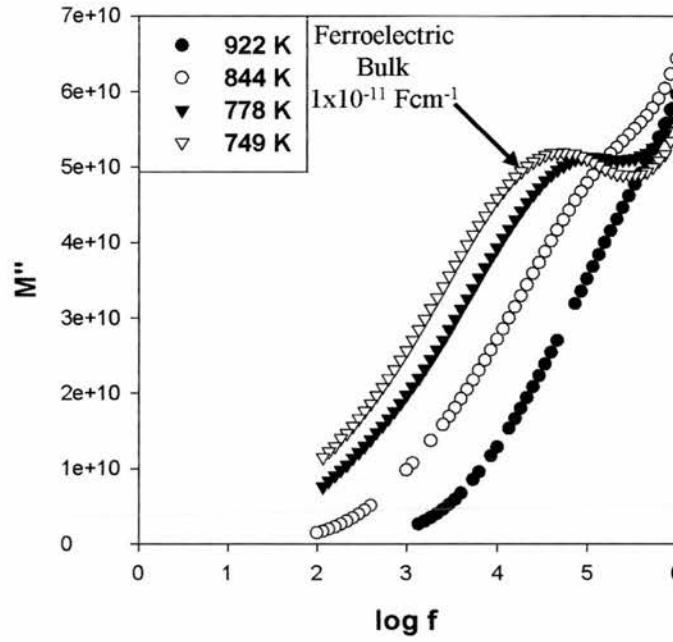


Figure 4.10. Spectroscopic plots of the imaginary modulus (M'') at different temperatures. The peak observed for the ferroelectric bulk (marked with arrow) gradually disappears with increasing the temperature.

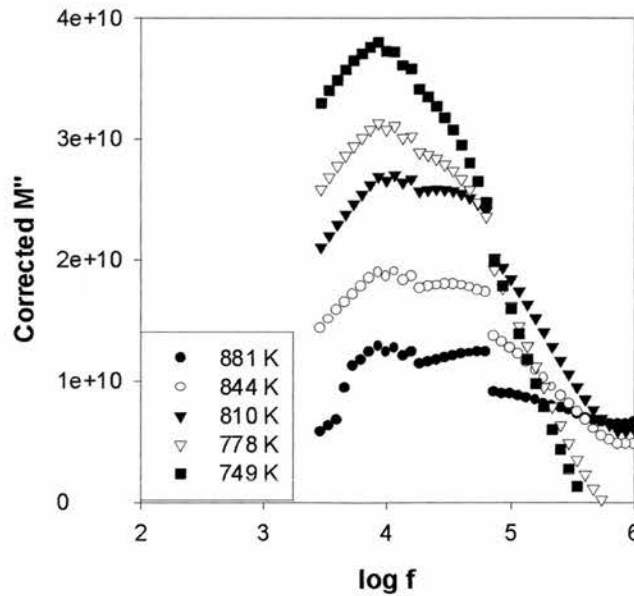


Figure 4.11. Corrected spectroscopic M'' plots. The capacitance associated to the process can be deduced from M''_{max} .

The capacitance presented a strong dependence with temperature as shown in figure 4.12 and it seems that the material suffers a ferroelectric transition at not so high temperatures. However the distortion introduced by the instrument at high frequency does not allow calculating the T_c accurately. A more careful investigation in the temperature range 300-700°C, looking at higher frequency values is required, although the ferroelectric nature of this phase is clear.

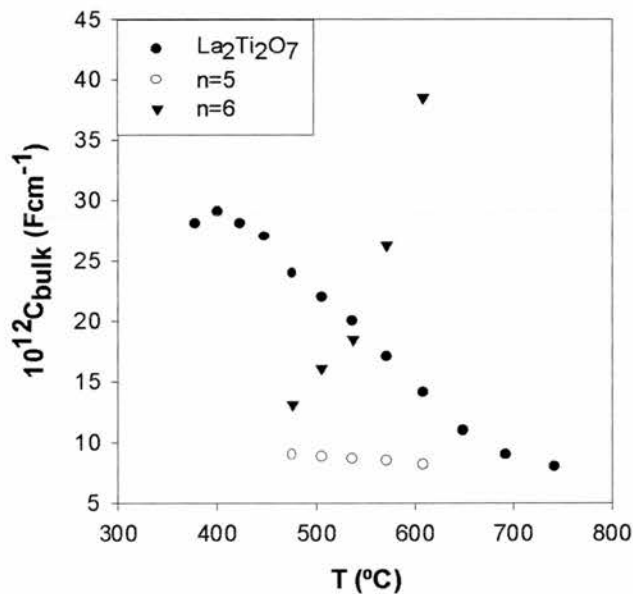


Figure 4.12. Bulk capacitance vs. temperature plots for the n=4, 5 and 6 members.

Ferroelectricity seems evident for the n=6 member and also it seems that a ferroelectric transition takes place around 650-700°C.

The Arrhenius plot reveals that the overall conductivity is low and comparable to that of the n=5 member due to the very high porosity in both cases ($\approx 35\%$) (figure 4.13). As a consequence, the bulk response is more important because it is not affected by porosity. The bulk conductivity in the n=6 member is higher than that of the n=4 and n=5. These results indicate that the conductivity increases with increasing size of the perovskite blocks.

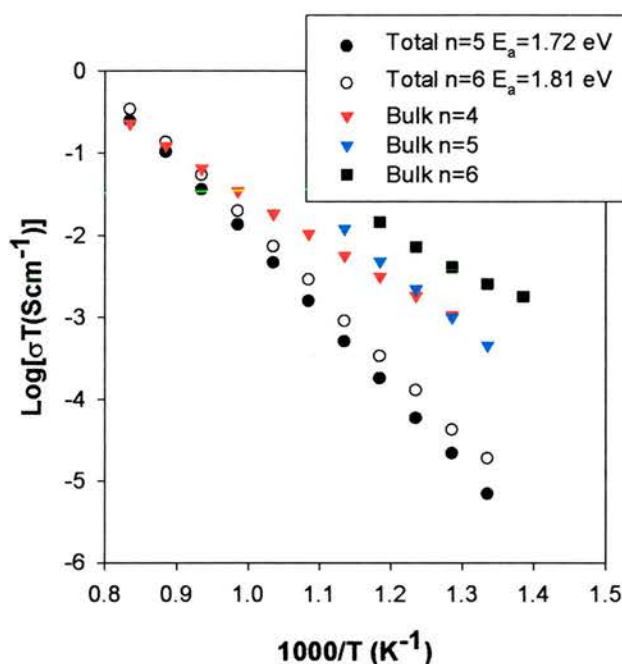


Figure 4.13. Arrhenius plots corresponding to the n=5 and 6 members. Bulk conductivity seems to increase with increasing the size of the perovskite slabs.

The low conductivity in the layered phases could be explained in terms of the oxygen rich layers impeding the transport of charge species, resulting in very low performances, no matter number of perovskite layers per block. At this point, no diffusion phenomena were detected in the low frequency range. Diffusion in oxide ion conductors is characterised by a response with slope of 45° in the impedance complex plane with rather high capacitance associated ($>10^{-4} \text{ Fcm}^{-1}$). Therefore oxygen ion conductivity seems negligible compared to the electronic contribution on the layered phases possibly because the excess oxygen is tightly bound to its crystallographic sites and hence, is not mobile at all.

4.2.1.4. $La_2Sr_2Ti_4O_{13}$ (n=8).

In the case of the n=8 and 10 compositions, the situation is somewhat different because they are not single phases as widely discussed in chapter 3. Therefore their responses might not be comparable to the previous layered phases described above. As for the n=8 member, the responses dominated by the grain boundary contribution (typically $1 \times 10^{-10} \text{ Fcm}^{-1}$) especially at high temperatures (60% dense) as shown in figure 4.14.a. At lower temperatures the bulk contribution becomes more important and causes the small lump observed in the high frequency range with an assigned capacitance of approximately $5 \times 10^{-12} \text{ Fcm}^{-1}$ (figures 4.14.b and 4.14.c).

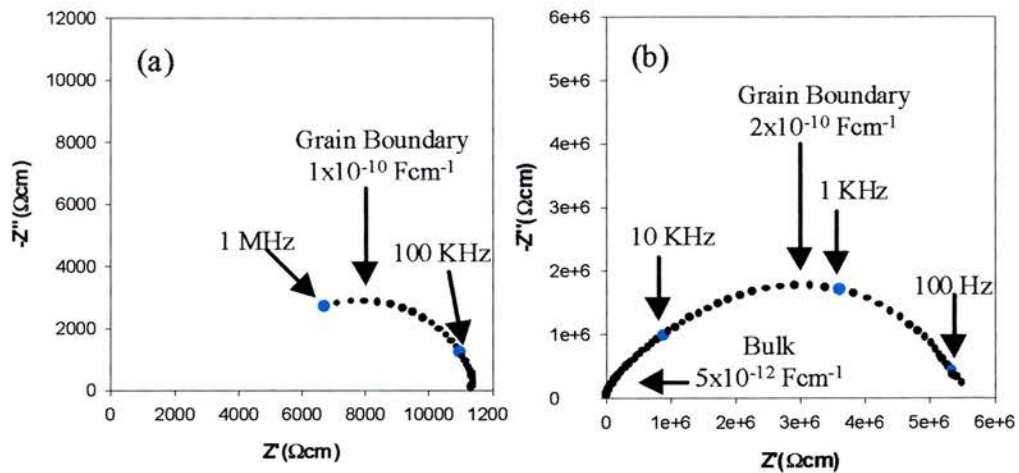


Figure 4.14. Geometry corrected Nyquist plots for the n=8 member at 1170 K (a) and 844 K (b).

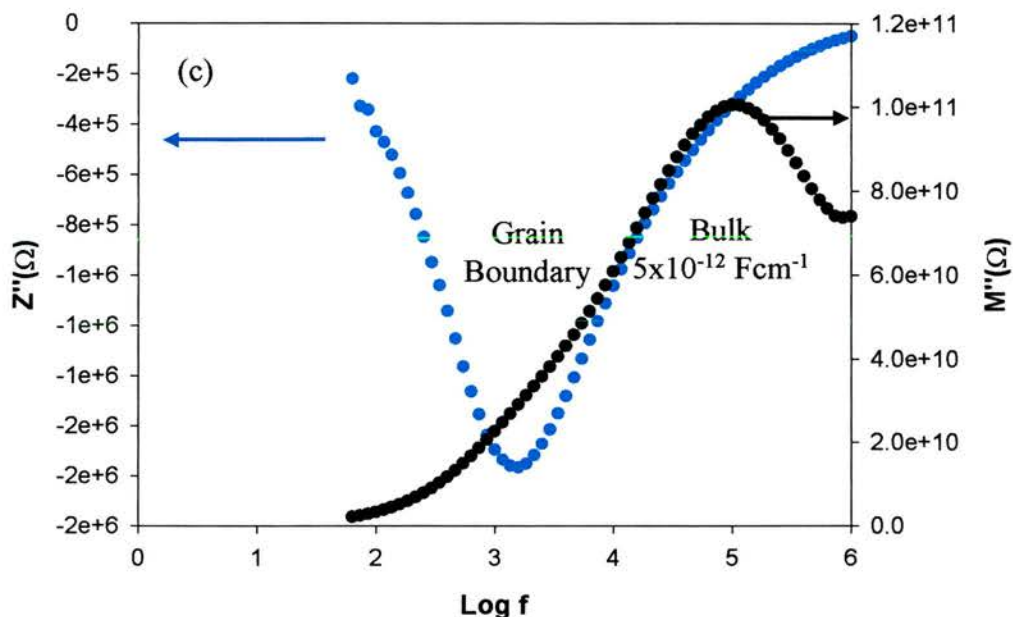


Figure 4.14.c. Spectroscopic plot of Z'' and M'' obtained at 844 K for $n=8$. The capacitance associated with the bulk is $5 \times 10^{-12} \text{ Fcm}^{-1}$

Although the capacitance assigned to the bulk processes is typical of paraelectric materials, i.e. order of magnitude of $10^{-12} \text{ Fcm}^{-1}$, studies of the temperature dependence of the capacitance reveals that it gently decreases with the temperature as occurred for $\text{La}_2\text{Ti}_2\text{O}_7$. The capacitance values are high for “normal” bulk responses and that could be related with presence of mixture of phases with some of them being monoclinic (ferroelectric) whereas some others are orthorhombic (non-ferroelectric) (figure 4.15).

The total conductivity is quite low, limited by the very low relative density (60%) and in the same order of magnitude as the previous members as shown on the Arrhenius plot (figure 4.16). Again, the most important features can be found on the bulk dependence with temperature, although the presence of irregular intergrowths of perovskite blocks impedes straightforward interpretations of the results. In this case

the conductivity drops compared to the lower members. This is reverse of earlier trend and that could be related with the $n=8$ and 10 compositions being irregular intergrowths of layered and cubic phases. This would imply that even at low concentration there are long-range crystallographic shears that result in very poor performances.

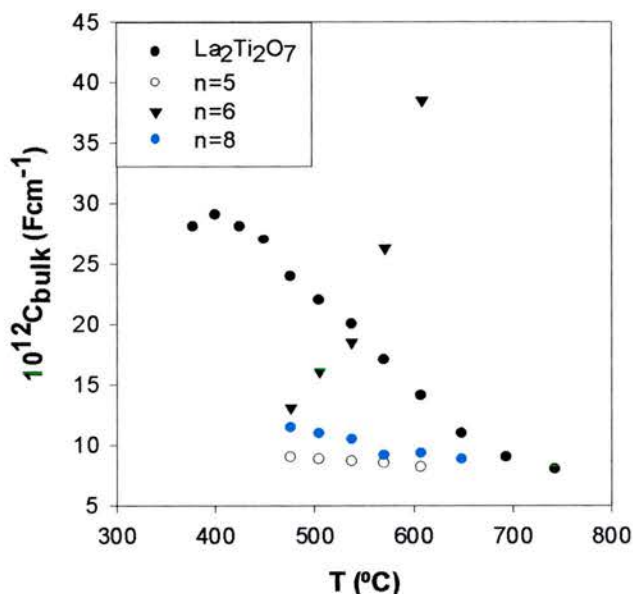


Figure 4.15. Bulk capacitance vs. temperature plot for the $n=4, 5, 6$ and 8 members. In the case of the $n=8$ member, the high capacitance associated with the bulk could be due to mixture of phases.

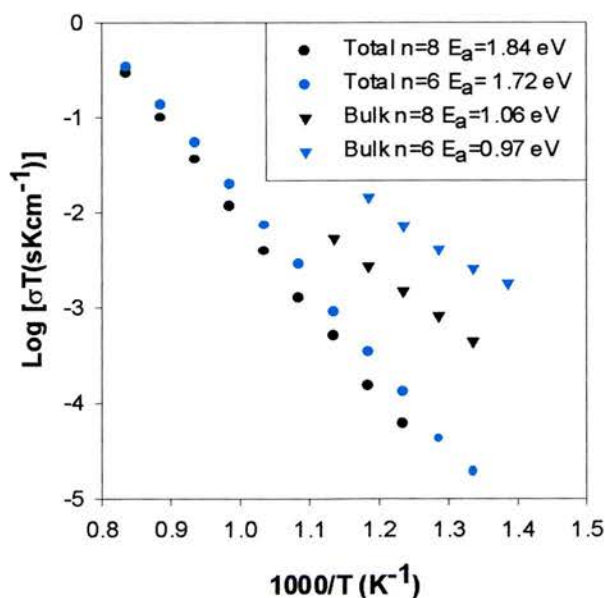


Figure 4.16. Arrhenius plots for the $n=6$ and 8 members. The low total conductivity may be caused by the fairly high porosity of the samples analysed.

4.2.2. Cubic phases.

4.2.2.1. $La_2Sr_4Ti_6O_{19}$ (n=12).

Although the grain boundary (typically 4×10^{-9} F) processes once again dominated the responses, the presence of the bulk (1×10^{-11} Fcm⁻¹) was discernible at low temperatures (figure 4.17), especially in the spectroscopic plot of the imaginary contribution of the electric modulus (M'') (figure 4.18). The resistance of the bulk was estimated from the peak position on such representation. The high values of the capacitance associated to the bulk are close to the typical values reported in the literature for materials with high dielectric constant.

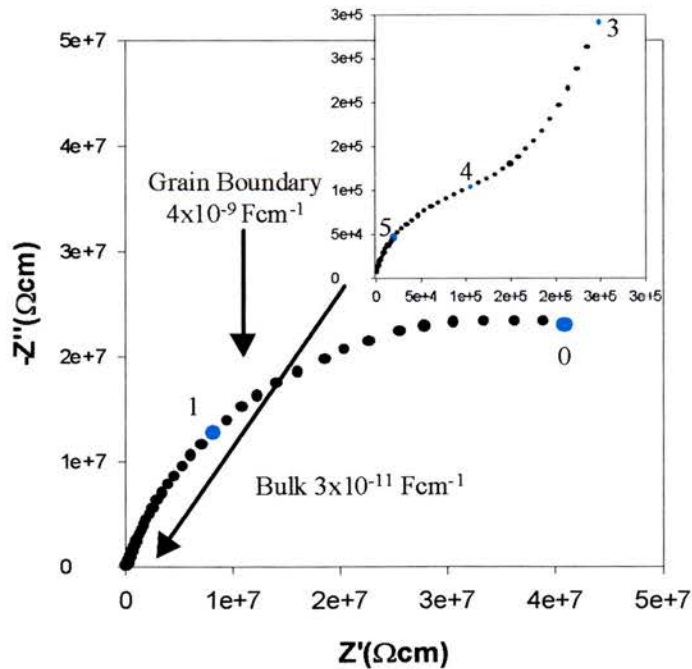


Figure 4.17. Nyquist plot for the n=12 member at 258°C measured in static air. The inset shows the response of the ferroelectric bulk in high frequency range. Numbers indicate $\log f$.

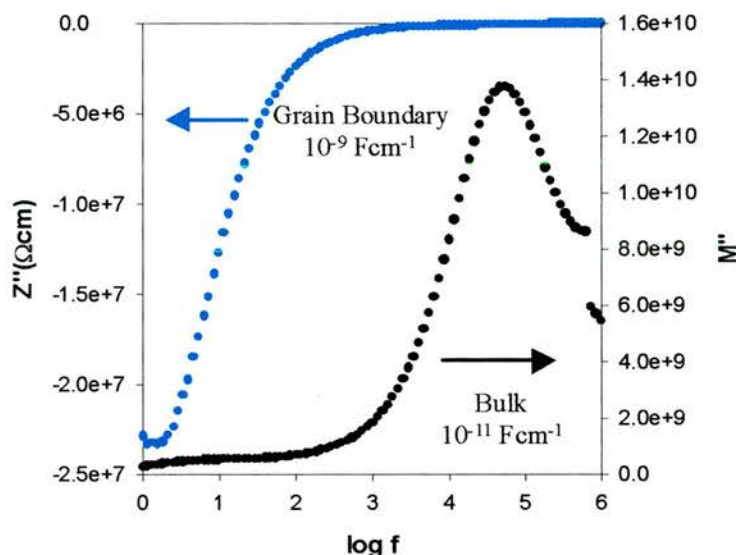


Figure 4.18. Spectroscopic for the imaginary impedance and modulus for the $n=12$ member at 258°C in air, highlighting the presence of the bulk response in the high frequency range.

The corresponding Arrhenius plot revealed a drastic change compared to the layered phases, i.e. there is an increase on the total conductivity of one order of magnitude (1.7 mScm^{-1} at 1198 K) together with an important drop in the activation energy from 1.8 eV to 1.3 eV (figure 4.19). The most likely interpretation for that change can be found in the structural changes observed from the “layered” members to the $n=12$ member. The crystallographic shears accommodating excess oxygen do not exist anymore. As discussed in the previous chapter, excess oxygen appears to be accommodated in short-range linear defects randomly distributed instead of the extended shears for the lower members. Thus, the insulating barriers do not appear and hence, the conduction paths are not so badly interrupted for members with $n \geq 12$. Furthermore, the bulk shows a rather high conductivity compared with the layered phases.

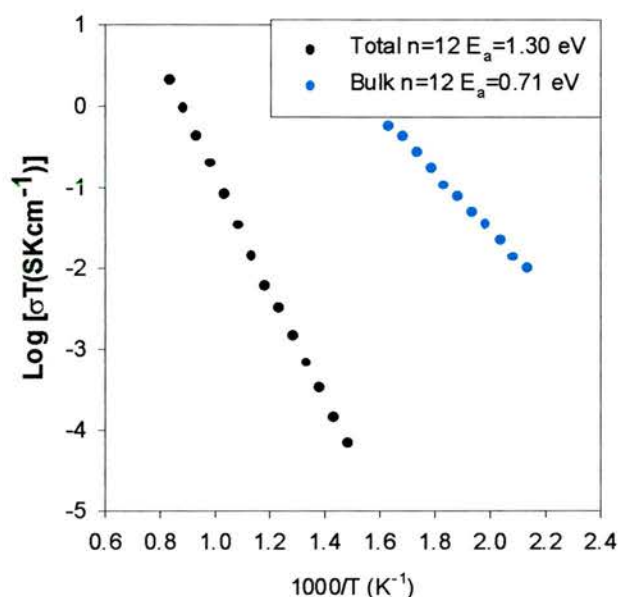


Figure 4.19. Arrhenius plots corresponding to the n=12 member in air. The high bulk conductivity is a clear evidence of the insulating nature of the grain boundaries in these phases.

Due to the higher conductivity found in this compound, a more exhaustive investigation was performed on the n=12 member, including studies at different densities and oxygen partial pressures as described next.

As mentioned above, from the Nyquist plots it may be seen that the grain boundary dominates the response of this material, and therefore better conductivity values could be obtained by improving the connectivity between grains. In this respect, studies at different relative densities were carried out revealing that indeed the conductivity increases with increasing relative density by almost one order of magnitude and also the E_a decreased (figure 4.20). This could be explained by the changing nature of the two types of grain boundaries, changing from showing a very good contact between grains at high relative densities and worse connectivity in less dense samples as shown on SEM images (figure 4.21).

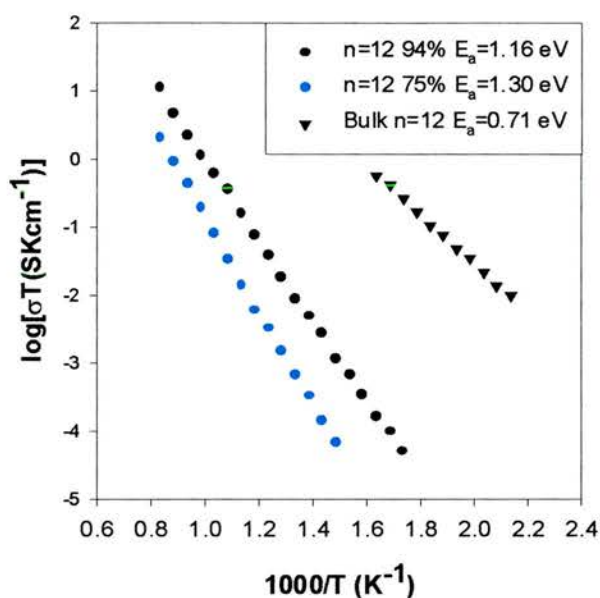


Figure 4.20. Comparative Arrhenius plots for $La_2Sr_4Ti_6O_{19}$ at 75% and 94% relative density.

Higher density yields an improvement in one order of magnitude of the conductivity. Bulk conductivity is obviously independent of the relative density.

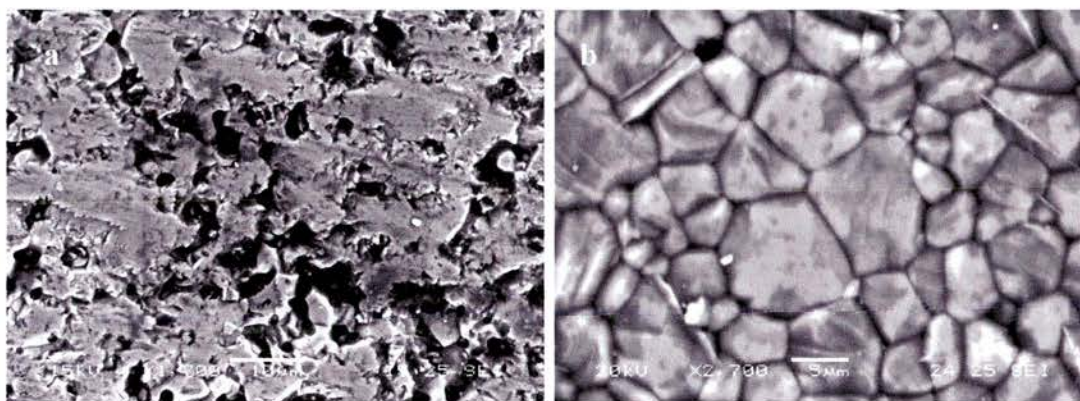


Figure 4.21. SEM images showing the microstructure of the $n=12$ member at 75% (a) and (94 %) of relative density respectively. A much better connectivity of the grains is found in the latter.

4.2.2.2. Impedance spectroscopy in different atmospheres in $n=12$.

A pronounced dependence of the total conductivity with oxygen partial pressure was found in the present case, showing features typical of an n-type conductor, i.e. higher conductivity at lower oxygen partial pressure. The activation energy calculated from the corresponding Arrhenius plots (figure 4.22) revealed the

same tendency, and it decreased as the oxygen partial pressure ($P(O_2)$) did so, from 1.3 eV for the sample measured in air to 0.3 eV for the sample measured in dry argon. The decrease in the activation energy in addition to the increase in conductivity at lower $P(O_2)$ must be explained by the gradual reduction of Ti^{4+} to Ti^{3+} . The more reducing the conditions, the more Ti^{3+} (larger number of charge carriers) is present in the sample, which leads to an enhancement of the electronic conductivity. In fact, TGA experiments performed in samples pre-reduced in the atmospheres used in impedance spectroscopy revealed that the loss of oxygen is gradually larger for the more reducing conditions, which indicates the formation of more Ti^{3+} . Experiments performed in more reducing conditions (wet and dry 5% H_2 /Ar) confirm n-type conductivity for the n=12 member.

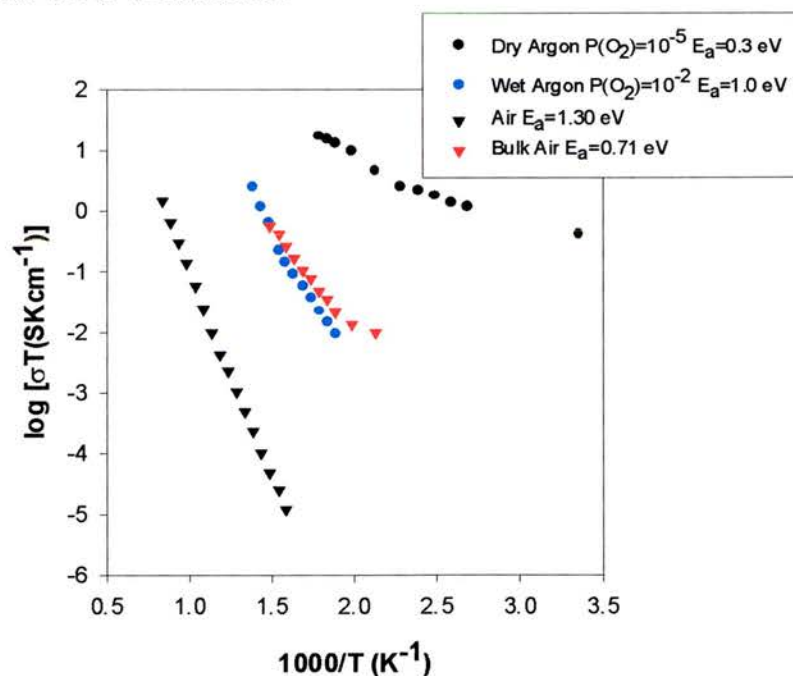


Figure 4.22. Arrhenius plots for $La_2Sr_4Ti_6O_{19}$ in air, wet Ar and dry Ar.

In the Nyquist plots of the sample measured in dry Ar at room temperature, it is possible to clearly observe two semicircles. The first corresponds to a typical grain boundary response ($C=1 \times 10^{-9} \text{ Fcm}^{-1}$) whilst the other was assigned to an electrode

response ($C=10^{-4} \text{ Fcm}^{-1}$), possibly related to a Schottky barrier (figure 4.23.a) occurring in the interface of the Pt electrode and the material studied. Schottky barriers have been described in the literature for SrTiO_3 [7]. One might argue that the electrode response observed under for the $n=12$ member measured in Ar can be related with diffusion phenomena. Nevertheless the diffusion processes are characterised by a 45° slope in the low frequency range of the impedance complex plot, which is not the case. It should be considered that at room temperature diffusion can not have such good values. At higher temperatures the electrode response is less important (figure 4.23.b) and above 300°C only the grain boundary can be observed. In wet Ar, similar responses were observed and sometimes it was possible to distinguish between the responses for the bulk and the grain boundary using the spectroscopic plots of the complex impedance (Z'') and complex modulus (M'') similar to those of the experiments performed in air.

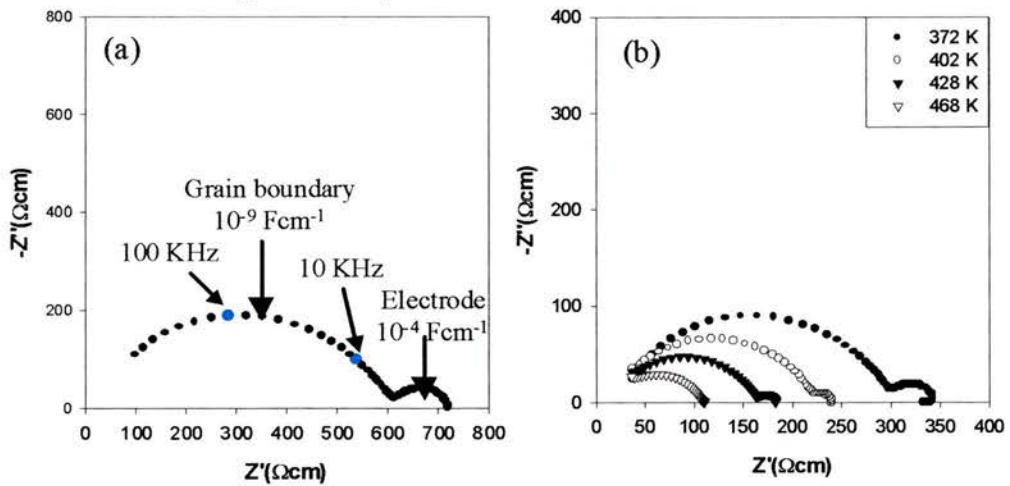


Figure 4.23. Geometry corrected Nyquist plots for the $n=12$ member measured in flowing dry Ar at room temperature (a) and a series of temperatures (b) where the electrode response becomes gradually less important. Correction for the inductance due to the wires of the jig is included.

4.2.2.3. $La_2Sr_5Ti_7O_{22}$ (n=14).

A similar situation was found for the n=14 member. As is common in this series of compounds, the major contribution came from the grain boundaries, even though the relative density was 99%. This is further evidence of the insulating nature of the grain boundaries (figure 4.24).

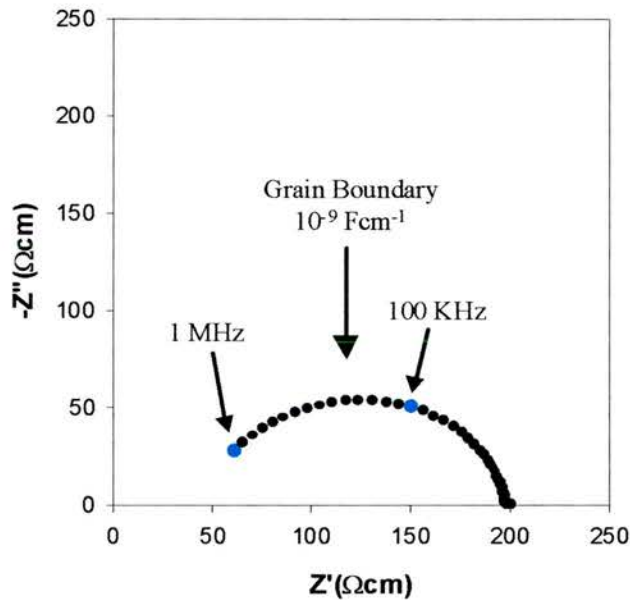


Figure 4.24. Geometry corrected Nyquist plot for the n=14 member at 981 K.

The corresponding Arrhenius plot revealed that the (overall) conductivity was increased by two orders of magnitude in comparison to the n=12 member, i.e. 0.15 Scm^{-1} at 1198K (figure 4.25). Such a large increase in the conductivity may be explained in terms of the higher relative density, which necessarily implies a better connectivity between grains. Moreover, higher density slows the reduction-oxidation processes down. It should be noted that the very high sintering temperatures used during the synthesis of these phases (typically 1500°C) provoke their partial reduction. The oxygen is almost fully recovered during the cooling down process to room temperature in the case of porous samples, because the diffusion is easier. On

the contrary, in very dense samples the diffusion of oxygen is not facilitated and therefore in the process of cooling down, dense samples remain partially reduced. In other words, there are more charge carriers due to the presence of Ti^{3+} formed at high temperatures. That could certainly explain the higher overall conductivity observed for the $n=14$ member of the $\text{La}_4\text{Sr}_{n-4}\text{Ti}_n\text{O}_{3n+2}$ series. As already pointed out, data from the bulk give straight information from the nature of the material rather than information relying on the microstructure. Unfortunately, it is not possible to get any information from the bulk conductivity because the relaxation frequency was out of the range measured. Presumably, the bulk conductivity in $n=14$ is similar to that in $n=12$.

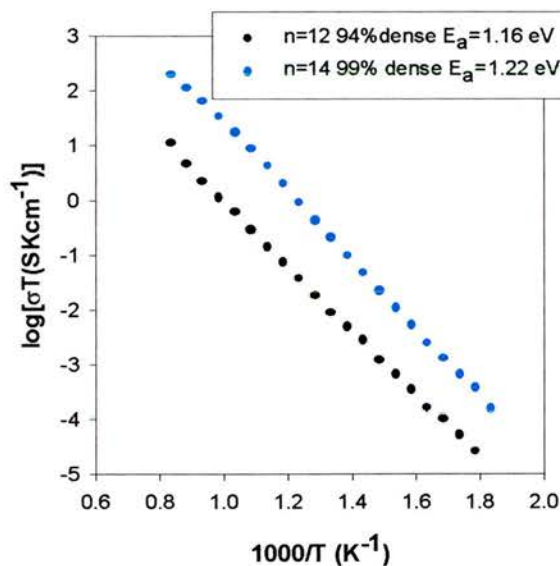


Figure 4.25. Comparative Arrhenius plots corresponding to the $n=12$ and $n=14$ members.

Conductivity is one order of magnitude larger for the latter.

4.2.2.4. SrTiO_3 ($n=\infty$).

The $n=\infty$ member obviously showed analogous behaviour to the $n=12$ and 14 members with the difference that, additionally, an electrode response was present with an assigned capacitance of $2 \times 10^{-6} \text{ Fcm}^{-1}$. This may be due to a Schottky barrier in the

interface between the metallic electrodes and $SrTiO_3$ as occurred for the $n=12$ member under argon and reported in the literature [7]. Figure 4.26 shows a typical complex plot (a) and the corresponding M'' and Z'' spectroscopic plots for $SrTiO_3$ at $505^\circ C$. Capacitance of $6 \times 10^{-12} \text{ Fcm}^{-1}$ was assigned to the bulk, which is in agreement with the high dielectric constant reported for single crystals and ceramics of $SrTiO_3$ [8-9].

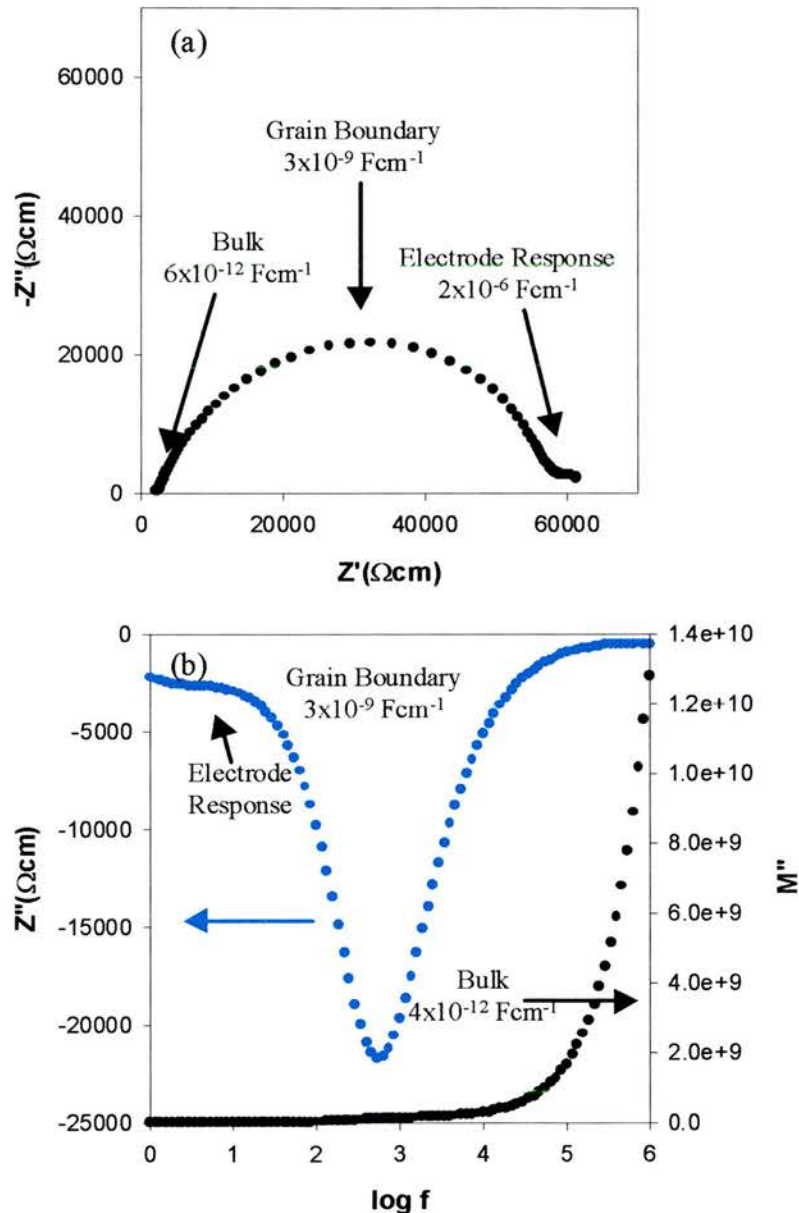


Figure 4.26. Geometry corrected complex impedance plot for $SrTiO_3$ at 749 K (a) and the corresponding M'' and Z'' spectroscopic plots showing the presence of three electrochemical processes: bulk, grain boundary and electrode.

A question that may arise when observing the Arrhenius plot (figure 4.27) is why the conductivity for $SrTiO_3$ is lower than for the $n=14$ member when the relative density is also 99%. The presence of local defects seems to facilitate the reduction. The oxygen on those locations is more accessible and therefore the $n=14$ member will have more charge carriers under the same conditions. However, the most interesting feature is that the bulk conductivity for the $n=12$ member is significantly higher than for $SrTiO_3$, which emphasises the potential of the former as fuel cell material if the limitations arising from the grain boundaries are reduced.

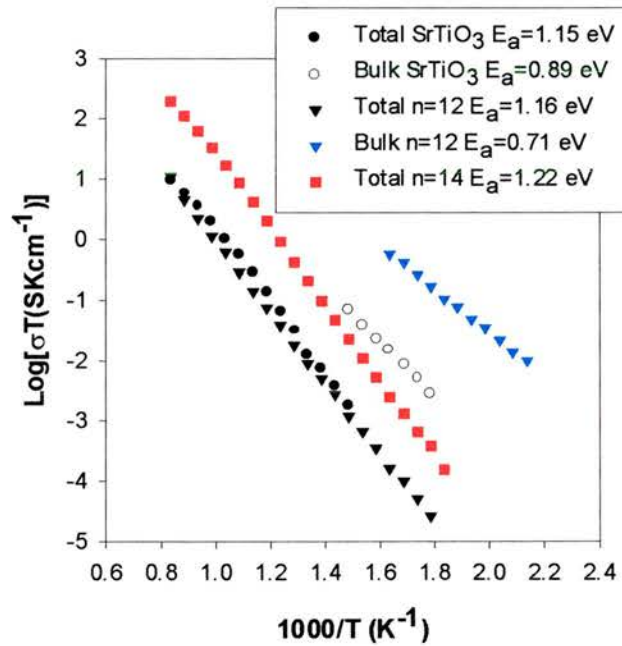


Figure 4.27. Arrhenius plots corresponding to the $n=12$ and 14 members and total and bulk conductivity for $SrTiO_3$.

It is very important to note the quite high conductivity found for the bulk in $SrTiO_3$, which is further evidence of the insulating nature of the grain boundaries.

4.2.3. Conclusions.

From the Arrhenius plot corresponding to the total conductivity it can be extracted that these phases present semiconducting behaviour in air, i.e. the conductivity is thermally activated. There are also other features of interest, such as the clear distinction between “layered” phases and “cubic” phases, the conductivity being much higher in the latter (figure 4.28).

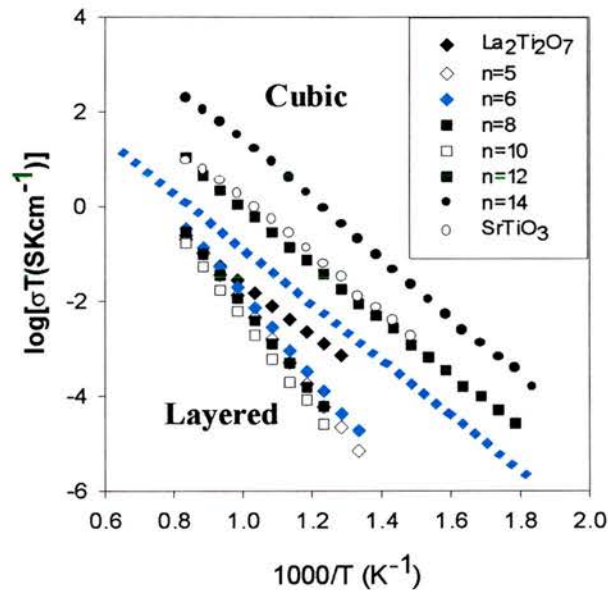


Figure 4.28. Arrhenius plots of the $\text{La}_4\text{Sr}_{n-4}\text{Ti}_n\text{O}_{3n+2}$ series.

The conductivity is also observed to drop for the $n=6$ and $n=8$ compared to $\text{La}_2\text{Ti}_2\text{O}_7$, which could be explained in terms of the porosity increasing with advancing to higher n . That would also cause the increase of E_a with increasing the porosity (table 4.1). Thus, porous samples would also explain the grain boundary response being dominant in complex impedance plots. In fact, the poor grain boundary response masks the bulk response and typically only a single arc with an associated capacitance of 10^{-10} - $10^{-11} \text{ Fcm}^{-1}$ is observed in the Nyquist plots of the layered members. Nevertheless, at lower temperature some deviations from the ideal

response are observed, which are related with the electrochemical response due to the bulk as already discussed for each individual member of the $\text{La}_4\text{Sr}_{n-4}\text{Ti}_n\text{O}_{3n+2}$ series.

For members with $n > 11$, the conductivity increases quite dramatically due to the lack of extended crystallographic shears regularly distributed in the structure, which act as insulator barriers. The responses are dominated by the grain boundaries despite the high relative densities, which is clear evidence of their insulating nature. Nevertheless, it seems that in the $\text{La}_4\text{Sr}_{n-4}\text{Ti}_n\text{O}_{3n+2}$ family the best properties are within the non-layered phases.

n	Density (gcm^{-3})	Pellet density (gcm^{-3})	Relative density (%)
4	5.79	4.95	85
5	5.56	4.11	74
6	5.45	3.68	68
8	5.34	3.08	60
12	5.25	4.95	94
14	5.22	5.15	99
∞	5.10	5.11	99

Table 4.1. Relative densities of the $\text{La}_4\text{Sr}_{n-4}\text{Ti}_n\text{O}_{3n+2}$ series.

One might argue that total conductivity is dominated in most of the cases by the grain boundary contribution and thus, is not giving information from the material itself, but information about the microstructure instead. The Arrhenius plots for the bulk conductivity show the same general trends observed before, with higher conductivity for the cubic phases (figure 4.29). As for the layered phases, it seems that the conductivity increases with increasing the number of layers in the single phases in the case of the $n=4, 5$ and 6 members. The $n=8$ composition do not follow that pattern, mainly because their responses come from phases intergrowing irregularly. This causes shortage of reliable data.

The low bulk conductivity in the layered phases could be explained in terms of the crystallographic shears (oxygen rich planes) impeding the transport of charged species as mentioned for the $n=4$ member. Additionally, the preparation of samples by classic solid state reaction causes such insulating barriers to be distributed randomly in every possible direction as a consequence of the different orientation between grains.

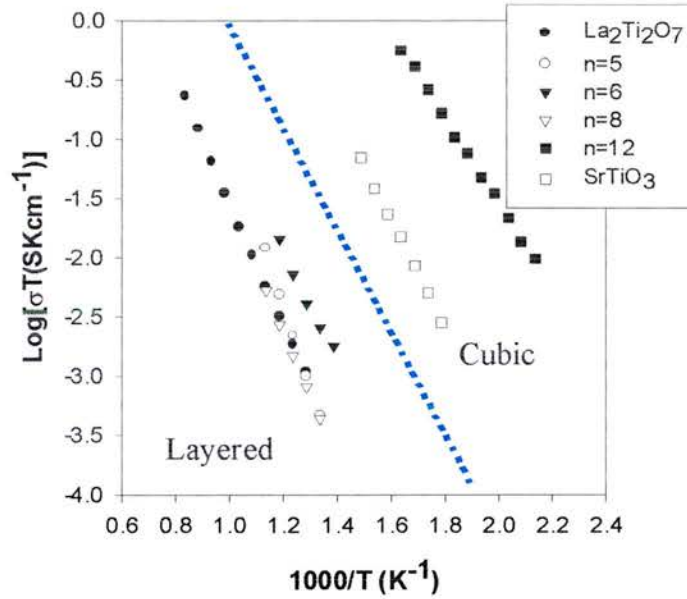


Figure 4.29. Arrhenius plot of the bulk conductivity for the $\text{La}_4\text{Sr}_{n-4}\text{Ti}_n\text{O}_{3n+2}$ series. Once again the cubic phases present higher conductivity.

Figure 4.30 shows the evolution of the activation energy throughout the series. There is no simple correlation between the experimental points, although the activation energy seems to be lower for the cubic phases.

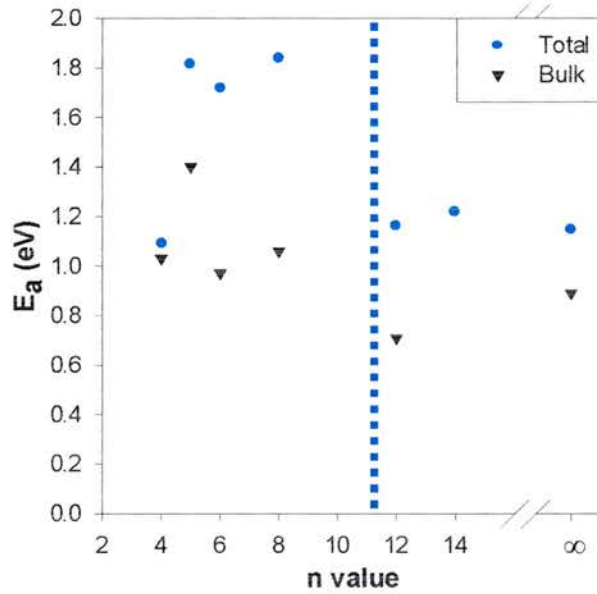


Figure 4.30. Plot of the activation energy vs. n in the $\text{La}_4\text{Sr}_{n-4}\text{Ti}_n\text{O}_{3n+2}$ series.

Studies on the temperature dependence of the bulk capacitance reveal the ferroelectric nature of the $n=4$ and $n=6$ members. In the case of the $n=5$ member, the centrosymmetric unit cell renders a non-ferroelectric phase. As for higher n members, the disorder reduces the tendency to be ferroelectric phases. Of special interest is the $n=6$ member because a ferroelectric transition seems to occur at intermediate temperatures and this could be attractive for technological applications.

The grain boundary capacitances generally observed indicates that fairly well ordered grain boundaries are formed, despite the fairly large porosity (up to 40%) of the sample. There is some depression of the semicircle which may relate to porosity; however, the most important role of the porosity is to facilitate gas diffusion and hence reduction of the grain boundaries. High porosity may also be responsible for the fairly low ferroelectric bulk capacitance found for the $n=4$ member.

Studies carried out in a variety of atmospheric conditions revealed that these compounds are basically n-type electronic conductors, i.e. higher conductivity with decreasing oxygen partial pressure. That could imply very good electrical properties at the very reducing anode operating conditions. In this respect, the next sections deal with the electrical properties of the n=12 member at very low $\text{P}(\text{O}_2)$.

As for the diffusion phenomena, no evidence of ionic transport were found in the impedance spectroscopy studies performed. However there exists the possibility that some oxide ion conductivity occurs being masked by the major contribution. In order to study minor ionic contributions to the total conductivity, techniques such as oxygen permeability or faradic efficiency measurements are strongly recommended and they could mean a very interesting project for the near future. Preliminary oxygen permeability measurements carried out in oxidising conditions uncovered a quite low ionic contribution of about $5 \times 10^{-5} \text{ Scm}^{-1}$ at 1000°C for the n=12 member. Nevertheless studies performed in reducing conditions are also required.

4.3. Four terminal techniques.

Under more reducing conditions, i.e. flowing 5% H_2/Ar , the conductivity of the n=12 member was higher than the Pt paste used to paint the electrodes in IS. Therefore, four terminal techniques were used to overcome such limitation. Thus, the conductivity of $\text{La}_2\text{Sr}_4\text{Ti}_6\text{O}_{19.5}$ was evaluated as a function of temperature (section 4.3.1) and $\text{P}(\text{O}_2)$ (section 4.3.2).

4.3.1. Temperature dependence.

The temperature dependence of the conductivity for the $n=12$ member in reducing conditions was evaluated by measuring in dry and wet flowing H_2/Ar atmospheres (figure 4.31). The samples were initially annealed at high temperature (950°C) until equilibrium was achieved. In dry H_2/Ar , a metallic behaviour was found with conductivity dropping from 60 Scm^{-1} at room temperature to 40 Scm^{-1} at 950°C . These values are somewhat higher than the values reported for the A-site deficient perovskites $\text{Sr}_{1-3x/2}\text{La}_x\text{TiO}_{3-\delta}$ [10]. The interstitial oxygen in $\text{La}_2\text{Sr}_4\text{Ti}_6\text{O}_{19-\delta}$ placed in randomly distributed oxygen shears (linear defects) might be easily removed under reducing conditions and therefore the reduction of Ti^{4+} to Ti^{3+} is favoured. As a consequence there is more Ti^{3+} for the same $P(\text{O}_2)$, which explains the higher values in conductivity found. These results also revealed a discrepancy with recent studies by O. Marina *et al.* that have reported a semiconducting behaviour in similar compositions prepared in air [2], probably due to the longer time under reducing conditions used to achieve the complete reduction of the sample in our experiments. In addition, our results agree with those reported in previous studies in the $\text{La}_{1-x}\text{Sr}_x\text{TiO}_3$ system, where metallic behaviour was observed in ultra-reducing conditions [11].

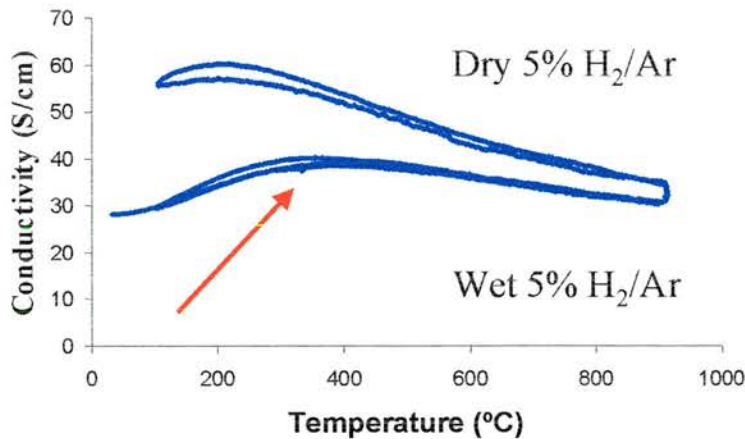


Figure 4.31. Temperature dependence of the conductivity in both dry and wet 5% H_2/Ar .

Furthermore, the sample measured in wet H_2/Ar showed the presence of an insulator-metal transition at around 400°C . This metal-insulator transition could have a number of origins, i.e. that the distribution of Ti^{3+} changes in a similar fashion as occurs in Ti_4O_7 (Magnéli phases) [12]. At temperatures below 400°C , Ti^{3+} is distributed forming long-distance couples ($\text{Ti}^{3+}\text{-O-Ti}^{3+}$) that disappear at higher temperatures leading to Ti^{3+} randomly distributed in the structure. Ordering in couples leads to a partial localisation of electrons avoiding in this way the formation of a metallic band due to the presence of some discrete energy levels. At temperatures above 400°C , the Ti^{3+} are not in couples anymore, facilitating in this way the formation of the metallic band. Alternatively, this metal-insulator transition could be understood in terms of a change from dominant metallic to dominant semiconductor on cooling. The two components could be both in the bulk or it could be a semiconducting grain boundary and a metallic grain. Thus at high temperature the grain component would dominate, whereas at low temperature the grain boundary is dominating. The last hypothesis could certainly agree with the observed insulating nature of the grain boundary in very dense $n=12$ and $n=14$ members. The lower conductivity observed in wet H_2/Ar might be explained by the fact of partial oxidation

(higher $\text{P}(\text{O}_2)$) decreasing the amount of Ti^{3+} leading to a lower conductivity due to the smaller number of charge carriers.

4.3.2. Conductivity as a function of the $\text{P}(\text{O}_2)$.

Measurements in a range of $\text{P}(\text{O}_2)$ at different temperatures could also help in the search of any traces of ionic contributions to the total conductivity as a consequence of changes in the slope of the $\log \sigma$ vs. $\text{P}(\text{O}_2)$ plots.

The electrical tests under controlled $\text{P}(\text{O}_2)$ were performed on $\text{La}_2\text{Sr}_4\text{Ti}_6\text{O}_{19.6}$ in the range from 10^{-5} atm down to 10^{-20} atm at 900, 950 and 1000°C. The results do confirm that this phase is in fact an n-type electronic conductor as indicated from the slopes of $-1/4$ (figure 4.32).

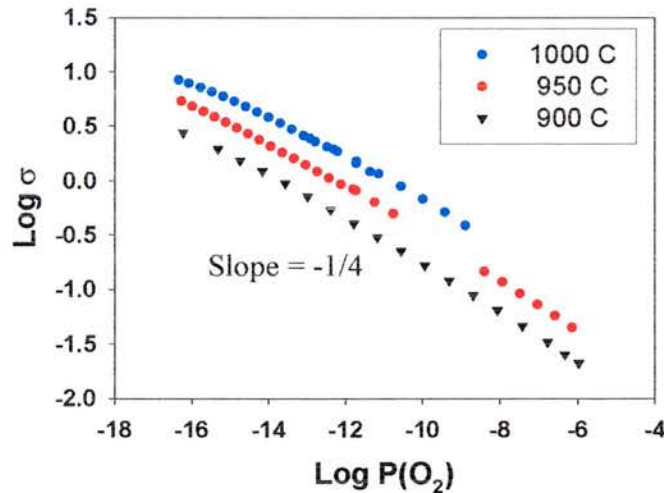


Figure 4.32. Variation of the conductivity vs. oxygen partial pressure, which confirms n-type electronic conductivity for the $n=12$ member in reducing conditions.

No evidences of changes in the conduction mechanism from n-type to p-type were distinguishable even for the higher $\text{P}(\text{O}_2)$ data. P-type conduction is commonly

associated with molecular oxygen filling vacancies. Ti prefers to be six co-ordinated and therefore transport of vacancies is not favoured at all.

As stated before, the presence of interstitial oxygen within the perovskite framework might possibly enhance the ionic transport. Nevertheless, no evidence of ionic transport was found by means of ac impedance, which would indicate the preference of Ti to be hexa-coordinated and thus the transport of charged species other than electrons is impeded. Thermogravimetric analysis can be used in order to estimate the concentration of protonic defects, because they are created mainly by dissociative water uptake. However, no evidence of water uptake was observed for $\text{La}_2\text{Sr}_4\text{Ti}_6\text{O}_{19.8}$ in any of the atmospheres used.

4.3.3. Thermopower measurements.

Thermopower measurements are usually carried out under controlled $\text{P}(\text{O}_2)$ atmospheres to investigate the charge carrier concentration and also the mobility. This technique is based on the Seebeck effect, i.e. the generation of a difference in the electrical power after imposing a temperature gradient [13]. Seebeck coefficients are defined as:

$$\alpha = \frac{-k}{e} \ln\left(\frac{N}{n}\right) \text{ [equation 4-3]}$$

where N is the density of states of either the conduction band (n-type) or the valence band (p-type). On the other hand n is the concentration of electronic carriers either electrons [e^-] or holes [p^\bullet].

The studies performed on the n=12 member confirm the n-type character of this phase as extracted from the negative values.

On the α vs. $\log \sigma$ plot (figure 4.33), there is a quite interesting feature taking place at quite low oxygen partial pressure: the product of the charge carrier concentration and the charge carrier mobility does not seem to be affected by the temperature. Knowing that

$$\sigma = ne\mu \text{ [equation 4-4]}$$

where n is the number of carriers and μ the mobility. Then, substituting on equation [4-3]

$$\alpha = -\frac{k}{e} [\log Ne\mu - \log \sigma] \text{ [equation 4-5]}$$

Thus, from figure 4.33 the slope is a constant k/e and the intercept with the y-axis gives an estimate of both mobility and concentration of charge carriers. At very low $P(O_2)$ the slope changes indicating that there are at least two intercepts per temperature and hence the model is not simply applied, which may be interpreted as a metal to insulator transition taking place. Hence, in the more conducting region, i.e. lower $P(O_2)$ since this material is an n-type conductor, the different lines converge into just one. The extrapolation of that section at very low $P(O_2)$ would give the same intercept independent of the temperature.

The transition temperature is different from one experiment to another, and there are a number of factors that may cause this: slightly different chemical composition, changes in the atmospheric conditions, etc

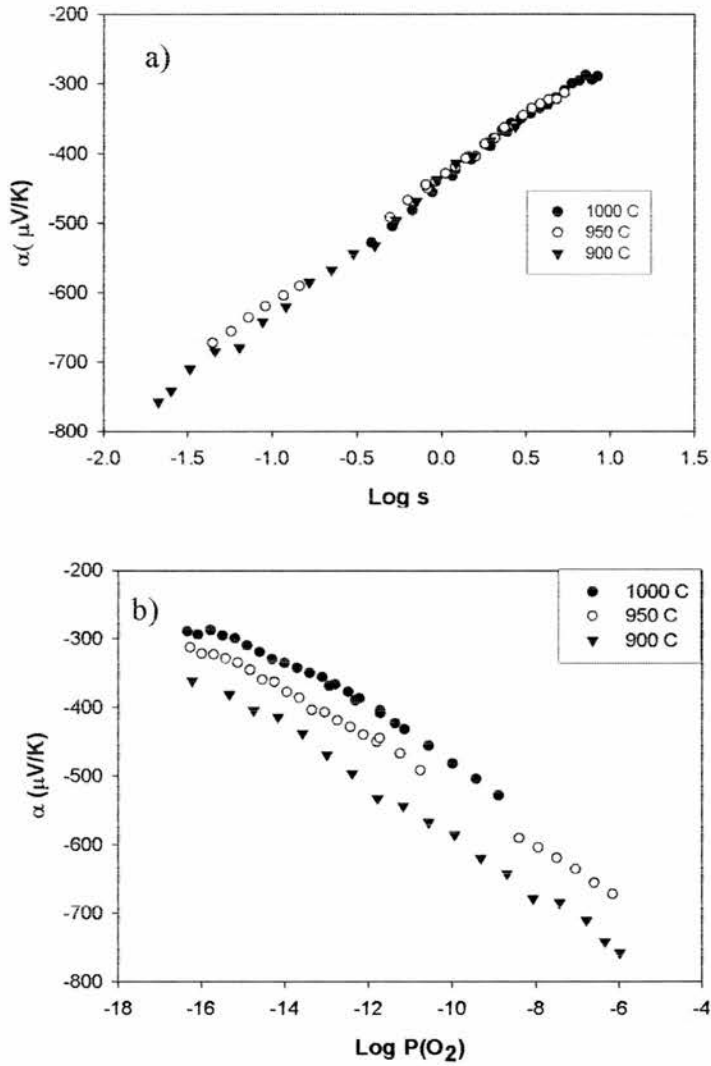


Figure 4.33. Seebeck coefficients vs. log conductivity plot, showing what it seems to be a metal to insulator transition (a). (b) Seebeck coefficients vs. log $P(\text{O}_2)$ plot.

4.4. Fuel Cell Tests.

The $n=12$ member ($\text{La}_2\text{Sr}_4\text{Ti}_6\text{O}_{19.5}$) was considered a good candidate as anode for a fuel cell because of its quite high conductivity in reducing conditions as already mentioned. Preliminary fuel cell tests were performed on a single cell using a 2mm thick YSZ electrolyte. LSM was chosen as cathode and reduced $\text{La}_2\text{Sr}_4\text{Ti}_6\text{O}_{19.5}$ as anode. Figure 4.34 shows the polarisation resistance (R_p) series using the three-electrode configuration described in section 2.4.

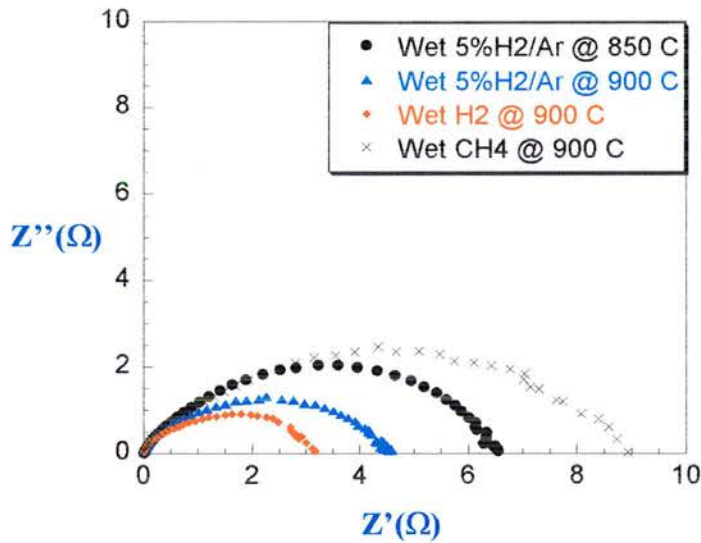


Figure 4.34. Polarisation resistance obtained at OCV using $\text{La}_2\text{Sr}_4\text{Ti}_6\text{O}_{19.5}$ as anode.

In wet 5% H_2 /Ar the R_p is $6.59\Omega\text{cm}^2$ at 850°C , which is somewhat better than the values reported for the similar stoichiometry $\text{La}_{0.35}\text{Sr}_{0.65}\text{TiO}_3$, i.e. $52\Omega\text{cm}^2$ [2]. This large difference in polarisation resistance may be attributed to the long-time reduction before our tests in order to achieve the highest electrical conductivity on the preparation of materials and anode, as the true chemical composition of the two materials is not significantly different. The R_p decreases with increasing temperature and thus it dropped to $4.56\Omega\text{cm}^2$ at 900°C under the same conditions. The R_p is also

sensitive to hydrogen concentration and the polarisation dropped to $2.97\Omega\text{cm}^2$ at 900°C in wet H_2 , i.e. more reducing conditions. The responses in wet CH_4 were worse and almost three times larger than in wet H_2 indicating that $\text{La}_2\text{Sr}_4\text{Ti}_6\text{O}_{19.8}$ itself is not a suitable anode material for direct methane fuel cells.

The fuel cell performance studied in a two-electrode configuration single cell (chapter 2, figure 2.4) using $\text{La}_2\text{Sr}_4\text{Ti}_6\text{O}_{19.8}$ as anode and $\text{La}_{0.8}\text{Sr}_{0.2}\text{MnO}_3$ as cathode is shown in figure 4.38. Current densities of 75 and $119\text{mA}/\text{cm}^2$ at 600mV were achieved at 850 and 900°C respectively when wet H_2 was applied as the fuel, whereas the maximum power density is $76\text{mW}/\text{cm}^2$ at a potential of 0.47V. Working in wet CH_4 atmosphere the maximum current density is about $78\text{mA}/\text{cm}^2$ at 900°C , which is quite low, but still comparable with the state of the art materials used as anodes in SOFC. The performance of the cell is limited by the anode polarisation as can be observed in the voltage-current curves. In such curves it is possible to observe from the changes in the slope how the drop in the voltage is not only due to an IR drop but also to some other factors in either the catalytic or the ionic transport part. Both aspects may have to be improved to obtain a high performance anode. In this respect, O. Marina and co-workers recently reported studies of $\text{LaSrTiO}-\text{CeO}_2$ composites as anodes for fuel cells, obtaining very promising results [3]. The ionic contribution might be enhanced by control of the chemical composition. Regarding changes in chemical composition, doping with Sc and Nb on the B-sites have been attempted and the results will be discussed in next chapters. Finally, it should be mentioned that no carbon deposition was observed after the fuel cell tests indicating that methane cracking did not occur. That is a good aspect to be considered since the formation of carbon deposits is one of the main drawbacks of the state of the art anode Ni/YSZ.

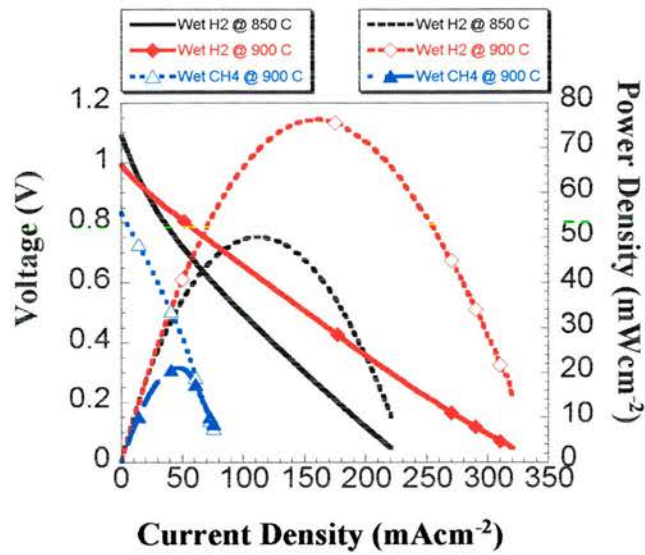


Figure 4.35. Fuel cell performance curves using $\text{La}_2\text{Sr}_4\text{Ti}_6\text{O}_{19.8}$ as anode, LSM as cathode and YSZ as electrolyte.

4.5. Conclusions.

Rather low total conductivity was found for the $\text{La}_4\text{Sr}_{n-4}\text{Ti}_n\text{O}_{3n+2}$ series in air, especially for the layered phases, with quite high E_a . The responses were generally dominated by the grain boundary contribution, probably as a consequence of the fairly high porosity. The presence of the extended crystallographic shears regularly distributed in the structure is the most likely explanation for the low conductivity for the layered phases.

The capacitance associated to the bulk response in layered phases with odd number of layers per block showed a Curie-Weiss like dependence with temperature, which is usually symptomatic of ferroelectricity.

For the “non-layered” the properties were more promising, although the grain boundaries still limited their performance in air and, for instance, the $n=12$ member showed quite high metallic conductivity of 60 Scm^{-1} under reducing conditions. This indicates the potential of titanates as anode materials because of the very low $P(\text{O}_2)$ in operating conditions. The presence of local defects accommodating excess oxygen facilitates somewhat the reduction of Ti^{4+} to Ti^{3+} , which is translated in more charge carriers under the same reducing conditions in comparison to the A-deficient $\text{Sr}_{1-3x/2}\text{La}_x\text{TiO}_{3-\delta}$.

The cubic members of the $\text{La}_4\text{Sr}_{n-4}\text{Ti}_n\text{O}_{3n+2}$ series seem to be good candidates as anode materials for SOFC, giving performances comparable to the state of the art materials in the case of the $n=12$ member. However, the rather high conductivity observed under reducing conditions does not seem to be enough to have a high performance material because both the ionic contribution and the catalytic aspect must be improved. The use of CeO_2 -composites has been recently demonstrated to overcome such limitations offering very promising performance for a working SOFC. Chemical modifications could also offer an alternative by inducing some ionic conductivity.

4.6. References.

1. J. Canales Vázquez, S. W. Tao and J. T. S. Irvine, *Solid State Ionics*, **159**, 2003, 159.
2. O. A. Marina, N. L. Canfield and J. W. Stevenson, *Solid State Ionics*, **149** (2002), 21.

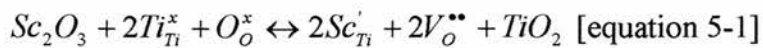
3. O.A. Marina and L.R. Pederson, *Proceedings of the 5th European Solid Oxide Fuel Cell Forum (Lucerne/Switzerland 2002)*, 481.
4. K. Ohi, S. Ishii and H. Omura, *Ferroelectrics*, **137 (1-4)** (1992), 133-138.
5. D. C. Sinclair and A. R. West, *Phys. Rev. B*, **39(18)** (1989), 13486.
6. F. Lichtenberg, A. Herrnberger, K. Wiedenmann and J. Mannhart, *Progress in Solid State Chemistry*, **29** (2001), 1.
7. H. W. Schmalte, T. Williams, A. Reller, A. Linden, J. G. Bednorz, *Acta Crystallographica*, **B49** (1993), 235.
8. Alan J. Feighery, *Ph. D. Thesis*, St Andrews (1998).
9. J. Robertson, *J. Vac. Sci. Technol. B*, **18(3)** (2000), 1785.
10. M. Vollmann and R. Waser, *J. Am. Ceram. Soc.*, **77** (1994), 235.
11. J. C. C. Abrantes, J. A. Labrincha and J. R. Frade, *J. Eur. Ceram. Soc.*, **20** (2000), 1603.
12. P. R. Slater, D. P. Fagg and J. T. S. Irvine, *J. Mater. Chem.*, **7-12** (1997), 2495.
13. Joseph E. Sustom, Susan M. Kauzlarich and P. Klavins, *Chem. Mater.*, **4** (1992), 346.
14. M. Marezio, D. Tranqui, S. Lakkis and C. Schlenker, *Phys. Rev. B*, **16** (1977), 2811.
15. P. J. Gelling, H. J. M. Bouwmeester: "The CRC Handbook of Solid State Electrochemistry", CRC Press, 1997.
16. S. Nanamatsu, M. Kimura, K. Doi, S. Matsushita, N. Yamada, *Ferroelectrics*, **8** (1974), 511.

Chapter 5. Sc-substituted $\text{La}_4\text{Sr}_{n-4}\text{Ti}_n\text{O}_{3n+2}$	172
5.1. Introduction	172
5.2. Synthesis	173
5.3. Structural characterisation	173
5.3.1. XRD	173
5.3.2. TGA	179
5.3.3. TEM on Sc-substituted $\text{La}_4\text{Sr}_8\text{Ti}_{12}\text{O}_{38-\delta}$	181
5.3.3.1. $\text{La}_2\text{Sr}_4\text{Ti}_{5.7}\text{Sc}_{0.3}\text{Ti}_{18.85}$ ($x=0.3$)	181
5.3.3.2. $\text{La}_2\text{Sr}_4\text{Ti}_{5.5}\text{Sc}_{0.5}\text{Ti}_{18.75}$ ($x=0.5$)	184
5.4. Electrical properties on Sc-substituted phases	189
5.4.1. $\text{La}_2\text{Sr}_4\text{Ti}_{5.7}\text{Sc}_{0.3}\text{Ti}_{18.85}$ ($x=0.3$)	190
5.4.2. $\text{La}_2\text{Sr}_4\text{Ti}_{5.5}\text{Sc}_{0.5}\text{Ti}_{18.75}$ ($x=0.5$)	191
5.4.2.1. Ac impedance spectroscopy	191
5.4.2.2. Four terminal techniques	193
5.4.3. $\text{La}_2\text{Sr}_4\text{Ti}_{5.0}\text{Sc}_{1.0}\text{Ti}_{18.50}$ ($x=1.0$)	194
5.4.4. $\text{La}_2\text{Sr}_4\text{Ti}_{5.0}\text{Sc}_{1.5}\text{Ti}_{18.25}$ ($x=1.5$)	197
5.5. Summary	199
5.6. References	201

5. Sc-substituted $\text{La}_4\text{Sr}_{n-4}\text{Ti}_n\text{O}_{3n+2}$.

5.1. Introduction.

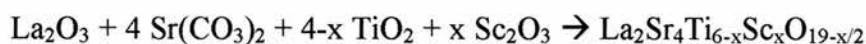
As discussed in previous chapters, the $n=12$ member of the $\text{La}_4\text{Sr}_{n-4}\text{Ti}_n\text{O}_{3n+2}$ series of compounds showed rather interesting properties, which made a potential anode material for fuel cells technology. It was pointed out however that the performance of a fuel cell with that phase alone as anode was limited due to both catalytic and ionic transport considerations. Catalytic aspects may be improved by the utilisation of $(\text{La},\text{Sr})\text{TiO}_3\text{-CeO}_2$ composites as already mentioned. On the other hand, ionic conduction might be improved by changes in the chemical composition. The replacement of Ti^{4+} by lower valence cations would force the removal of oxygen from the structure in order to maintain the electroneutrality in the crystal, and thus creating oxygen vacancies that might favour ionic transport. Sc^{3+} was considered as a suitable candidate to substitute Ti from the B-sites due to their similar ionic radii and also because there are some studies reporting proton conduction in systems such as Mg-doped LaScO_3 [1]. The creation of oxygen vacancies can be written by Kroger-Vink notation as:



In the present chapter the effect of replacing Ti^{4+} by Sc^{3+} was evaluated in both the structural and electrical properties.

5.2. Synthesis.

The samples were prepared following the formula:



with $x=0.3, 0.5, 1.0$ and 1.5 that corresponds of substitution levels of 5, 8.3, 16.6 and 25 % respectively. The samples will be named after their Sc content x . Thus the excess oxygen will be reduced gradually with increasing x , as listed in table 5-1.

x	Formula	δ
0	$\text{La}_2\text{Sr}_4\text{Ti}_6\text{O}_{19}$	0.167
0.3	$\text{La}_2\text{Sr}_4\text{Ti}_{5.7}\text{Sc}_{0.3}\text{O}_{18.85}$	0.142
0.5	$\text{La}_2\text{Sr}_4\text{Ti}_{5.5}\text{Sc}_{0.5}\text{O}_{18.75}$	0.125
1.0	$\text{La}_2\text{Sr}_4\text{Ti}_{5.0}\text{Sc}_{1.0}\text{O}_{18.5}$	0.083
1.5	$\text{La}_2\text{Sr}_4\text{Ti}_{4.5}\text{Sc}_{1.5}\text{O}_{18.25}$	0.042

Table 5-1. Excess oxygen (δ) as a function of the Sc content in the Sc-substituted series.

5.3. Structural characterisation.

5.3.1. X-rays.

XRD was used for the preliminary structural studies and to evaluate the changes caused by the substitution of Ti by Sc in $\text{La}_2\text{Sr}_4\text{Ti}_6\text{O}_{19-\delta}$. Tables 5-2 to 5-4 list the refined XRD data for the Sc-doped series (figures 5.1-5.3). The unit cells did not suffer noticeable changes and remained as simple cubic perovskite until $x=1.0$, where the XRD peaks become very broad. However, as an approximation it was still indexed

as a simple cubic perovskite. For $x=1.5$ there is apparently a mixture of phases that could be due to the rather high level of substitution on the B-site of the perovskite, which would imply a longer sintering time in order to obtain homogeneous samples.

$2\theta_{\text{obs}}$	hkl	$2\theta_{\text{cal}}$	Int	d_{obs}	d_{cal}
22.699	100	22.703	9	3.9143	3.9137
32.329	110	32.324	100	2.7669	2.7674
39.864	111	39.864	22	2.2596	2.2595
46.366	200	46.363	33	1.9567	1.9568
52.220	210	52.222	5	1.7503	1.7502
57.643	211	57.648	30	1.5978	1.5977
67.658	220	67.656	15	1.3837	1.3837

$2\theta_{\text{obs}}$	hkl	$2\theta_{\text{cal}}$	Int	d_{obs}	d_{cal}
22.715	100	22.720	10	3.9115	3.9106
32.352	110	32.349	100	2.7650	2.7652
39.899	111	39.897	25	2.2577	2.2578
46.404	200	46.401	35	1.9552	1.9553
52.266	210	52.265	5	1.7489	1.7489
57.695	211	57.696	32	1.5965	1.5965
67.713	220	67.715	15	1.3827	1.3826

Table 5-2. Refined XRD data for $x=0.3$ in oxidising (top) and reducing conditions (bottom)

indexed as a simple cubic perovskite, $a=3.9137(4)$ Å and $a=3.9106(3)$ Å respectively.

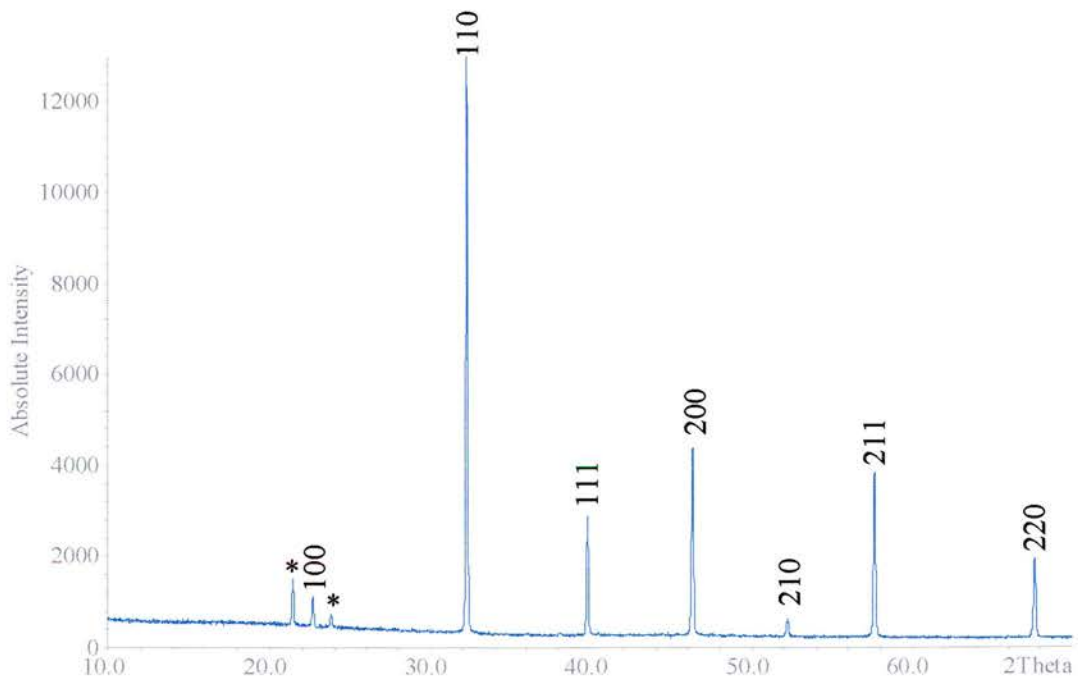


Figure 5.1. XRD pattern corresponding to $x=0.3$ in oxidising conditions indexed as a simple cubic perovskite. * denotes vaseline peaks.

$2\theta_{\text{obs}}$	hkl	$2\theta_{\text{cal}}$	Int	d_{obs}	d_{cal}
22.657	100	22.655	9	3.9214	3.9218
32.260	110	32.255	100	2.7727	2.7731
39.777	111	39.778	20	2.2643	2.2643
46.252	200	46.261	26	1.9613	1.9609
52.104	210	52.105	3	1.7539	1.7539
57.515	211	57.517	18	1.6011	1.6011
67.503	220	67.496	7	1.3865	1.3866

$2\theta_{\text{obs}}$	hkl	$2\theta_{\text{cal}}$	Int	d_{obs}	d_{cal}
22.680	100	22.679	11	3.9175	3.9176
32.291	110	32.290	100	2.7701	2.7702
39.822	111	39.822	21	2.2619	2.2618
46.313	200	46.314	28	1.9588	1.9588
52.163	210	52.165	4	1.7521	1.7520
57.584	211	57.584	21	1.5993	1.5994
67.579	220	67.578	8	1.3851	1.3851

Table 5-3. Refined XRD data for $x=0.5$ in oxidising (top) and reducing (bottom) conditions indexed as a simple cubic perovskite, $a=3.9218(6)$ Å and $a=3.9176(1)$ Å respectively.

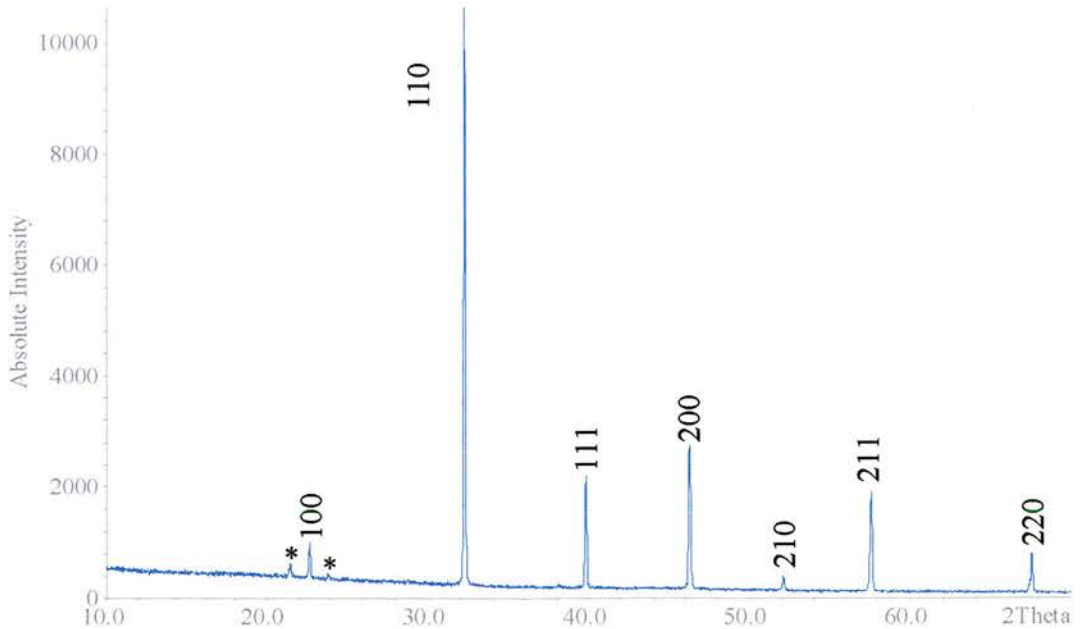


Figure 5.2. XRD pattern for $x=0.5$ in oxidising conditions. * denotes vaseline peaks.

$2\theta_{\text{obs}}$	hkl	$2\theta_{\text{cal}}$	Int	d_{obs}	d_{cal}
22.609	100	22.606	10	3.9297	3.9302
32.196	110	32.184	100	2.7780	2.7791
39.679	111	39.689	17	2.2697	2.2691
46.143	200	46.157	18	1.9657	1.9651
51.977	210	51.985	4	1.7579	1.7576
57.398	211	57.382	23	1.6041	1.6045
67.334	220	67.333	14	1.3895	1.3895

$2\theta_{\text{obs}}$	hkl	$2\theta_{\text{cal}}$	Int	d_{obs}	d_{cal}
22.615	100	22.616	15	3.9286	3.9284
32.200	110	32.199	100	2.7777	2.7778
39.713	111	39.708	19	2.2678	2.2681
46.179	200	46.179	25	1.9642	1.9642
52.003	210	52.011	4	1.7571	1.7569
57.411	211	57.410	17	1.6038	1.6038
67.370	220	67.367	6	1.3889	1.3889

Table 5-4. Refined XRD data for $x=1.0$ in oxidising (top) and reducing (bottom) conditions indexed as a simple cubic perovskite, $a=3.930(1)$ Å and $a=3.9284(4)$ Å respectively

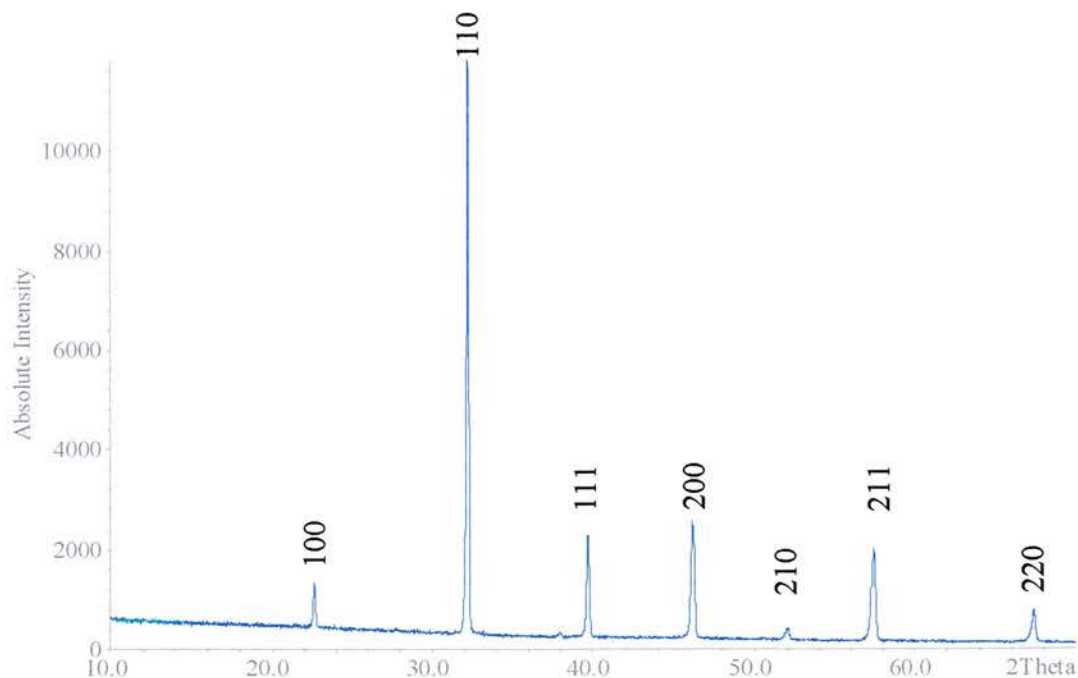


Figure 5.3. XRD pattern for $x=1.0$. The fairly broad peaks might indicate that $x=1.0$ is not a single phase.

Figure 5.4 shows the evolution of the $(220)_p$ peak with the Sc content. From $x=1.0$ broadening of the peak is observed and moreover extra reflections appear for $x=1.5$, which can be explained by the presence of two phases with similar unit cells as EDS analyses suggest. It should be noted that **all** the reflections were similarly broadened in addition to the presence of extra reflections, which would also imply that it is not the case of any distortion common to perovskites.

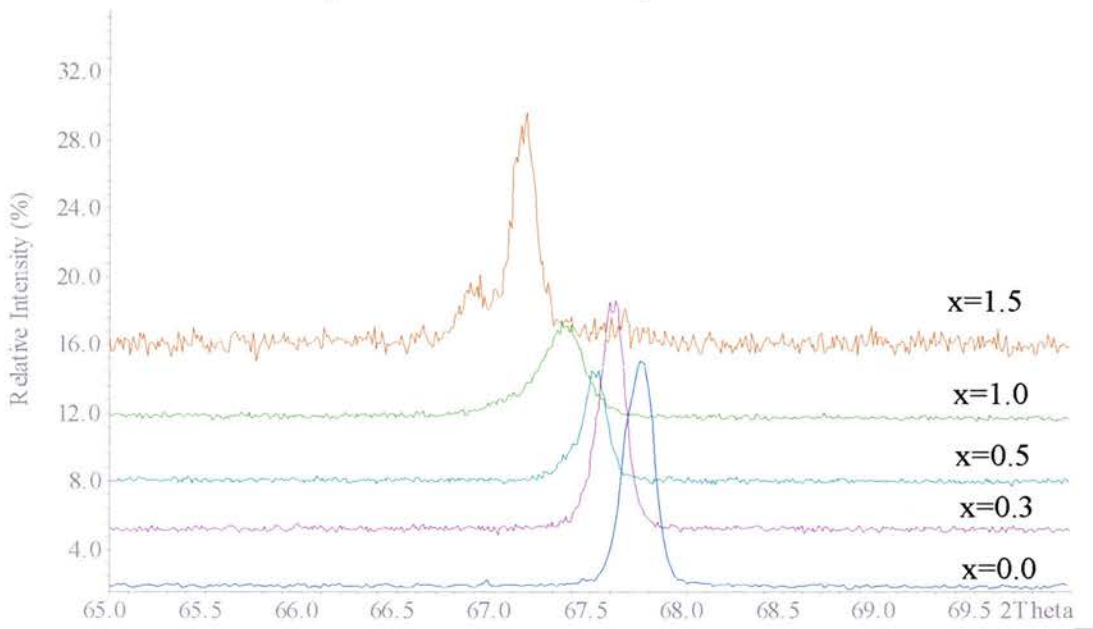


Figure 5.4 $(220)_p$ reflection on the scandium-substituted series. An extra reflection appears for $x=1.5$.

It should also be observed that the relative density diminishes with the Sc concentration under the same synthetic conditions as listed in table 5-5.

x	Density (gcm^{-3})	Relative density (%)
0	4.95	94
0.3	5.04	95
0.5	4.63	87
1.0	4.25	81
1.5	3.81	72

Table 5-5. Relative densities of the Sc-substituted series under the same synthetic conditions.

The unit cell parameters expanded with increasing Sc content, which is related with Sc^{3+} being 20% larger than Ti^{4+} , i.e. 0.87\AA vs. 0.75\AA (table 5-5 and figure 5.5). Reduction was found not to significantly affect the structure causing only a slight shrinkage of the unit cell as occurs for the non-substituted material, despite the colour change from pale yellow to dark blue. For the reduced phases, the unit cell also expanded with increasing the Sc content. This is a quite interesting conclusion because Sc^{3+} and Ti^{3+} have very similar ionic radii and therefore they should modify the unit cell in the same manner. However, it has been reported that Ti^{3+} tends to form pairs, which results in the shortening of the Ti-Ti distances despite its larger size in comparison to Ti^{4+} in the $\text{Ti}_n\text{O}_{2n-1}$ system [2-3]. The lower overall positive charge will reduce repulsion between consecutive metallic cations and thus the distances become shorter. In perovskites one should not speak about direct Ti-Ti bond. Instead long distance Ti-O-Ti coupling can be regarded, which might be also shortened by the presence of Ti^{3+} .

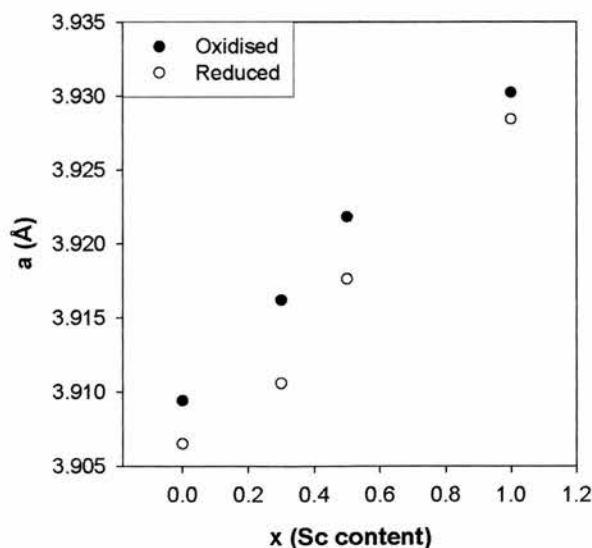


Figure 5.5. Evolution of the cell parameters with the Sc content. The unit cell expands with increasing the Sc content in both reduced and oxidised phases.

x	Oxidised (Å)	Reduced (Å)
0.0	3.9094	3.9065
0.3	3.9162	3.9106
0.5	3.9218	3.9176
1.0	3.9302	3.9284

Table 5-5. Unit cell parameters for the Sc-substituted series.

There is no evidence of layered structure, i.e. characteristic X-rays peaks in the 2θ range [26-30], which is consistent with the gradual decrease in the oxygen content of these phases with increasing Sc content as listed in table 5-1. The lower concentration of extra oxygen impedes the formation of crystallographic shears as a regular feature of the crystal structure.

5.3.2. TGA.

As mentioned in the introduction, the substitution of Ti^{4+} by Sc^{3+} causes the removal of oxygen in order to maintain the electroneutrality of the crystal. As a consequence, there should be *a priori* “less” excess oxygen compared to $\text{La}_4\text{Sr}_8\text{Ti}_{12}\text{O}_{38.8}$. In previous chapters, it has been suggested that the presence of excess oxygen accommodated in linear defects facilitates the reduction of Ti^{4+} to Ti^{3+} because the oxygen is somewhat “more available”. Therefore, the decrease in excess oxygen would hypothetically lead to an increased difficulty in reducing these compounds. TGA experiments performed on pre-reduced samples allow the monitoring of the changes in oxygen content from oxidised to reduced samples. As prepared powders of $x=0.0$, $x=0.3$ and $x=0.5$ material were reduced by heating up to 1000°C in flowing 5% H_2/Ar . The resultant dark-blue powders were then heated up to 900°C in flowing air at 10 K/minute, held isothermally for several hours to reach equilibrium and finally cooled down at 10 K/minute.

From the results shown in figure 5.6, it can be seen that the re-oxidation is gradually faster, i.e. steeper slopes at high temperature considering that the same ramp rate was used for each experiment, with increasing Sc content. Also the amount of oxygen regained is gradually smaller, which could be due to Sc^{3+} promoting the stabilisation of Ti in the 4+ oxidation. A lower concentration of Ti^{3+} will have a negative effect on the electronic conductivity as discussed in section 5.3, because there will be less charge carriers.

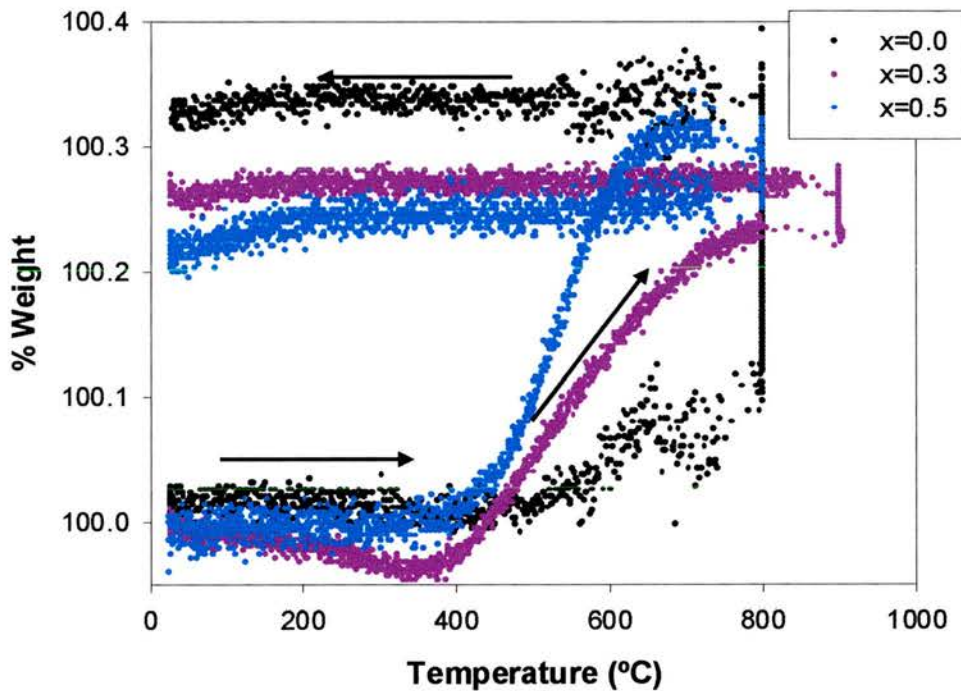


Figure 5.6. TGA experiments for $x=0.0, 0.3$ and 0.5 . The amount of oxygen regained during the re-oxidation gradually decreases with increasing the Sc content.

From the % of weight regained for each compound, it is possible to estimate approximately the amount of oxygen that has been removed during the reduction. Therefore, the stoichiometry for the reduced phases is as follows: $\text{La}_{1/3}\text{Sr}_{2/3}\text{TiO}_{3.1267}$ ($x=0.0$), $\text{La}_{1/3}\text{Sr}_{2/3}\text{Ti}_{0.95}\text{Sc}_{0.05}\text{O}_{3.1100}$ ($x=0.3$) and $\text{La}_{1/3}\text{Sr}_{2/3}\text{Ti}_{0.917}\text{Sc}_{0.083}\text{O}_{3.0967}$ ($x=0.5$) as listed in table 5-6.

x	Formula (oxidised)	Formula (Reduced)	$\Delta\delta$
0.0	$\text{La}_{1/3}\text{Sr}_{2/3}\text{TiO}_{3.167}$	$\text{La}_{1/3}\text{Sr}_{2/3}\text{TiO}_{3.127}$	-0.040
0.3	$\text{La}_{1/3}\text{Sr}_{2/3}\text{Ti}_{5.7}\text{Sc}_{0.3}\text{O}_{3.142}$	$\text{La}_{1/3}\text{Sr}_{2/3}\text{Ti}_{5.7}\text{Sc}_{0.3}\text{O}_{3.110}$	-0.032
0.5	$\text{La}_{1/3}\text{Sr}_{2/3}\text{Ti}_{5.5}\text{Sc}_{0.5}\text{O}_{3.125}$	$\text{La}_{1/3}\text{Sr}_{2/3}\text{Ti}_{5.5}\text{Sc}_{0.5}\text{O}_{3.097}$	-0.028

Table 5-6. Summary of the TGA results revealing that reduction (as loss of oxygen) is gradually less extensive with increasing Sc content.

5.3.3. TEM studies on Sc-substituted $\text{La}_2\text{Sr}_4\text{Ti}_6\text{O}_{19}$.

TEM studies were performed for the doped phases considered single phases, i.e. $x=0.3$ and $x=0.5$. Despite doping with Sc on the B-sites, these phases still have nominal oxygen overstoichiometry in comparison to the parental ABO_3 and TEM may bring some light to elucidate whether excess oxygen is accommodated in local defects or via a different mechanism.

5.3.3.1. $\text{La}_2\text{Sr}_4\text{Ti}_{5.7}\text{Sc}_{0.3}\text{O}_{18.85}$ ($x=0.3$).

As for the non-substituted material, SAED revealed the presence of superstructure reflections doubling only the $[111]_p$ as shown in figure 5.7.

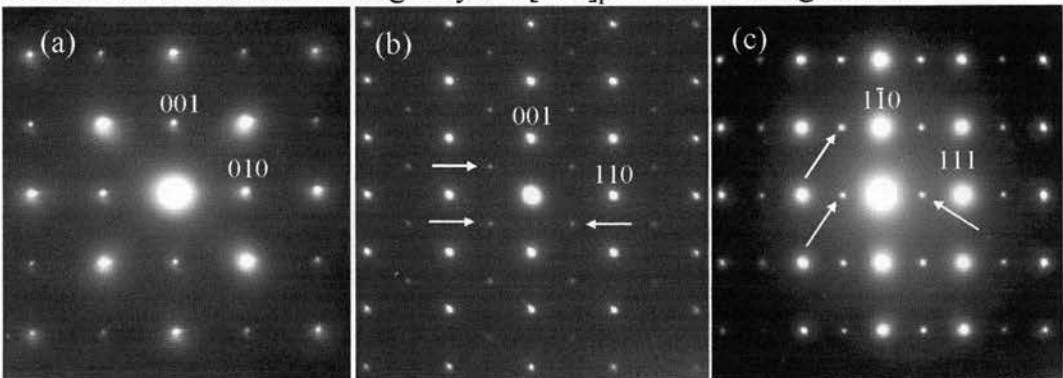


Figure 5.7. SAED patterns corresponding to $x=0.3$ showing views down the $[100]_p$ (a), $[1-10]$ (b) and $[11-2]_p$ (c) respectively. Superstructure reflections along the $[111]_p$ are marked with arrows.

The presence of superstructure reflections at $\{\frac{1}{2}\frac{1}{2}\frac{1}{2}\}_p$ seem to indicate that the subtle average tilting of the octahedra found for $x=0.0$ is still present and thus, the unit cell is a face centred cubic with $a=2a_p$.

Occasionally, it is possible to observe directly by HRTEM the doubling of the $[111]_p$ as marked in figure 5.8, which is further evidence of the similarity between the non-substituted and substituted phases.

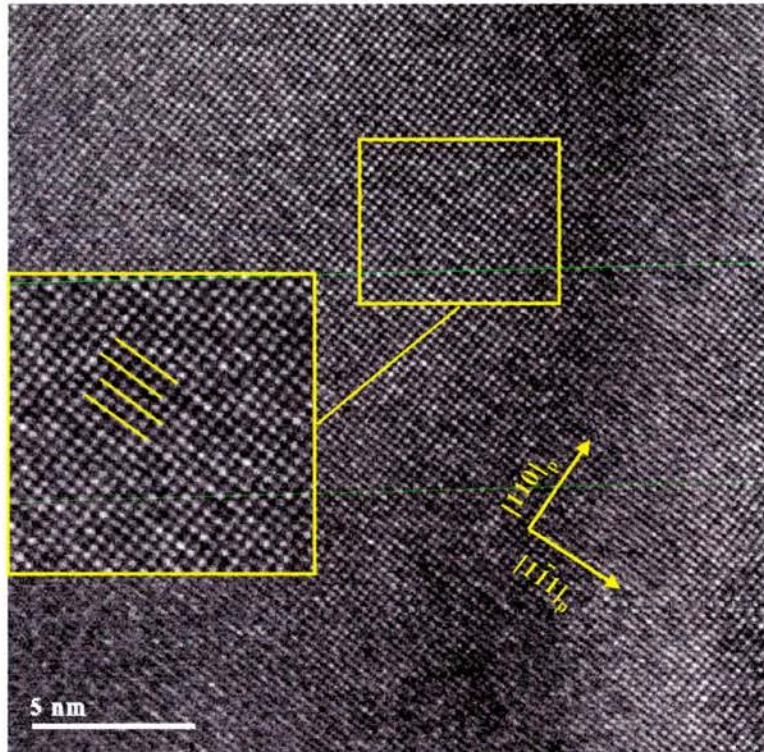


Figure 5.8. HRTEM image viewing down the $[11-2]_p$ projection in $x=0.3$. The inset shows a zoom of a region in which the contrast of the image clearly reveals the doubling of the $[111]_p$.

HRTEM images taken down the $[100]_p$ revealed the presence of nanodomain defects giving rise to dark contrast in some regions of the specimen as occurred for $x=0.0$, although the concentration was undoubtedly lower (figure 5.9). Hence there are local defects (linear) where the extra oxygen is presumably accommodated. The

structural type is kept despite doping with Sc, although the lower excess oxygen content renders the creation of fewer defects.

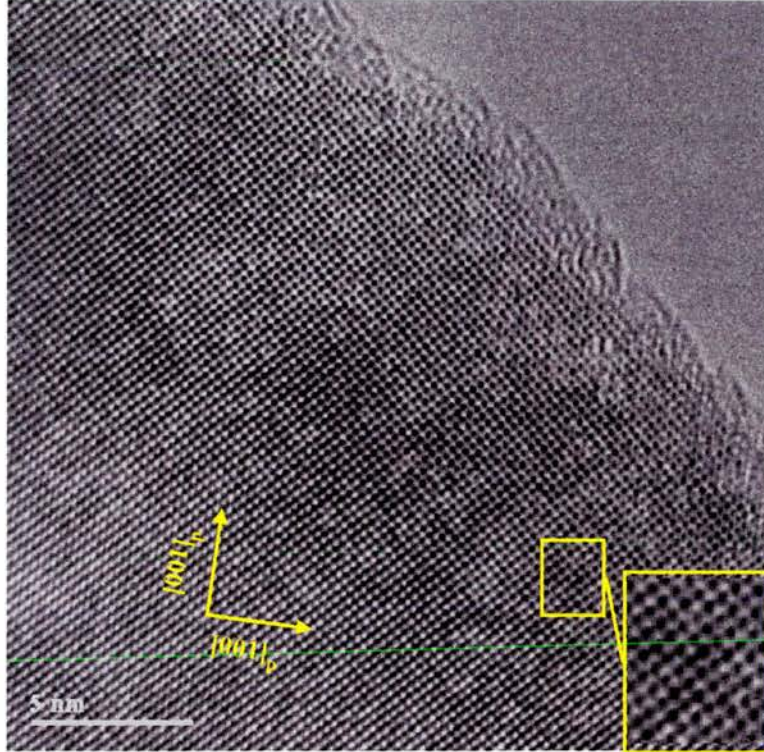


Figure 5.9. HRTEM image corresponding to the $[100]_p$ zone axis. Local defects are present although in lower concentration compared to the $n=12$ member of the $\text{La}_4\text{Sr}_{n-4}\text{Ti}_n\text{O}_{3n+2}$ series.

The inset shows a zoom of one of such defects.

One important change found by TEM is the lack of domains with modulated structures down the $[110]$ projection. Defects accommodating excess oxygen are in lower concentration and therefore they do not interact to form large clusters easily, which is the most likely mechanism to explain the short-range oxygen shears observed in $x=0.0$. However, in some regions of the crystal, it is possible to observe some sort of very subtle modulation that could be considered as the first stage in the formation of the crystallographic shears (figure 5.10). The excess oxygen (δ) for $x=0.3$ is approximately the same than for the $n=14$ member in the non-substituted series, i.e. $\delta=0.14$. Indeed, no extended defects were found in that case as happens

here, which may be considered as a further evidence that excess oxygen is the driving force in the creation of such modulated structures observed for the $n=12$ member in the $\text{La}_4\text{Sr}_{n-4}\text{Ti}_n\text{O}_{3n+2}$ series. For $\delta < 0.15$, excess oxygen is accommodated in more localised defects. When $0.15 < \delta < 0.20$, there exist short range extended defects, whereas for $\delta > 0.20$ a layered structure appears.

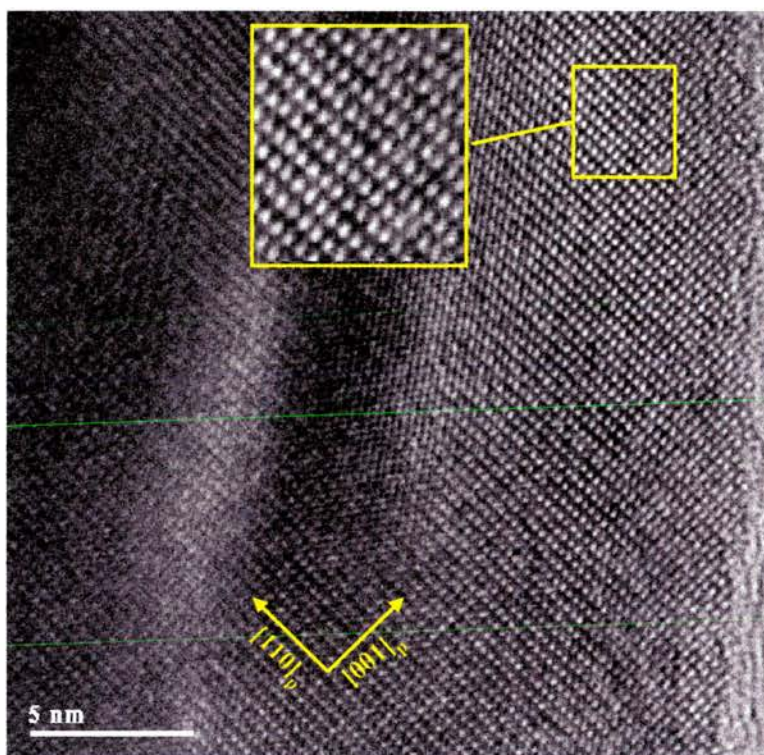


Figure 5.10. HRTEM image taken down the $[1-10]_p$ projection in $x=0.3$. The inset shows a barely distinguishable short range modulation of the crystal structure.

There are still a significant number of defects where extra oxygen can be accommodated, despite its lower concentration on the Sc-substituted phases. The lack of clusters of defects could possibly facilitate the mobility of the excess oxygen through the structure.

5.3.3.2. $La_2Sr_4Ti_{5.7}Sc_{0.5}O_{18.75}$ ($x=0.5$).

TEM studies performed on $x=0.5$ are in agreement with the results presented for $x=0.3$. Again superstructure reflections appeared doubling only the $[111]_p$ direction as shown in figure 5.11.

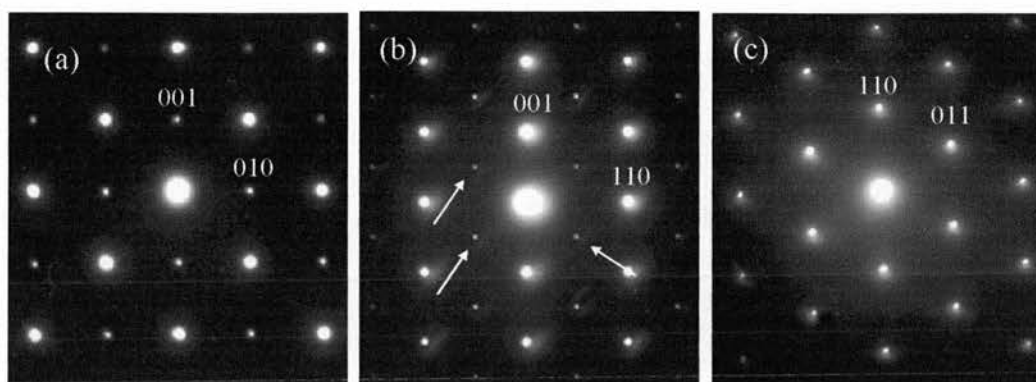


Figure 5.11. SAED patterns corresponding to the $[100]_p$ (a), $[1-10]_p$ (b) and $[111]_p$ (c) respectively for $x=0.5$. Superstructure reflections still appear doubling the $[110]_p$.

Hence, tilting of octahedra in the perovskite framework still occurs as a consequence of the antiphase tilting in $x=0.0$. However, one might think that such distortion is not caused by local defects, since δ is getting very small (0.125).

HRTEM images taken down the $[100]_p$ revealed that the concentration of local defects (dark contrast areas) is indeed lower as a consequence of the smaller amount of excess oxygen and in most of the cases they are barely distinguishable. Nevertheless there are still a few (figure 5.12). Presumably, when $\delta < 0.1$, the excess oxygen is accommodated as point defects randomly distributed and thus the detection by direct TEM observation will become extremely difficult, if not impossible because

contrast in TEM images is given by columns of atoms. Therefore the detection of single isolated defects is highly unlikely.

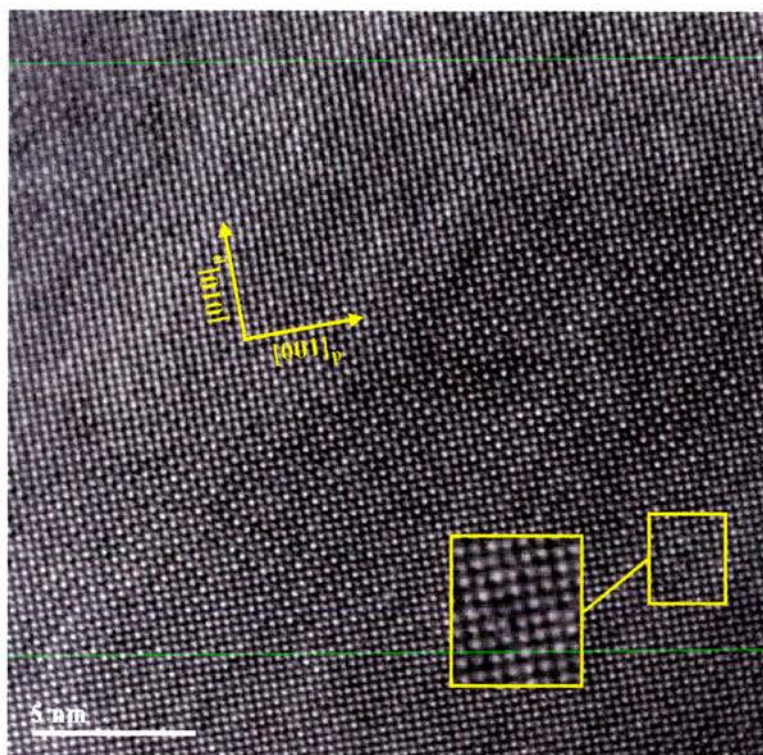


Figure 5.12. HRTEM viewing down the $[100]_p$ projection in $x=0.5$. The structure looks almost like a perfect cubic perovskite except for the presence of local defects (inset) in very low concentration.

As for the presence of shearing typically observed in images corresponding to the $[110]_p$ zone axis, these could not be detected in the present case (figure 5.13). The low concentration of defects impedes the formation of large clusters that give the very strong contrast observed in the HRTEM images corresponding to $x=0.0$. Consequently, the presence of any subtle modulation can not be detected in the present case. As the concentration of defects decreases, these tend to be isolated and therefore detection is gradually more difficult.

It seems clear at this stage, that the concentration of excess oxygen determines the extension of the defects. At very low values of δ , excess oxygen is accommodated in local defects that gradually increase their size, giving rise to extended defects. At sufficiently high oxygen content, the defects become “more extended”, i.e. they become a regular feature in the crystal structure and can be detected by XRD. Figures 5.14 and 5.15 show a summary of this evolution and another with TEM images respectively. In the former, the formation of either layered or cubic phases is evaluated as a function of the excess oxygen content or, in other words the number of layers per perovskite block (n). In the latter, some relevant TEM pictures are presented, in which is shown the evolution of the structural evolution observed in excess oxygen titanates, from well ordered extended crystallographic shears to local defects.

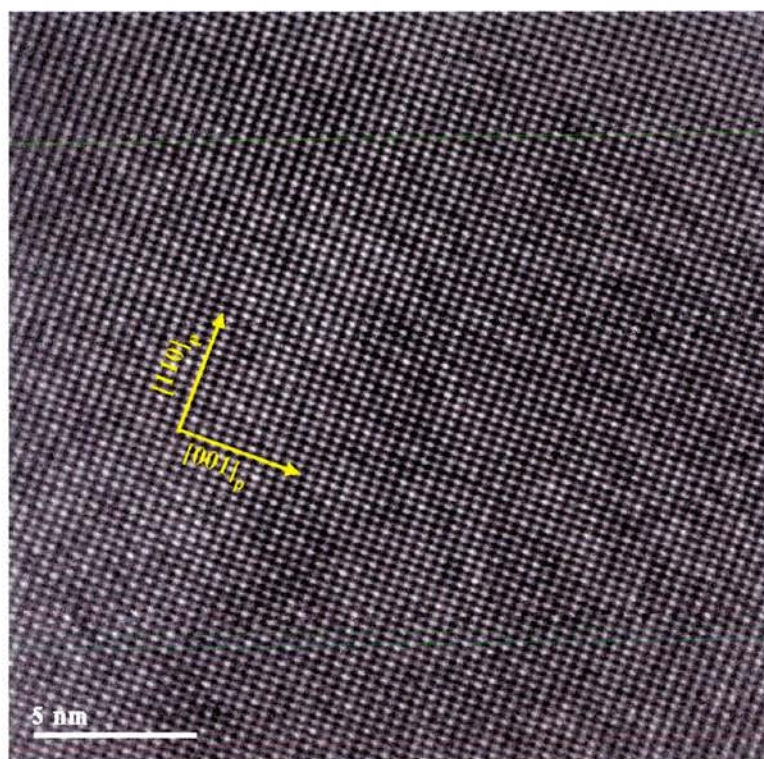


Figure 5.13. HRTEM image corresponding to a view of the $[100]_p$ zone axis. The presence of shearing or modulation cannot be detected.

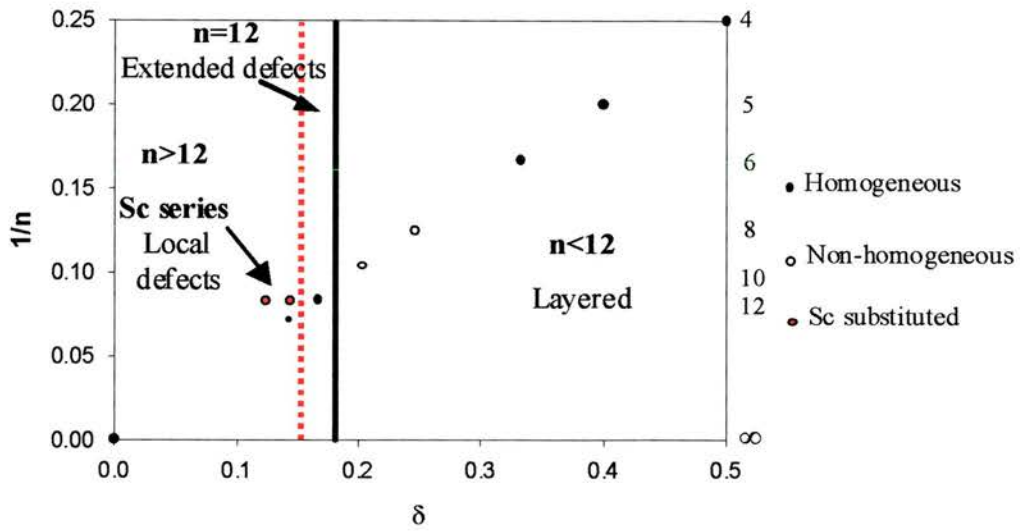


Figure 5.14. Structural evolution of the systems studied as a function of the oxygen content (δ)

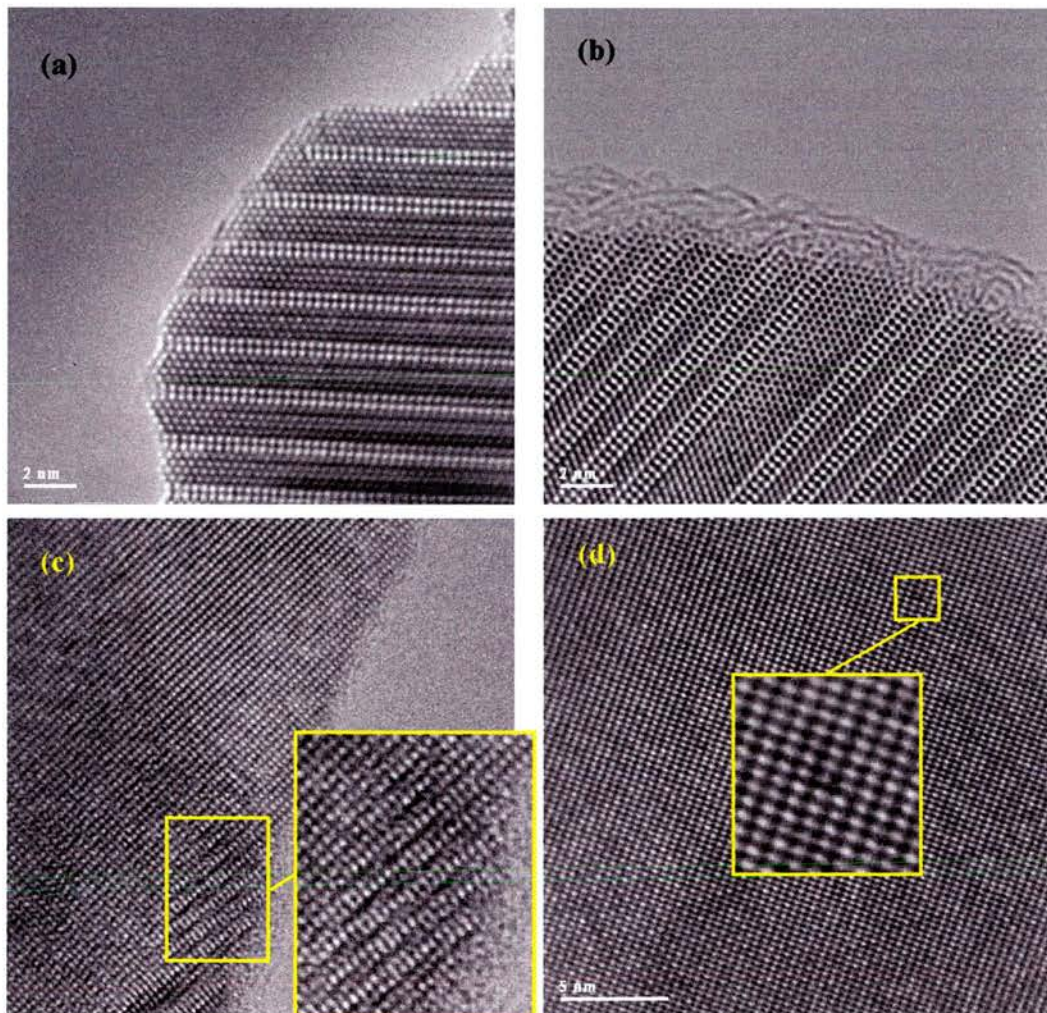


Figure 5.15. HRTEM images showing some representative examples of the structural evolution shown by the phases studied as a function of the oxygen stoichiometry: crystallographic shears regularly distributed (a) irregularly distributed (b), linear defects (c) and local defects (d).

5.4. Electrical properties in Sc-substituted phases.

The electrical properties of the Sc-substituted series were investigated mainly by means of ac impedance spectroscopy. It is crucial to study the effect of introducing Sc on the B-site and thus reducing the amount of excess oxygen in comparison to the non-substituted phase. Also the creation of oxygen vacancies might imply some improvements in the ionic conductivity in comparison to the non-substituted phase, which potentially could improve the performance of these phases as anode materials in fuel cells technology.

Some considerations that should be taken into account: Sc^{3+} stabilises Ti in the 4+-oxidation state as suggested by TGA results and therefore the conduction will be *a priori* lower than $x=0.0$, because the creation of electronic defects will be impeded. On the other hand, in the previous chapter it was postulated that crystallographic shears might ruin the conductivity in the layered phases and clusters of local defects were regarded as the first stage in the formation process of such oxygen rich planes. The presence of Sc^{3+} would decrease the amount of local defects and therefore it is quite unlikely to have extended defects as shown in the previous section and that could possibly affect to the total conductivity. Consequently, there might be two main processes competing: fewer charge carriers but also fewer impediments. Additionally, some ionic conductivity might be induced by the creation of oxygen vacancies.

5.4.1. $\text{La}_2\text{Sr}_4\text{Ti}_{5.7}\text{Sc}_{0.3}\text{O}_{18.85}$ ($x=0.3$).

As happened for the Sc-free phases the response on the complex impedance plane was dominated by the grain boundary contribution. Therefore the insulating nature of the grain boundaries is not overcome (figure 5.16). The Nyquist plots were fitted with equivalent circuit models (non-linear fitting), using typically two RC elements, one associated with the bulk (typically $6 \times 10^{-12} \text{ Fcm}^{-1}$) and another with the grain boundary (typically $3 \times 10^{-9} \text{ Fcm}^{-1}$) response. No diffusion processes are detected appearing at low frequencies in the range of temperatures studied (200-1000°C), which indicates that the ionic conductivity, if any, is very small compared to the electronic contribution as happened for $x=0.0$.

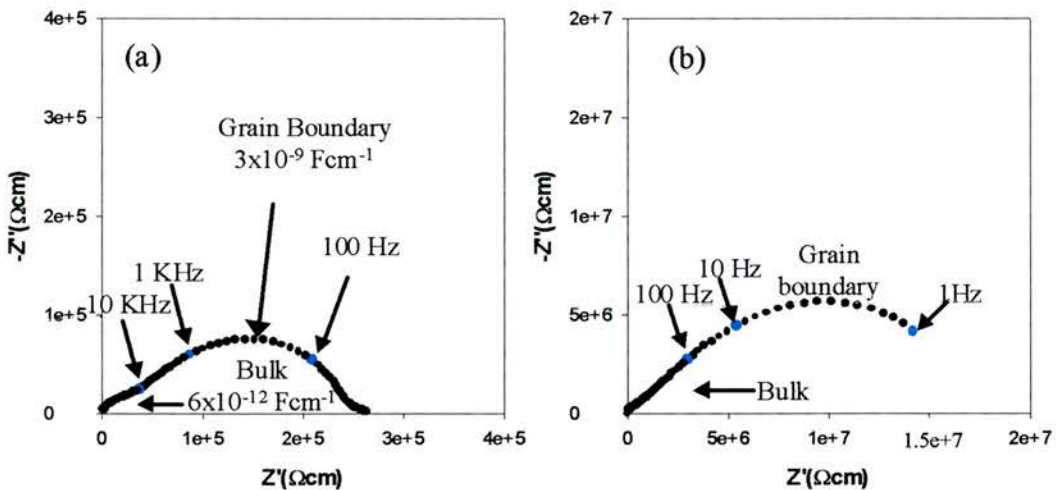


Figure 5.16. Nyquist plots for $x=0.3$ at 476°C (a) and 339°C (b). The responses are clearly dominated by the grain boundary response, despite the material being dense (95%).

The corresponding Arrhenius plot (figure 5.17) reveals that both total and bulk conductivity of $x=0.3$ is lower than $x=0.0$, whilst the activation energy is slightly higher. Special attention must be paid to the bulk conductivity because it is intrinsic to the material, whereas in the overall conductivity other factors related to sintering also

apply. It should be noted that the samples measured were as prepared and thus when dense (as is the present case), they are partially reduced due to the very high reaction temperature. The presence of Sc^{3+} facilitates the re-oxidation and therefore, under the same conditions $x=0.3$ has less charge carriers, i.e. lower conductivity.

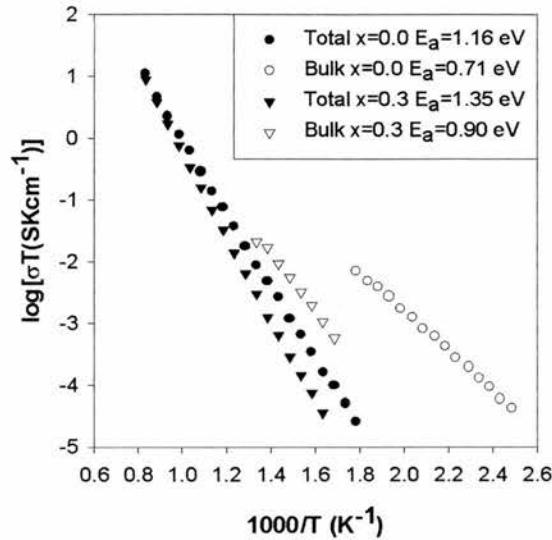


Figure 5.17 Arrhenius plot for $x=0.0$ and $x=0.3$. The presence of Sc reduces the conductivity.

5.4.2. $\text{La}_2\text{Sr}_4\text{Ti}_{5.5}\text{Sc}_{0.5}\text{O}_{18.75}$ ($x=0.5$).

5.4.2.1. Ac impedance spectroscopy.

Increasing the Sc content does not seem to significantly affect the responses, which are dominated once again by the grain boundary contribution (assigned capacitance of typically $8 \times 10^{-9} \text{ Fcm}^{-1}$) as shown in figure 5.18.

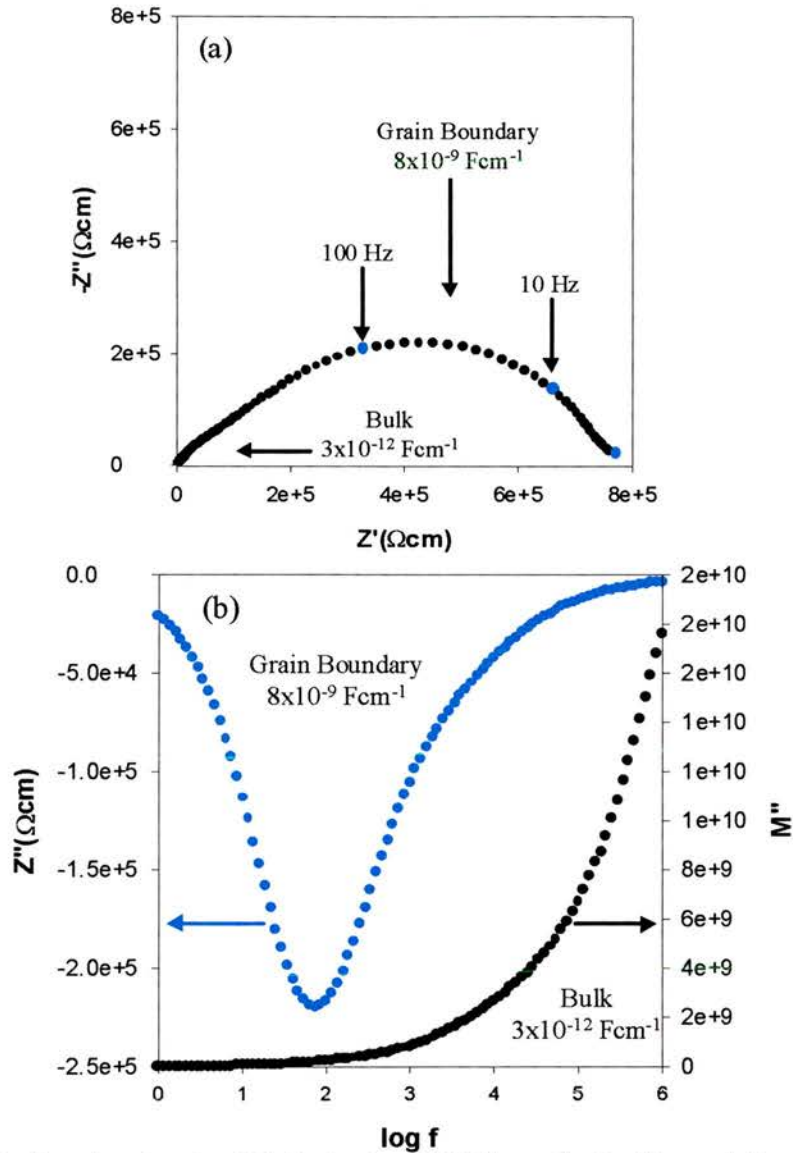


Figure 5.18a. Nyquist plot of $x=0.5$ obtained at 449°C in static air. The grain boundary contribution clearly dominates the overall response. **Figure 5.18b** shows a spectroscopic plot of the imaginary impedance (Z'') and modulus (M'') for $x=0.5$ at 449°C measured in air.

The Arrhenius plot reveals that the total conductivity is almost identical to $x=0.3$, although the bulk conductivity is slightly lower, again related to the smaller amount of Ti^{3+} retained from the high reaction temperature in comparison to $x=0.3$ (figure 5.19). Looking back to the TGA data (figure 5.6), it is clear that re-oxidation is faster with increasing the Sc content, hence σ will decrease, which matches with the impedance results.

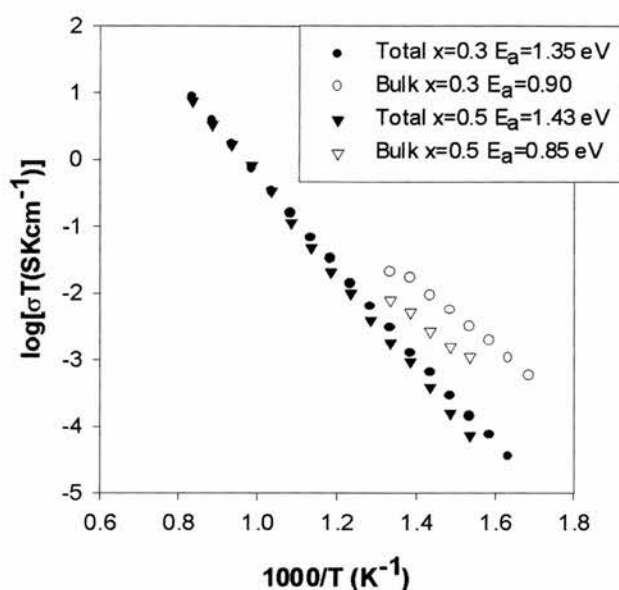


Figure 5.19. Arrhenius plots corresponding to $x=0.3$ and $x=0.5$. A Drop in the conductivity is observed when increasing the Sc content.

5.4.2.2. Four terminal techniques.

As occurred for the non-substituted phases, conductivity increased drastically upon reduction, which makes ac impedance an unsuitable technique to estimate it. The temperature dependence of the conductivity of $x=0.5$ in reducing conditions was evaluated by measuring in dry and wet flowing H_2/Ar atmospheres (figure 5.20). The samples were initially annealed at high temperature (950°C) until equilibrium was achieved. In the most reducing conditions (dry H_2/Ar) quite high total conductivity in the range of temperatures studied, e.g. 10 Scm^{-1} . However the most important feature must be found in the metal to insulator transition observed at $250\text{-}300^\circ\text{C}$. This metal-insulator transition could be understood in terms of a change from dominant metallic to dominant semiconductor on cooling. The two components could be a semiconducting grain boundary and a metallic grain. Thus at high temperature the grain component would dominate, whereas at low temperature the grain boundary is

dominating. This would agree with the results observed for the Sc-free sample in wet H_2/Ar and also with the insulating nature of the grain boundaries postulated by impedance results. The lower conductivity in comparison to the non-substituted phase might be explained by Sc^{3+} stabilising Ti^{4+} , hence decreasing the amount of Ti^{3+} leading to a lower conductivity due to the smaller number of charge carriers. In slight more oxidising conditions (wet 5% H_2/Ar) the sample acts as a semiconductor in temperature range studied.

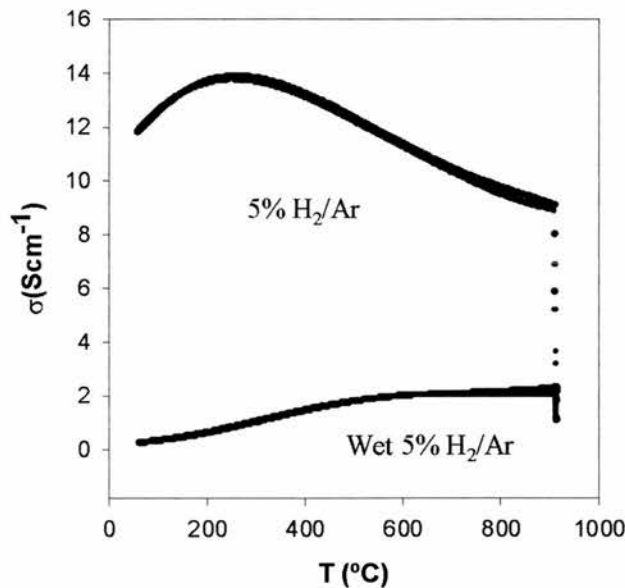


Figure 5.20. Total conductivity in reducing conditions for $x=0.5$ as a function of the temperature.

A metal to insulator transition is observed in the more reducing conditions at 250-300°C.

5.4.3. $\text{La}_2\text{Sr}_4\text{Ti}_{5.0}\text{Sc}_{1.0}\text{O}_{18.50}$ ($x=1.0$).

Similar behaviour was found for $x=1.0$. Grain boundary contributions again dominate the responses, confirming their insulating nature. The responses were fitted using two R-CPE elements in series as shown in figure 5.21 instead of two RC elements used before, because Debye responses used for the earlier examples did not adequately model these phases. This is related with the lower relative density in the

samples with higher Sc content compared to the samples with lower content. The distortion observed in the low frequency range is due to the thermal fluctuation in the furnace, rather than an electrochemical process. The presence of diffusion phenomena or any other electrode response is not detected.

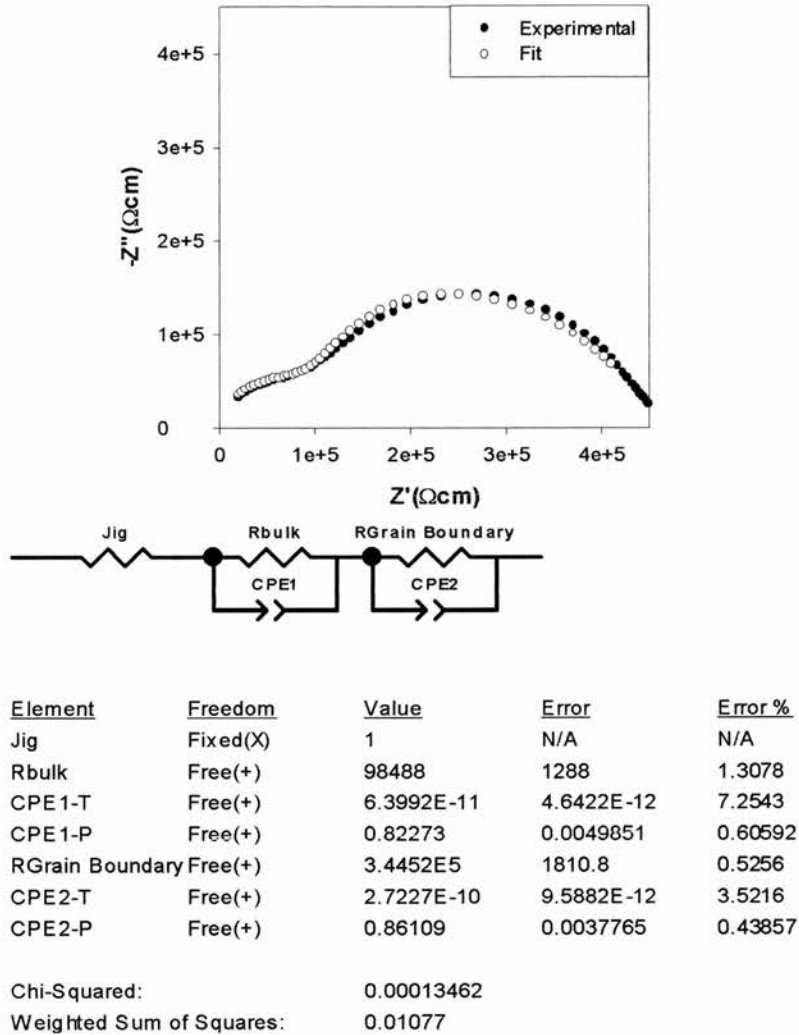


Figure 5.21. Nyquist plot for $x=1.0$ at 608°C adjusted using equivalent circuits. The fit is quite good as can be extracted from both the plot and the fitting parameters

It should be noted that the parameter CPE-T is not identical to the capacitance associated with the process. The capacitance can be estimated from the definition of the relaxation frequency:

$$RC = \frac{1}{2\pi f} = (RQ)^{1/n} \quad [\text{equation 5-2}]$$

From equation 5-2, the capacitance can be calculated as

$$C = R^{-\frac{n+1}{n}} Q^{1/n} \text{ [equation 5-3]}$$

Thus, the capacitance associated with the bulk is $5 \times 10^{-12} \text{ Fcm}^{-1}$ whereas is $6 \times 10^{-11} \text{ Fcm}^{-1}$ for the grain boundary. The fairly low capacitance associated with the grain boundary can be attributed to the high porosity of the pellet used during ac impedance measurements (20%).

The Arrhenius plot reveals that the bulk conductivity drops compared to $x=0.5$, which is further evidence indicating that the presence of Sc has a negative effect in the conductivity (figure 5.22). The total conductivity also drops as a consequence of both the lower bulk conductivity and the higher porosity.

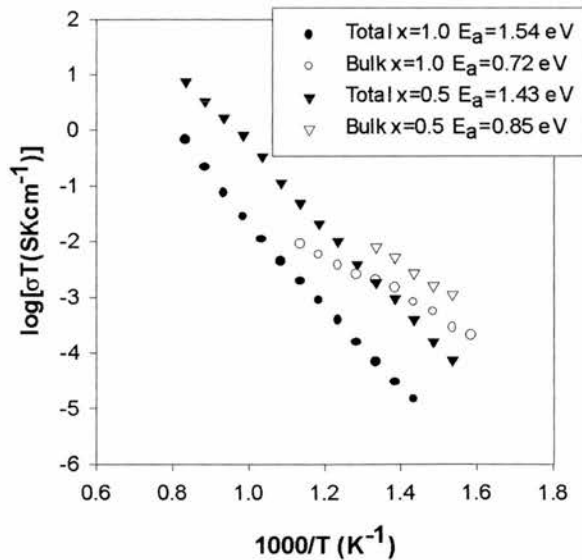


Figure 5.22. Arrhenius plots for $x=0.5$ and 1.0 . The conductivity keeps dropping with increasing the Sc content.

5.4.4. $\text{La}_2\text{Sr}_4\text{Ti}_{4.5}\text{Sc}_{1.5}\text{O}_{18.25}$ ($x=1.5$).

The last composition attempted of the Sc substituted phases follows the general trends observed through the series, i.e. the responses are dominated by the grain boundary contribution ($10^{-10} \text{ Fcm}^{-1}$) as shown in figure 5.23.

It should be noted that in the spectroscopic plot of the imaginary modulus (figure 5.23b) there appears again the tail of a peak in the high frequency range, which could be due to an artefact caused by the experimental setup

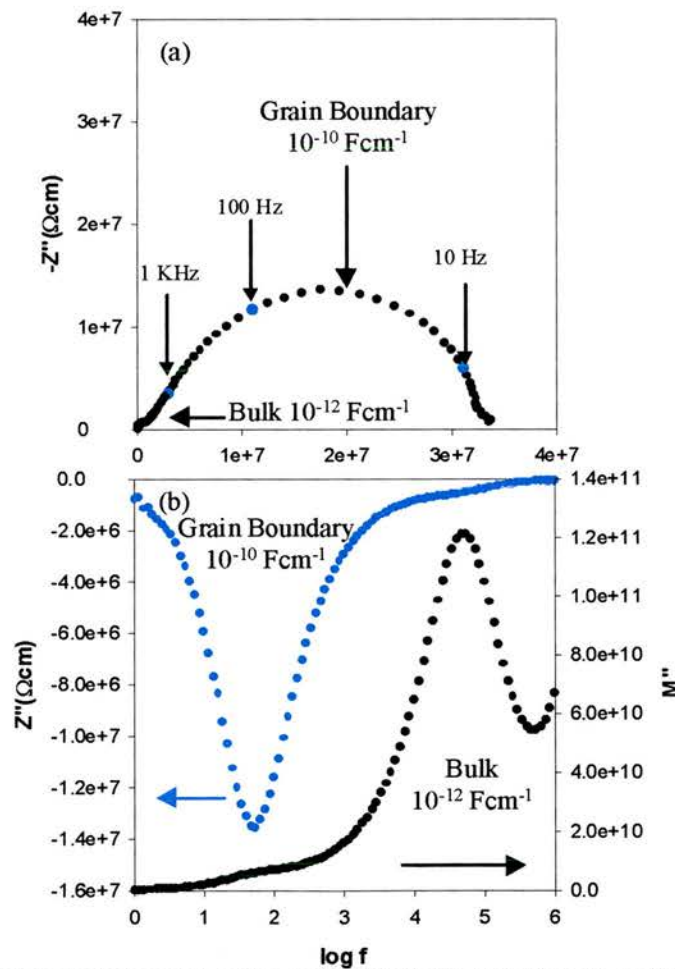


Figure 5.23. Nyquist plot (a) and spectroscopic plot of the imaginary impedance (Z'') and modulus (M'') for $x=1.5$ at 449°C .

In the Arrhenius plot, the conductivity was found to further decrease as expected from the general tendency observed for lower substitution level as shown in figure 5.24.

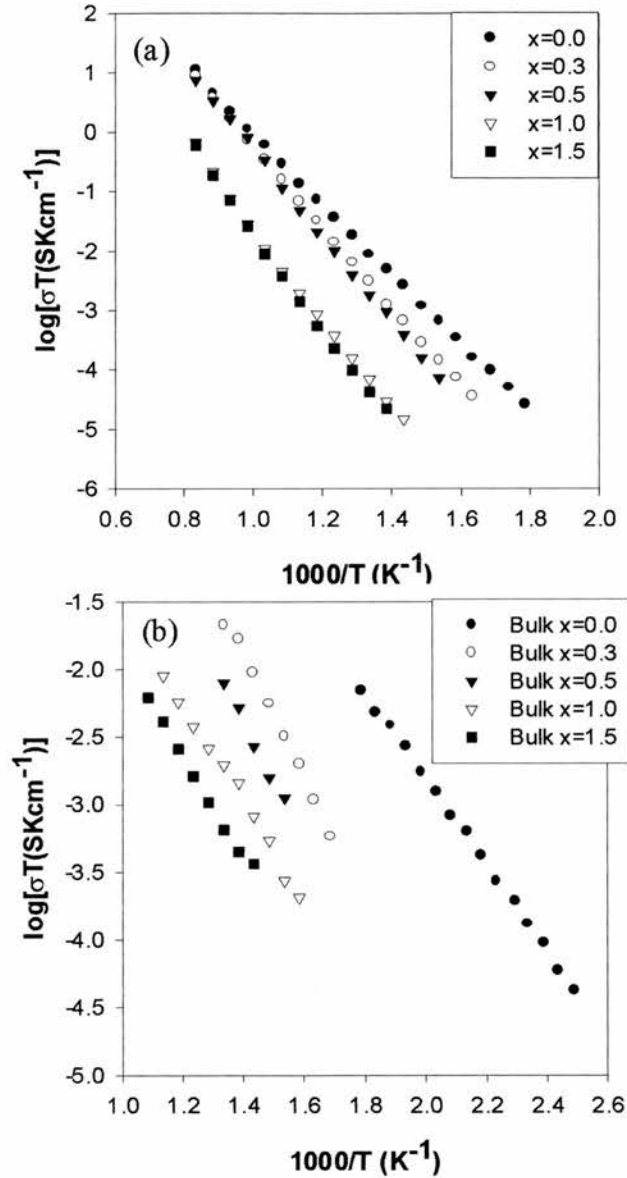


Figure 5.24. Arrhenius plot of the total conductivity (a) and bulk conductivity (b) of the Sc series.

Conductivity gradually drops as the concentration of Sc increases.

Therefore the substitution of Ti^{4+} by Sc^{3+} on the B-site of the perovskite framework does not have a positive effect on the electrical properties of these phases. On contrary, the conductivity drops as a function of the Sc content. On the other hand,

the presence of Sc accelerates the process of re-oxidation, which may be a benefit in the potential use of these materials as oxygen sensors.

5.5. Summary.

The effects in both the structure and the electrical properties caused by substitution at different levels of Ti^{4+} by Sc^{3+} on the $n=12$ member of the $\text{La}_4\text{Sr}_{n-4}\text{Ti}_n\text{O}_{3n+2}$ series have been investigated. Such substitution causes a decrease in the amount of excess oxygen in order to maintain the electroneutrality. Also the presence of Sc^{3+} helps to accelerate the re-oxidation of Ti to the 4+ state as shown by TGA.

XRD revealed that the unit cell is still a simple cubic perovskite until $x=1.0$. At a higher level of substitution a mixture of phases appears. The unit cell gradually expands as the concentration of Sc increases, which could relate to the larger ionic radius of Sc^{3+} vs. Ti^{4+} . Reduced phases show slight shrinkage in comparison to the oxidised phases, although their unit cell also expands with the Sc content. This is a quite interesting result because Sc^{3+} and Ti^{3+} have very similar ionic radii and therefore a priori they should modify the unit cell in the same manner. The formation of long distance $\text{Ti}^{3+}\text{-O-Ti}^{3+}$ or even $\text{Ti}^{3+}\text{-O-Ti}^{4+}$ pairs seems a quite likely explanation for such unit cell evolution.

As for the unsubstituted composition, superstructure reflections appear along the $[110]_p$, which causes the re-definition of the unit cell as face centred cubic with cell parameter $a=2a_p$. Subtle tilting of the octahedra within the perovskite framework is the most likely explanation for such doubling of the unit cell. The tilting is

presumably related with the accommodation of extra oxygen beyond the ABO_3 stoichiometry as well. The formation of linear defects results in a local distortion, which renders an average subtle tilting.

The smaller amount of excess oxygen in Sc-substituted phases, caused a reduction in the number and size of the local defects where it is placed until they become so diluted that are scarcely discernible by HRTEM. Therefore, a wide range in oxygen overstoichiometry has been covered in the course of this work, from large amounts that render more or less ordered crystallographic shears to very local defects covering just 2-3 unit cells.

The electrical properties are obviously affected and the conductivity drops with increasing Sc content due to the gradual decrease of the charge carriers concentration. As for ionic transport, no diffusion processes are detected by impedance spectroscopy, indicating that the overall response is dominated by the electronic contribution. The preference of these B-cations to be hexa-coordinated may be an important factor that impedes better ionic transport.

These results indicate that the Sc series may not improve the performance of the non-substituted phase as anode in a working fuel cell. The substitution of Ti by cations with preference for coordination other than octahedral such as Ga or Mn, could be an interesting research topic for the future.

5.6. References.

1. D. Lybye and N. Bonanos, *Solid State Ionics*, **125** (1-4) (1999), 339.
2. Y. Le Page and P. Strobel, *J. Solid State Chem.*, **43** (1982), 314.
3. Y. Le Page and P. Strobel, *J. Solid State Chem.*, **44** (1982), 273.
4. M. Marezio, D. Tranqui, S. Lakkis and C. Schlenker, *Phys. Rev. B*, **16(5)** (1977), 2811.

Chapter 6. Nb-substituted $\text{La}_4\text{Sr}_{n-4}\text{Ti}_n\text{O}_{3n+2}$	202
6.1. Introduction	202
6.2. Structural characterisation	203
6.3. Electrical properties on Nb-substituted phases	216
6.3.1. $\text{La}_2\text{Sr}_4\text{Ti}_{5.7}\text{Nb}_{0.3}\text{Ti}_{19.15}$ ($x=0.3$)	216
6.3.2. $\text{La}_2\text{Sr}_4\text{Ti}_{5.5}\text{Nb}_{0.5}\text{Ti}_{19.25}$ ($x=0.5$)	219
6.4. Conclusions	224

6. Nb-substituted $\text{La}_4\text{Sr}_{n-4}\text{Ti}_n\text{O}_{3n+2}$.

6.1. Introduction.

The effect of substituting $\text{La}_2\text{Sr}_4\text{Ti}_6\text{O}_{19}$ with a trivalent cation (Sc^{3+}) was investigated in the previous chapter. It was observed that the substitution of Ti^{4+} by a lower valence cation results in a decrease of the excess oxygen in the structure. The opposite approach was attempted in this chapter: the substitution of Ti with a higher valence cation, Nb^{5+} . Such substitution should imply an increase in the oxygen content and therefore, the structure and properties should be *a priori* comparable to some of the lower n members in $\text{La}_4\text{Sr}_{n-4}\text{Ti}_n\text{O}_{3n+2}$ series, i.e. the layered phases.

Samples were prepared by solid state reaction according to the general formula $\text{La}_2\text{Sr}_4\text{Ti}_{6-x}\text{Nb}_x\text{O}_{19+x/2}$, with $x=0.3$ and $x=0.5$, which corresponds to 5 and 8.3% of substitution on the B-sites of the perovskite. Nb-substituted samples present a similar amount of excess oxygen to that of the $n=10$ member as shown in table 6-1.

Formula	Excess oxygen (δ)
$\text{La}_2\text{Sr}_4\text{Ti}_6\text{O}_{19}$ ($n=12$)	0.167
$\text{La}_2\text{Sr}_3\text{Ti}_5\text{O}_{16}$ ($n=10$)	0.200
$\text{La}_2\text{Sr}_2\text{Ti}_4\text{O}_{13}$ ($n=8$)	0.250
$\text{La}_2\text{Sr}_4\text{Ti}_{5.7}\text{Nb}_{0.3}\text{O}_{19.15}$	0.192
$\text{La}_2\text{Sr}_4\text{Ti}_{5.5}\text{Nb}_{0.5}\text{O}_{19.25}$	0.208

Table 6-1 Excess oxygen relative to the ABO_3 stoichiometry.

6.2. Structural characterisation.

XRD revealed that indeed the Nb-substituted compounds were very close structurally speaking to the $n=10$ member in the $\text{La}_4\text{Sr}_{n-4}\text{Ti}_n\text{O}_{3n+2}$ series as the oxygen content δ suggested (figure 5.1). Nb-substituted samples also presented peaks in the range $28-31^\circ$ in 2θ , which is representative of layered phases as discussed in chapter 3. The characteristic reflection at slightly higher 2θ values than the (110) of the simple cubic unit cell also appears. There is almost no variation between the two different Nb contents, although the extra reflection at 33° gets bigger with increasing x (figure 5.1.b). Thus, the XRD patterns of the Nb-substituted can be indexed as a mixture of phases: cubic + layered.

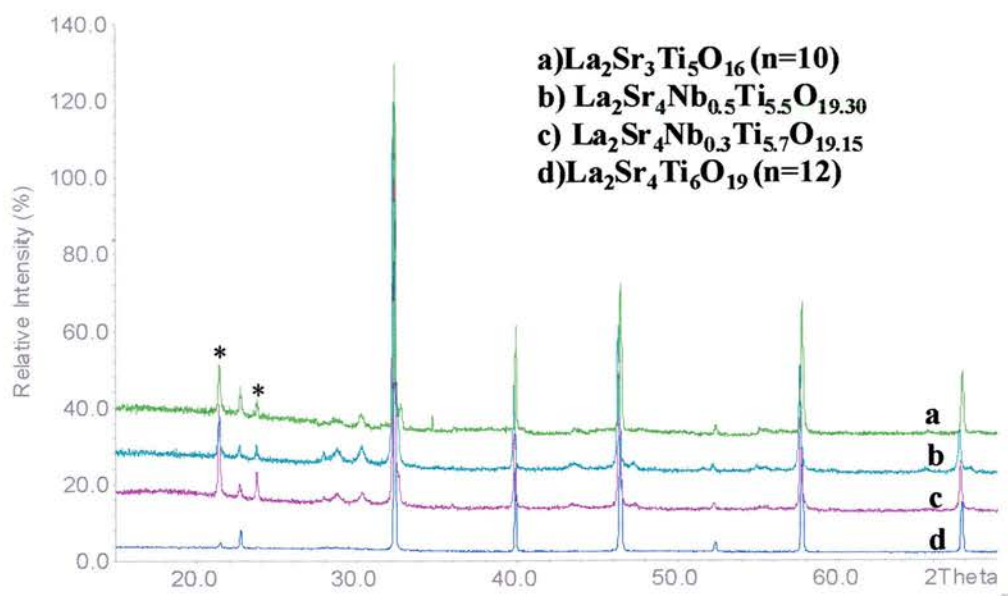


Figure 6.1a. XRD patterns of the Nb-substituted phases compared to the $n=10$ and $n=12$ members of the $\text{La}_4\text{Sr}_{n-4}\text{Ti}_n\text{O}_{3n+2}$ series. * denotes vaseline peaks.

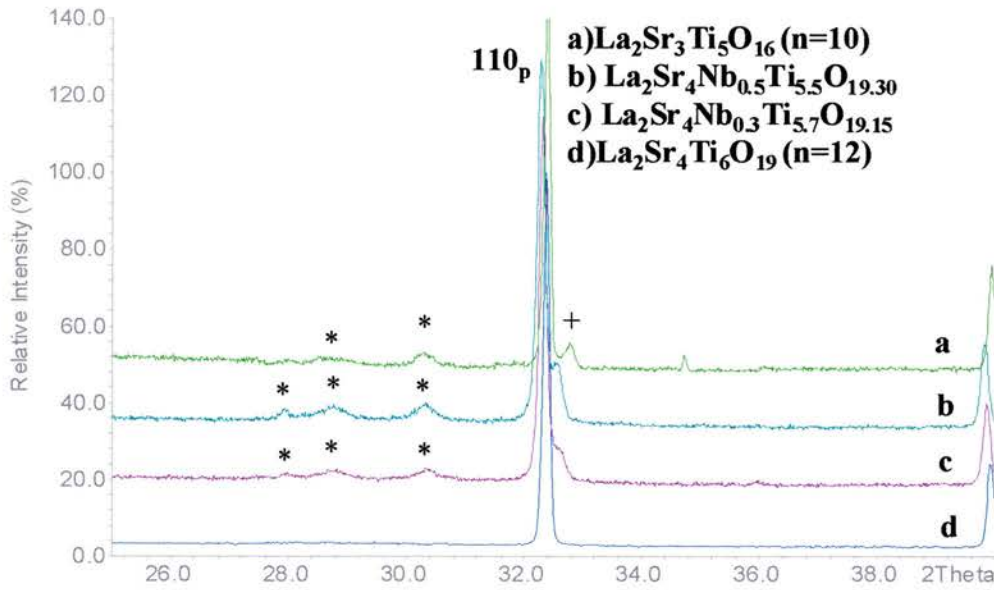


Figure 6.1b. Detailed XRD pattern focusing on the 110_p peak. * indicates characteristic “layered” peaks and + the extra reflection at 33° .

The presence of the characteristic reflections of the layered phases indicates that excess oxygen is the cause in the formation of layered structures. It is not only a particular element causing the layered structure, but the excess of positive charge compared to a perovskite that is compensated by the creation of oxygen rich planes. Therefore, there is a vast range of cationic substitutions that potentially would lead to the formation of layered perovskites. The formation of such layered structures is favoured for oxygen content higher than 3.18, comparing to the ABO_3 parental perovskite as depicted in figure 6.2. At 3.167, the structure is pseudo-cubic as discussed in chapters 3 and 5, characterised by the presence of local defects randomly distributed within the perovskite matrix. On the other hand, at higher oxygen contents, the characteristic peaks of layered compounds appear because the excess oxygen is accommodated in crystallographic shears in a concentration high enough to become a regular feature in the structure. The link between both structural-types should be

found in local defects reaching a concentration sufficient high to form “clusters” or extended defects, and in the end crystallographic shears.

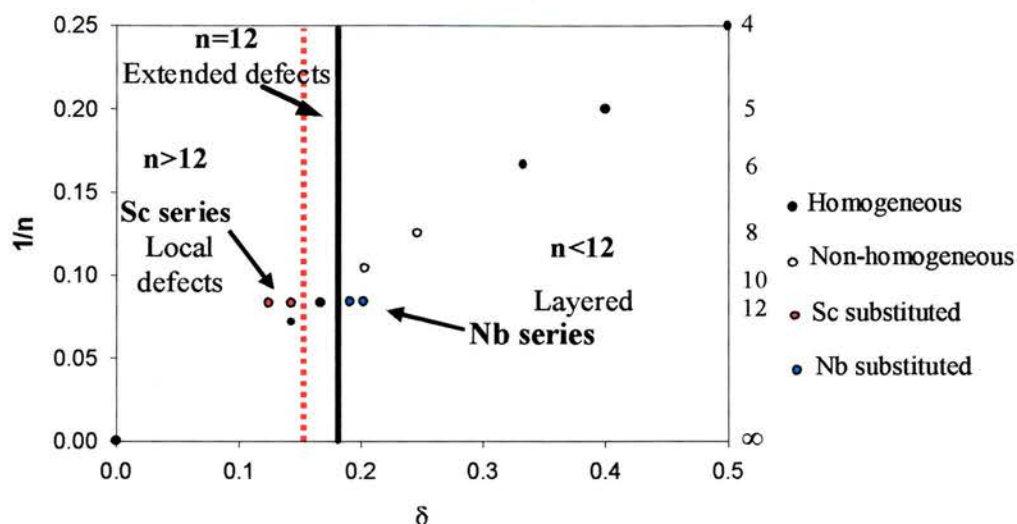


Figure 6.2. Structure as a function of the oxygen overstoichiometry (δ). The presence of Nb causes an increase in the oxygen content due to the surplus of positive charge provided in comparison to Ti^{4+} .

TEM studies confirm the presence of the layered structure cohabiting with perovskite domains for $x=0.3$ as shown in figure 6.3, which is in agreement with that described for $n < 12$ in the $\text{La}_4\text{Sr}_{n-4}\text{Ti}_n\text{O}_{3n+2}$ series. There is a very important feature observed in this figure: the layered regions seem to cluster in nanodomains rather than give rise to crystallographic shears randomly distributed within the perovskite framework. EDS studies performed on the crystal shown in figure 6.3 reveals that there is chemical segregation, which may help to understand the nature of layered perovskites. The layered region presents an anomalous high La and Nb content whereas the Sr is somewhat lower than expected. On the other hand, the perovskite domains have lower La and Nb content, closer to the expected theoretical values as listed in table 6-2.

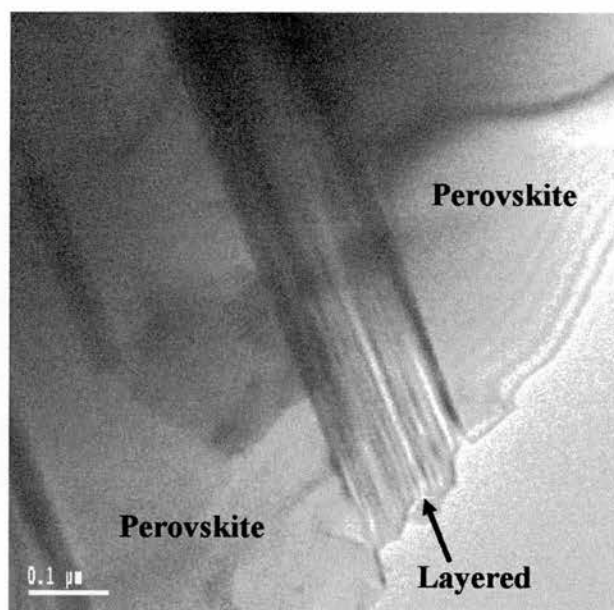


Figure 6.3. HRTEM image at low magnification showing the presence of a layered domain imbedded in a perovskite matrix.

Element	% (layered)	%(perovskite)	%(theoretical)
Ti	42	48	47.5
Nb	4	1	2.5
La	24	17	16.7
Sr	30	35	33.3

Table 6-2. EDS results for $\text{La}_2\text{Sr}_4\text{Nb}_{0.3}\text{Ti}_{5.7}\text{O}_{19.15}$. La content is higher than expected in the layered domains.

These results could help to understand the mechanism of formation of $\text{A}_n\text{B}_n\text{O}_{3n+2}$ phases for lower n values (figure 6.4). Two phases are formed during an early stage of the reaction: a simple cubic perovskite, presumably with stoichiometry very close to SrTiO_3 , and a layered phase with composition very close to $\text{La}_2\text{Ti}_2\text{O}_7$ (and probably $\text{Sr}_2\text{Nb}_2\text{O}_7$). After that, both phases react giving larger perovskite blocks within the layered domains due to the incorporation of perovskite layers. As a consequence of this, the formation of homogeneously distributed large perovskite blocks is a very slow process that requires extremely long reaction times at high temperature, as observed for $n < 12$ in the non-substituted series.

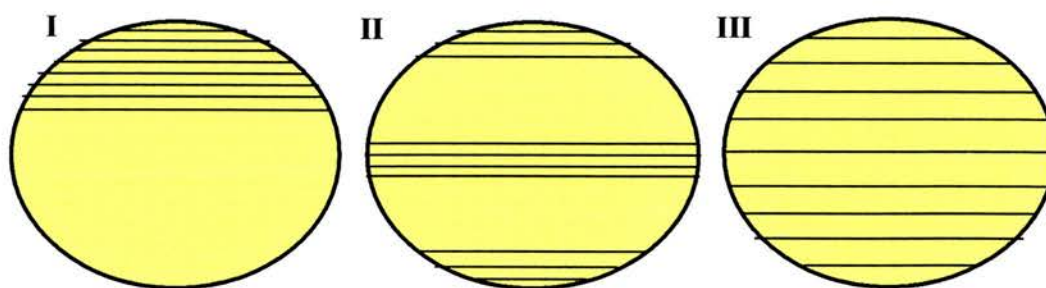


Figure 6.4. Schematic mechanism of reaction proposed for $\text{A}_n\text{B}_n\text{O}_{3n+2}$ layered perovskite for large n . During the first stage, two phases are formed (I). Then the two phases start to intergrow in an irregular fashion (II) to finally render a homogeneous distribution of the two phases, i.e. creating a new phase (III).

If the mechanism proposed is correct, one might think that the presence of La on the A-sites (and Nb on the B-sites) of the perovskite is the cause of the formation of the crystallographic shears, due to oxygen compensation for the excess of positive charge resulting from the substitution of Sr (and Ti). Moreover, La and Nb might be expected to be in slightly higher concentration in the shear layers than in the perovskite blocks, as EDS reveals (see above). However, care must be taken in the interpretation of the model/mechanism proposed because one might be misled and think that La should not be present in the bulk of the perovskite domains. It should be noticed that the layered regions observed in this particular sample are in much lower concentration than the perovskite domains. If La were only at the end of the perovskite blocks, then the stoichiometry would not correspond to $\text{La}_2\text{Sr}_4\text{Ti}_{5.7}\text{Nb}_{0.3}\text{O}_{19.15}$. Then, there is also La within the perovskite matrix although in lower concentration and possibly giving rise to short range crystallographic oxygen shears as occurred for the undoped material. In fact, in figure 6.5 it is possible to see the formation of one of these crystallographic oxygen shears in the middle of a

perovskite block, which seems to suggest that the mechanism of the shear formation relates to oxygen agglomeration along the shears.

The situation for Nb is more complicated because its theoretical ratio (2.5%) is within the experimental error. However, the difference with the non-substituted composition is obvious and it is reasonable to think that Nb tends to concentrate in the layered domains to give rise to structures related to $\text{Sr}_2\text{Nb}_2\text{O}_7$, i.e. isostructural to the $\text{La}_4\text{Sr}_{n-4}\text{Ti}_n\text{O}_{3n+2}$ series.

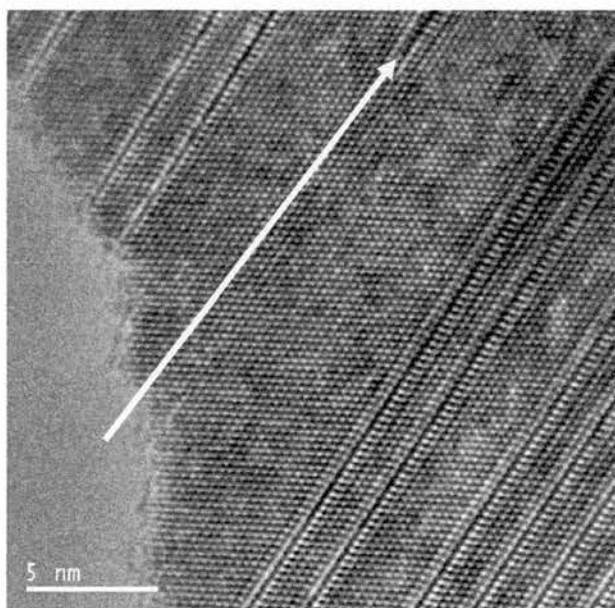


Figure 6.5. HRTEM image of the irregular intergrowth of diverse-sized perovskite blocks in $\text{La}_2\text{Sr}_4\text{Nb}_{0.3}\text{Ti}_{5.7}\text{O}_{19.8}$ viewed down the $[1-20]_m$ of a layered unit cell. The arrow indicates the formation of a crystallographic shear in the middle of the perovskite block.

Figure 6.6 shows some selected HRTEM images showing the irregular intergrowth of diverse sized perovskite blocks down the $[111]_p$ projection on a cubic perovskite or, in other words, the $[1-20]_m$ projection on a monoclinic layered perovskite based on $\text{La}_2\text{Ti}_2\text{O}_7$. This zone axis is a suitable choice because it is probably the one that most clearly shows the relation between the two structural

motifs, i.e. the ABO_3 perovskite and the $\text{A}_n\text{B}_n\text{O}_{3n+2}$ layered compound. The perovskite blocks show a hexagonal pattern that changes to square at the crystallographic shears.

Annealing at high temperature for extremely long periods of time would presumably yield perovskite blocks joined by crystallographic shears homogeneously distributed within the crystals.

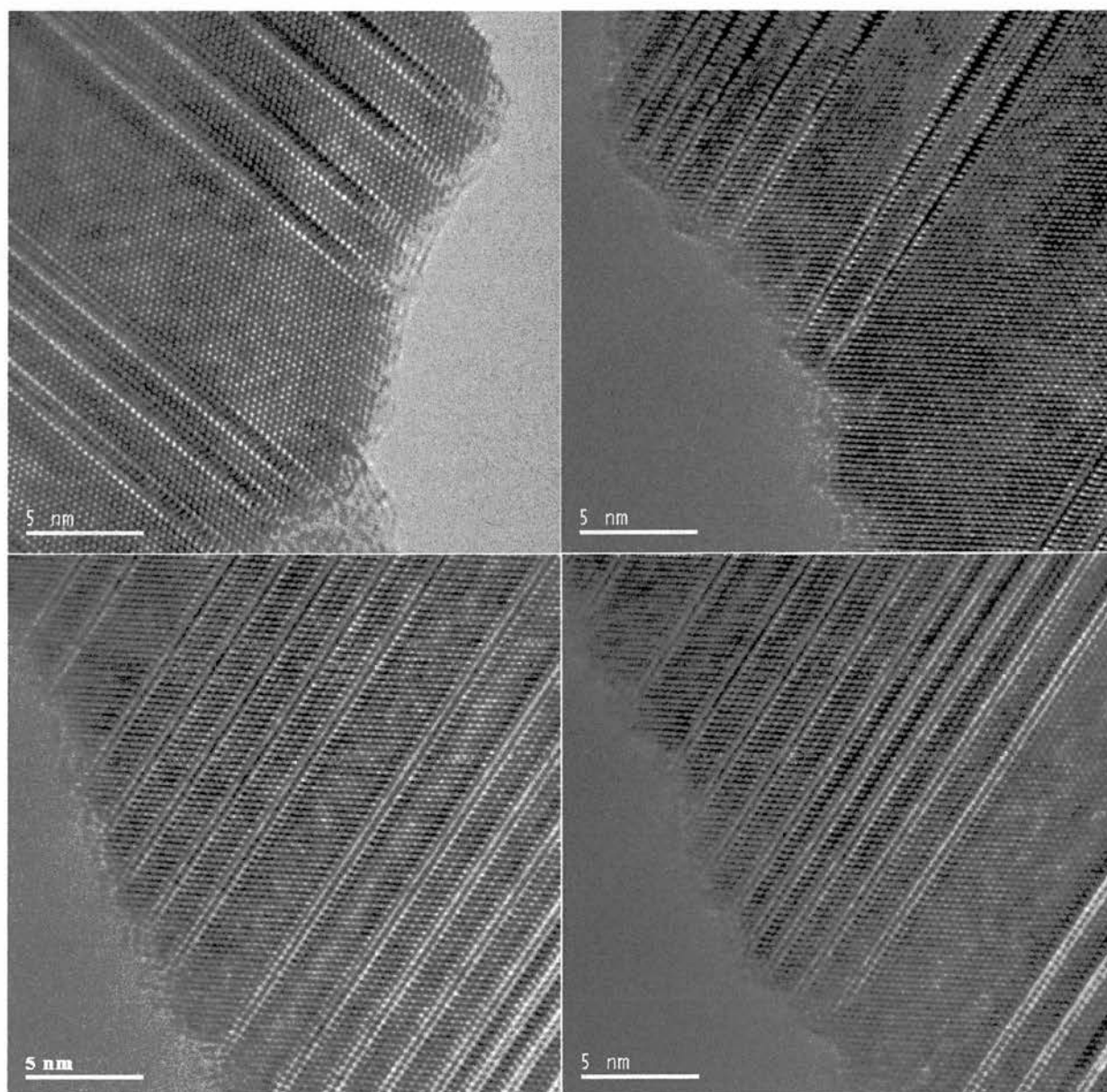


Figure 6.6. Selection of HRTEM showing the irregular intergrowth of diverse-sized perovskite blocks viewed down the $[1-20]_m$ (equivalent to $[111]_p$) in $x=0.3$.

Figure 6.7 shows some selected SAED patterns corresponding to the $[111]_p$ zone axis on a cubic perovskite, i.e. $[1-20]_m$ based on a monoclinic unit cell, showing clearly the presence of superstructure reflections together with some diffuse scattering, as result of the irregular intergrowth of diverse-sized perovskite blocks. The different aspect of the SAED patterns is a result of the heterogeneous distribution in size of the perovskite blocks. All of them have in common the $\{110\}_p$ reflections, whilst the weaker reflections indicate the heterogeneous nature of the sample studied.

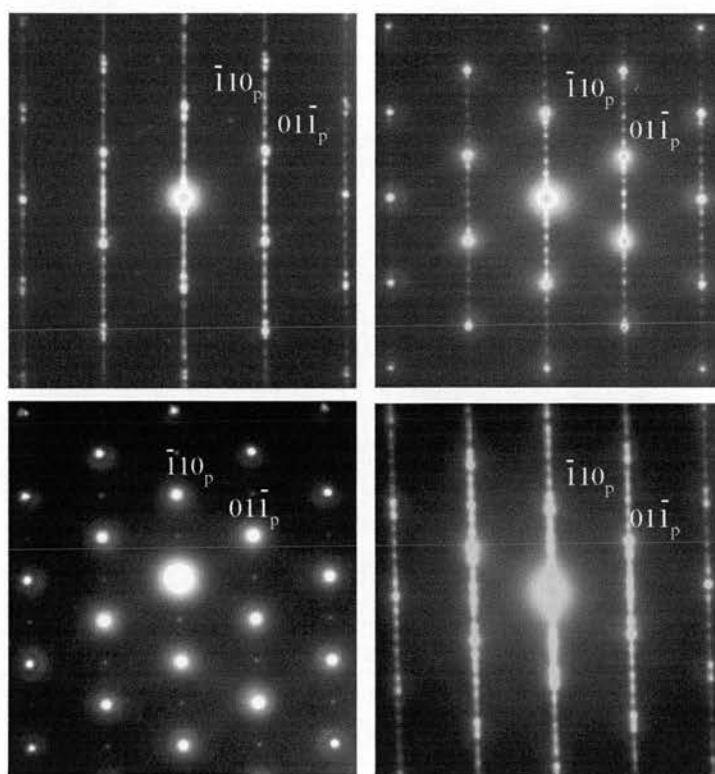


Figure 6.7. Selected SAED patterns showing different aspect of projections down the $[111]_p$ zone (equivalent to the $[1-20]_m$) axes for several crystallites, which indicates the heterogeneity of $x=0.3$ in synthetic conditions used.

Figure 6.8 gives additional information of the complexity of these phases, showing a HRTEM that would correspond to a view down the $[111]_p$ projection on a cubic perovskite. Crystallographic shears are not detected in this crystal. There exists however, a large number of nanodomains in dark contrast, which would have a similar

origin to those observed in the non-substituted material. La (and possibly some Nb) presumably causes the presence of local defects in the structure, where the extra oxygen beyond the ABO_3 stoichiometry is accommodated maintaining the electroneutrality of the crystals. Their large concentration in the crystal suggests that they are close to giving rise to extended defects in the form of crystallographic oxygen shears.

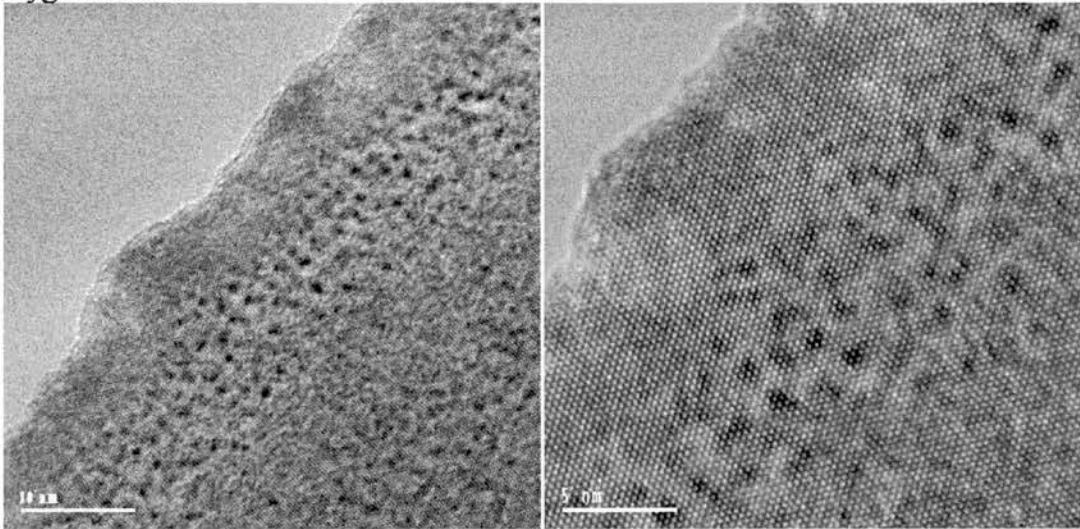


Figure 6.8. HRTEM images viewing down the $[111]_p$ projection on a perovskite for $x=0.3$. A large amount of local defects is evident (dark contrast areas).

It should be noted that the diffuse scattering observed in the corresponding SAED pattern must be related to the large amount of defects, otherwise the pattern should resemble the $[111]_p$ on SrTiO_3 (figure 6.9).

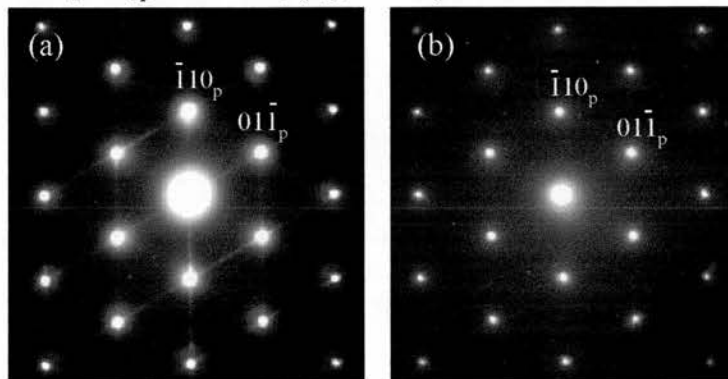


Figure 6.9. SAED patterns viewing down the $[111]_p$ projection for $x=0.3$ (a) and SrTiO_3 (b). The presence of streaking due to disorder along $\{110\}_p$ is evident in the former.

Further evidence to confirm that local defects in enough high concentration will yield extended crystallographic shears, lies in the lack of such local defects when the formation of layered domains occurs (figure 6.10). No local defects can be observed within the perovskite blocks in the layered domains.

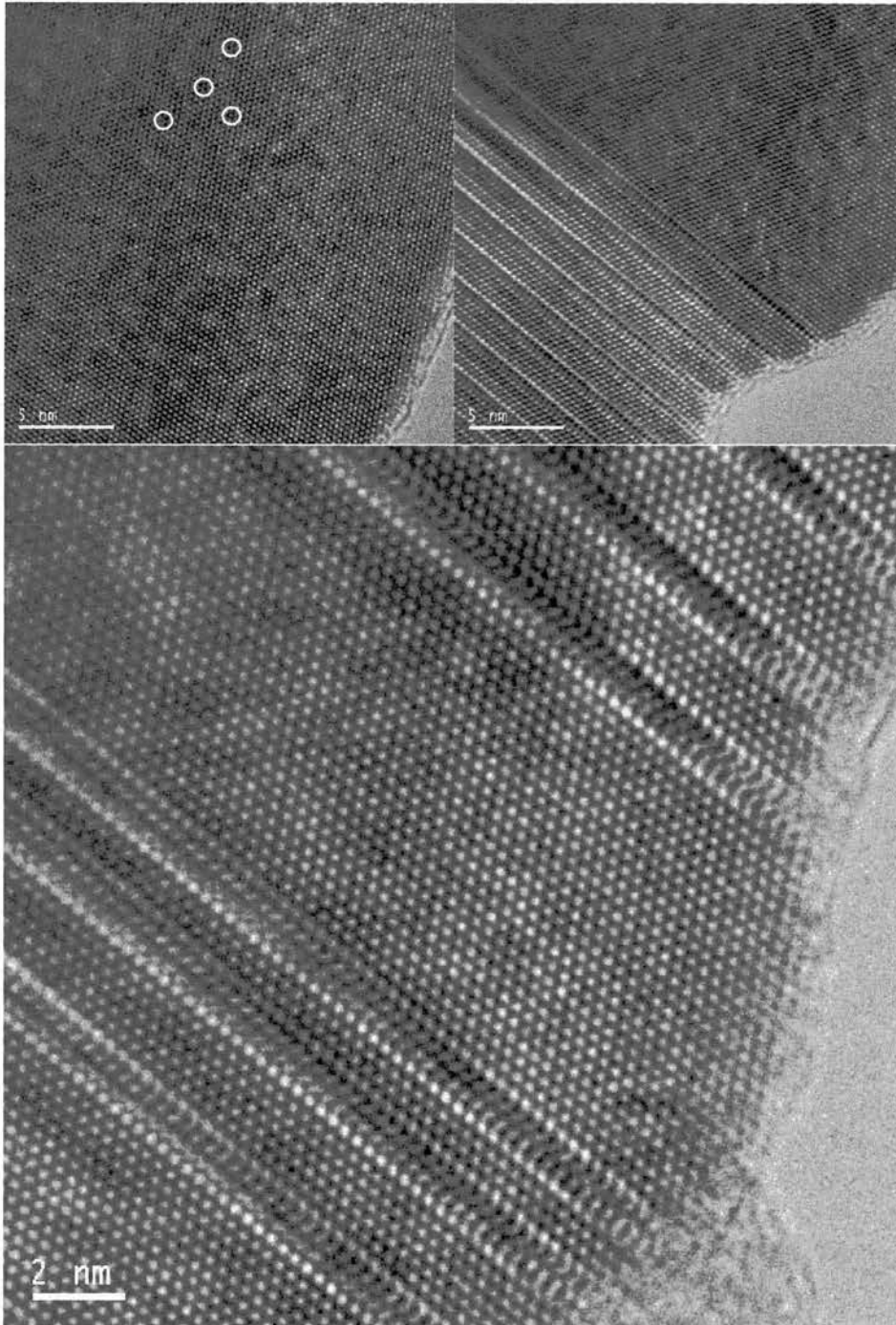


Figure 6.10. Selected HRTEM images viewing down the $[111]_p$ or $[1-20]_m$ zone axes in $x=0.3$. The formation of the extended crystallographic shears results in lower concentration of local defects within the blocks.

As for the non-substituted phase, the presence of local defects rather than crystallographic shears (extended defects) is a function of concentration. In the region shown in figure 6.11a, the amount of excess oxygen is not large enough to give rise to extended defects, whereas in other regions of the crystal (figure 6.11b) their formation is favoured. This could be explained in terms of cation segregation and thus causing the presence of a mixture of several “phases” related to the primitive cubic perovskite.

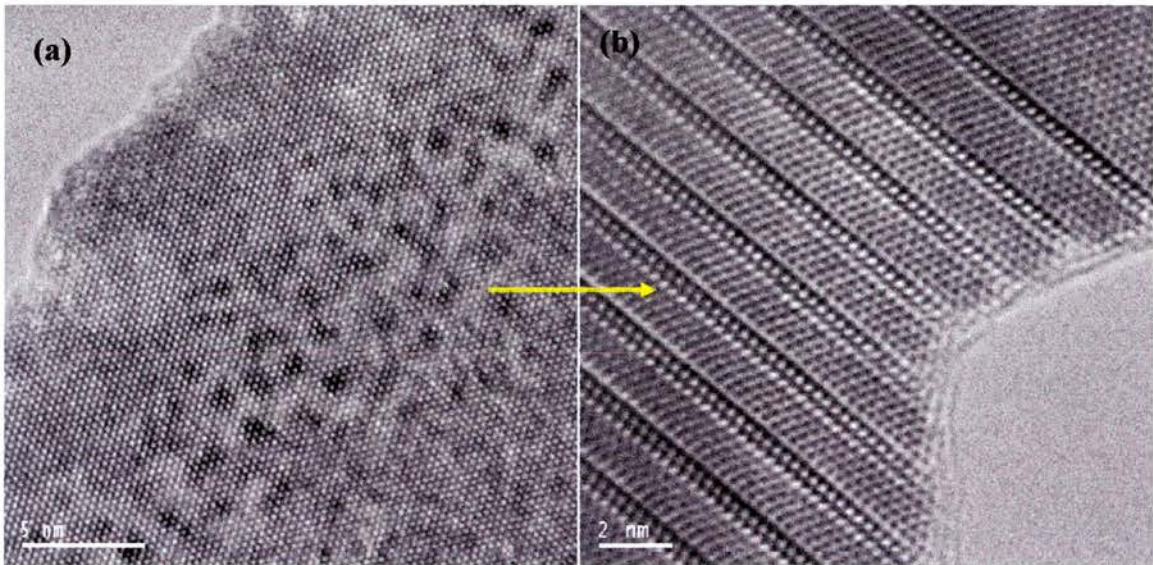


Figure 6.11. HRTEM images showing crystallites with high concentration of local defects in $x=0.3$ ($[1-20]$ zone axis) (a) and with extended crystallographic shears (b). Transformation from one to another is just a matter of concentration.

The layered phases are obviously related to $\text{La}_2\text{Ti}_2\text{O}_7$, having approximately the same a and b unit cell parameters, i.e. $a \approx 7.8 \text{ \AA}$ and $b \approx 5.5 \text{ \AA}$ (figure 6.12a), only changing the c -axis as the perovskite blocks become larger since the mechanism of accommodating excess oxygen is the same. On the other hand, cubic domain crystals are more similar to the primitive cubic perovskite, $a \approx 3.9 \text{ \AA}$ (figure 6.12b). It should be kept in mind that annealing for extremely long periods should render perovskite blocks regularly distributed in the crystal.

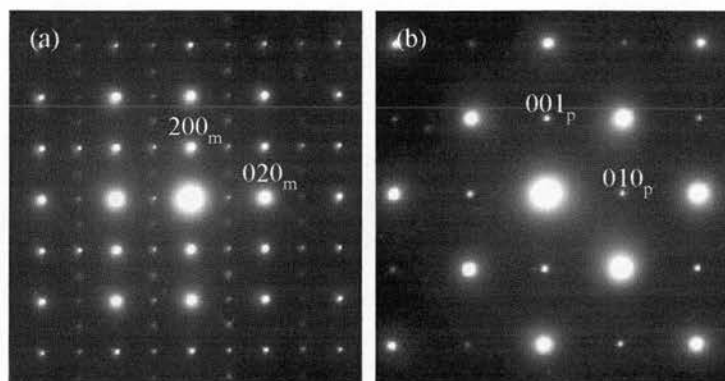


Figure 6.12. SAED patterns showing a view down the $[001]_m$ projection based on a $\text{La}_2\text{Ti}_2\text{O}_7$ -like unit cell (a) and the $[100]_p$ zone axis based on simple cubic perovskite in $x=0.3$.

TEM studies performed for higher Nb content, i.e. $x=0.5$, are in agreement with these results and disorder along the c -axis is also present as suggested in the SAED pattern shown in figure 6.13.

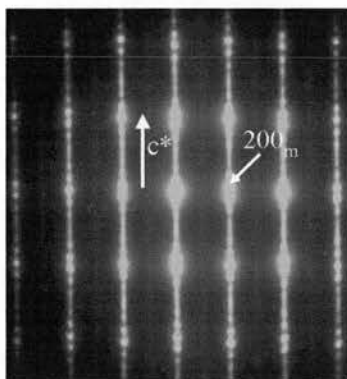


Figure 6.13. SAED pattern viewing down the $[010]_m$ based on a $\text{La}_2\text{Ti}_2\text{O}_7$ -like unit cell for $x=0.5$. Streaking along the c -axis is evident, which indicates disorder along that particular direction.

Figure 6.14 shows that there exists a relation between the layered and cubic phases. Thus the $[010]_m$ zone axis of the layered phases is related to the $[1-10]_p$ in the cubic domains. Therefore the brightest reflections along the c -axis for the layered

reflections (i.e. $(00n)_l$, where n is the number of layers per block), corresponds to a d-spacing of 2.75\AA , which is d_{hkl} of $\{110\}_p$.

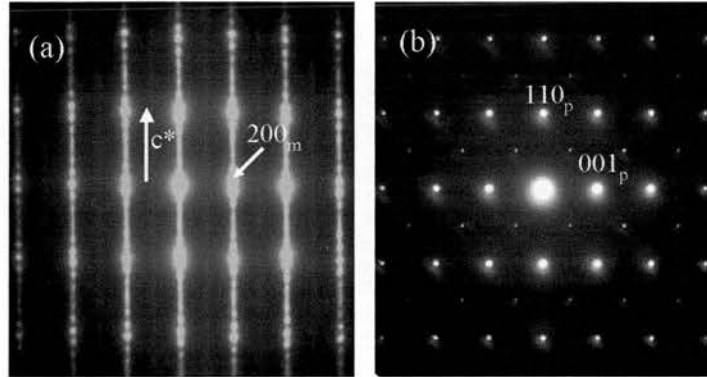


Figure 6.14. SAED patterns showing the relation between the $[010]_m$ (a) and the $[-110]_p$ (b) zone axes on layered ($x=0.5$) and cubic phases respectively ($x=0.0$).

TEM images indicate that indeed there is still an irregular intergrowth of layered and cubic domains (figure 6.15). As may be expected from the higher Nb content, the concentration of layered domains is also higher.

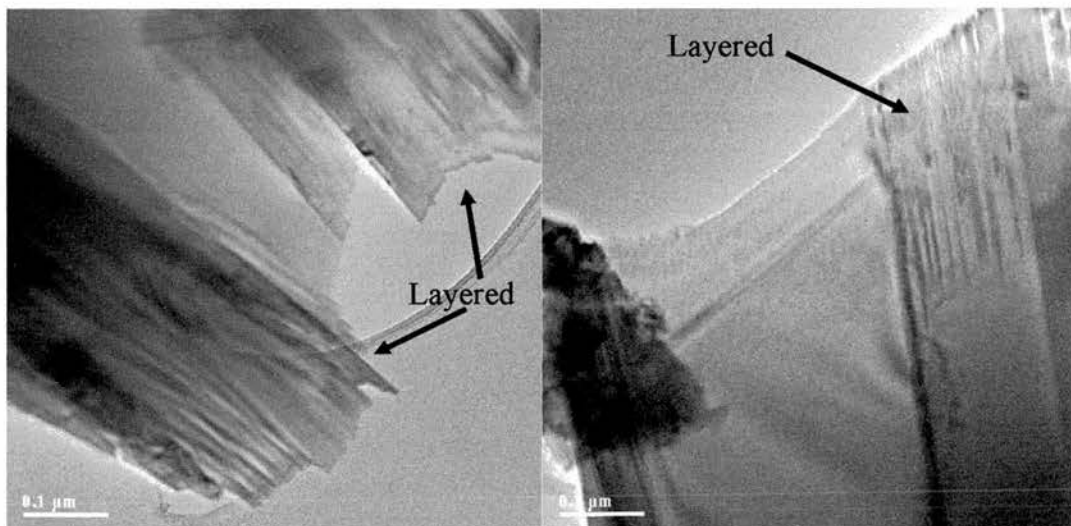


Figure 6.15. Low magnification TEM images showing layered and cubic domains cohabiting in the crystallites of $x=0.5$.

The presence of layered phases in the Nb-substituted phases also opens the possibility to investigate the formation of such phases in systems other than titanates. Niobates and tantalates have already been reported as layered perovskite for compositions with $n=4$ and 5. There is no apparent reason why higher n values cannot be synthesised, apart from the point of view of the very slow kinetics.

To our best knowledge, there are no reported investigations using cations such as Zr or V, which also could form layered perovskites. Synthesis and characterisation of new layered structures using “new” transition metals as B-cation could be a very interesting research topic for the future.

6.3. Electrical properties on Nb-substituted $\text{La}_2\text{Sr}_4\text{Ti}_6\text{O}_{19}$.

The electrical properties of the Nb-substituted phases can be evaluated using ac impedance spectroscopy as used for the non-substituted and Sc-substituted phases. The presence of layered domains will affect the total conductivity, making it drop due to the insulating nature of the crystallographic shears (low electrical conduction in the oxygen rich planes). However the presence of Nb may change the results obtained for the layered phases of the $\text{La}_4\text{Sr}_{n-4}\text{Ti}_n\text{O}_{3n+2}$ series.

6.3.1. $\text{La}_2\text{Sr}_4\text{Ti}_{5.7}\text{Nb}_{0.3}\text{O}_{19.15}$ ($x=0.3$).

The first distinctive feature compared to most of the phases in the non-substituted phases is that the responses are dominated by the bulk instead of the grain boundary. No low frequency responses related to electrode processes can be detected,

which could imply very low ionic conductivity, if any. The responses were analysed using the equivalent circuit model. A typical example is shown in figure 6.16.

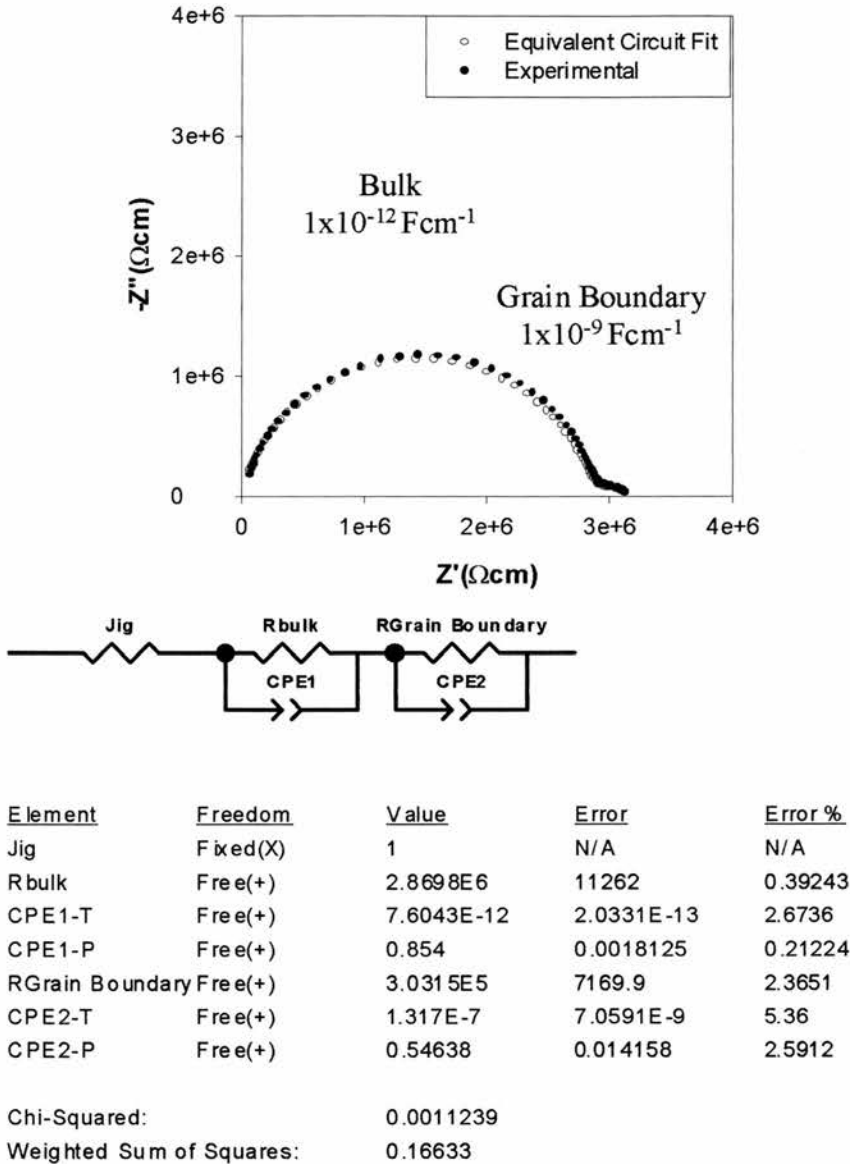


Figure 6.16. Equivalent circuit fitting for the response of $x=0.3$ at 608°C .

Although the results of the fitting are acceptable and look fairly good in the impedance complex plot, using the imaginary modulus formalism it is found that at high frequency, the tail of another electrochemical process is present (figure 6.17). Therefore another R-CPE element should be used to fit the response. However, it

should be kept in mind that the experimental setup affects the high frequency range causing an artificial response.

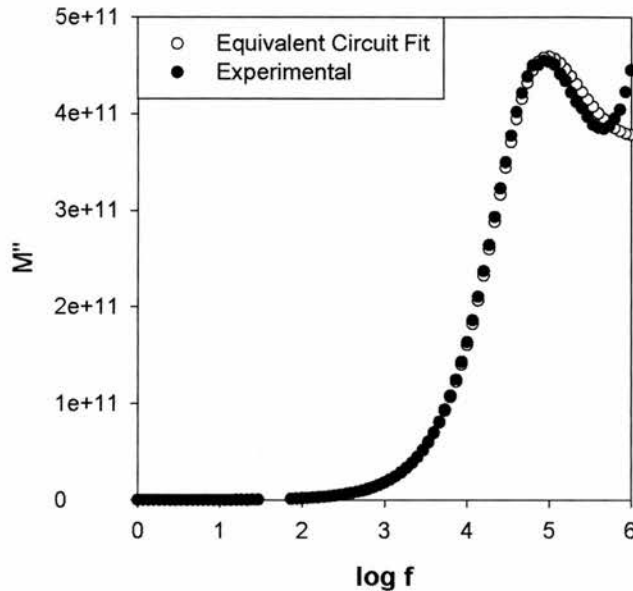


Figure 6.17. Spectroscopic imaginary modulus (M'') plot vs frequency for $x=0.3$ at 608°C and the corresponding simulated plot. At high frequency it appears a tail that is due to the instrument.

The corresponding Arrhenius plot (figure 6.18) confirms that indeed the bulk contribution is dominating the responses. The conductivity drops dramatically compared to the non-substituted phase, e.g. three orders of magnitude! These values are comparable to those of the layered phases on the $\text{La}_4\text{Sr}_{n-4}\text{Ti}_n\text{O}_{3n+2}$ series, as can be expected from their almost identical structure. There is however, a quite distinctive feature in the Nb-substituted samples which is the change in the slope observed, i.e. a change in the activation energy that occurs at approximately 600°C . The activation energy has two components, one related to enthalpy of migration (ΔH_m) and another related to the enthalpy of formation of new defects (ΔH_f). At low temperatures ΔH_m

dominates whilst from temperatures above 600°C, the formation of defects becomes significant and therefore its contribution is added to the enthalpy of migration.

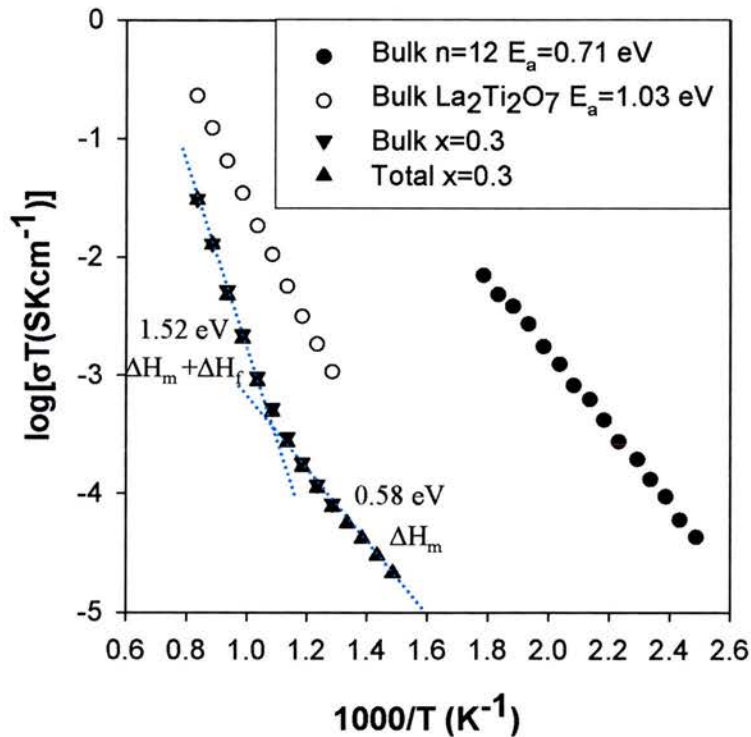


Figure 6.18. Arrhenius plots of $x=0.3$ compared to $x=0.0$ and $\text{La}_2\text{Ti}_2\text{O}_7$. The conductivity for $x=0.3$ is comparable to the layered phases. The change in the activation energy at approximately 600°C is evident.

6.3.2. $\text{La}_2\text{Sr}_4\text{Ti}_{5.5}\text{Nb}_{0.5}\text{O}_{19.25}$ ($x=0.5$).

Similar behaviour is found for $x=0.5$. The responses are dominated by the bulk contribution (figure 6.19a), although at lower temperatures the grain boundary becomes more important (figure 6.19b and c), as can be expected from the lower relative density compared to $x=0.3$ (85% vs. 95%). As in the previous case analysed,

no low frequency processes that could be related to an electrode response are detected.

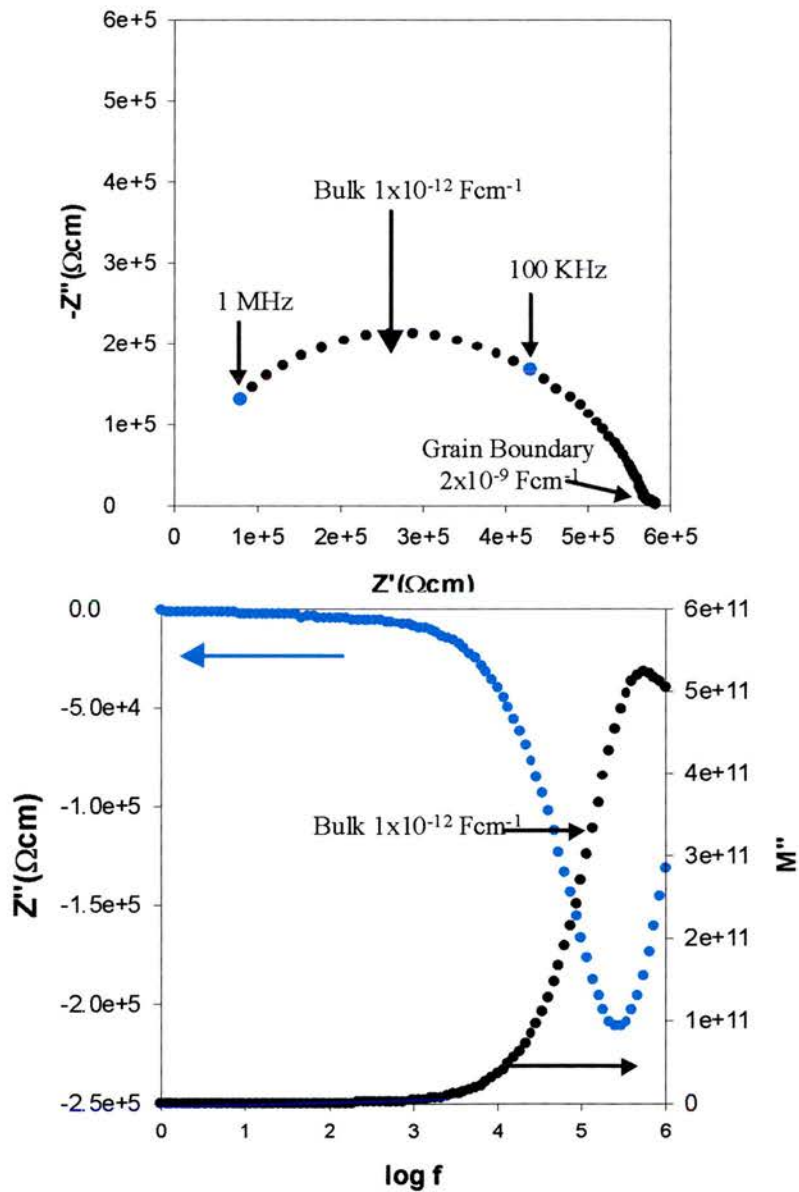


Figure 6.19a. Nyquist plot (top) and the spectroscopic plot of the imaginary contributions of the impedance (Z'') and modulus (M'') (bottom) for $x=0.5$ at 608°C . At this temperature, the bulk clearly dominates the global response.

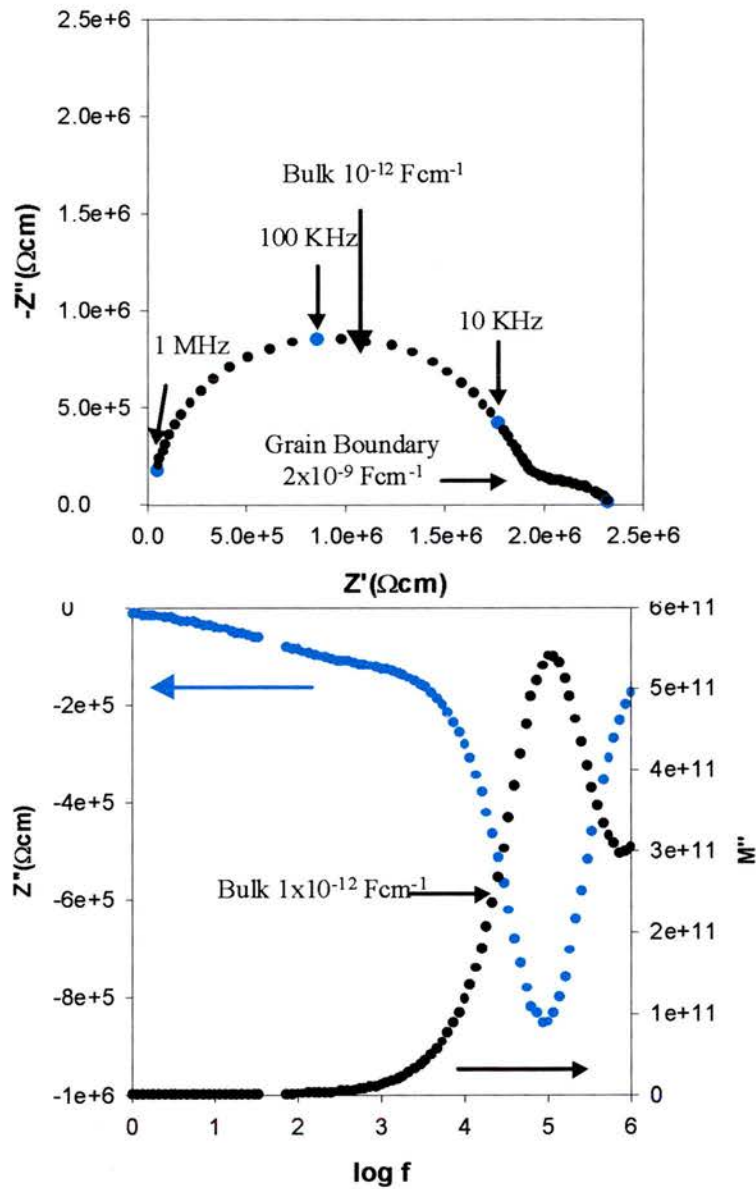


Figure 6.19b. Nyquist plot (top) and spectroscopic plots for the imaginary impedance (Z'') and modulus (M'') for $x=0.5$ at 449°C . The grain boundary becomes gradually more important as the temperature decreases.

Again the spectroscopic plots of the imaginary modulus (M'') reveal the presence of a high frequency electrochemical process assigned to the experimental setup (figure 6.19c).

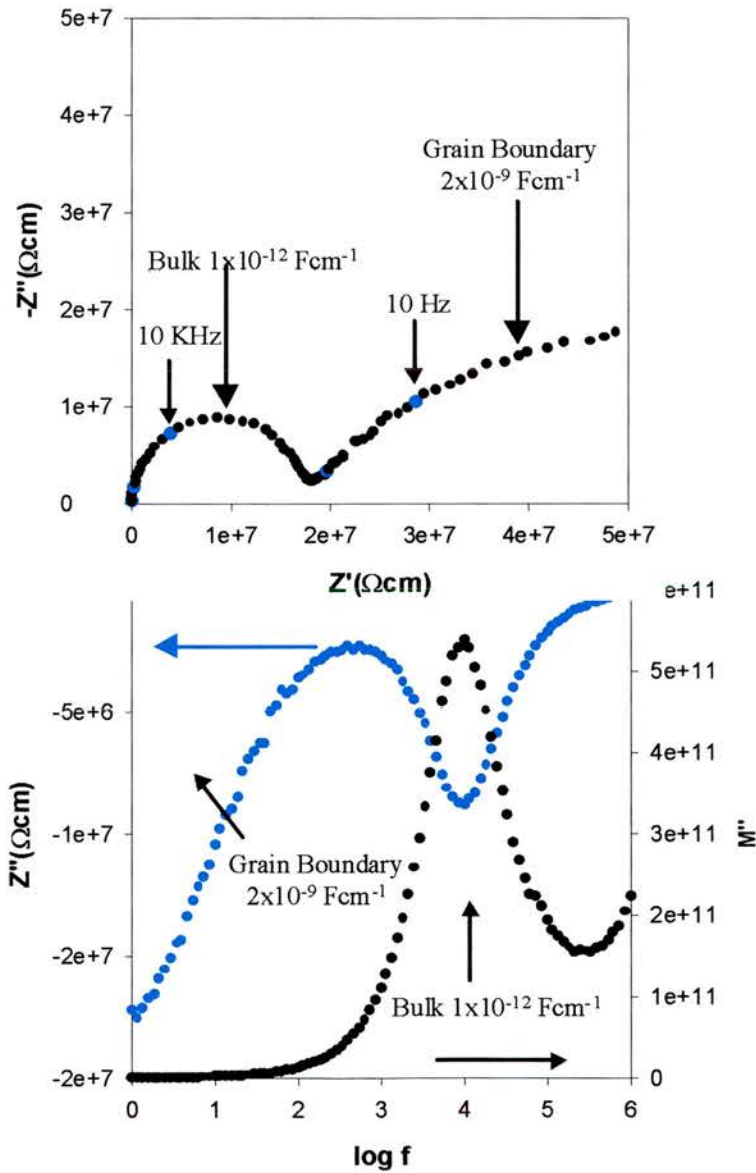


Figure 6.19c. Complex impedance (top) and Z''/M'' spectroscopic plots for $x=0.5$ at 287°C . The grain boundary becomes dominant at low temperatures. The tail that appears in the high frequency range is due to the experimental setup.

It is very important to note that there exists no evidence of ferroelectricity despite the presence of layered domains because the capacitance is constant with temperature and with rather low values. This could imply that although Nb induces the formation of layered phases, the distortion of the octahedra might be different (and smaller) to that caused by La. Further work in Nb-substituted (single) phases is required to prove this.

The corresponding Arrhenius plot (figure 6.20) reveals that the conductivity is increased in comparison to $x=0.3$. Again there is a change in the slope at approximately 600°C and the values of activation energy are almost identical at high temperature. At low temperature there exists a deviation from the previous sample studied, which is due to the importance of the grain boundary contribution at low temperatures. Considering the grain boundary contribution, it can be observed that the bulk conductivity follows the same trends for the two Nb-substituted phases studied, i.e. activation energy of 0.53 eV vs 0.57 eV for $x=0.5$ and $x=0.3$ respectively in the low temperature section. As for the higher conductivity with increasing Nb, the complexity of the system should be noted, i.e. mixture of phases, impeding a simple explanation. However as the same activation energy was found for the two temperature sections, one might think that the only difference between the two phases is the number of charge carriers. As discussed in previous chapters, samples prepared by traditional solid state reaction retain part of the high temperature structure, i.e. they are partially reduced. Nb(V) is quite likely to be reduced to Nb(IV) and therefore the production of electrons will be higher with increasing the Nb content.

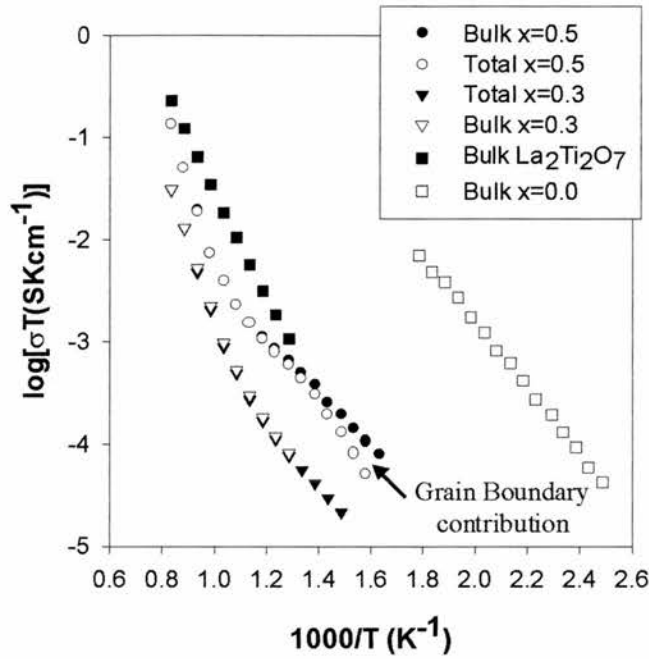


Figure 6.20. Arrhenius plots comparing the conductivity of $x=0.5$ with $x=0.3$, $x=0.0$ and $\text{La}_2\text{Ti}_2\text{O}_7$. At low temperatures the grain boundary contribution causes a change in the activation energy of the total conductivity.

6.4. Conclusions.

The substitution of Ti (IV) by Nb (V) in the pseudo-cubic $n=12$ member of the $\text{La}_4\text{Sr}_{n-4}\text{Ti}_n\text{O}_{3n+2}$ series, results in the formation of layered domains that cohabit with perovskite domains as shown by TEM. The two domains intergrow in an irregular fashion, which presumably may be overcome by annealing at high temperatures for extremely long periods of time.

The formation of layered phases is a consequence of the excess oxygen introduced into the structure when substituting Ti by Nb. This further confirms that the formation of crystallographic shears is mainly due to the excess oxygen concentration and thus it would be possible to produce either pseudo-cubic or layered phases by choosing the appropriate cation in the appropriate amount. This also opens a wide research field on the synthesis and characterisation of new layered structures that may present interesting properties, e.g. ferroelectricity.

Ac impedance spectroscopy reveals that the conductivity drops compared to the non-substituted phase, as expected from samples showing increased layered domains. On the other hand, the global response is dominated by the bulk contribution, especially at high temperatures. This is an improvement vs. the layered phases in the non-substituted series, where in addition to the poor bulk conductivity, the grain boundary limits further the conductivity. Hence, Nb as a sintering aid seems very important and future work will be carried out on the optimisation of the properties of the n=12 member of the parent series by improving the grain boundary response.

No evidence of ferroelectricity was found in the two compositions studied, which could indicate subtle differences in the structure of layered phases, with less distorted octahedra.

The mechanism of conductivity changes at approximately 600°C in both compositions, which may be explained by two contributions to the activation energy, one dominating at low temperature whilst at high temperature both contribute. That

leads to an increase in the activation energy at high temperatures. Perhaps, Nb is easier to reduce/oxidise and hence, there appears a defect creation region. Also the lower migration activation energy in comparison to the parent series is interesting and maybe Nb causes it.

Nb content also plays an important role because the conductivity increases with increasing Nb concentration. Partial reduction of Nb (V) to Nb (IV) at the high reaction temperatures seems to be the most likely explanation. Thus at higher Nb content, there would be more electrons produced, which results in a noticeable increase of the conductivity without showing any changes in the mechanism of conduction since the activation energy is practically identical for $x=0.3$ and $x=0.5$.

An exhaustive study of layered perovskites in niobates would be ideal to contrast with the results extracted from the present work and thus improve our knowledge on layered systems and their potential application as anode materials for fuel cells.

7. Conclusions.

A new family of layered perovskites $\text{La}_4\text{Sr}_{n-4}\text{Ti}_n\text{O}_{3n+2}$ has been investigated and a structural model proposed. The structure can be described in terms of n -layer thick $\{110\}$ perovskite blocks, which are joined by crystallographic shears caused by the oxygen over-stoichiometry. For an odd number of layers, the c -axis is doubled due to reverse tilting ('canting') between consecutive blocks, rendering orthorhombic unit cells.

When n is greater than 6 or even for samples of $n=5$ or $n=6$ that have not been adequately annealed, diverse-sized perovskite blocks co-exist as both XRD and TEM suggest. Annealing for very long periods would presumably yield homogeneous samples containing perovskite blocks of regular size for values of $n>6$.

For n values higher than 11, the layered structure apparently disappears and pseudo-cubic symmetry is achieved. HRTEM studies show that the substitution of Sr^{2+} by La^{3+} on the A-site of a perovskite leads to the presence of randomly distributed linear defects as crystallographic oxygen shears imbedded in the perovskite matrix, where the excess oxygen is accommodated. Therefore, it can be stated that the extra oxygen beyond the ABO_3 stoichiometry in these phases is accommodated in rich oxygen defect regions instead of A-site cation vacancies as was widely believed. At high La content the linear defects become extended and, thereby, detectable by XRD as they become an ordinary feature in the crystal structure, although they can be irregularly distributed as occurs for the intermediate members of the $\text{La}_4\text{Sr}_{n-4}\text{Ti}_n\text{O}_{3n+2}$ family.

AC impedance spectroscopy brings to light a marked difference between layered and pseudocubic phases. The former are very poor electronic conductors presumably due to the oxygen rich layers acting as insulator barriers. The electronic conductivity increases drastically when the oxygen shears become smaller and therefore the conduction paths for the electrons are not interrupted. No traces of diffusion phenomena that may relate to ionic transport can be observed, which indicates that the ionic conductivity, if any, is negligible in comparison to the electronic contribution.

Ferroelectricity must be expected from the 'even layered members' ($n=2k+1$) of the $\text{La}_4\text{Sr}_{n-4}\text{Ti}_n\text{O}_{3n+2}$ series as a consequence of the strong distortion of the TiO_6 octahedra within the slabs, which leads to a permanent polarisation. On the other hand, doubling of the c-axis in the 'odd members' ($n=2k$) causes compensation from one block to the next, cancelling the permanent polarisation of individual blocks. Hence, centrosymmetric unit cells do not show ferroelectricity.

The $n=12$ member ($\text{La}_4\text{Sr}_8\text{Ti}_{12}\text{O}_{38-\delta}$) is an n-type electronic conductor that shows quite promising overall conductivity of 60 Scm^{-1} at room temperature in the most reducing conditions, i.e. 5% H_2/Ar whereas at higher oxygen partial pressure, it undergoes a metal to insulator transition.

Fuel cell tests performed using the $n=12$ member as anode material indicate that this material has a quite good performance (76 mWcm^{-2}), comparable to the state of the art materials, although efforts must be directed to improve both the ionic conductivity and catalytic aspects.

The substitution of Ti by Sc in the B-sites results in the removal of part of the excess oxygen to maintain the electroneutrality. XRD revealed that the unit cell is still a simple cubic perovskite up to levels of substitution of $x=1.0$. At higher levels of substitution mixture of phases appears.

The smaller amount of excess oxygen in Sc-substituted phases causes a reduction in the number and size of the local defects where it is placed until they become so diluted that are scarcely discernible by HRTEM.

The electrical properties are obviously affected and the conductivity drops with increasing Sc content. This seems to be related with Sc facilitating the re-oxidation of Ti^{3+} to Ti^{4+} when ceramic samples are cooled after sintering. As for ionic transport, no diffusion processes are detected by impedance spectroscopy, indicating that the overall response is dominated by the electronic contribution.

A greater excess of oxygen is achieved by substituting Ti by Nb on the B-site, which results in a mixture of phases, i.e. layered and cubic phases. This indicates that excess oxygen (δ) is the driving force that induces the formation of the oxygen rich layers as a regular feature in the structure and also that the value of δ can be controlled. From $La_4Sr_{n-4}Ti_nO_{3n+2}$ series and Sc and Nb-substituted phases, it can be concluded that the transition from layered to random linear defects occurs at $\delta \approx 0.167$.

The presence of layered domains in the Nb-substituted phases renders rather low overall conductivity. However, the grain boundary contribution was greatly improved, and therefore Nb as sintering aid seems very important to optimise the

properties of the higher n members of the parent series by improving the grain boundary response.

The suitability of the cubic phases as anode materials depends upon improvement mainly in two aspects: ionic conductivity and catalytic activity. This could be somehow overcome by using composites as already investigated by Marina *et al.* or, alternatively, by introducing cations such as Mn, Ga or Mg in the B-site. Additionally, the study on the effect of such substitutions in the structure opens a wide scope of research for the near future.

Appendix	231
A.1. Introduction	231
A.2. Transmission Electron Microscopy	234
A.3. Conclusions	244
A.4. References	245

Appendix. TEM studies and image simulation of CaTi_{0.4}Fe_{0.6}O_{3-δ}.

Structural studies by means of TEM were performed on the CaTi_{1-x}Fe_xO_{3-δ} system as part of a collaboration with Dr. Filipe Figueiredo at the University of Aveiro (Portugal) [1]. The interest in these mixed oxides arises from their ability to accommodate oxygen vacancies in order to maintain the electroneutrality when substituting Ti⁴⁺ by Fe³⁺. Ordering of oxygen vacancies has been related with high mixed conductivity [2-4], making these oxides potential materials for high temperature electrochemical applications, in particular gas separation membranes [2,5-7]. The present study is focused on x=0.6 due to the important electrical properties reported in the literature.

A.1. Introduction.

As mentioned in previous chapters the perovskite structure can be described in terms of a three dimensional framework of BO₆ octahedra sharing corners and the larger A cation placed on the 12 co-ordinated sites left by such network. The name of this structure comes after the mineral with the same name, which is no other than CaTiO₃. Ironically, the structure of CaTiO₃ mineral is a distortion from the archetype SrTiO₃, where the TiO₆ octahedra are tilted as shown in figure A.1, which is due to the smaller size of Ca²⁺ in comparison to Sr²⁺. The new unit cell is not cubic but orthorhombic ($\sqrt{2}a_c \times 2a_c \times \sqrt{2}a_c$) with cell parameters a=5.44 Å, b=7.64 Å, c=5.38 Å, space group Pnma.

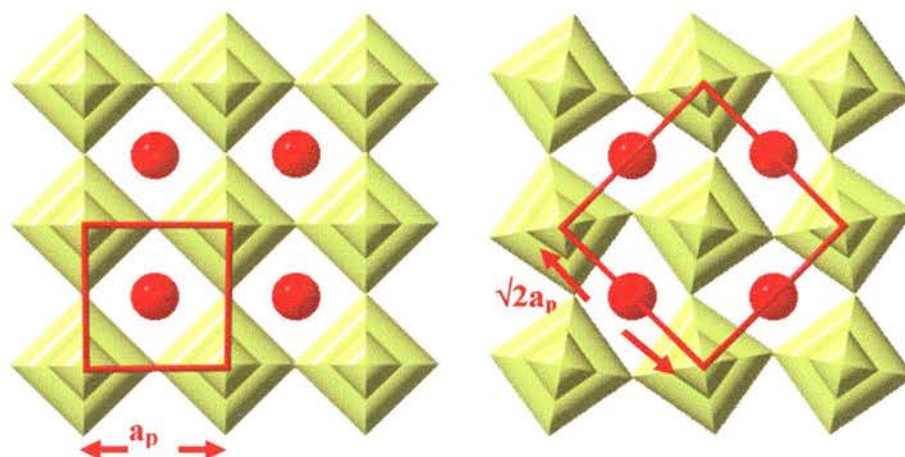


Figure A.1. Schematic representation of the structures of SrTiO_3 (left), CaTiO_3 (right) viewed down the $[010]$ projection.

Further modifications from the parent cubic perovskite may be achieved by substitution with lower valence cations, e.g. Fe, which removes oxygen from the lattice in order to maintain electroneutrality and thus, changing locally co-ordination polyhedra from octahedra to tetrahedra. Oxygen vacancies may be distributed regularly leading to different perovskite superstructures depending on the stacking sequence of the co-ordination polyhedra as described in the pioneering work of Grenier *et al.* [8]. On the other hand, the vacancies may also remain disordered occupying pentacoordinated sites around Fe [8-13].

One of the best-known perovskite-based superstructures involving ordering of oxygen vacancies is brownmillerite, $\text{Ca}_2\text{Fe}_2\text{O}_5$ (figure A.2). The brownmillerite shows an “intergrowth” of octahedra (O) and tetrahedra (T) layers with a stacking sequence along the b -axis of one tetrahedra per octahedra, being consecutive tetrahedra layers orientated in opposite directions, i.e. following a sequence like ...OTOT’OTOT’..., which implies that the b axis is $4a_c$.

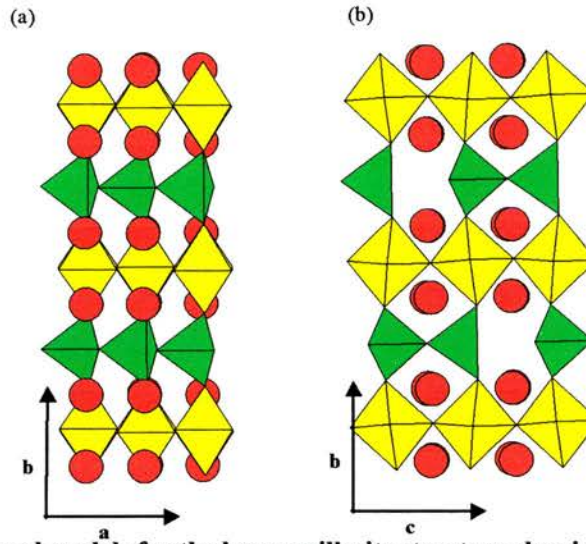


Figure A.2. Structural models for the brownmillerite structure showing clearly the sequence OTOT' along the b -axis ($4a_p$).

In 1976, Grenier and co-workers first described the existence of intergrowth of two or more basic structural motifs in various proportions in intermediate phases between the perovskite CaTiO_3 and the brownmillerite $\text{Ca}_2\text{Fe}_2\text{O}_5$ in the $\text{CaTi}_{1-x}\text{Fe}_x\text{O}_{3-\delta}$ system [14]. In these materials, perovskite-like octahedra layers “intergrow” with tetrahedra layers forming ordered sequences as occurs in the $\text{Ca}_x\text{La}_{1-x}\text{FeO}_{3-y}$ system [15-16]. The facility of this intergrowth can be attributed to the mentioned close relationship existing between the structures of the end members. In fact, it could be regarded as local anion vacancies ordering instead of the intergrowth of different structural motifs. Thus, the a and c axes remain practically unchanged whereas b changes as a function of the stacking sequence.

The border between ordered and disordered phases is a function of the Fe substitution level, the temperature and the oxygen partial pressure. All these three factors determine the concentration of oxygen vacancies in the structure. Indeed, published XRD studies obtained in both oxidised and reduced compositions reveal

large differences. While the reduced phases are orthorhombic, the oxidised counterparts are apparently cubic as reported for the analogous Ca_{1-x}La_xFeO_{3-δ} by Alario-Franco and co-workers in the early 80s [16-19]. These authors, based in detailed TEM studies, suggested that the apparent cubic symmetry was a consequence of sets of microdomains perpendicular to each other of Ca₂LaFe₃O₈ orthorhombic phases. Fe⁴⁺ was believed to exist in the domain walls. Very little has been advanced on the microdomain structure, in particular intergrowths and domain boundaries. These microstructures may be of importance to properties such as electronic or ionic conduction.

Some previous works reported an apparent cubic unit cell (3.87 Å) in samples prepared in air [2,3], although the samples prepared in reducing conditions were indexed with orthorhombic unit cells formed as the result of the long range ordering of oxygen vacancies along the *b*-axis [8,10,12]. The preliminary XRD work performed in the present study revealed that CaTi_{0.4}Fe_{0.6}O_{3-δ} has an orthorhombic unit cell (space group Pcm2₁) with parameters a=5.5295(3) Å, b=11.2045(6) Å and c=5.4379(3) Å, although the much stronger intensity main reflections suggested a pseudo-cubic unit cell.

A.2. Transmission Electron Microscopy

HRTEM studies revealed that CaTi_{0.4}Fe_{0.6}O_{3-δ} is not homogeneous on the nanometer scale. The SAED pattern shown in the inset of figure A.3 reveals d-spacings of 11.2 Å along one of the axes, confirming that a simple cubic unit cell is not sufficient to describe the real structure of this material. The stoichiometric

similarity and the apparent b -axis being $3x a_p$ (a_p is the unit cell parameter of a perovskite) suggest that the unit cell should be similar to that of $\text{Ca}_3\text{TiFe}_2\text{O}_8$ [8]; i.e. $\sqrt{2}a_p \times 3a_p \times \sqrt{2}a_p$ orthorhombic unit cell, space group $Pcm2_1$ with the cell dimensions $a = 5.53 \text{ \AA}$, $b = 11.2 \text{ \AA}$ and $c = 5.44 \text{ \AA}$. In addition diffuse scattering along the b^* axis is clearly observed indicating a disorder phenomenon along that particular direction. Indeed, the corresponding HRTEM (figure A.3) showed a complex irregular intergrowth of two phases, marked as A and B. The former is $\text{Ca}_3\text{TiFe}_2\text{O}_8$ -like since its b -axis is measured to be 11.2 \AA and the other principal axis is about 5.4 \AA . The latter could be considered as a CaTiO_3 -like unit cell, i.e. $\sqrt{2}a_p \times 2a_p \times \sqrt{2}a_p$, as the corresponding d -spacings (7.8 and 5.5 \AA) suggest.

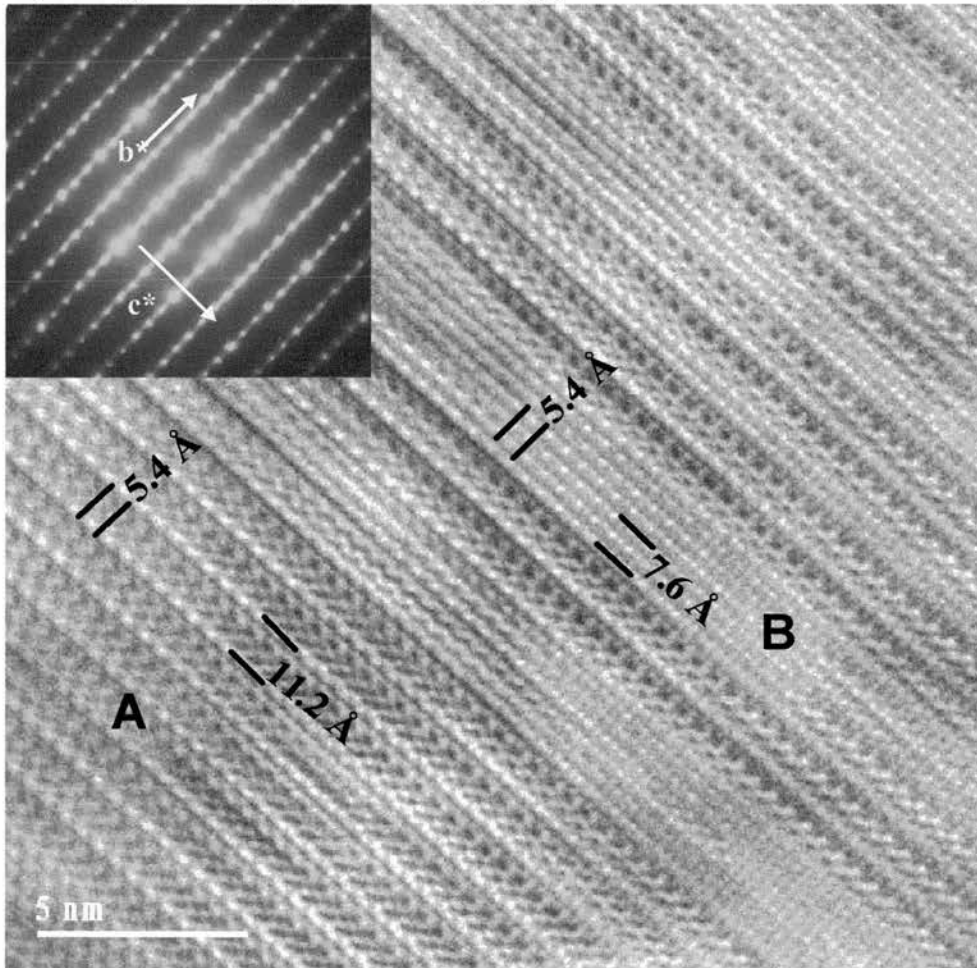


Figure A.3. HRTEM showing the intergrowths of two phases: A – $\text{Ca}_3\text{TiFe}_2\text{O}_8$ and B – CaTiO_3 ($[100]$ zone axis). The inset corresponds to the SAED pattern.

Occasionally some domains showing a longer b axis of 15.5 Å were discernible, which would correspond to a $\sqrt{2}a_p \times 4a_p \times \sqrt{2}a_p$ unit cell (figure A.4). Hence phases with different oxygen vacancy content or, in other words, different stacking sequences cohabit in “ $\text{CaTi}_{0.4}\text{Fe}_{0.6}\text{O}_{3-\delta}$ ”.

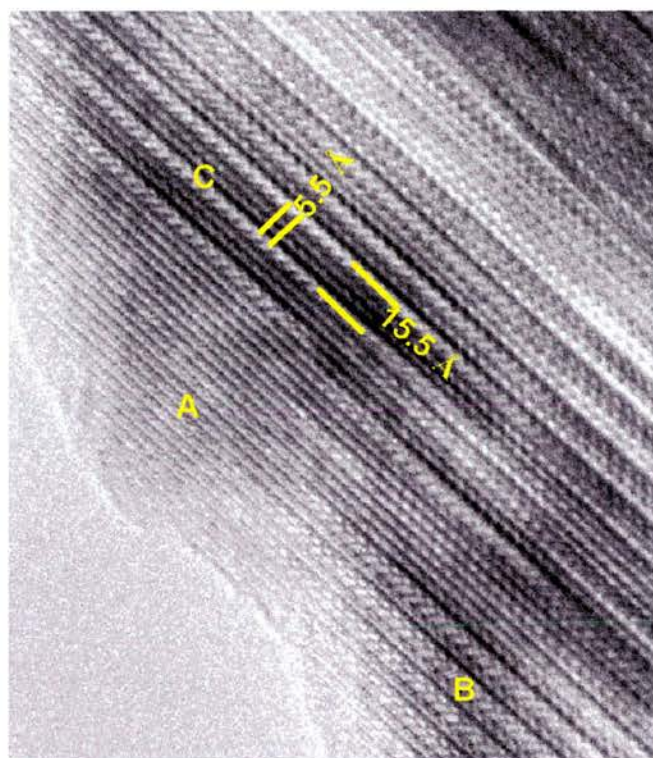


Figure A.4. HRTEM image showing the irregular intergrowths of A- CaTiO_3 , B- $\text{Ca}_3\text{TiFe}_2\text{O}_8$ and C- $\text{Ca}_4\text{Ti}_2\text{Fe}_2\text{O}_{11}$ (d-spacing 15.5Å) viewed down the [001] zone axis.

Investigations carried out in some other crystals revealed predominant $\text{Ca}_3\text{TiFe}_2\text{O}_8$ domains as depicted with a HRTEM image and the corresponding SAED pattern in figure A.5, showing a view on the [101] projection. On the other hand, there existed some domains that corresponded to the CaTiO_3 type structure as can be observed in figure A.6, although in lower concentration. It is worth noting that the corresponding SAED patterns can obviously be indexed with the CaTiO_3 unit cell.

However, simulation of the images indicates the presence of some Fe substituting Ti. Indeed the diamond-shape contrast observed in the experimental image cannot be reproduced if the B-sites are exclusively occupied by Ti. The best result (inset of figure A.6) is achieved when replacing Ti by Fe (which may be hexacoordinated Fe^{3+} or Fe^{4+} and also pentacoordinated Fe^{3+}) in two of the four B-site positions. The atomic positions of the Fe-doped CaTiO_3 unit cell are listed in table A-1.

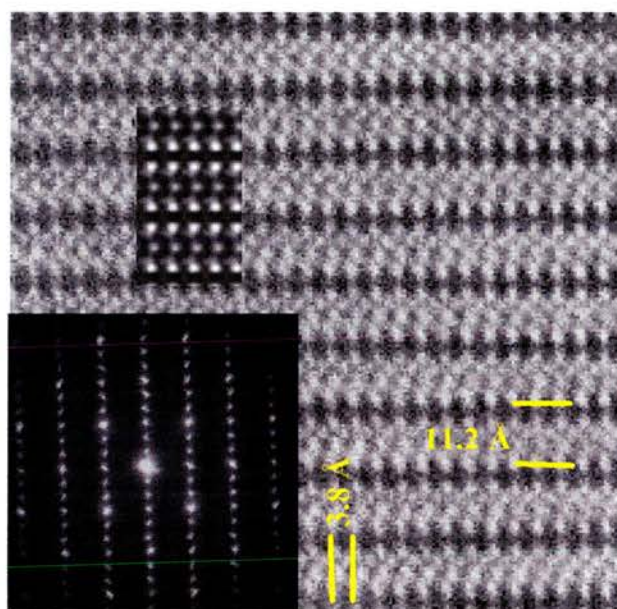


Figure A.5. HRTEM image and corresponding SAED pattern of a $\text{Ca}_3\text{TiFe}_2\text{O}_8$ -like domain along the [101] zone axis. The simulated image was taken at defocus -500 \AA and thickness 101 nm .

According to Grenier *et al.* [8-9], $\text{Ca}_3\text{TiFe}_2\text{O}_8$ is the $n=3$ member of a series of intermediate phases $\text{Ca}_n(\text{Ti,Fe})_n\text{O}_{3n-1}$ between the perovskite CaTiO_3 ($n=\infty$) and the brownmillerite $\text{Ca}_2\text{Fe}_2\text{O}_5$ ($n=2$). As mentioned before, perovskite-like octahedra layers “intergrow” with tetrahedra layers forming ordered sequences, in these materials. $\text{Ca}_3\text{TiFe}_2\text{O}_8$ is formed by inserting a tetrahedra layer out of three, i.e. ...OOTOOT.... (figure A.7). The exact stoichiometry of $\text{Ca}_3\text{TiFe}_2\text{O}_8$ corresponds to lower Ti/Fe ratio in comparison with the composition prepared in the present work. Thus one would also expect the presence of additional phase(s) with higher Ti/Fe ratio

such as $\text{Ca}_4\text{Ti}_2\text{Fe}_2\text{O}_{11}$ if thermodynamic equilibrium was attained, at least if all Fe(III) is assumed. Indeed, although quite rarely, a fringe spacing of about 15.5 Å characteristic of $\text{Ca}_4\text{Ti}_2\text{Fe}_2\text{O}_{11}$ [20] could also be observed (figure A.4). It might therefore seem surprising to see the formation of a Fe containing CaTiO_3 -like phase in addition to the main phase ($\text{Ca}_3\text{TiFe}_2\text{O}_8$) in “ $\text{CaTi}_{0.4}\text{Fe}_{0.6}\text{O}_3$ ”; however, this largely reflects the degree of disorder in high Fe content phases due to the difficulties in achieving extensive long range ordering.

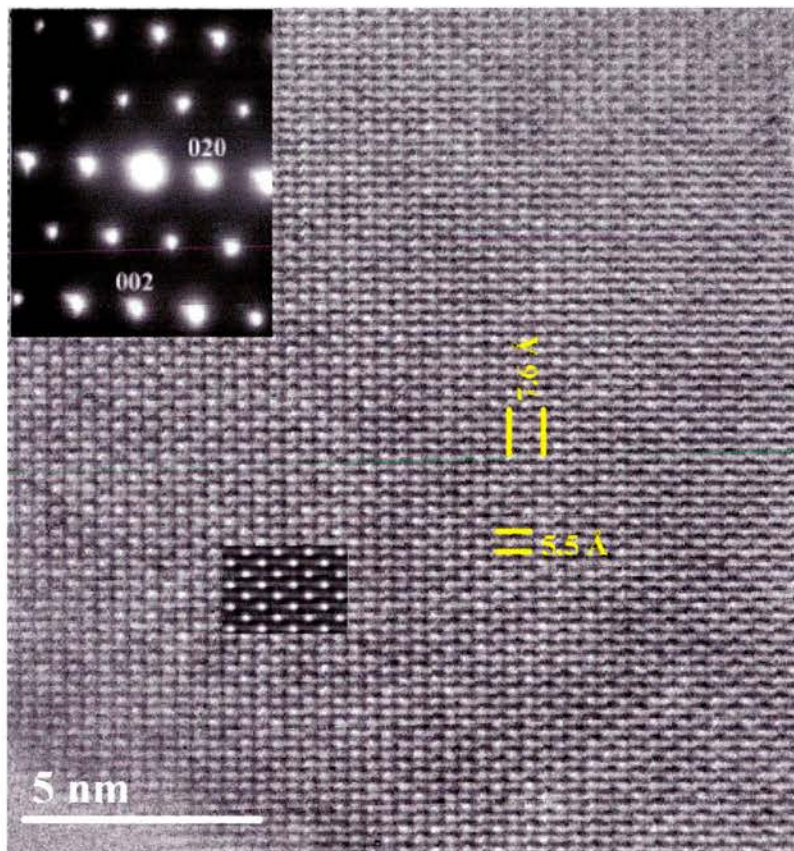


Figure A.6 HRTEM image showing a view down the [100] zone axis on Fe doped $\text{CaTiO}_{3-\delta}$. The two insets show the corresponding SAED pattern and the simulated image (defocus -400 Å, thickness 50 nm) respectively. A model with 20% Fe substitution of the Ti sites in nano-ordered manner was used (see table A-1).

Element	x-coordinate	y-coordinate	z-coordinate	Occupancy factor
Ca	0.00000	0.25000	0.01667	1.00000
Ca	0.50000	0.75000	0.51667	1.00000
Ca	0.00000	0.75000	0.98333	1.00000
Ca	0.50000	0.25000	0.48333	1.00000
Ti	0.00000	0.00000	0.50000	0.60000
Ti	0.00000	0.50000	0.50000	1.00000
Ti	0.50000	0.50000	0.00000	0.60000
Ti	0.50000	0.00000	0.00000	1.00000
Fe	0.00000	0.00000	0.50000	0.40000
Fe	0.50000	0.50000	0.00000	0.40000
O	0.21062	0.95991	0.69931	1.00000
O	0.26438	0.04009	0.22431	1.00000
O	0.73562	0.95991	0.77569	1.00000
O	0.78438	0.04009	0.30069	1.00000
O	0.92172	0.23750	0.49639	1.00000
O	0.07828	0.76250	0.50361	1.00000
O	0.76438	0.45991	0.27569	1.00000
O	0.71061	0.54009	0.80069	1.00000
O	0.23562	0.54009	0.72431	1.00000
O	0.28938	0.45991	0.19931	1.00000
O	0.42172	0.23750	0.00361	1.00000
O	0.57828	0.76250	0.99639	1.00000

Table A-1. Atomic positions for the model CaTiO_3 -like phase used in HRTEM image simulation

in figure A.6. Note that Fe occupies only two of the four B-site positions.

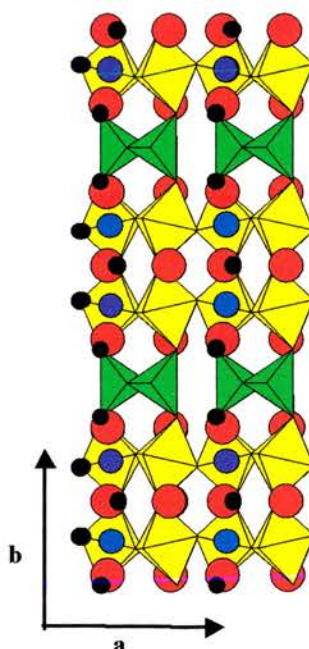


Figure A.7. Structure of $\text{Ca}_3\text{TiFe}_2\text{O}_8$, showing the sequence OOTOOT along the b -axis.

The pseudocubic symmetry suggested by the stronger reflections on the XRD pattern suggests that the above mentioned microdomains are aligned along three

perpendicular directions in such a manner that the symmetry of each set of microdomains is metrically cubic, as $\text{Ca}_3\text{TiFe}_2\text{O}_8$ the major phase [14-15,17]. Indeed, figure A.8 illustrates this situation where the principal diffraction reflections could be indexed considering either $\text{Ca}_3\text{TiFe}_2\text{O}_8$ or CaTiO_3 unit cells on the [010] projections. This could be interpreted as the result of the superposition of two patterns corresponding to two microdomains perpendicular to each other. The existence of diffuse scattering is further evidence of the significant disorder in at least two of the three main axes.

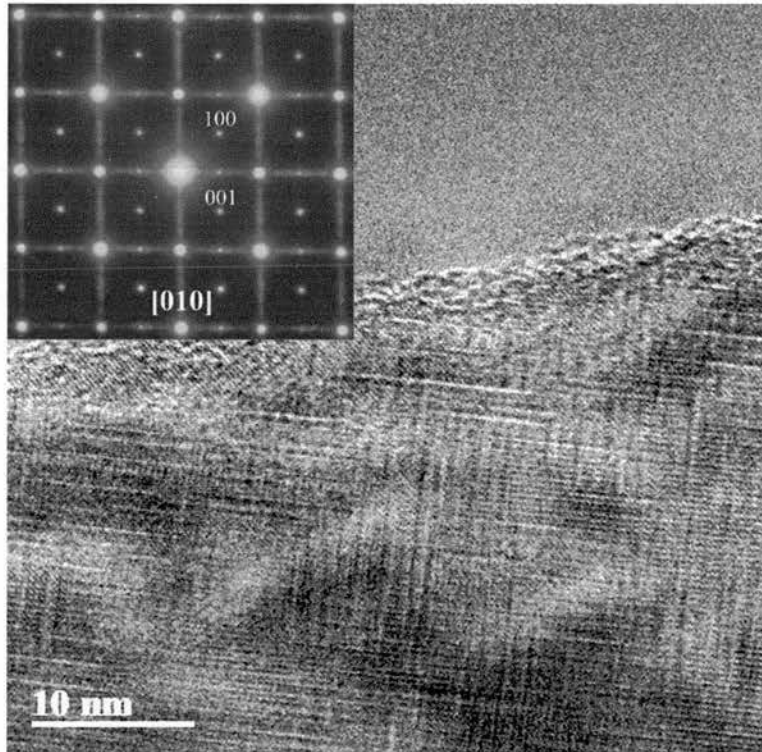


Figure A.8. HRTEM and SAED pattern showing the cubic symmetry of two sets of perpendicular domains viewed down the CaTiO_3 unit cell [010] direction.

To date, it has not been well established how different phases are connected along the b axis. However, connection via oxygen planes seems the most intuitive approach. For the CaTiO_3 phase the choice is quite easy since the oxygen planes are somewhat equivalent. However in the $\text{Ca}_3\text{TiFe}_2\text{O}_8$, there exist several possibilities

arising from the ...OOTOOT... stacking sequence. One might think that because CaTiO_3 is made uniquely from BO_6 octahedra, the most likely oxygen plane to form the interface in $\text{Ca}_3\text{TiFe}_2\text{O}_8$ would be one linking two consecutive octahedra in the stacking sequence. Oxygen planes where tetrahedral co-ordination is involved would be chemically different, although the connection is also possible as occurs for the brownmillerite $\text{Ca}_2\text{Fe}_2\text{O}_5$. Therefore the model of the intergrowth was built by joining the two separated unit cells on an oxygen plane as marked in figure A.10 and then the images were calculated for the operating conditions. As can be observed in figure A.10, the fitting is satisfactory in this case. Other possibilities, including O-T connection, were also attempted leading to simulated images that did not correspond to the experimental one.

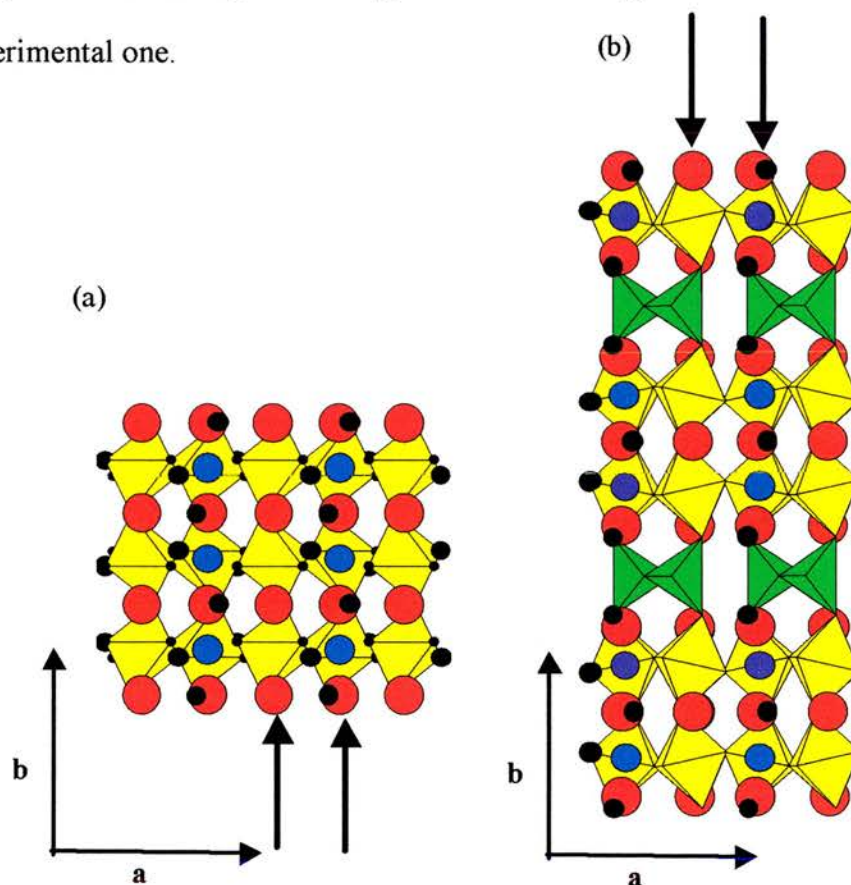


Figure A.9. Structural models for CaTiO_3 (a) and $\text{Ca}_3\text{TiFe}_2\text{O}_8$ (b). The arrows indicate the oxygen planes shared in the interface.

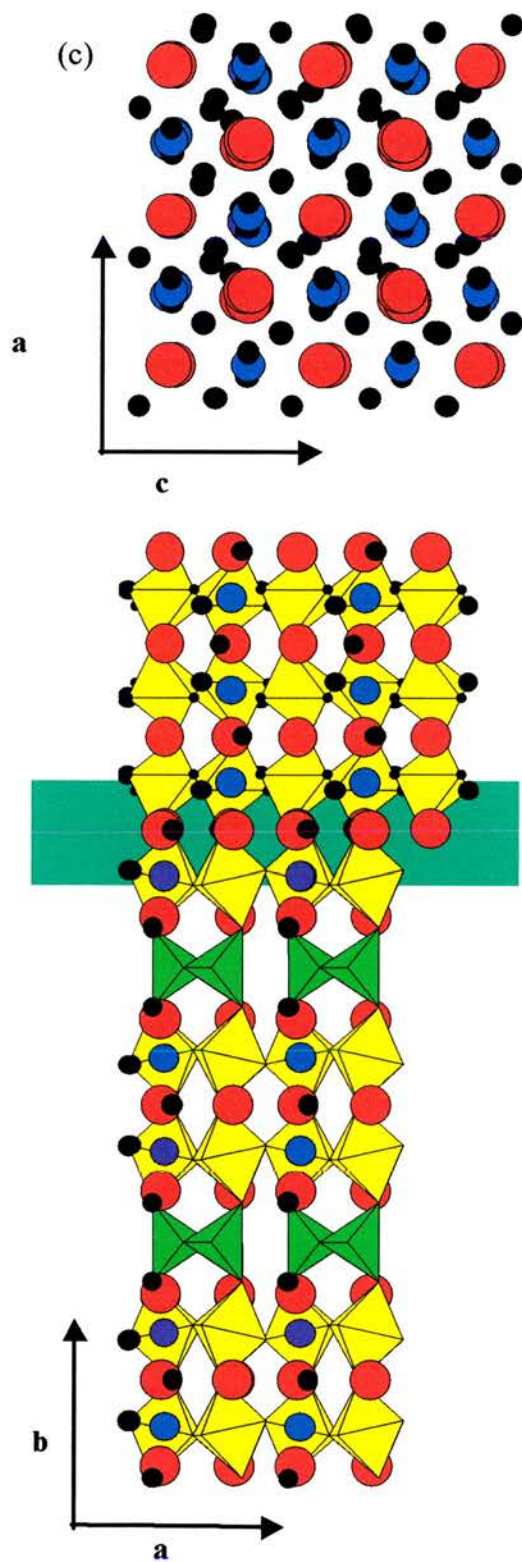


Figure A.9c shows the projection down the [010] of a superposition of the structural motifs involved in the intergrowth, whilst figure A.9d. shows a schematic structural model of the intergrowth of the two phases along the b -axis.

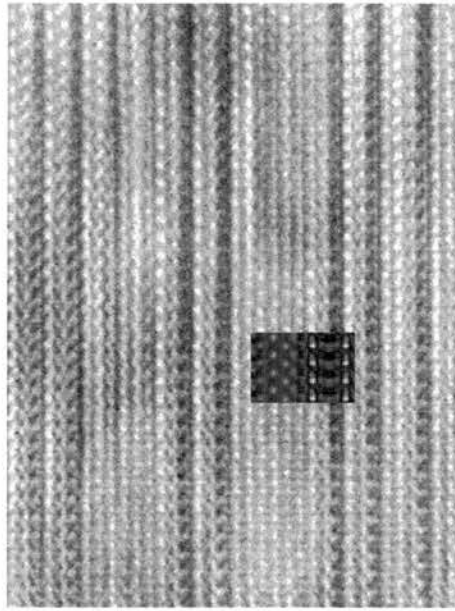


Figure A.10. HRTEM image of the intergrowth region with the corresponding simulated image.

The experimental conditions were found to be: defocus -430 \AA and thickness 53 nm .

Alario-Franco and co-workers [16] suggested that domain walls play a decisive role in accommodating the excess oxygen in the analogous calcium-lanthanum ferrite system. Therefore, an O-O join at the domain boundaries would be a strong justification for Fe^{IV} at those specific locations.

Contrary to the calcium lanthanum ferrite, the structure in the bulk Ti-containing materials is very inhomogeneous. This is perhaps because the extent of the excess oxygen is much smaller in this case with overall stoichiometry of $\text{CaTi}_{0.4}\text{Fe}_{0.6}\text{O}_{2.71}$ as determined by coulometry [4] and consistent with the Mössbauer data presented in ref [1].

Therefore, changes in the oxygen stoichiometry should be reflected not only in the size as suggested for $\text{Ca}_2\text{LaFe}_3\text{O}_{8.235}$ [14,17], but also in the level of structural inhomogeneity in the bulk of the domains. Moreover, the microdomain textured

$\text{Ca}_{0.63}\text{La}_{0.37}\text{FeO}_{3-\delta}$ phase was obtained after quenching from high temperature (1400°C) in air, while $\text{CaTi}_{0.4}\text{Fe}_{0.6}\text{O}_{2.71}$ forms during the cooling down process [14]. One further difference between the iron based-phases and the Fe-substituted titanates is the presence of Ti^{4+} , which facilitates the occurrence of perovskite-like domains, possibly including some Fe^{4+} .

A.3. Conclusions.

The structure of Fe^{4+} -containing perovskite-based oxides ($\text{CaTi}_{1-x}\text{Fe}_x\text{O}_3$) may be very different from that observed in the same material prepared under reducing conditions. In such cases, the first apparent difference is often found in routine powder XRD analysis. The pattern of the oxidised samples seems to correspond to that of a pseudocubic unit cell whilst lower symmetry is clearly evident for the totally reduced compounds. In a superficial analysis, the differences are simply interpreted as an increase in symmetry for the oxidised samples. However, TEM reveals a far more complex structure characterised by a microdomain texture where the domains are aligned perpendicularly along the three axes. The average symmetry of such domain network is, at least metrically, cubic although the symmetry of the domains themselves is orthorhombic. TEM studies showed that such structural arrangement is also apparent for $\text{CaTi}_{0.4}\text{Fe}_{0.6}\text{O}_{3-\delta}$. Different domains are connected via oxygen planes within an octahedral environment as corroborated by simulation of HRTEM images. These domains consist in irregular intergrowths of orthorhombic CaTiO_3 - and $\text{Ca}_3\text{TiFe}_2\text{O}_8$ -like phases along the b axis.

These results are consistent with the Mössbauer spectra studied by Dr. Figueiredo and Dr. Waerenborgh, and show that the structure is sensitive to a fraction of Fe^{4+} as low as ca. 4% of the total amount of Fe. The high level of disorder within the microdomains suggests that the excess oxygen may be accommodated not only at the domain walls and the minority CaTiO_3 -layers, but also in the border regions of the intergrown phases. This could be also a consequence of the short time (2 h) given to homogenise the material at high temperature.

A.4. References.

1. J. Canales-Vázquez, F. M. Figueiredo, J. C. Waerenborgh, W. Zhou, J. R. Frade and J. T. S. Irvine, submitted to *Chemistry of Materials*.
2. H. Iwahara, T. Esaka and T. Mangahara, *J. Appl. Electrochem.*, **18** (1988), 173.
3. D. Sutija, T. Norby, P. A. Osborg and P. Kofstad, *Electrochem. Soc. Proc.*, eds. S. C. Singhal and H. Iwahara: Electrochemical Society, **93-4** (1993), 552.
4. F. M. Figueiredo, J. C. Waerenborgh, V. V. Kharton, H. Näfe and J. R. Frade, *Solid State Ionics*, **156** (2003), 371.
5. T. Esaka, T. Fujii, K. Suwa and H. Iwahara, *Solid State Ionics*, **40/41** (1990), 544.
6. H. Itoh, H. Asano, K. Fukuroi, M. Nagata, H. Iwahara, *J. Am. Ceram. Soc.*, **80**[6] (1997), 1359.
7. F. M. Figueiredo, V. V. Kharton, J. C. Waerenborgh, A. P. Viskup, E. N. Naumovich and J. R. Frade, *J. Am. Ceram. Soc.*, in press.

8. J. C. Grenier, G. Schiffmacher, P. Caro, M. Pouchard and P. Hagenmuller, *J. Solid State Chem.*, **20**, 365-379 (1977).
9. J. C. Grenier, M. Pouchard, P. Hagenmuller, G. Schiffmacher, P. Caro, *J. Physique Colloque*, **C7 38** (1977), CA.
10. A. I. Becerro, C. A. McCammon, F. Langenhorst, R. J. Angel, F. Seifert, *Phase Transitions*, **69** (1999), 133.
11. McCammon, A. I. Becerro, F. Langenhorst, R. J. Angel, S. Marion, F. Seifert, *J. Phys.: Condens. Matter.*, **12** (2000), 2969.
12. A. I. Becerro, F. Langerhorst, R. J. Angel, S. Marion, C. A. McCammon, F. Seifert, *Phys. Chem. Chem. Phys.*, **2** (2000), 3933.
13. J. C. Waerenborgh, F. M. Figueiredo, J. R. Frade, M. T. Colomer, J. R. Jurado, *J. Phys.: Condens. Mat.*, **13** (2001), 8171.
14. J. C. Grenier, J. Darriet, M. Pouchard and P. Hagenmuller, *Mater. Res Bull.*, **11** (1976), 1219.
15. J. C. Grenier, F. Menil, M. Pouchard and P. Hagenmuller, *Mater. Res. Bull.*, **12**, 79 (1977)
16. M. A. Alario-Franco, M. J. R. Hence, M. Vallet-Regí, J. M. González-Calbet, J. C. Grenier, A. Wattiaux and P. Hagenmuller, *J. Solid State Chem.*, **46** (1983), 23.
17. M. A. Alario-Franco, J. M. González-Calbet, M. Vallet-Regí and J. C. Grenier, *J. Solid State Chem.*, **49** (1983), 219.
18. J. M. González-Calbet, M. Vallet-Regí, M. A. Alario-Franco and J. C. Grenier, *Mater. Res. Bull.*, **18** (1983), 285.

19. J. C. Grenier, M. Pouchard, P. Hagemuller, M. J. R. Henche, M. Vallet-Regí, J. M. González-Calbet and M. A. Alario-Franco, *R. Chimie Minérale*, **20** (1983), 726.
20. S. Hövmoller, X. Zou, D. Neng Wang, J. M. González-Calbet and M. Vallet-Regí, *J. Solid State Chem.*, **77** (1988), 316.